Processes Driving Non-Maxwellian Distributions in High Energy Density Plasmas

Arthur Edward Turrell

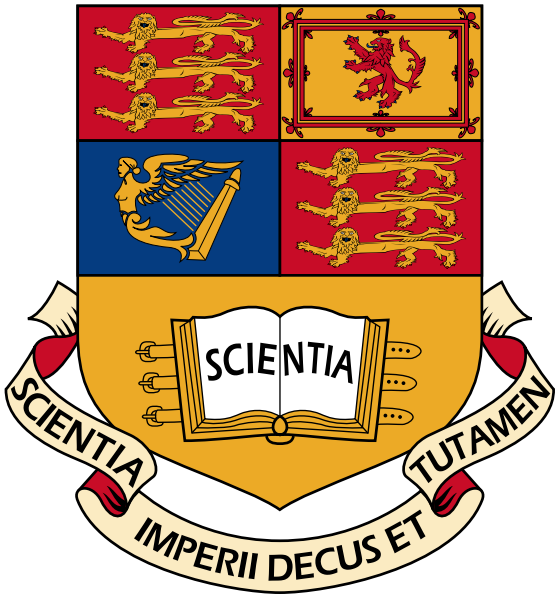

Submitted in partial fulfillment of the requirements for the degree of Doctor of Philosophy of Imperial College London.

Department of Physics

The Blackett Laboratory

Imperial College

London

SW7 2BZ

July 2013

Dedicated to the memory of my father.

Copyright Declaration

Declaration of Originality

I hereby certify that the material in this thesis, which I submit for the degree of Doctor of Philosophy, is entirely original unless otherwise cited or acknowledged in the text.

Arthur Edward Turrell

29/07/2013

Acknowledgements

My first thanks are to my family and step-family, who have only ever asked that I do my best, and who have always given me the freedom to learn for myself, and to choose my own path.

I used that freedom to go to university. This was an unusual choice at my school, where few went on to do A-levels, and only 43% left with five good GCSEs, but it was undoubtedly the single best choice I have ever made. I had no idea what a joy getting an education would be, or how it would improve my life.

I wish to thank St. Aidan's College, University of Durham, for taking a chance by offering me a place to study Natural Sciences when all that I had to offer *vis á vis* mathematics qualifications was a rather underwhelming GCSE. I learnt a great deal in Durham, and not only about mathematics and physics.

I would also like to thank Selwyn College, University of Cambridge, for providing such an exciting academic atmosphere, rigorous mathematical training, and, most importantly, many of my close friends. My short time there was very difficult, due to the loss of two close family members, but it opened many doors, including the one that led to the plasma physics group at Imperial College.

Whilst undertaking my PhD at Imperial, I have been aided by useful discussions with many talented physicists. A special mention should be made of my HEDP colleagues; Ed Hill's input has been valuable on countless occasions, and I have had many useful conversations with Oliver Pike. I am also indebted to my partner, friends, and office mates, for providing welcome distractions throughout the last few years.

My two supervisors, Steve Rose and Mark Sherlock, have shown relentless enthusiasm for my work during my PhD, even when mine has temporarily faltered. I am extremely grateful to them for the time and effort they have spent helping me, and for their guidance, which has allowed me to develop as an independent academic. Their ideas, suggestions, support, and impressive knowledge of physics, have been absolutely crucial to the development of this thesis.

Abstract

The purpose of this thesis is to explore the driving of non-Maxwellian distributions of particles in high energy density plasmas in a few select cases, with particular reference to efforts to produce a net gain in energy via inertial confinement fusion (ICF).

Non-Maxwellian distributions are typically short-lived, as distributions are forced toward equilibrium by collisions, and are rarely static as a net transfer of energy must occur to sustain them. This makes non-Maxwellian distributions challenging to study with conventional approaches to plasma physics. The strategy adopted in this work to understand their evolution, and their effects, is a kinetic approach in which particles are individually accounted for.

The specific cases presented are that of degenerate electrons during the heating of the cold fuel shell in hotspot ignition schemes, ion-ion inverse bremsstrahlung absorption of laser radiation, and large-angle Coulomb collisions. New computational algorithms based on the Monte Carlo technique are presented, and are capable of modelling the salient aspects of the phenomena explored. Important results which form part of this thesis include that conventional models underestimate degenerate electron temperatures long after the plasma ceases to be degenerate, that it may be possible to induce temperatures of keV in light-ion species with high power, short pulse lasers, and that consideration of large-angle collisions changes interactions in a plasma in several significant ways. Of most interest are the ability of large-angle collisions to decrease equilibration times, drive athermal tails on distribution functions, and increase the overall yield from fusion reactions relative to small-angle only simulations.

Conventions and Symbols I

Symbol	Description
i, j, k	Species or particle labels
q_i or Z_i	Charge or atomic number of particle of species i in units of e
T_i	Temperature of species i in units of energy
m_i	Mass of particle of species i
n_i	Number density of species i
N_i	Number of particles, or simulation particles, of species i
r_i	Particle sphere radius of species i, $r_i = (4\pi n_i/3)^{-1/3}$
r_0	Total particle sphere radius, $r_0 = \left(\sum r_i^{-3}\right)^{-1/3}$
m_{ij}	Reduced mass of species i and j, $m_{ij} = m_i m_j/(m_i + m_j)$
ρ	Mass density; **or** charge density; **or** resistivity
$\mathbf{v}$	Velocity
$\mathbf{v}_{ij}$	Relative velocity between i and j, $\mathbf{v}_{ij} \equiv \mathbf{v}_i - \mathbf{v}_j$
$v_{i,\mathrm{th}}$	Thermal speed of species i, $v_{i,\mathrm{th}}^2 = 3T_i/m_i$
λ_D	Debye length, $\lambda_\mathrm{D}^2 = \sum \frac{\epsilon_0 T_i}{n_i q_i^2 e^2}$
λ_dB	The de Broglie wavelength, $\lambda_\mathrm{dB} = \hbar/\left(2m v_\mathrm{th}\right)$
λ_C	Compton wavelength, $\lambda_\mathrm{C} = h/\left(mc\right)$
N_D	Number of particles in a Debye sphere, $N_\mathrm{D} = \frac{4}{3}\pi n_e \lambda_\mathrm{D}^3$
g	Plasma coupling parameter, $g = 1/(n_e \lambda_\mathrm{D}^3)$
ω_{pe}	Plasma frequency, $\omega_{pe} = (n_e e^2/\epsilon_0 m_e)^{1/2}$
$\ln \Lambda_{ij}$	Coulomb logarithm between i and j
$f_i(\mathbf{x}, \mathbf{v}, t)$	Distribution function of species i
$\mathcal{C}(x)$	Cumulative density function, $\mathcal{C}(x) = \int_0^x f(x')\mathrm{d}x'$
$f_\mathrm{MB}(\mathbf{v})$	Maxwell-Boltzmann distribution
$f_\mathrm{MC}(\mathbf{v})$	Distribution from Monte Carlo simulation
$f_\mathrm{FD}(\mathbf{v})$	Fermi-Dirac distribution
η	Degeneracy parameter
$\psi(\mathbf{r}, t)$	Wavefunction at position $\mathbf{r}$ and time t
$\mathbf{E}$	Electric field strength
$\mathbf{B}$	Magnetic field flux density
$\mathbf{J}$	Current density
I	Intensity
n_c	Relativistic critical density
a_0	Dimensionless electric wave strength parameter
$\dot{W}$	Absorption or emission in units of energy per unit time per unit volume

Conventions and Symbols II

Symbol	Description
ρR	Areal density
dsr	Down-scattered neutron ratio
ϕ	Electric potential; **or** azimuthal angle in spherical co-ordinates $0 \leq \phi < 2\pi$
θ	Scattering angle in c.o.m. frame; **or** polar angle in spherical co-ordinates $0 \leq \theta \leq \pi$
χ	Scattering angle in the laboratory frame
b	Impact parameter
$b_\perp$	Impact parameter for scattering through $\pi/2$ (species labels suppressed)
b_ϕ	Impact parameter based on solving potential equation (species labels suppressed)
b_c	Cut-off impact parameter (species labels suppressed)
θ_c	Cut-off in angle (species labels suppressed)
$\frac{\mathrm{d}\sigma}{\mathrm{d}\Omega}$	Differential cross-section
σ	Total cross-section; **or** standard deviation of distribution
μ	Mean of distribution: discrete, $\mu = \frac{1}{N}\sum_i^N x_i$, or continuous, $\mu = \frac{1}{b-a}\int_a^b xf(x)\mathrm{d}x$
μ_n	nth centralised moment of distribution function, $\mu_n = \int (x-\mu)^n f(x)\mathrm{d}x$
κ	Excess kurtosis, $\kappa = \mu_4/\sigma^4 - 3$
$X \sim \mathcal{N}(\mu, \sigma^2)$	X distributed normally with mean μ and standard deviation σ
$U \sim \mathcal{U}(a, b)$	Random number U uniformly distributed on (a, b)
$k \in \mathbb{Z}$	k is a member of the integers
$k \in \mathbb{N}$	k is a member of the natural numbers excluding zero
$\lfloor x \rfloor$	Largest integer not greater than x, $\lfloor x \rfloor = \max\{m \in \mathbb{Z} \,\vert\, m \leq x\}$
$\langle x \rangle$	Average of quantity x
δ_{ij}	Kronecker 'delta function'
$\delta(x)$	Dirac 'delta function'
$\alpha, \beta, \gamma, ...$	Vector and tensor indices
$\epsilon_{\mu\nu\kappa}$	Levi-Civita symbol (anti-symmetric)
t	Time
Δt	Computational timestep in finite difference scheme
w	Particle weighting in computation, $w = n/N$
c	Speed of light *in vacuo*, 2.9979×10^8 m s^{-1} in S.I. units
ϵ_0	Permittivity of free space, 8.8542×10^{-12} F $\cdot$ m^{-1} in S.I. units
μ_0	Permeability of free space, $4\pi \times 10^{-7}$ N $\cdot$ A^{-2} in S.I. units
e	Absolute value of the electronic charge, 1.6022×10^{-19} C in S.I. units
$\hbar$	Reduced Planck's constant, $\hbar = h/2\pi = 6.63 \times 10^{-34}/2\pi$ J $\cdot$ s in S.I. units
α_f	Fine structure constant, $\alpha_f = 1/137 = e^2/(4\pi\epsilon_0\hbar c)$

Contents

List of Figures

List of Tables

Chapter 1

Introduction

This thesis aims to explore the driving of non-Maxwellian distributions in high energy density plasmas. The plasma conditions examined are similar to those encountered in attempts to achieve a net gain in energy from inertial confinement fusion (ICF) experiments at the US National Ignition Facility (NIF). The results are split into three different topics: electron degeneracy, ion-ion inverse bremsstrahlung absorption, and large-angle collisions. The consequences of the driven non-Maxwellian distributions studied include changing the rate of fusion reactions, decreasing the rate of absorption of laser energy, accelerating inter-species equilibration, and modifying transport coefficients.

This Chapter is concerned with the motivation for, and background to, the research undertaken. §1.1 explains the origins of nuclear fusion, and the continued attempts to turn fusion into an energy source. §1.2 explains the arguments for fusion as a power source, particularly from the point of view of meeting Earth's energy needs in the future and preventing climate change by offering a clean alternative to fossil fuels. Details of the basic physics of a self-sustaining fusion reaction - a situation known as ignition - are discussed in §1.3, including the energy balance in a 'burning' plasma, and an overview of the stages of an ICF plasma as envisaged on NIF. A summary of the content of subsequent chapters can be found in §1.4.

1.1 Nuclear fusion

Nuclear fusion is the process whereby two ions coalesce to form new ions and an amount of energy proportional to the total change in mass is released, as according to Einstein's mass-energy equivalence principle. This release of energy powers all stars, and has the highest energy density of any abundant fuel.

The pioneering science fiction author H. G. Wells is sometimes credited with predicting the nuclear age, as it is the premise of a story he published in 1914 [1]. However, it was Eddington who realised that Einstein's mass-energy equivalence principle meant that nuclear reactions could be the source of the Sun's energy. He made a prescient speech on the topic [2], arguing in 1920 that

> "If, indeed, the sub-atomic energy in the stars is being freely used to maintain their great furnaces, it seems to bring a little nearer to fulfillment our dream of controlling this latent power for the well-being of the human race, or for its suicide."
>
> – A. Eddington

Ernest Rutherford, discoverer of the structure of the atom, was not convinced, saying in 1933 that nuclear energy was "moonshine" [3]. However, three of the four in the nuclear quartet of a nuclear fission reactor, nuclear fission bomb, and nuclear fusion (or hydrogen) bomb had been demonstrated by 1952, with only nuclear fusion left.

There were pioneering but poorly funded attempts to build controlled nuclear fusion devices right at the dawn of the nuclear age: in the US in 1938 [3], in Oxford in 1939 by Peter Thonemann, and by George Thompson and Moses Blackman at Imperial College in 1946, who filed a patent for a 'pinch' device [4, 5]. Two doctoral students at Imperial College began the UK's experimental campaign by building a small device in 1949. However, it was Argentina which really stimulated research into controlled fusion by claiming to have achieved it in 1951 [6]; the claim turned out to be false but the headlines prompted better funded research in the UK, US, and the then USSR. Edward Teller, recalling his time working on the first hydrogen bomb in 1952, said [7]

> "No sooner was it done than every politician and every bureaucrat descended upon us saying, 'Now you must solve the problem of controlled fusion'."
>
> – E. Teller

Fusion research then began in earnest worldwide. Two strategies for confinement of the ionised material, plasma (the subject of Chapter 2), emerged; one using magnetic fields, and the other using implosions of fuel to create the densities and temperatures in which fusion reactions become self-sustaining. The problem of containing plasma for the length of time required for fusion reactions to occur was succinctly described by Edward Teller in 1954 as being [8]

"...like trying to confine jelly with rubber bands."

– E. Teller

Teller said this after it became clear that controlled thermonuclear fusion would be far more difficult to achieve than any of the other parts of the nuclear quartet. The two methods for confining plasma are known as magnetic confinement fusion (MCF) and inertial confinement fusion (ICF), both of which aim to achieve a net gain in energy from the deuterium-tritium fusion reaction.

This thesis is more concerned with ICF, which uses the inertia of the fuel to provide confinement for just long enough for fusion reactions to take place. The conditions for fusion created by radiation initiated implosion were first suggested by Klaus Fuchs in 1946, before he was arrested for spying on the US for the USSR. Stanislaw Ulam at Lawrence Livermore National Laboratory (LLNL) continued the work, and the first hydrogen bomb used the 'Teller-Ulam configuration' whereby a fission explosion creates a large radiation field which, via ablative pressure, compresses fuel and ignites fusion reactions. Both the US and USSR desperately sought peaceful applications of the enormous release of energy, including, incredibly, landscaping and sealing out-of-control oil wells [2].

Another of the more unusual proposals was setting off a series of hydrogen bombs in an underground chamber in order to produce energy. The number of bombs required to do this for practical power generation is, and was considered at the time to be, both impractical and fearsome. One of the scientists working on this idea, for Teller, was J. Nuckolls who joined LLNL in the late 1950s [9]. His job was to calculate just how many bombs it would be possible to explode before the rubbish accumulating at the bottom of the chamber went critical. While Teller thought that bigger was better, Nuckolls began to think that smaller bombs might be more sensible, and decided to calculate just how small a fusion explosion it was possible to make. The idea of ICF came to Nuckolls at this time, and he realised that a capsule of fuel just a few millimetres across could still explode and release a more manageable amount of energy. But there was a problem - how could such a small pellet of fuel be driven? To be a politically acceptable and commercially viable source of energy, the small fusion explosions would need to be entirely separate from fission explosions.

In 1960, T. Maiman built the first laser [10] and Nuckolls immediately saw that it could be the non-nuclear driver of fusion that was needed to make controlled thermonuclear inertial confinement viable. Between 1960 and 1972, Nuckolls worked on an idea called indirect-drive, where radiation is absorbed and re-emitted before compressing the fuel, but his

work was classified. The idea of using lasers to drive fusion had also occurred to scientists in Britain, where, again, it was classified. Two Soviet scientists also proposed the idea of inertial confinement fusion in 1963 [2]. In 1972, Nuckolls was permitted to publish a paper which explained how laser compression of deuterium and tritium could work but, in order to get past the censors, he had to say that the laser illuminated the fuel directly, rather than indirectly in the manner he had actually been considering. While much of the work in Britain, the US, and USSR was still conducted in secret, countries with no such classification were beginning to do research too. Japan was openly publishing by the 1980s, which was frustrating for those working on ICF in secret in other countries, including Paul Drake and John Lindl at LLNL in the US [8],

> "You could follow their learning curve. We could have saved them five years of work."
>
> – J. Lindl

Secret experiments were undertaken in the late 70s, and throughout the 80s, by the UK and the US. Though many of the details are still classified, pioneering experiments led by S. Rose and P. Roberts from the UK demonstrated the first successful implosions of fusion targets in the 1980s [11] and so proved the concept of small scale radiation implosion. A subsequent US experiment obtained similar results, and determined that laser energies of 20 – 100 MJ would be required to ignite capsules [2]. A report on the US programme states that the tests

> "...demonstrated excellent performance, putting to rest fundamental questions about the basic feasibility of achieving high gain."

ICF, and its eventual goal of inertial fusion energy (IFE), has been pursued ever since via a sequence of experimental campaigns on lasers capable of delivering larger and larger amounts of energy to a target. A system capable of delivering an energy of 1.8 MJ to a target has been built, and is known as the National Ignition Facility (NIF), and a similar machine, Laser Mégajoule (LMJ), is being constructed in France. The goal of NIF is to achieve ignition, that is to create a self-sustaining wave of fusion reactions in an ICF fuel capsule with a scientific gain in energy of one. This means as much energy is produced from fusion reactions as is originally delivered to the target. Though this is different from a true 'wall plug' gain, in which the inefficiencies of the laser system are taken into account, or indeed from the gain needed for commercial feasibility, it is the first and necessary step in demonstrating the potential of ICF. The basic physics of ignition, and of ICF, are described in §1.3.

1.2 The need for fusion

There are compelling arguments for developing nuclear fusion as a power source. The strongest is that the fuels currently relied upon to provide electricity, and most other forms of energy, are not sustainable and will eventually run out. These include coal, oil, and gas of which there are proven reserves for 162, 51, and 56 years respectively using known reserves and consumption levels at the end of 2012 [12]. Coal, oil, and gas currently make up 87% of world primary energy consumption. Proven reserves may not reflect the true amount of a fuel which is left, but it is unlikely that undiscovered reserves are many orders of magnitude larger than those which are known, and undiscovered reserves may be expensive to extract. Much has been made of the shale revolution, which allows extraction of previously inaccessible oil and gas by 'fracking', a method using pressurised water and chemicals to force oil and gas contained in small fissures in underground rocks to rise to the surface. The increase in production of gas by this method has been particularly large in North America, and may allow the US to become self-sufficient in energy. It will certainly allow the US to produce far less CO_2, as burning gas is less polluting than burning coal or oil. However, fracking is unlikely to be the solution to the *global* energy crisis; for the period 2008-2012 the increase in US production of gas was only 1.2%. Over the same time period, world consumption of gas grew by 1.1% (as did production). Even with a global doubling or tripling of proven reserves of gas due to fracking, the fossil fuel horizon will still be in roughly the next 50-150 years, and the energy use of the world will have to decrease substantially if new methods of power generation are not introduced.

A decline in demand for energy is extremely unlikely, barring some global crisis. Although energy use per capita has reduced slightly in OECD countries, it is fast rising in the countries with the largest populations. The desire to achieve higher living standards in developing countries has resulted in an increase in energy use, and there is a very strong correlation between a country's GDP and its energy use as shown in Fig. 1.1. The most populous countries are quickly climbing the curve. Though it is feasible that energy use per capita could be brought to a sustainable level, the world population is growing and is set to continue to do so for the future, with some stabilisation above 9 billion by 2075 according to a United Nations forecast [13]. The world population since 1960 is shown in Fig. 1.2. These population driven increases in energy demand will almost certainly happen against a background of dwindling supply.

There are additional arguments in favour of reducing the use of fossil fuels; they produce particulate air pollution, which has long-term negative effects on health [14], and they are a source of geo-political tensions, with some countries using the supply of their natural resources for political gain.

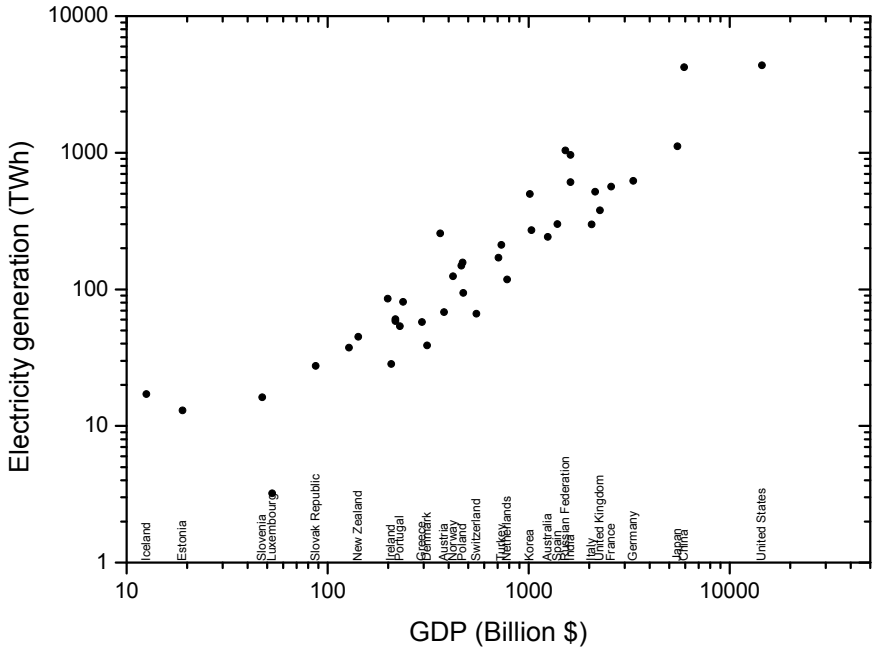

Figure 1.1: GDP and electricity generation are strongly correlated. Data from the OECD/IMF.

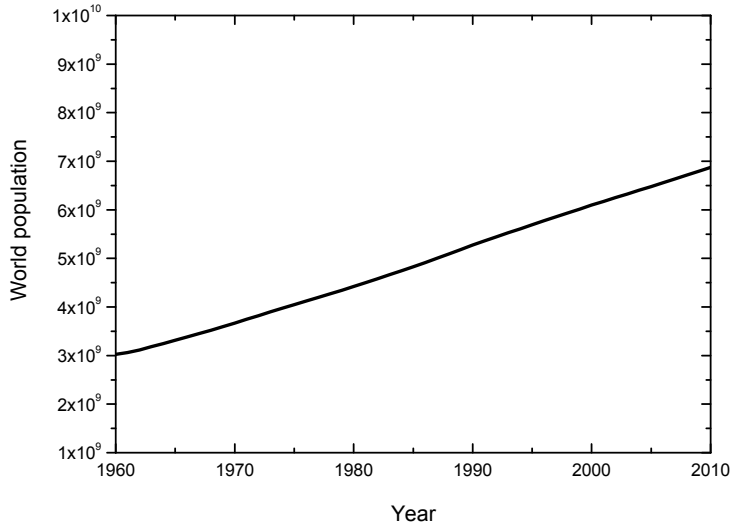

Figure 1.2: World population since 1960. Forecasts indicate continued growth in the short term, and stabilisation by 2075. Data from the World Bank.

The most discussed negative effect of fossil fuels is the release of CO_2 and the potential for global, and possibly irreversible, climate change that a large concentration of CO_2 in the atmosphere causes. CO_2 in ppm (parts per million by volume) recently reached a historic high of 400. Recent reports [15] suggest that stabilisation at 450 ppm of CO_2 still gives a $\sim$50% chance of a 2°C rise in global average temperature compared to the

pre-industrial average temperature. A recent forecast by BP is for carbon emissions from energy use to increase by 26% between 2011 and 2030, which would mean CO_2 closer to 500 ppm than 450 ppm. The 'dirtiest' fossil fuel, coal, is also the fastest growing by consumption [12]. The current UK target, written into law by the 2008 Climate Change Act, is to reduce emissions of CO_2 by at least 80% by 2050 (relative to 1990 levels).

Pressure to relinquish fossil fuels as the primary source of energy is strong. Unfortunately, alternatives are not forthcoming. Fossil fuel based electricity generation has a small geographical footprint, is extremely reliable, is easily scalable, and is cheap relative to alternatives (ignoring negative externalities). Although renewable technologies are far less polluting, they do not have these particular advantages. It is unlikely that renewable technologies such as hydro-electricity, wind, solar, wave, and biomass will be able to provide all of the energy required by the UK, or the world [16]. Nuclear fission has many of the advantages of fossil fuels in terms of reliability, scalability, and geographical footprint. There is enough fissile fuel to last beyond the fossil fuel horizon of 50-100 years, depending on the costs of extraction and developments in reactor technology, although there is probably not enough for thousands of years of power. Fission remains deeply unpopular due to the possibility of nuclear accidents, such as radiation leaks and meltdowns. These rare, catastrophic events aside, it produces little air pollution. Nuclear fission is also extremely safe - it has the fewest deaths per joule of electricity generated out of coal, peat, oil, gas, biomass, hydro-electricity and wind power [16].

It might be expected that a nuclear fusion reactor would be subject to similar rules, regulations and operational procedures as current fission reactors and so have a similar level of safety - with two important and beneficial exceptions. The first is that there is no chance of any runaway process such as meltdown, as only that fuel which is required is added to the reactor chamber, and the second is that the amount and level of the radioactive waste from fusion is far less, lasting on the order of a hundred years rather than on the order of millions.

A final argument in favour of fusion is that the fuel is extremely abundant. Deuterium occurs naturally: 33 grams in every tonne of seawater. Tritium must be bred in reactors from Lithium, and it is Lithium which is the limiting factor in deuterium-tritium fusion. Estimates of how much energy the world's Lithium could provide if used in fusion reactors vary, but (assuming extraction from seawater) it is comfortably hundreds of thousands of years. If deuterium-deuterium fusion could be developed, there would be enough fuel for millions of years based on current energy consumption and world population. The easy accessibility of seawater means, in principle, that fusion fuel would be free of the political issues associated with oil and gas production.

Given the historical trend for ever growing energy consumption, developing fusion power can be seen as part of the natural evolution of power production. Widespread fusion power would allow energy to be generated at a rate unprecedented in human history, and may initiate a new era of energy use akin to the introduction of steam power, and the industrial revolution that it catalysed.

1.3 The physics of ignition

In this discussion on the basic physics of ignition, the argument of Atzeni and Meyer-ter-Vehn's comprehensive textbook [17] is followed closely. In a fusion reaction, the amount of energy released per reaction, Q, is proportional to the total change in mass,

$$Q = \left(\sum_i m_i - \sum_f m_f \right) c^2$$

where i and f denote initial and final states respectively. There are many fusion reactions which produce energy, some of which are shown in Table 1.1. The fusion reaction with the largest cross-section for reaction at the lowest energy is that between deuterium and tritium, referred to as 'd' and 't' respectively. The energy released is $Q_{dt} = 17.6$ MeV and the reaction is

$$\mathrm{d} + \mathrm{t} \longrightarrow \alpha\ (3.5\ \mathrm{MeV}) + \mathrm{n}\ (14.1\ \mathrm{MeV})$$

All nuclear fusion power schemes must satisfy the fundamental property of producing more energy than is taken to initiate the fusion reactions. All fusion schemes seek to achieve a net gain G such that $G > 1$, in order to prove *scientific* feasibility. Commercial feasibility is quite different, and $G \sim 30 - 100$ or more might be needed. The simplest scenario is that of a geometry independent, perpetually burning plasma (in which fuel may be replaced). The energy losses per unit time per unit volume from a plasma can be described with just two terms accounting for electron-ion bremsstrahlung emission, $\dot{W}_b$, and loss of energy confinement, $3nT/\tau_E$ where τ_E is an energy confinement time. These losses are balanced by any auxiliary heating supplied, $\dot{W}_{\mathrm{aux}}$, and any fusion energy which is both produced, and then retained, in the plasma. Given neutrons have no charge this is almost exclusively from the α particles for deuterium-tritium fusion, and so the energy per unit time per unit volume retained in the plasma is $\dot{W}_{\mathrm{fusion}}/5$. The factor of $1/5$ is due to conservation of momentum between the neutron and Helium nucleus produced. Let

$$\mathcal{Q} = \frac{\dot{W}_{\mathrm{fusion}}}{\dot{W}_{\mathrm{aux}}}$$

Reactants		Products
d+d	$\longrightarrow$	t (1.01 MeV) + p (3.02 MeV)
d+d	$\longrightarrow$	He^3 (0.82 MeV) + n (2.45 MeV)
d+t	$\longrightarrow$	α (3.5 MeV) + n (14.1 MeV)
d+He^3	$\longrightarrow$	α (3.6 MeV) + p (14.7 MeV)
t+t	$\longrightarrow$	α + 2n + 11.3 MeV
t+He^3	$\longrightarrow$	α + p + n + 12.1 MeV
t+He^3	$\longrightarrow$	α (4.8 MeV) + d (9.5 MeV)
t+He^3	$\longrightarrow$	He^5 (12.4 MeV) + p (11.9 MeV)
p+Li^6	$\longrightarrow$	α (1.7 MeV) + He^3 (2.3 MeV)
p+Li^7	$\longrightarrow$	2α + 17.3 MeV
d+Li^6	$\longrightarrow$	2α + 22.4 MeV
p+Be^{11}	$\longrightarrow$	3α + 8.7 MeV
n+Li^6	$\longrightarrow$	α (2.1 MeV) + T (2.7 MeV)

Table 1.1: A selection of exothermic fusion reactions [18].

be the efficiency of the reactor. Ignition is defined as $\mathcal{Q} = \infty$, i.e. the fusion reactions are completely self-sustaining and require no auxiliary power. Ignition is the first goal of NIF. In order to balance emission and absorption of energy, the plasma must satisfy

$$\dot{W}_b + \frac{3nT}{\tau_E} = \dot{W}_{\text{fusion}} \left(\frac{1}{\mathcal{Q}} + \frac{1}{5} \right)$$

Given that

$$\dot{W}_{\text{fusion}} = \frac{1}{4} n^2 \langle \sigma v \rangle Q_{\text{dt}} \quad \text{and;} \quad \dot{W}_b = C_b n_e^2 \sqrt{T}$$

where $\langle \sigma v \rangle$ is the fusion reactivity, defined in Appendix C, and C_b is a constant, this gives

$$n\tau_E = \frac{3T}{\frac{1}{4}\left[(1/\mathcal{Q} + 1/5)\right] Q_{\text{dt}} \langle \sigma v \rangle - C_b \sqrt{T}} \tag{1.1}$$

where the left hand side is known as the confinement parameter [17]. (1.1) is satisfied for a fusion plasma operating in a steady state. It was originally derived by Lawson [19] with $\mathcal{Q} = 2.5$ recovering the famous Lawson criterion for fusion power.

Lawson developed equation (1.1) with steady state MCF in mind, and ICF, being a pulsed

power scheme, benefits from a slightly different perspective. Consider an assembled sphere of plasma of radius R_f at uniform temperature T and mass density ρ. The time that this sphere remains assembled is limited by the time it takes a rarefaction wave to travel from the outside of the sphere inwards (assuming zero external pressure on the sphere surface). The wave travels with the sound speed of the plasma, which is given by

$$c_s = \sqrt{\frac{2T}{\langle m \rangle}}$$

with $\langle m \rangle$ the average atomic fuel mass. The confinement time of the sphere of fuel is given by

$$\tau_{\text{conf}} = \frac{R_f}{c_s}$$

so that the position of the wave in time is $R(t) = R_f - c_s t$. In ICF, the characteristic time for fusion reactions is $\tau_{\text{fusion}} = \frac{1}{\langle \sigma v \rangle n}$, which allows a Lawson-like expression to be written;

$$n\tau_{\text{conf}} = \frac{\rho R_f}{\langle m \rangle c_s}$$

and it can be seen that the areal density, ρR_f, is of the greatest importance for the confinement. To calculate the fraction of fuel burnt, the propagation of the rarefaction wave into the plasma, and the corresponding reduction in the number of fusion reactions which can take place, must be taken into account. A robust model [20] of the fractional burn-up in a sphere of plasma taking into account these factors is given by

$$f_{\text{burn-up}} \approx \frac{\rho R_f}{H_B + \rho R_f}$$

where

$$H_B = \frac{8 c_s \langle m \rangle}{\langle \sigma v \rangle}$$

is the burn parameter, and is given for a wide range of conditions by $H_B \approx 6$ g cm^{-2} [21]. It can be shown that heating of the whole sphere of fuel does not guarantee a gain in energy large enough for inertial fusion energy (IFE). A better strategy for achieving high gain is the hotspot, or central, ignition scheme which is used on NIF. In this scheme, a central hotter region with lower mass density provides a 'spark' which then ignites the rest of the fuel.

NIF consists of 192 laser beams delivering a peak power of 500TW in laser energy at a wavelength $\lambda = 1.053\mu$m, which is frequency tripled to deliver up to 1.8 MJ onto the target [22]. The laser beams are incident on a Gold (Au) 'hohlraum', or hollow room, which absorbs the UV light and re-emits it as x-rays with a radiation temperature of

∼300 eV. Inside the hohlraum is a fuel capsule which has a radius of a few millimetres. The absorption and subsequent re-emission of the radiation has the effect of providing an even bathing of the fuel capsule with x-rays. ICF with a hohlraum is known as indirect drive, and the main benefits are that the smoother radiation fields are less susceptible to hydrodynamic instabilities (such as the Rayleigh-Taylor instability), that ablation by x-rays is more effective than by electron conduction (the mechanism in direct-drive), and any non-uniformity of beam intensity is removed [21]. The laser pulse is shaped in time to produce a series of four shockwaves, which eventually converge inside the fuel capsule. The internal energy of matter changes as $\mathrm{d}E = T\mathrm{d}S - P\mathrm{d}V$, and the succession of shock waves is designed so as to provide isentropic compression of the capsule, i.e. compression which eliminates the $T\mathrm{d}S$ term, which is heat transfer Q, as much as possible.

The capsule itself consists of an outer ablation material, for instance diamond-like carbon or plastic, a cold, dense fuel shell of deuterium-tritium ice, and a central gas fill, also composed of deuterium and tritium, which are shown in Fig. 1.3:a. Radiation incident on the capsule causes ablation, and conservation of momentum initiates an implosion via a rocket-effect. This is shown in Fig. 1.3:b. Subsequent shocks cause the implosion velocity to increase. When the shocks coalesce and hit the centre, the temperature of the gas fill jumps, and the shocks are reflected, which slows the implosion. Much of the kinetic energy of the implosion is converted into internal energy, some compression is still occurring, and a hotspot forms - a region with a high temperature but relatively low mass density. The hotspot is surrounded by the shell of colder, much more dense fuel. This assembled hotspot stage is shown in Fig. 1.3:c. In this type of ICF, the pressure is very similar across the hotspot and dense shell at this stage, even while the mass density and temperature are very different.

This is the point at which ignition can occur, if the right conditions are present. Subsequent references to ρ, R and T refer to the hotspot mass density, radius and temperature respectively. Cold fuel parameters are designated with a subscript 'c'. The instantaneous rate of change of energy density (where energy density is ϵ) in the hotspot under isobaric conditions is given by

$$\frac{\mathrm{d}\epsilon}{\mathrm{d}t} = \dot{W}_{\mathrm{dep}} - \dot{W}_{\mathrm{b}} - \dot{W}_{\mathrm{e}}$$

where $\dot{W}_{\mathrm{e}} \approx \frac{3A_e T^{7/2}}{\ln \Lambda R^2}$ is thermal conduction by electrons across the surface of the hotspot into the cold fuel, and $\dot{W}_{\mathrm{dep}}$ is the energy deposited by fusion reactions in the hotspot. Given that neutrons generally do not stop in the hotspot,

$$\dot{W}_{\mathrm{dep}} = f_\alpha \dot{W}_\alpha = f_\alpha \dot{W}_{\mathrm{fusion}}/5 = f_\alpha A_\alpha \rho^2 \langle \sigma v \rangle$$

where A_α has absorbed the constants and f_α is the fractional absorption of αs in the

hotspot. The bremsstrahlung emission may be re-written as $\dot{W}_\mathrm{b} = A_\mathrm{b}\rho^2 T^{1/2}$. Evidently, the hotspot will heat if $\dot{W}_\mathrm{dep} > \dot{W}_\mathrm{b} + \dot{W}_\mathrm{e}$, which is equivalent to

$$(\rho R) > \left(\frac{3A_e T^{7/2}/\ln\Lambda}{A_\alpha \langle\sigma v\rangle f_\alpha - A_\mathrm{b} T^{1/2}} \right)^{1/2}$$

which is known as the self-heating condition for a hotspot. This is an instantaneous expression; it does not capture how hotspot conditions change over time and is not the same as ignition.

A broader perspective is gained from considering a hotspot which expands and accumulates mass. Ignition is equivalent to the expansion of the hotspot into the cold fuel via the propagation of a 'burn wave' of fusion reactions. Energy conservation in a burning plasma, with M the mass of the hotspot and eM its energy, so that e is specific energy (energy per unit mass), may be written as

$$\frac{\mathrm{d}\,(eM)}{\mathrm{d}t} = \left(\dot{W}_\alpha - \dot{W}_\mathrm{b}\right) \frac{4}{3}\pi R^3 - p4\pi R^2 u$$

with $p = \Gamma_\mathrm{B}\rho T$ pressure, and $u = \frac{\mathrm{d}R}{\mathrm{d}t}$ the velocity of the burn wave. Γ_B is the gas constant per unit mass for T in units of energy. The velocity of the burn wave may be given by

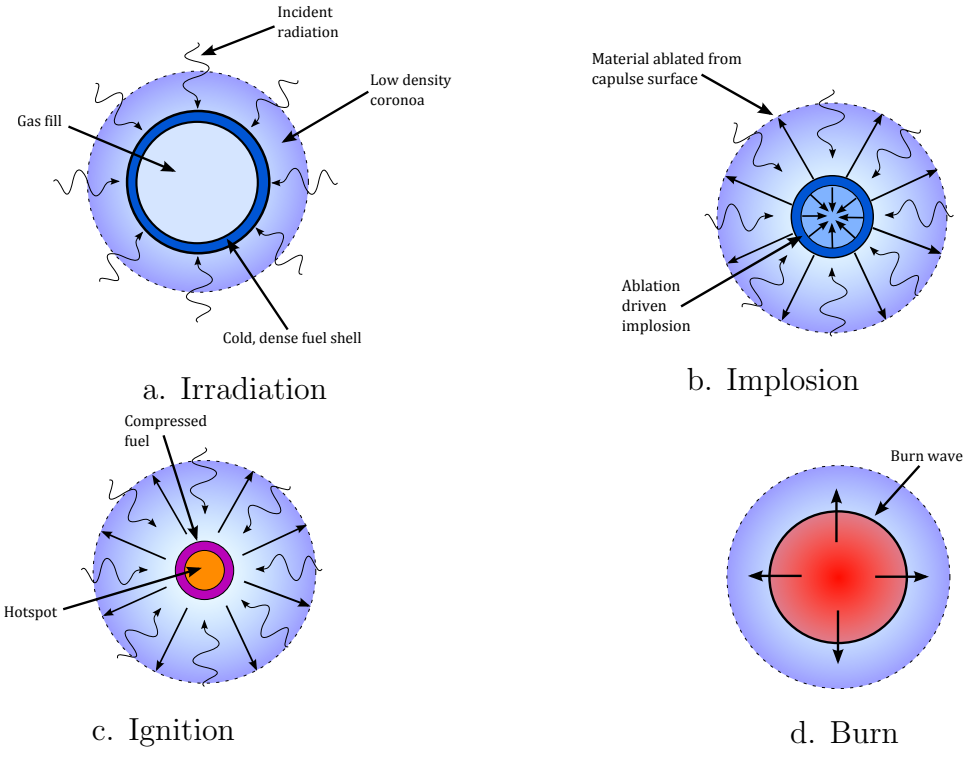

a. Irradiation

b. Implosion

c. Ignition

d. Burn

Figure 1.3: Four schematic diagrams of inertial confinement by spherical implosion.

assuming that the plasma is an ideal gas with a strong shock propagating through it so that

$$u = \sqrt{\frac{e}{2}} \left(\frac{\rho}{\rho_\mathrm{c}}\right)^{1/2} = \left(\frac{3}{4}\Gamma_\mathrm{B} T \frac{\rho}{\rho_\mathrm{c}}\right)^{1/2}$$

Using the definition of mass in the hotspot as mass with a specific energy e, the rate of accretion of mass into the hotspot can be defined as

$$e\frac{\mathrm{d}M}{\mathrm{d}t} = \left[\dot{W}_\alpha \left(1 - f_\alpha\right) + \dot{W}_\mathrm{e}\right] \frac{4}{3}\pi R^3$$

If $t_* = R/u$ is the characteristic hydrodynamic time, then

$$K_\alpha = \frac{\dot{W}_\alpha t_*}{\rho e}$$

is the dimensionless ratio of the energy carried by α particles in a time t_* to the instantaneous internal energy of the plasma. For a burn wave to propagate, this must be growing as a function of time,

$$\frac{t_*}{K_\alpha}\frac{\mathrm{d}K_\alpha}{\mathrm{d}t} > 0$$

The equations for the hotspot evolution may also be cast in a dimensionless form;

$$\begin{aligned}
\frac{t_*}{T}\frac{\mathrm{d}T}{\mathrm{d}t} &= K_\alpha f_\alpha - K_\mathrm{b} - K_\mathrm{e} - 2 \\
\frac{t_*}{\rho}\frac{\mathrm{d}\rho}{\mathrm{d}t} &= K_\alpha \left(1 - f_\alpha\right) + K_\mathrm{e} - 3
\end{aligned}$$

where K_b and K_e are defined analogously to K_α. Using the approximation that $\langle\sigma v\rangle \propto T^2$, which is good for $T \approx 7 - 20$ keV, this can be written as

$$\frac{t_*}{K_\alpha}\frac{\mathrm{d}K_\alpha}{\mathrm{d}t} = \frac{1}{2}\left(K_\alpha + K_\mathrm{b} - 3\right)$$

and, as long as this is positive at $t = 0$, it will remain positive, and cause K_α to grow indefinitely over time, thus igniting the fuel. Therefore,

$$\left(\dot{W}_\alpha - \dot{W}_\mathrm{b}\right)_{t=0} t_* > 3\left(\rho e\right)_{t=0}$$

is the condition, which may be rewritten as a Lawson-type inequality

$$\rho R T > \frac{9\sqrt{3}}{4}\frac{\Gamma_\mathrm{B}^{3/2} T^{5/2}}{A_\alpha\langle\sigma v\rangle - A_\mathrm{b} T^{1/2}} \left(\frac{\rho}{\rho_\mathrm{c}}\right)^{1/2} = \frac{1.1\left(T\ /\mathrm{keV}\right)^{1/2}}{1 - 3.47\left(T\ /\mathrm{keV}\right)^{-3/2}} \left(\frac{\rho}{\rho_\mathrm{c}}\right)^{1/2}\ \mathrm{g/cm}^{-2}$$

for the overall ignition and burn wave propagation. Satisfaction of this criterion leads to

a fully burning plasma, as shown in Fig. 1.3:d.

The conditions required for the central ignition scheme on NIF are listed in more detail in Table D.1 of Appendix D [23, 24]. Direct measurements of these important parameters of a fuel capsule are made extremely difficult by the small scale, high energy densities, and short timescales involved, so typically they must be inferred. Several performance metrics using more easily measurable quantities have been developed to determine how close ICF experiments are to achieving ignition including the ITF (ignition threshold factor), ITFX (ignition threshold factor - experimental), and GLC (generalised Lawson criterion) [25, 26]. The key physical parameters required for ignition on NIF using more detailed models are

$$T_{\mathrm{HS}} = 5 - 12 \text{ keV} \quad \text{and;} \quad (\rho R)_{\mathrm{HS}} > 0.2 - 0.5 \text{ g cm}^{-2} \quad \text{and;} \quad (\rho R)_{\mathrm{fuel}} > 1 \text{ g cm}^{-2}$$

where “HS” refers to a hotspot parameter.

1.4 Summary of contents

Chapter 2 provides the theoretical background to this work, including a brief overview of the basic properties of plasmas. The concepts are useful for subsequent chapters, and several important definitions are included in §2.1, §2.2, and §2.3. §2.4 discusses the temperature and density regime with which this thesis is primarily concerned, and §2.5 examines possible approaches to calculations in the aforementioned regime.

Chapter 3 details Monte Carlo, the computational method used to obtain many of the results presented. §3.1 and §3.2 have details of the operation of the code developed, and §3.3 tests the code on a selection of problems with known analytical solutions.

Chapter 4 has details of an extension to Monte Carlo methods for degenerate plasmas. Degenerate plasmas occur during compression of the cold fuel shell in hotspot ignition. The basic properties of degeneracy are set out in §4.2, and of the algorithm in §4.3. Benchmarking is presented in §4.4, while §4.5 compares conventional models of degenerate temperature equilibration against numerical simulation, finding a 21% difference in electron temperature for ICF relevant conditions.

Chapter 5 is concerned with the phenomenon of ion-ion inverse bremsstrahlung (IIIB) absorption. §5.2 explains the process, §5.3 some circumstances in which it might be observable, and §5.4 how it can be modelled. In §5.5, two interesting properties of IIIB are presented for the first time; the driving of non-Maxwellian distributions, and, through manipulation of density, mix of ion species, and pulse shape, the heating of light ions to temperatures in the keV on timescales of femtoseconds.

Chapter 6 forms an introduction to the topic of discrete and large-angle collisions in plasmas. §6.1 examines the general theory of large-angle scattering, the exact conditions where large-angle collisions can be expected to occur based on a new model, and large-angle modifications to the Rutherford cross-section. §6.2 is a review of other work in the field.

Chapter 7 incorporates the model developed in Chapter 6 into a new computational method for discrete collisions. The operation of the algorithm is set out in §7.2. Simulations comparing small-angle and large-angle scattering are presented in §7.3.1, and simulations of the driving of non-Maxwellian distributions by fusion reactions are presented in §7.3.2 and §7.3.3. These simulations find that large-angle collisions significantly decrease equilibration times and drive distributions for which there is a substantial change in yield relative to both a Maxwellian with the same average energy, and simulations with no large-angle collisions.

Finally, **Chapter 8** concludes with a summary of the main results of this thesis, along with suggestions for the direction of future research.

Chapter 2

Theoretical background

2.1 Plasma fundamentals

Qualitatively, plasmas are collections of partially or fully ionised particles which are quasi-neutral, that is they are neutral above certain length and time scales. Collective behaviour dominates plasmas as the electromagnetic potential at any point typically has contributions from a large number of charged particles. The fundamental length scale is the Debye length,

$$\lambda_{\mathrm{D}}^2 = \sum_i \frac{\epsilon_0 T_i}{n_i q_i^2 e^2} \tag{2.1}$$

where the sum runs over all species. This is the length scale over which a plasma is shielded; particles separated by distances $r > \lambda_{\mathrm{D}}$ do not directly influence one another. It is also the length scale of neutrality and leads naturally to the notion of a Debye sphere (a sphere of radius λ_{D}) as the volume over which a plasma is approximately neutral. Quasi-neutrality is a necessary condition for a plasma. Quasi-neutrality is only satisfied if there are many particles available in a Debye sphere to carry out screening, so that

$$\frac{4}{3}\pi n \lambda_{\mathrm{D}}^3 \gg 1 \tag{2.2}$$

and this ensures that collective effects dominate binary collisions. n is the total number density. Note that this is equivalent to the condition that the ratio of potential energy to kinetic energy should be small, i.e. (omitting the ion terms in equation (2.1))

$$g = \frac{e^2}{\epsilon_0 T_e \lambda_{\mathrm{D}}} = \frac{1}{n_e \lambda_{\mathrm{D}}^3} \ll 1 \tag{2.3}$$

where g is known as the plasma parameter [27]. Strongly coupled plasmas have $g \approx 1$; weakly coupled implies $g \longrightarrow 0$. It is also a measure of the importance of collisions,

as collision strength is proportional to potential energy. The work presented is only concerned with collisional plasmas with $g > 0$.

The time scale over which a plasma is neutral is also a parameter of fundamental importance. Small perturbations from neutrality set up oscillations in charge carrying species in a plasma. The highest frequency oscillations are from the most mobile charge carriers, typically electrons. The reciprocal of this is the time scale of neutrality,

$$\omega_{\mathrm{pe}} = \sqrt{\frac{n_e e^2}{\epsilon_0 m_e}}$$

The result of this oscillatory behaviour is that the plasma is opaque to electromagnetic waves with frequencies below the plasma frequency. Note that this oscillation carries no information as the group velocity is $v_g = \partial\omega/\partial k = 0$. Taking into account the thermal energy of the electrons does give a non-zero group velocity. ω_{pe} gives the most basic plasma time scale, but more involved time scales corresponding to particular processes, such as the energy loss rate of a high energy particle in a Maxwellian background of plasma particles, also exist. These standard rates are referred to in this work as Landau-Spitzer theory [28, 29] and are summarised in Appendix B.

2.2 Rutherford scattering

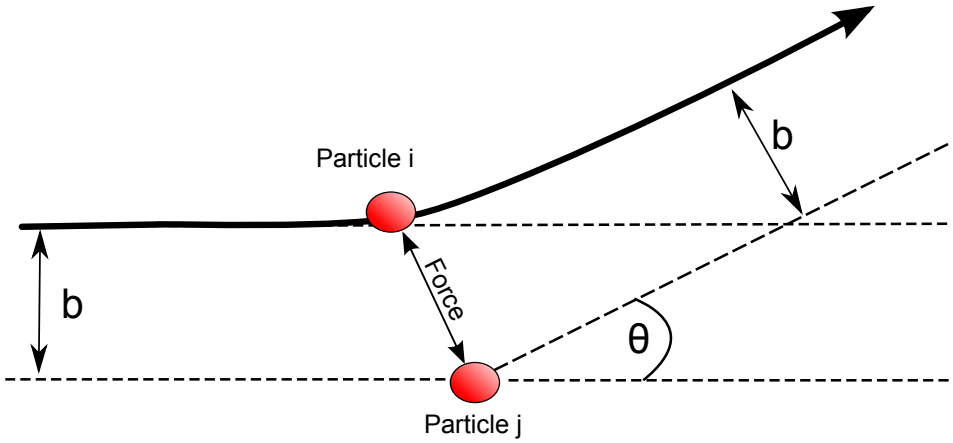

Figure 2.1: Rutherford scattering between two particles i and j with impact parameter b and scattering angle θ.

A binary collision between two charged point particles occurs via the electromagnetic, or Coulomb, force. Two charged particles i and j exert an electromagnetic force on each

other $\mathbf{F}_{ij} = -\mathbf{F}_{ji}$ where

$$F_{ij} = \frac{e^2 q_i q_j}{4\pi\epsilon_0 r_{ij}^2}$$

and r_{ij} is the separation distance. Fig. 2.1 shows a single scattering event between two charged particles with zero centre-of-mass position velocity. The centre-of-mass frame scattering angle θ is the angle through which each particle scatters in the centre-of-mass frame relative to its initial velocity, also in the centre-of-mass frame. The relationship between impact parameter, b, and θ is [30]

$$b = b_\perp \cot\left(\frac{\theta}{2}\right) \tag{2.4}$$

Note that $b_\perp$ is the impact parameter corresponding to $\theta = \pi/2$, and is

$$b_\perp = \frac{e^2 q_i q_j}{4\pi\epsilon_0} \frac{1}{m_{ij} v_{ij}^2}$$

The scattering angle in the laboratory frame, χ, is defined as exit velocity angle relative to initial velocity angle. For a charged particle i scattering off of particle j it is

$$\cot\chi = \frac{V}{v_i}\frac{m_i}{m_{ij}}\csc\theta + \cot\theta$$

where $\mathbf{V} = \frac{m_i\mathbf{v}_i + m_j\mathbf{v}_j}{m_i + m_j}$ is the velocity of the centre-of-mass position in the laboratory frame. For an initially stationary target particle j, this reduces to

$$\cot\chi = \frac{m_i}{m_j}\csc\theta + \cot\theta \tag{2.5}$$

Using the small-angle approximation in addition to $v_j = 0$ gives the simple relation

$$\chi = \frac{m_j}{m_i + m_j}\theta$$

The classical differential cross-section, $\frac{\mathrm{d}\sigma}{\mathrm{d}\Omega}$, is proportional to the probability that a particle going through a background of other particles of density n undergoes $n\mathrm{d}\sigma$ collisions per unit length which scatter it into a solid angle $\mathrm{d}\Omega = \sin\theta \mathrm{d}\theta\mathrm{d}\phi$. A schematic of a particle scattering into $\mathrm{d}\Omega$ is shown in Fig. 2.2. The classical cross-section based on equation (2.4) is the Rutherford cross-section in the centre-of-mass frame

$$\frac{\mathrm{d}\sigma}{\mathrm{d}\Omega} = \frac{b_\perp^2}{4\sin^4\frac{\theta}{2}} = \left(\frac{e^2 q_i q_j}{4\pi\epsilon_0}\right)^2 \frac{1}{m_{ij}^2 v_{ij}^4}\frac{1}{4\sin^4\frac{\theta}{2}} \tag{2.6}$$

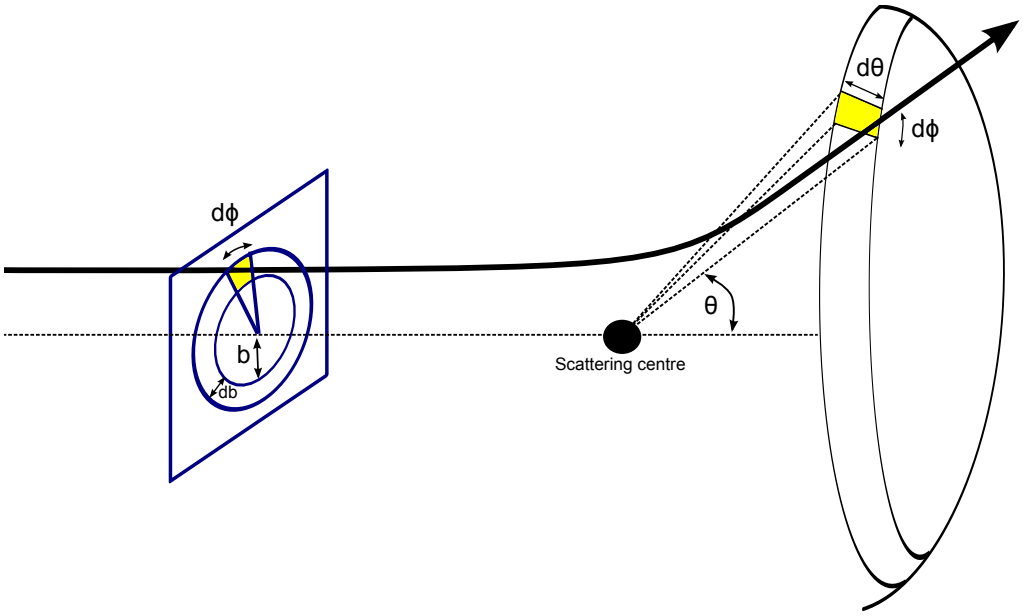

Figure 2.2: Schematic of scattering showing the solid angle $\mathrm{d}\Omega = \sin\theta \mathrm{d}\theta \mathrm{d}\phi$.

It is the cross-section for binary interactions in non-relativistic charged particle-particle collisions. Though it is a classical cross-section, the first order quantum mechanical calculation of the cross-section, using the Born approximation and a Yukawa potential, produces the same result in the $\lambda_\mathrm{D} \longrightarrow \infty$ limit (with λ_D the screening length in the Yukawa potential).

Interactions in a plasma are not binary because of the large number of particles interacting simultaneously. So, the Rutherford cross-section does *not* include the complicated collective behaviour of plasmas or the associated screening at distances on the order of the Debye length. It is also only appropriate for small-angles, as extra physics begins to become important at larger angles. This extra physics includes the addition of spin, indistinguishability, and the nuclear force, and is discussed in Chapter 6. However, most plasmas are dominated by small-angle, long-range collisions for which a screened Rutherford cross-section is sufficient.

2.3 The Coulomb logarithm

Divergences arise when applying the pure Rutherford differential cross-section to calculations in plasmas. These divergences are not physical. Removing them gives rise to $\ln\Lambda$, the Coulomb logarithm, as the following example illustrates. Consider the lab frame energy loss $\mathrm{d}E$ of a projectile particle i travelling (without loss of generality) in the x-direction and undergoing collisions with a background of stationary targets of species

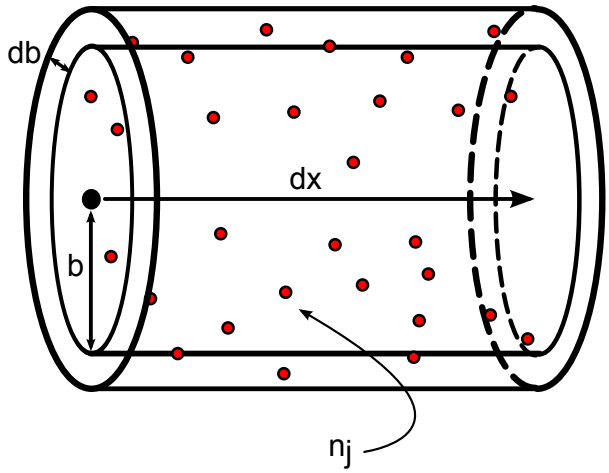

Figure 2.3: A particle going through an infinitesimal distance dx having collisions with a stationary background species j of density n_j.

j. Let $\mathbf{v}|_{\rm com}$ denote a velocity in the centre-of-mass frame, and $\mathbf{v}_{ij}$ the initial relative velocity. The final velocity in the lab frame of the projectile is, using equation (2.5) and that $\mathbf{v}_i|_{\rm com} = \mathbf{v}_i - \mathbf{V} = m_{ij}\mathbf{v}_i/m_i$,

$$\mathbf{v}_i' = \mathbf{v}_i'|_{\rm com} + \mathbf{V} = \left(\frac{m_{ij}v_i}{m_j} + \frac{m_{ij}v_i}{m_i}\cos\theta, \frac{m_{ij}v_i}{m_i}\sin\theta\right)$$

The final kinetic energy of the projectile is

$$\begin{aligned} E' = \frac{1}{2}m_i v_i'^2 &= \frac{1}{2}m_i v_i^2\left(\frac{m_{ij}^2}{m_j^2} + \frac{2m_{ij}^2}{m_i m_j}\cos\theta + \frac{m_{ij}^2}{m_i^2}\right) \\ &= \frac{1}{2}m_i v_i^2\left[1 + \frac{2m_{ij}^2}{m_i m_j}(\cos\theta - 1)\right] \\ &= \frac{1}{2}m_i v_i^2\left[1 + \frac{2m_{ij}^2}{m_i m_j}2\sin^2\frac{\theta}{2}\right] \end{aligned}$$

The change in kinetic energy is $\Delta E = E - E'$,

$$\Delta E = \frac{1}{2}m_i v_i^2 \frac{4m_{ij}^2}{m_i m_j}\frac{1}{1 + \left(\frac{b}{b_\perp}\right)^2} \tag{2.7}$$

where equation (2.4) is used. In an infinitesimal distance dx the number of encounters with stationary targets j will be $n_j {\rm d}x 2\pi b {\rm d}b$, as shown in Fig. 2.3. Multiplying this by the loss per encounter, ΔE, and integrating over all possible impact parameters gives the

infinitesimal loss of energy. Then

$$\frac{\mathrm{d}E_i}{\mathrm{d}x} = E_i \frac{8\pi n_j m_{ij}^2}{m_i m_j} b_\perp^2 \int \frac{b}{b_\perp^2 + b^2} \mathrm{d}b \tag{2.8}$$

The integral part, without other constants, evaluates to

$$\lim_{b' \longrightarrow \infty} \left[\frac{1}{2} \ln \left(b_\perp^2 + b^2 \right) \right]_0^{b'}$$

which is logarithmically divergent.

The small-angle approximation, and equation (2.4), are often used to set $\frac{1}{b^2/b_\perp^2+1} \approx \frac{b_\perp^2}{b^2}$ in equation (2.8). This results in the expression being divergent as $b \longrightarrow 0$ too, but this is simply a consequence of using the small-angle approximation. A standard approach is to use the small-angle approximation, introducing the $b \longrightarrow 0$ divergence, and then to regulate this divergence by introducing a minimum impact parameter. $b_\perp$ is often chosen, and this effectively omits hard collisions with $\theta > \pi/2$. Unless otherwise stated, in this work the minimum impact parameter is set to zero in integrations similar to those appearing in equation (2.8), thereby avoiding the large-angle divergence. This is a simplification which assumes Coulombic point particles which is the adopted convention throughout. It is possible to set a minimum impact parameter which takes account of the finite size of the nucleus for the Coulomb force [31].

The small-angle divergence is also unphysical and can be regulated by introducing a maximum impact parameter. The origin of the small-angle divergence is that, though the contributions to the cross-section from remote interactions are diminishing due to distance, the number of remote interactions becomes infinite at large distances. This is a property of the slow $1/r^2$ fall-off of the Coulomb force, or, equivalently, that the Rutherford cross-section implicitly assumes an infinite interaction time. The Rutherford cross-section is designed for binary collisions, and the cavalier approach of applying it to a particle undergoing many collisions simultaneously is the origin of the divergence. However, within a plasma, charges are not free to remotely interact over an infinite distance for an infinitely long time; there is screening of charges at length scales beyond λ_D implying that the upper limit in impact parameter should be λ_D. This corresponds to the smallest angle through which a particle may scatter according to equation (2.4) being

$$\frac{b_\perp}{\lambda_\mathrm{D}} = \tan \frac{\theta_\mathrm{min}}{2} \approx \frac{\theta_\mathrm{min}}{2}$$

and the integral becomes

$$\frac{1}{2}\ln\left(1+\frac{\lambda_{\mathrm{D}}^2}{b_\perp^2}\right)\approx\ln\left(\frac{\lambda_{\mathrm{D}}}{b_\perp}\right)=\ln\Lambda$$

which is the Coulomb logarithm. As $b_\perp$ is dependent on the two species involved in the collision, the Coulomb logarithm may be denoted $\ln\Lambda_{ij}$ and there are $(N^2-N)/2$ different values for N distinct plasma species. In general, species labels are implicit on $\ln\Lambda$ and $b_\perp$. For completeness, the full expression of equation (2.8) is

$$\frac{\mathrm{d}E_i}{\mathrm{d}x}=\frac{4\pi n_j}{m_j v_i^2}\left(\frac{e^2 q_i q_j}{4\pi\epsilon_0}\right)^2\ln\Lambda_{ij} \tag{2.9}$$

The Coulomb logarithm naturally arises in many calculations of quantities of interest in plasma physics, particularly in the calculation of relaxation times and kinetic cross-sections. Kinetic cross-sections have the general definition

$$\sigma_k=\int(1-\cos^k\theta)d\sigma,\ k\in\mathbb{N} \tag{2.10}$$

$k=1$ gives a quantity known variously as the transport, diffusion, or slowing-down cross-section due to it being proportional to the loss of directed particle velocity in a scattering event. With $k=2$, the cross-section describes the deflection of particles as it is proportional to the mean-square increment in transverse particle velocity. All plasma kinetic cross-sections give rise to a Coulomb logarithm factor [29].

The assertion in §2.2 that small-angle, long-distance interactions dominate plasmas can be shown by integrating equation (2.8). Small-angles correspond to larger impact parameters, while small impact parameters correspond to large scattering angles. If the integral in (2.8) is split [29] into near and far parts I_n and I_f with a cut-off determined by equation (2.4) in the small-angle approximation

$$\theta=\frac{2b_\perp}{b}<1$$

so that the cut-off is $2b_\perp$

$$I_n=\int_0^{2b_\perp}\frac{b\mathrm{d}b}{b_\perp^2+b^2}=\ln\sqrt{5}\approx 1$$
$$I_f=\int_{2b_\perp}^{\lambda_{\mathrm{D}}}\frac{b\mathrm{d}b}{b_\perp^2+b^2}=\frac{1}{2}\ln\left(\frac{\lambda_{\mathrm{D}}^2+b_\perp^2}{5b_\perp^2}\right)\approx\ln\left(\frac{\lambda_{\mathrm{D}}}{b_\perp}\right)$$

where the last step is justified by the condition on the plasma coupling parameter in equation (2.3) (ignoring ion contributions);

$$\frac{b_\perp}{\lambda_\mathrm{D}} \sim \frac{e^2}{\epsilon_0 m_e v_{e,\mathrm{th}}^2}\frac{1}{\lambda_\mathrm{D}} \approx g \ll 1$$

so

$$\frac{I_n}{I_f} \sim \frac{1}{\ln\Lambda} < 1$$

and the far interactions dominate the near ones, and small angles contribute more strongly to the exchange of energy than large angles. This is the justification for most approaches to plasma physics concentrating on long-range, small-angle interactions. It can be further seen that the mean square angle of deviation, $\langle\theta^2\rangle$, from an initial direction is also dominated by small-angle collisions. This is equivalent to the $k = 2$ cross-section in equation (2.10). The cross-section for a single deflection of $\theta = \pi/2$ in a 'hard-sphere' scattering collision is $\sigma = \pi b_\perp^2$ but the mean square deflection effective 'cross-section' taking into account many small-angle scattering events is

$$\sigma_{\langle\theta^2\rangle} = \int \theta^2 \frac{\mathrm{d}\sigma}{\mathrm{d}\Omega}\mathrm{d}\Omega = \frac{\pi b_\perp^2}{2}\int_{\theta_\mathrm{min}}^{\theta_\mathrm{c}} \frac{\theta^2 \sin\theta \mathrm{d}\theta}{\sin^4(\theta/2)}$$

Taking into account only small-angle scattering means cutting off the integration over angle, and $\theta_c = 1$ is chosen as the cut-off. Applying the small-angle approximation gives

$$\sigma_{\langle\theta^2\rangle} = \frac{\pi b_\perp^2}{2}\int_{\theta_{min}}^{1} \frac{2^4 \mathrm{d}\theta}{\theta} = 8\pi b_\perp^2 \ln\Lambda \tag{2.11}$$

so that the ratio of cross-sections for deflections is $\sigma_{\langle\theta^2\rangle}/\sigma = 8\ln\Lambda$. So diffusion in angle is $8\ln\Lambda$ more likely via small-angle collisions than via large-angle collisions. However, there are situations encountered in Chapters 6 and 7 where $\ln\Lambda{\sim}1$ or large energy exchanges in a single collision are of interest. The effects of near interactions can then be important enough to warrant inclusion in calculations. It should be stressed that the Coulomb logarithm is approximate, rather than exact, because the integration limits are approximate, despite originating from physical insights. As the Coulomb logarithm varies only weakly with its parameters, this is not generally a problem but it is more of an issue in the $\ln\Lambda{\sim}1$ regime.

In this work, the Coulomb logarithm of Gericke, Murillo, and Schlanges [32] is adopted where

$$\ln\Lambda = \frac{1}{2}\ln\left(1 + \frac{b_\mathrm{max}^2}{b_\mathrm{ref}^2}\right) \tag{2.12}$$

The effective maximum and minimum impact parameters are defined as

$$b_{\max}^2 = \lambda_{\mathrm{D}}^2 + r_0^2 \tag{2.13}$$

$$b_{\mathrm{ref}}^2 = \lambda_{\mathrm{dB}}^2 + b_{\perp}^2 \tag{2.14}$$

respectively, where particle labels are suppressed, $r_0 = (4\pi \sum_i n_i/3)^{-1/3}$ is the particle sphere radius, and $\lambda_{\mathrm{dB}} = \max\{\hbar/2m_i v_i, \hbar/2m_j v_j\}$ is the de Broglie wavelength. The de Broglie wavelength is introduced because the uncertainty principle 'smears out' particles over $\Delta x \geq \hbar/p$ for $b < \Delta x$, reducing the energy loss relative to using $b_\perp$ in some circumstances [31]. This is a semi-classical correction, and the simplest quantum mechanical calculation of the kinetic cross-section, using the first order Born approximation, naturally obtains a Coulomb logarithm with a minimum impact parameter of λ_{dB}. The root sum of squares in equations (2.13) and (2.14) ensures continuity between the different possible values of $b_{\max}$ and b_{ref} and, as the Coulomb logarithm is approximate, the slight overestimation of both maximum and minimum impact parameters is acceptable. There are many different formulae available for the Coulomb logarithm, and it is difficult to determine which best reflects reality [33, 32, 34, 35, 36, 37]. Nothing precludes the use of another of those which are available.

In the context of particle-particle collisions, $\ln\Lambda$ may either be calculated for each collision using the relevant particle velocities, which is computationally expensive as it must be carried out many times per timestep, or using the global temperatures for the relevant species meaning it is just calculated once per timestep for each combination of species. Using the 'per collision' logarithm can make a significant difference to the scattering when far from thermodynamic equilibrium [38].

Theories which provide models of average plasma behaviour omit $\ln\Lambda$ from the integrations over distribution functions because $\ln\Lambda$ varies slowly with changing energy, especially if $\ln\Lambda \gg 1$. To make useful comparisons against conventional theories using averaged models, such as Landau-Spitzer, $\langle\ln\Lambda\rangle$ is occasionally used in simulations. An averaged $\ln\Lambda$ only requires changes to equation (2.12) in the b_{ref} term;

$$\lambda_{\mathrm{dB}} = \max\left\{\frac{\hbar}{2m_i v_{i,\mathrm{th}}}, \frac{\hbar}{2m_j v_{j,\mathrm{th}}}\right\}$$

$$b_{\perp} = \frac{q_i q_j}{4\pi\epsilon_0} \frac{1}{m_{ij}\left(v_{i,\mathrm{th}}^2 + v_{j,\mathrm{th}}^2\right)}$$

where $v_{i,\mathrm{th}}^2 = 3T_i/m_i$.

Throughout the rest of this work, λ_D is used to mean b_max, and $b_\perp$ to mean b_ref so that

$$\ln\Lambda = \frac{1}{2}\ln\left(1+\frac{\lambda_\mathrm{D}^2}{b_\perp^2}\right)$$

is equivalent to equation (2.12) unless otherwise stated. This is to tidy up notation and aid understanding. Other modifications to the Coulomb logarithm are sometimes necessary; these are described in the relevant chapters.

2.4 Regime of interest

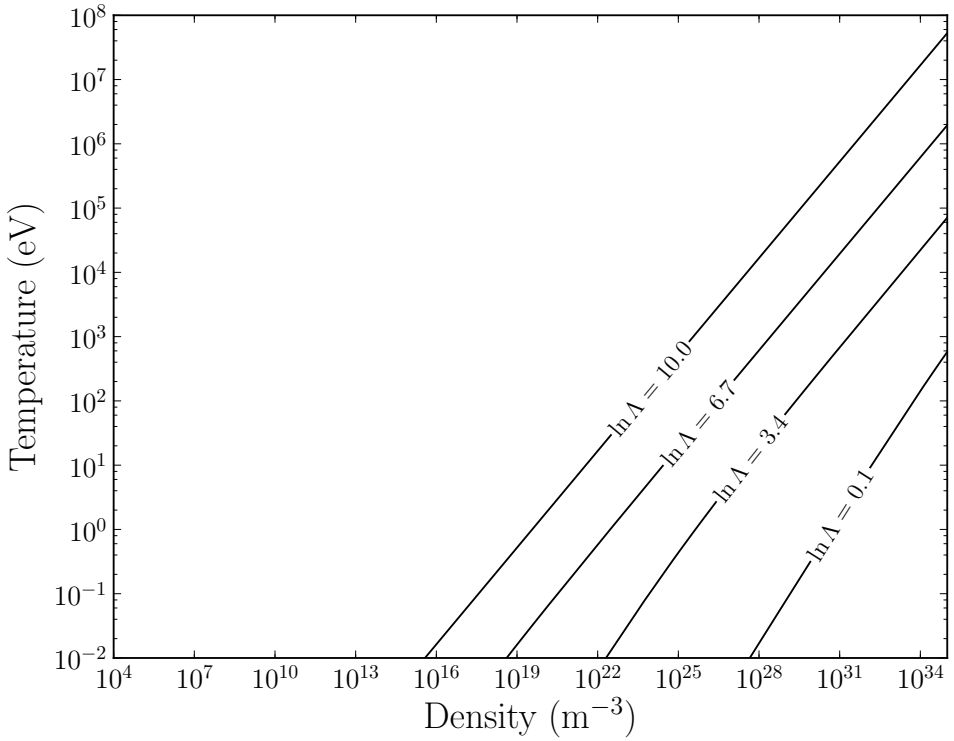

Figure 2.4: Values of $\ln\Lambda$, using the definition of equation (2.12), over a range of temperatures and densities for an equimolar electron-proton plasma.

This work is concerned with the driving of non-Maxwellian distributions in a few specific cases. These specific cases are generally in the moderately to strongly coupled regime, $\ln\Lambda \leq 5$, which includes high intensity laser-plasma interactions [39], inertial confinement fusion [23], degenerate plasmas [40], and stellar cores [41, 42].

Fig. 2.4 shows $\ln\Lambda$ for a range of temperatures and densities, using equation (2.12). Of

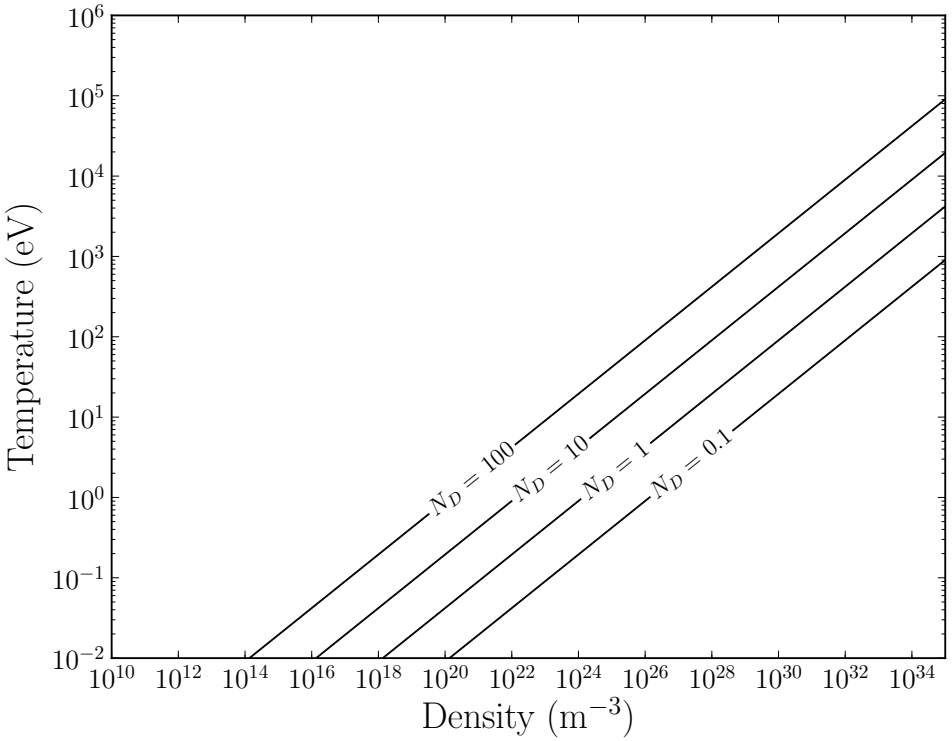

Figure 2.5: $N_\mathrm{D} = \frac{4}{3} n_e \lambda_\mathrm{D}^3$ for an equimolar electron-proton plasma.

course, different formulae exist for $\ln\Lambda$, so the number of particles in a Debye sphere is a more universal measure: N_D is shown in Fig. 2.5.

In the $\ln\Lambda \leq 5$ regime, distributions take longer to relax because plasma relaxation times are $\tau \propto 1/\ln\Lambda$. Distortions away from Maxwellians take longer to recover with small $\ln\Lambda$, and a comprehensive understanding of non-Maxwellian distributions and their persistence is more necessary. Large-angle scattering and discrete collisions, covered in Chapters 6 and 7, have been shown to be roughly of importance $1/\ln\Lambda$ relative to small-angle collisions so that the small $\ln\Lambda$ regime also coincides with the effect of large-angle collisions being largest.

Many of the theoretical tools used for plasmas rely on $N_\mathrm{D} \gg 1$ or $\ln\Lambda > 1$ and so are less applicable in the moderately to strongly coupled regime, as is explored in §2.5.

It is useful to express ratios of the fundamental plasma length scales λ_D, r_i, $b_\perp$, and λ_dB in a form in which they are convenient functions of typical high energy density plasma conditions. These ratios are calculated in the most simple case, in which a charge of e is

assumed for all species. The classical ratio of length scales is

$$\frac{\lambda_{\mathrm{D}}}{b_{\perp}} = \left(\frac{\epsilon_0}{e^2}\right)^{3/2} \sqrt{\frac{T_i}{n_i}} 4\pi m_{ij} v_{ij}^2 \approx 52 \frac{\left(T_e \ /\mathrm{keV}\right)^{3/2}}{\sqrt{n_e \ /10^{31} \ \mathrm{m}^{-3}}}$$

for $b_{\perp}$ for protons and electrons with the assumption that $T_e > T_p$, and taking the electron only term in the Debye length. This result is halved when using all electron parameters. For electrons, the de Broglie wavelength can, for $\lambda_{\mathrm{dB}} > b_{\perp}$, be the smaller length scale of interest;

$$\frac{\lambda_{\mathrm{D}}}{\lambda_{\mathrm{dB}}} = \sqrt{\frac{\epsilon_0 T_i}{n_i e^2}} \frac{2 m_e v_{\mathrm{th,e}}}{\hbar} \approx 3.38 \times 10^{32} \frac{T_e}{\sqrt{n_e}} = 17.1 \frac{\left(T_e \ /\mathrm{keV}\right)}{\sqrt{n_e \ /10^{31} \ \mathrm{m}^{-3}}}$$

This occurs when the following ratio is less than one;

$$\frac{b_{\perp}}{\lambda_{\mathrm{dB}}} = \frac{e^2}{4\pi\epsilon_0} \frac{2}{m_e v_{\mathrm{th,e}}^2} \frac{2 m_e v_{\mathrm{th,e}}}{\hbar} \approx 8.37 \times 10^{-9} \frac{1}{\sqrt{T_e}} = 0.66 \frac{1}{\sqrt{\left(T_e \ /\mathrm{keV}\right)}}$$

corresponding to $T_e > 2.3$ keV. The relevant expression for ions requires temperatures in the MeV.

Finally, for $n_e = n_p$,

$$\frac{\lambda_{\mathrm{D}}}{r_i} = \sqrt{\frac{\epsilon_0 T_e}{n_e e^2}} \left(\frac{4\pi n_p}{3}\right)^{1/3} \approx 2.58 \frac{\sqrt{\left(T_i \ /\mathrm{keV}\right)}}{\left(n_e \ /10^{31} \ \mathrm{m}^{-3}\right)^{1/6}}$$

is the ratio of the Debye length to the ion sphere radius.

Evidently, the plasma theory breaks down as $g \longrightarrow 1$, but it is useful to have a more exact quantitative limit to the application of plasma theories so as to avoid their improper use in conditions for which other physics is dominant. This is particularly true for the regime under consideration as some of the conditions encountered are very close to the low temperature, high density regime in which ion-ion correlations cannot be ignored. This regime is characterised by having $g \geq 1$, so that ions become bound to each other. Using the Coulomb logarithm identified in equations (2.12) and (2.13) means that simulations should be limited to $\ln \Lambda \gtrsim 2.6$, or, equivalently, $N_{\mathrm{D}} \gtrsim 10$ according to Gericke, Murillo and Schlanges [32]. This is satisfied for all simulations shown except for some special cases in Chapter 4 which include modifications appropriate for the lower temperatures that are considered, and these still satisfy $N_{\mathrm{D}} \gtrsim 1$.

2.5 Approaches to plasma physics

A full solution of the equations of motion of particles in a plasma is analytically impossible, as it is an N-body problem. To make any progress toward calculating properties of interest, approximations must be made. The properties of interest are non-Maxwellian distributions and the effects of large-angle collisions, so the merits of each theory with respect to these properties are given particular emphasis.

The most fundamental theoretical description of the entire classical plasma, without approximation, comes from Liouville's theorem [43] which states that the all-particle distribution function, $f_N = f_N(\mathbf{q}_1, \ldots, \mathbf{q}_N, \mathbf{p}_1, \ldots, \mathbf{p}_N, t)$, is constant along the phase trajectories of a closed system. The phase space has $6N$ degrees of freedom, where $\mathbf{q}_i$ and $\mathbf{p}_i$ are generalised co-ordinates and momenta respectively. Liouville's equation for a classical plasma at time t is then

$$\frac{\partial f_N}{\partial t} + \sum_{i=1}^{N} \dot{\mathbf{q}}_i \frac{\partial f_N}{\partial \mathbf{q}_i} + \sum_{i=1}^{N} \left(-\frac{\partial \phi_i^{ext}}{\partial \mathbf{q}_i} - \sum_{j=1}^{N} \frac{\partial \phi_{ij}}{\partial \mathbf{q}_i} \right) \frac{\partial f_N}{\partial \mathbf{p}_i} = 0 \tag{2.15}$$

where ϕ^{ext} is any potential external to the plasma and ϕ_{ij} is the interaction potential between particles i and j. This can be transformed into a sequence of N equations, each relating two single-particle distribution functions, for instance $f^{(n)}$ to $f^{(n+1)}$. This is known as the Bogoliubov, Born, Green, Kirkwood and Yvon (BBGKY) hierarchy of equations, and it is exact for a classical plasma [44, 45]. The truncation of the BBGKY hierarchy at the second term leads to transport theory, the full derivation of which can be found in [44]. The transport equation is

$$\frac{\partial f}{\partial t} + \mathbf{v} \cdot \nabla f + \mathbf{F} \cdot \frac{\partial f}{\partial \mathbf{p}} = C(f) \tag{2.16}$$

where $C(f)$ is the rate of change of the distribution function due to collisions, and each species has its own distribution function f.

With $C(f) \equiv 0$, Vlasov's equation for 'collisionless' kinetic theory is recovered. 'Collisionless' is taken to mean that $C(f)$ is small enough to ignore relative to the other terms in (2.16). A necessary condition for this to be true is that $\nu \ll \omega$ where ν is the effective collision frequency and ω the frequency of variation of macroscopic fields entering via $\mathbf{F}$. Vlasov's equation is not describing a plasma without any collisions; Coulomb collisions are the only way that each particle can interact with each other particle. However, the interactions are dominated by long range collisions, at distances on the order of λ_D, rather than the short distance binary collisions which dominate gases. These long range interactions are collective and can be represented by a macroscopic field averaged over a large

number of particles in a similar way to classical fields in electrodynamics. This is why the collisionless Vlasov equation includes **F**, and it is assumed that the plasma motion generating these macroscopic fields is excluded from being considered in the collisional terms on the right hand side of equation (2.16). The force term **F** hides a lot of complexity; for a fully self-consistent solution to (2.16) it must include **E** and **B** fields both from external sources *and* from plasma motion. All fields, with or without $C(f) \equiv 0$, must also satisfy Maxwell's equations;

$$\nabla \cdot \mathbf{E} = \frac{\rho}{\epsilon_0} \qquad \nabla \times \mathbf{E} = -\frac{\partial \mathbf{B}}{\partial t}$$
$$\nabla \cdot \mathbf{B} = 0 \qquad \nabla \times \mathbf{B} = \mu_0 \mathbf{J} + \mu_0 \epsilon_0 \frac{\partial \mathbf{E}}{\partial t}$$

As collisions are of primary interest, only the full transport equation is considered in subsequent chapters.

In a collisional plasma, $C(f) \neq 0$, and techniques to evaluate $C(f)$ are required. The diffusion approximation is one approach to evaluating $C(f)$. As $|\Delta \mathbf{v}|/v \sim \theta$, $|\Delta \mathbf{v}|/v$ is small for a single collision if $\ln \Lambda \gg 1$ [29]. The small 'jumps' in phase space due to collisions can be regarded as a flux **j** in velocity space, so that

$$C(f) = \left[\frac{\partial f}{\partial t}\right]_{\text{coll}} = -\nabla_{\mathbf{v}} \cdot \mathbf{j}$$

The flux can be written as an infinite series, where each successive term allows the expression to depart further from a 'perfect' continuous flow where only those particles at the bounding surface of a volume will leave that volume in phase space, rather than particles in a neighbourhood of the bounding surface. To describe particles which travel further through phase space (for example, in a situation with large momentum transfer), more terms in the series are required. The infinite series is

$$j_\mu = a_\mu f + b_{\mu\nu} \frac{\partial f}{\partial v_\nu} + c_{\mu\nu\alpha} \frac{\partial^2 f}{\partial v_\nu \partial v_\alpha} + \cdots$$

As the changes in velocity phase space are generally small, the first two terms of the expansion are taken. These have the interpretation of being a dynamical friction [46] and a diffusion tensor in velocity space;

$$j_\mu = \frac{F_\mu}{m} f - D_{\mu\nu} \frac{\partial f}{\partial v_\nu}$$

The sum of the flux of i over all species, $\mathbf{j}_i = \sum_j \mathbf{j}_{ij}$, is implicit. For practical calcu-

lation the terms of the expansion are used and defined in terms of $\langle \Delta v_\mu \rangle$, $\langle \Delta v_\mu \Delta v_\nu \rangle$, $\langle \Delta v_\mu \Delta v_\nu \Delta v_\alpha \rangle$ etc., where [27]

$$\langle \Delta \mathbf{v} \rangle = \int \psi(\mathbf{v}, \Delta \mathbf{v}) \Delta \mathbf{v} \, \mathrm{d}(\Delta \mathbf{v})$$

represents the independent probability that $\mathbf{v}$ increments by $\Delta \mathbf{v}$ in a time Δt, and the flux becomes

$$j_\mu = f \langle \Delta v_\mu \rangle - \frac{1}{2} \frac{\partial}{\partial v_\nu} \left(f \langle \Delta v_\mu \Delta v_\nu \rangle \right)$$

Equation (2.16) with the above flux is the Vlasov-Fokker-Planck (VFP) equation which may be succinctly expressed in terms of Rosenbluth potentials [47].

The diffusion approximation as widely used with two terms of the expansion has its limitations: the truncation of the BBGKY hierarchy means that equation (2.16) is only applicable on length and timescales greater than λ_D and $1/\omega_\mathrm{pe}$ respectively. It is also constrained to small-angle scattering or $\ln \Lambda \gg 1$ as otherwise more than the first two terms in the expansion of the flux are required. Even for moderately coupled plasmas, with $2 \leq \ln \Lambda \leq 5$, another term in the expansion is required [48]. If large-angle scattering is appreciable, the diffusion approximation breaks down and can fail to take account of the large jumps in energy or momentum space. There is further discussion of the limitations of the Fokker-Planck approach, with respect to large-angle collisions, in Chapter 6.

Transport theory is not the only approach to solving problems in plasma physics. Fluid equations, derived by taking moments of the Vlasov-Fokker-Planck equation, yield another method. They are not closed, and so also require approximations to be made. This is because each moment equation is coupled to a moment equation of higher order. The two techniques for closing the equations are to either truncate them, by assuming some form of the higher moments, or to use an asymptotic expansion of the distribution in a small parameter ϵ which is usually the ratio of the mean-free-path for some process to the length scale of interest for that process,

$$f(\mathbf{x}, \mathbf{v}, t) = f_0(\mathbf{x}, \mathbf{v}, t) + \epsilon f_1(\mathbf{x}, \mathbf{v}, t) + \epsilon^2 f_2(\mathbf{x}, \mathbf{v}, t) + \cdots$$

where it is required that the base distribution function be a Maxwellian,

$$f_0(\mathbf{x}, \mathbf{v}, t) = n(\mathbf{x}) \left(\frac{m}{2\pi T(\mathbf{x})} \right)^{3/2} \exp \left[-\frac{m \mathbf{v}^2}{2T(\mathbf{x})} \right]$$

so that the system is in equilibrium to zeroth order. The truncation approach leads to ideal magnetohydrodynamics, which requires a short energy equilibrium time [49] meaning again that the plasma is never very far from equilibrium. Both fluid approaches

require some approximations which are not favourable for considering non-Maxwellian distributions. The plasma is assumed to be close to equilibrium and assumed not to be collisional. They also rely on ensemble averages, meaning that relatively rare events, such as large-angle collisions, are effectively ignored.

Another stratagem for deriving results in plasma physics is to examine the propagation of waves within plasmas. Generally this includes the macroscopic fields $\mathbf{E}$ and $\mathbf{B}$ satisfying Maxwell's equations but also the equations derived from the first three moments of the Vlasov equation assuming, in the simplest form, no viscosity or heat conduction,

$$\begin{aligned}
&\text{Zeroth moment:} && \frac{\partial n}{\partial t} + \nabla \cdot (n\mathbf{v}) = 0 \\
&\text{First moment:} && nm\frac{\mathrm{D}\mathbf{v}}{\mathrm{D}t} = qn\left(\mathbf{E} + \mathbf{v} \times \mathbf{B}\right) - \nabla p \\
&\text{Second moment:} && \frac{\mathrm{D}}{\mathrm{D}t}\left(pn^{-\gamma}\right) = 0
\end{aligned}$$

where $\mathrm{D}/\mathrm{D}t = \partial/\partial t + \mathbf{u}\cdot\nabla$ is the convective rate of change and $\mathbf{v}$ is the velocity, p pressure and n number density [49]. However this approach is limited by the same factors which mean that Vlasov's equation and the general fluid approach are not appropriate, as it is derived from them.

The complexity, and associated analytical intractability, of plasmas mean that all approaches are limited by some form of approximation. However, computational techniques can provide insight into the behaviour of plasmas in situations where more simple analytical results are not forthcoming. In this work, a particle based computational approach is taken and used to study non-Maxwellian distributions. The strengths and weaknesses of this approach are more fully explored in Chapter 3.

Chapter 3

Computation with Monte Carlo

3.1 Introduction

A new code, following Takizuka and Abe's prescription [50], has been developed for the study of non-Maxwellian distributions in plasmas in 0D3V. This Chapter explains both its operation, and its verification by a number of tests.

Monte Carlo methods have their origin in the Second World War [51] and became successful due to the arrival of automated computers (as opposed to the use of human 'computers'). Monte Carlo methods have many applications, including evaluating integrals in many dimensions and evaluating probability density functions [52]. Broadly, it is a class of methods that relies on using random, or pseudo-random, numbers in order to make samples of a quantity. In the limit of many samples, the quantity converges to the correct answer. This is in contrast to methods that employ direct evaluation of a function with a defined accuracy.

Monte Carlo algorithms for plasmas do not assume a particular distribution function, and can be adapted to allow any interaction to perturb that distribution function - not just those which represent small changes in energy or momentum, or only occur over certain timescales. This is particularly useful in kinetic problems which must be done self-consistently and with many species. It has been used, for instance, to reproduce and study the Langdon distribution [53, 54]. In plasmas far from equilibrium, Monte Carlo techniques can give results closer to molecular dynamics simulations than the Landau-Spitzer theory [28, 29], partially outlined in Appendix B, or Vlasov-Fokker-Planck codes [38]. They are also relatively simple computationally, and some Monte Carlo models for plasmas conserve both energy and momentum. The drawback is that the quality of

the result is dependent on the number of simulation particles, and the quality of the random number generator. Scaling up Monte Carlo simulations to problems with spatial extent is very expensive computationally, which is why methods exist [55] to weight particles to reduce the number required at the cost of explicit conservation of energy, or to decrease running time by grouping collisions together [56]. The code presented conserves energy and momentum explicitly. They are not appropriate in the limit of very strong coupling because of the break down of plasma theory when there are not enough particles in a Debye sphere to carry out screening. Some PIC (Particle-In-Cell) codes, specifically those with collisions, have many of the attractive features of Monte Carlo codes, and extra features such as macroscopic electric and magnetic fields. However, for the microphysics which is the subject of this thesis, global fields are less important and there is a trade-off between the inclusion of extra effects and the large number of particles per cell which would be required in PIC. PIC codes also suffer from numerical heating. Molecular dynamics simulations offer an even more fundamental approach but are very computationally intensive. Future research will seek to explore some of the topics presented using other types of code, with PIC and molecular dynamics codes strong contenders.

The central limit theorem provides the mathematical underpinning for Monte Carlo codes. For example, if the desired effect is to recreate a known distribution function with a number of simulation particles N (where N is many orders of magnitude less than in reality), then a sequence of independent and identically distributed random variables X_i with μ the average of the true distribution satisfies

$$\hat{X} = \lim_{N \longrightarrow \infty} \sqrt{N} \left(\frac{1}{N} \sum_{i=1}^{N} X_i - \mu \right) \longrightarrow \hat{X} \sim \mathcal{N}(0, \sigma^2)$$

i.e., the distribution of the left-hand side of the equation tends to a normal distribution as $N \longrightarrow \infty$. $X_i \sim \mathcal{N}(\mu, \sigma^2)$ signifies that X_i is normally distributed with mean μ and standard deviation σ. The replication of distribution functions improves as $\frac{1}{\sqrt{N}}$. To check that the desired level of accuracy is reached, μ and higher order moments may be calculated from simulation and compared to the theoretical values.

A random number generator is required for many of the calculations in the Monte Carlo code. It is extremely important that the generator can provide uniformly distributed values without any biases. The robust "ran2" random number generator is used, which has period $> 2 \times 10^{18}$ [57]. It produces random numbers $U \sim \mathcal{U}(0, 1)$, where $\mathcal{U}(0, 1)$ signifies that a variable is distributed uniformly on the real number line between 0 and 1.

3.2 Operation

The algorithm followed by the code is shown in Fig. 3.1. Global initial conditions are set by the user, including species information such as densities, temperatures (or non-Maxwellian distributions), and number of simulation particles. Particles are represented in the code by objects which store three dimensions of velocity and the relevant species type, which links to information such as charge and mass. To initialise the code, particles must be created in the appropriate number and distribution. The proportions of each type of particle are given by the ratio of densities of each species with a particle weighting w such that

$$n_i = wN_i \;\; \forall\, i\,; \qquad \text{and} \qquad w = \sum_i n_i / \sum_i N_i$$

where n_i is the density, and N_i is the number of simulation particles of species i. The density of electrons is always chosen so as to keep the plasma neutral. Particles are picked from the relevant distribution functions and $t = 0$ diagnostics run, both as described in §3.2.1. The collision loop is then run, beginning with the calculation of λ_D, $\ln\Lambda$ and Δt. The Coulomb logarithm employed is detailed in §2.3. Radiation is neglected.

Δt is taken as being proportional to the shortest relevant physical timescale of change in the plasma, $1/\nu$, and some useful values of ν can be found in Appendix B. Typically, $\Delta t = \frac{1}{10\nu}$, though it must also be set to keep scattering angles relatively small.

3.2.1 Particles and distribution functions

Particles are initialised according to a particular distribution in 0D3V. For distributions which are everywhere integrable, probability density functions (or distribution functions) can be integrated to the cumulative density function $\int_0^x f(x')\mathrm{d}x' = \mathcal{C}(x)$ and the cumulative density function is normalised such that $\mathcal{C}(0) = 0$ and $\lim_{x\to\infty} \mathcal{C}(x) = 1$. The cumulative density function is inverted to give

$$\mathcal{C}^{-1}(U) = x; \quad U \in (0, 1)$$

This represents a parametrisation of the real number line between 0 and 1 into the space of the variable. Randomly generated values of $U \sim \mathcal{U}(0, 1)$ in the domain of $\mathcal{C}^{-1}(U)$, generate values of x that occur with frequencies determined by the original probability density function.

The type of distribution function chosen varies depending on the application, but the

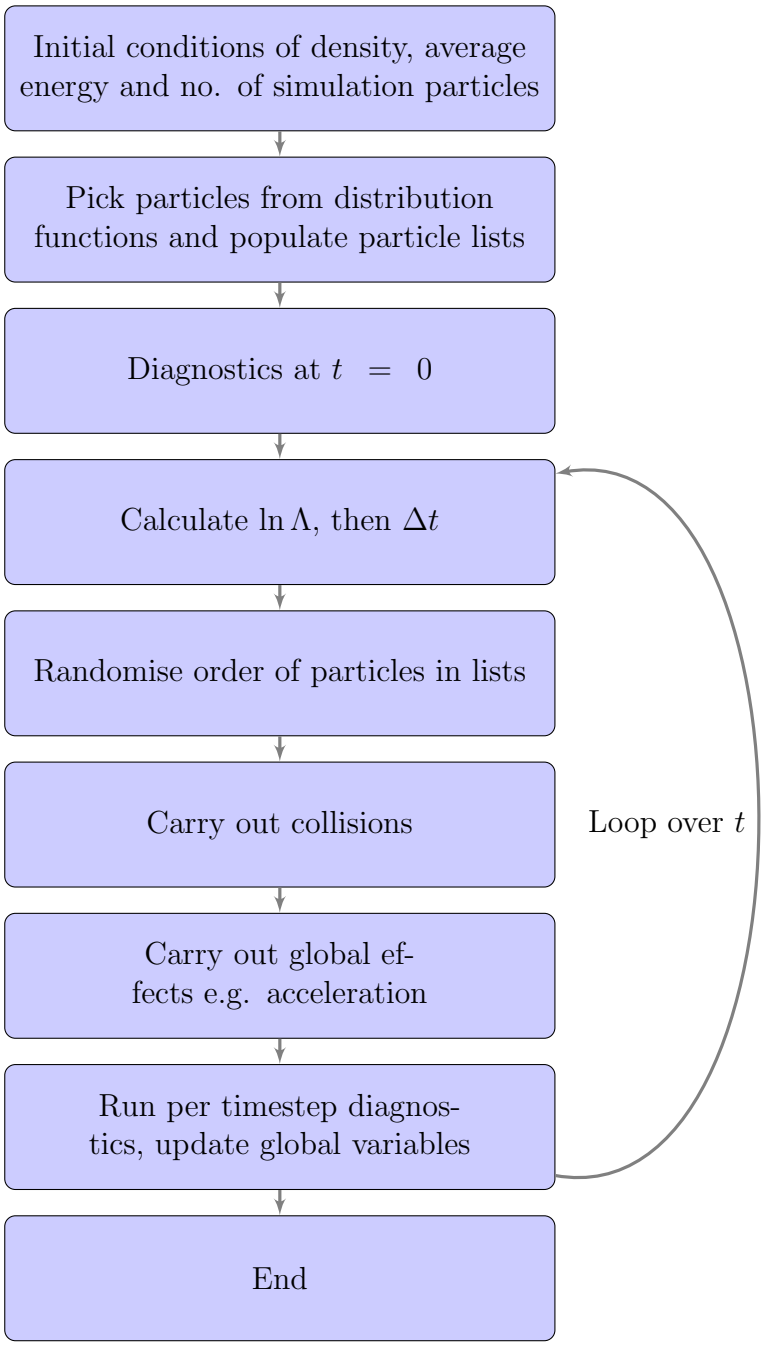

Figure 3.1: Schematic of the algorithm used by the Monte Carlo code.

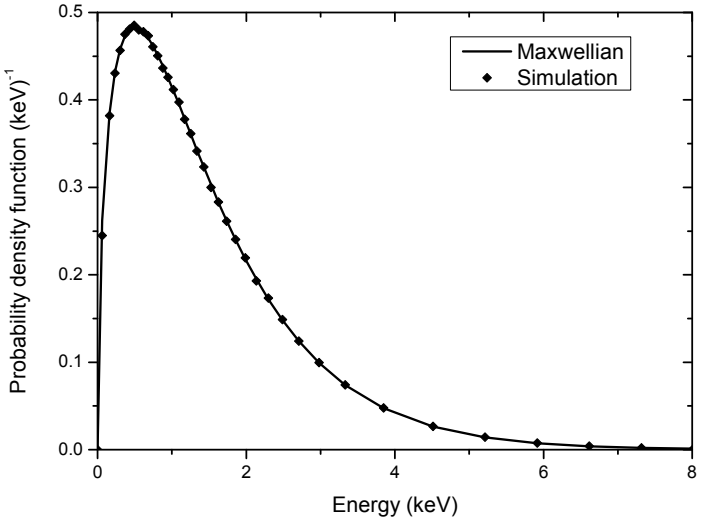

Figure 3.2: Electron distribution with $T_e = 1$ keV.

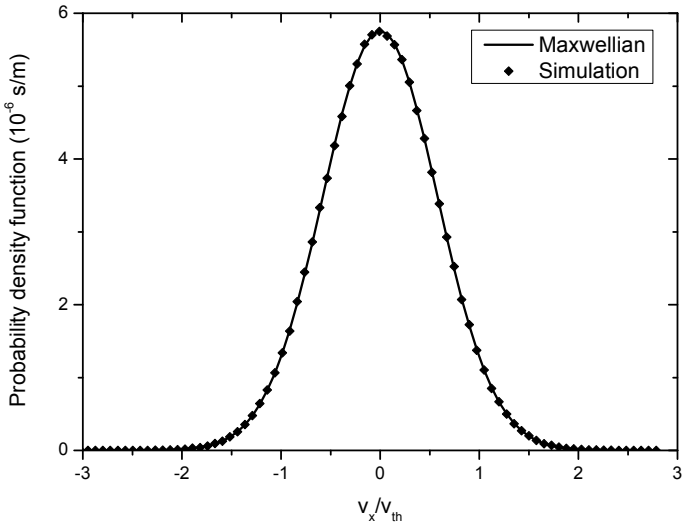

Figure 3.3: v_x component of velocity for a deuterium distribution at $T_d = 0.1$ keV.

default is the Maxwell-Boltzmann distribution,

$$f_{\mathrm{MB}}(\mathbf{v})d^3v = \left(\frac{m}{2\pi T}\right)^{3/2} \exp\left(-\frac{m\mathbf{v}^2}{2T}\right) d^3v$$

also referred to as a Maxwellian distribution. This is separable into a distribution $f_{\mathrm{MB}}(v_x)$ for each direction, with separate standard deviations of $\sigma = \sqrt{\frac{T}{m}}$. As Maxwellians are only properly integrable on the whole domain, otherwise giving an error function, it is computationally expensive to invert the cumulative density function. An efficient alternative, the Box-Muller transform [58], is used to determine v_i for each direction i

when creating a simulation particle. Four independent random numbers $U_j \in (0, 1)$ are generated, and the components of velocity are given by

$$v_x = \sqrt{\frac{-2T}{m} \ln(U_0)} \sin(2\pi U_1)$$
$$v_y = \sqrt{\frac{-2T}{m} \ln(U_0)} \cos(2\pi U_1)$$
$$v_z = \sqrt{\frac{-2T}{m} \ln(U_2)} \cos(2\pi U_3)$$

Fig. 3.2 is a comparison of simulation against theory for a Maxwellian distribution in energy, while Fig. 3.3 shows velocity in one direction. Both are taken from the $t = 0$ diagnostics. Monoenergetic and isotropic distributions,

$$f_{\text{Mono}}(E) = \delta(E - E_0)$$

are useful for simulating fusion created α-particles, with $f(x) = \delta(x - x_0)$ the usual Dirac delta function (a generalised function). For an isotropic distribution with a single energy, $v = (2E_0/m)^{1/2}$ is the radius of a sphere in velocity space. Randomly choosing a point on a 2-sphere, then scaling the values by v, gives the components of velocity:

$$\begin{aligned} v_x &= v\sqrt{1 - U^2}\cos\phi \\ v_y &= v\sqrt{1 - U^2}\sin\phi \\ v_z &= vU \end{aligned}$$

with $U \sim \mathcal{U}[-1, 1]$ and $\phi \sim \mathcal{U}[0, 2\pi)$. Mono-directional, mono-energetic beams are created with a small Gaussian velocity spread in each direction to avoid problems with the collision routine. A small spread is not unphysical.

In cases where distributions are close to equilibrium, the temperature is output as $T = 2\langle E\rangle/3$ for each species. Many of the distributions presented are not in equilibrium, but the output of 'temperature' with $T = 2\langle E\rangle/3$ is employed as a useful reference to other models. Alternatively, the average energy is presented directly. Distribution functions in, for example, energy are output by setting constant bin size ΔE over a range, and recording the counts of each species of particle appearing in the relevant bin relative to the total number of particles multiplied by the bin size;

$$f(E, E + \Delta E) = \frac{\text{Counts}\,[E, E + \Delta E]}{N_{\text{Total}} \cdot \Delta E}$$

with N_{Total} the total number of particles of that species, and $E+\Delta E/2$ vs. $f(E, E+\Delta E)$ plotted. $\int f(E)dE = 1$ is ensured by this equation as long as the counts are recorded over the entire energy range.

If the probability density is very non-uniform, a variable bin width distribution function diagnostic is used which creates a new bin every time $(\text{Counts}\left[E, E+\Delta E\right]/N_{\text{Total}}) >$ some sensitivity value, which is defined according to the application, but is generally $\sim$0.05. With large binwidths, the plotting of a point at $E+\Delta E/2$ can be misleading if much of the probability density actually lies toward, for example, E rather than $E+\Delta E$. A maximum binwidth proportional to the standard deviation of the appropriate equilibrium distribution prevents this occurring. An example distribution 62 ps into a simulation is shown in Fig. 3.4 to highlight how this diagnostic can cope with large energy ranges. The conditions are similar to ICF, but with a large proportion of fusion created α particles (10%) slowing down and driving a non-Maxwellian tail in a background population of tritium (not shown) and deuterium. The equivalent Maxwellian has the same average energy as the simulation distribution. Fig. 3.4 uses the discrete collision algorithm described in Chapter 7.

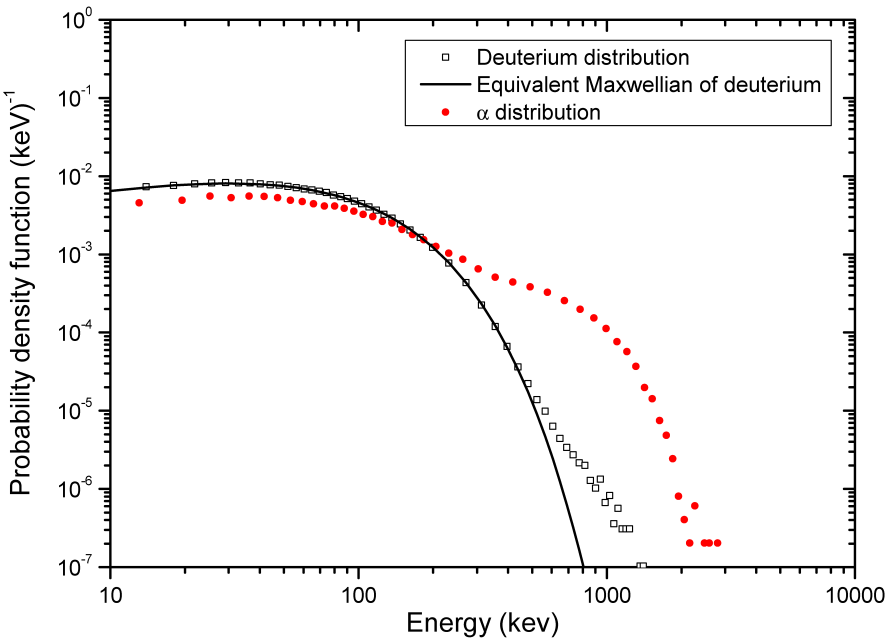

Figure 3.4: The variable bin width distribution function diagnostic showing an ICF scenario.

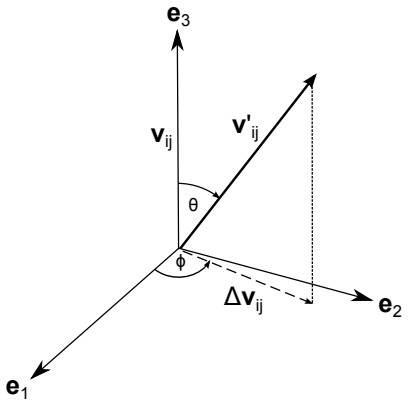

Figure 3.5: The scattering in the frame of relative velocity, with $\mathbf{v}_{ij} = v_{ij}\hat{\mathbf{e}}_3$.

3.2.2 Scattering

Which particles collide in a single timestep is determined by selecting pairs or triplets from lists of particles with neighbouring particles selected using the groupings algorithm of Takizuka and Abe [50]. To ensure that scattering is not carried out on the same pairs every timestep, the particles are randomly re-ordered each timestep, using a Fisher-Yates shuffle [59].

For two particles i and j, the relative velocity is $\mathbf{v}_{ij}$. In the frame of the relative velocity, in which $\mathbf{v}_{ij} = v_{ij}\hat{\mathbf{e}}_3$, a scattering through the centre-of-mass scattering angle θ in a time Δt produces a new relative velocity vector

$$\begin{pmatrix} 0 \\ 0 \\ v_{ij} \end{pmatrix} \mapsto \begin{pmatrix} v_{ij}\sin\theta\cos\phi \\ v_{ij}\sin\theta\sin\phi \\ v_{ij}\cos\theta \end{pmatrix}$$

where $\phi \sim \mathcal{U}(0, 2\pi]$. The geometry in this frame is shown in Fig. 3.5. The new particle velocities are given by

$$\mathbf{v}_i' = \mathbf{v}_i + \Delta\mathbf{v}_{ij} m_{ij}/m_i \tag{3.1}$$

$$\mathbf{v}_j' = \mathbf{v}_j - \Delta\mathbf{v}_{ij} m_{ij}/m_j \tag{3.2}$$

Note that although $\Delta\mathbf{v}_{ij}$ is non-zero in general in a collision, $\Delta v_{ij} \equiv 0$ ensuring conservation of energy, and conservation of momentum is ensured trivially by equations (3.1) and (3.2).

The scattering angle θ is not taken directly from the Rutherford cross-section because

of the divergence at $\theta = 0$, and because most plasmas are dominated by the multiple small-angle scattering regime. A statistical argument for the behaviour of the scattering angle is described succinctly in Jackson [31];

> Since successive collisions are independent events, the central limit theorem implies that for a large number of collisions, N_{coll}, the distribution in angle will be approximately Gaussian around the forward direction with a mean square angle
>
> $$\left\langle \Theta^2 \right\rangle = N_{\text{coll}} \left\langle \theta^2 \right\rangle$$

Angular brackets signify an average value. $\langle\theta^2\rangle$ is most often calculated using the small-angle approximation so that

$$\left\langle \theta^2 \right\rangle = \frac{1}{\sigma} \int \theta^2 \frac{\mathrm{d}\sigma}{\mathrm{d}\Omega} \mathrm{d}\Omega = \frac{\pi b_\perp^2}{2\sigma} \int \frac{\theta^2 \sin\theta}{\sin^4(\theta/2)} \mathrm{d}\theta = \frac{8\pi b_\perp^2}{\sigma} \int \frac{\mathrm{d}\theta}{\theta} = 8\pi b_\perp^2 \ln\Lambda/\sigma \tag{3.3}$$

The number of collisions in a distance Δs is given by $N_{\text{coll}} = n\sigma\Delta s = n\sigma v_{ij}\Delta t$ with $n = \min\{n_i, n_j\}$ and Δt the timestep, so

$$\left\langle \Theta^2 \right\rangle = n\Delta t v_{ij} 8\pi b_\perp^2 \ln\Lambda$$

where $\ln\Lambda = \frac{1}{2}\ln\left(\frac{b_\perp^2+\lambda_{\text{D}}^2}{b_\perp^2}\right)$. A number of terms have been omitted due to the small-angle approximation but their inclusion makes almost no difference to the value of $\langle\Theta^2\rangle$. P_{σ_1} is the probability of a collision using the 1st kinetic cross-section, using the definition of the kinetic cross-sections found in equation (2.10). There is a simple relation between $\langle\Theta^2\rangle$ and this probability; $1 - \cos\theta \approx \theta^2/2$ so $\langle\Theta^2\rangle = 2P_{\sigma_1}$. With $\langle\Theta^2\rangle$ computed, randomly generated values of $\theta \sim \mathcal{N}(0, \langle\Theta^2\rangle)$ are used as the scattering angles in the particle-particle collisions. To perform the generation of θ from random numbers $U_1, U_2 \sim \mathcal{U}(0,1)$, a Box-Muller transform [58] is used;

$$\theta = \sqrt{-2\left\langle\Theta^2\right\rangle \ln(U_1)} \cos(2\pi U_2)$$

If $|\theta| > \pi$, θ is chosen using $\theta \sim \mathcal{U}(0,\pi)$ but the timestep should be set so as to avoid this. If there is an odd number of particles in a list in which pairs of particles are to be collided, the first three are combined in three pairs and scattering angles selected from a normal distribution with half the usual variance.

For computational efficiency, Takizuka and Abe use $\delta \equiv \tan\frac{\theta}{2}$, and choose $\delta \sim \mathcal{N}(0, \langle\Theta^2\rangle/4)$. Then

$$\sin\theta = \frac{2\delta}{1+\delta^2} \quad \text{and;} \quad 1 - \cos\theta = \frac{2\delta^2}{1+\delta^2}$$

and all the terms in $\Delta\mathbf{v}_{ij}$ can be written in terms of δ. The small-angle approximation appears in $\langle\theta^2\rangle$, and also in the three equations for δ. The small-angle approximation leads to errors of up to 10% in $\Delta\mathbf{v}_{ij}$ at $\theta = \pi/4$, and greater errors for $\theta > \pi/4$ when using the δ approximation. To avoid this, Δt can be set small enough to ensure $\sqrt{\langle\Theta^2\rangle} < 5\pi/33$ so that $P(|\theta| > |\pi/4|) < 10\%$, but in the code $\theta \sim \mathcal{N}(0, \langle\Theta^2\rangle)$ is used directly and only the small angle approximation in equation (3.3) is retained.

3.2.3 Fusion of deuterium and tritium

The code has an option to include the T(d,n)^{4}He fusion reaction. There are two versions of inclusion of this reaction; one is a diagnostic mode and the other self-consistently produces α particles by using up deuterium and tritium particles. The former is limited to recording the rate of fusion reactions for the given conditions and comparing it to a Maxwell-Boltzmann distribution with the same average energy. It does not remove fused particles, nor does it release the energy or products of fusion. It is used only as a convenient way to compare the instantaneous reactivity for a set of conditions. The Bosch and Hale [60] parametrisation of both the fusion cross-section and the reactivity for Maxwell-Boltzmann deuterium and tritium distributions with average temperature T is used as the comparison value. The fusion reactivity for two particles i and j (always either deuterium and tritium, or tritium and deuterium) is

$$\langle\sigma_{\mathrm{F}} v_{ij}\rangle = \int\int f_i(\mathbf{v}_i) f_j(\mathbf{v}_j) \sigma_{\mathrm{F}}(v_{ij}) v_{ij} \mathrm{d}\mathbf{v}_i \mathrm{d}\mathbf{v}_j \tag{3.4}$$

in units of volume per unit time, and the rate per unit volume per unit time is

$$\frac{\mathrm{d}R}{\mathrm{d}V} = \frac{n_i n_j}{1+\delta_{ij}} \langle\sigma_{\mathrm{F}} v_{ij}\rangle$$

The Bosch Hale reactivity is $\langle\sigma_{\mathrm{F}} v_{ij}\rangle_{\mathrm{MB}}$. Full details of the fusion parametrisation can be found in Appendix C. Fig. 3.6 shows the code running with the diagnostic fusion output, and there is good agreement with both the Bosch and Hale parametrisation (shown) and other reference values [18] (not shown).

The second mode of operation, which is considerably more computationally intensive, is one in which fusion reactions cause deuterium and tritium particles to be removed and replaced with the charged fusion products (neutrons are neglected). A succession of deuterium and tritium collisions takes place after the Coulomb scattering algorithm is run in each timestep. The number and pairings are the same as with the Takizuka and Abe Coulomb collision algorithm. Over all collisions the theoretical α particle number

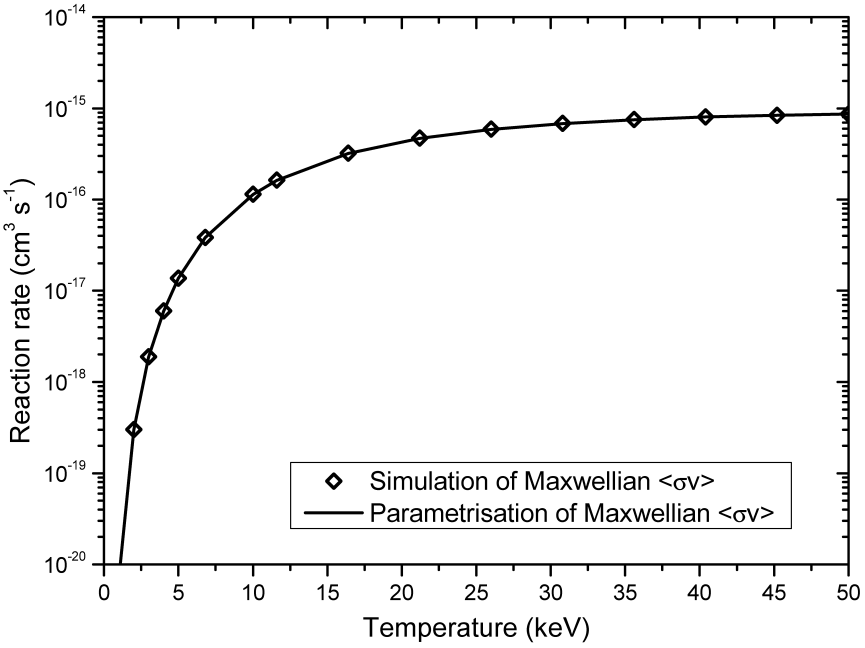

Figure 3.6: The first mode of operation; $\langle \sigma_{\mathrm{F}} v_{ij} \rangle$ for equimolar deuterium and tritium Maxwellian distributions over a range of temperatures.

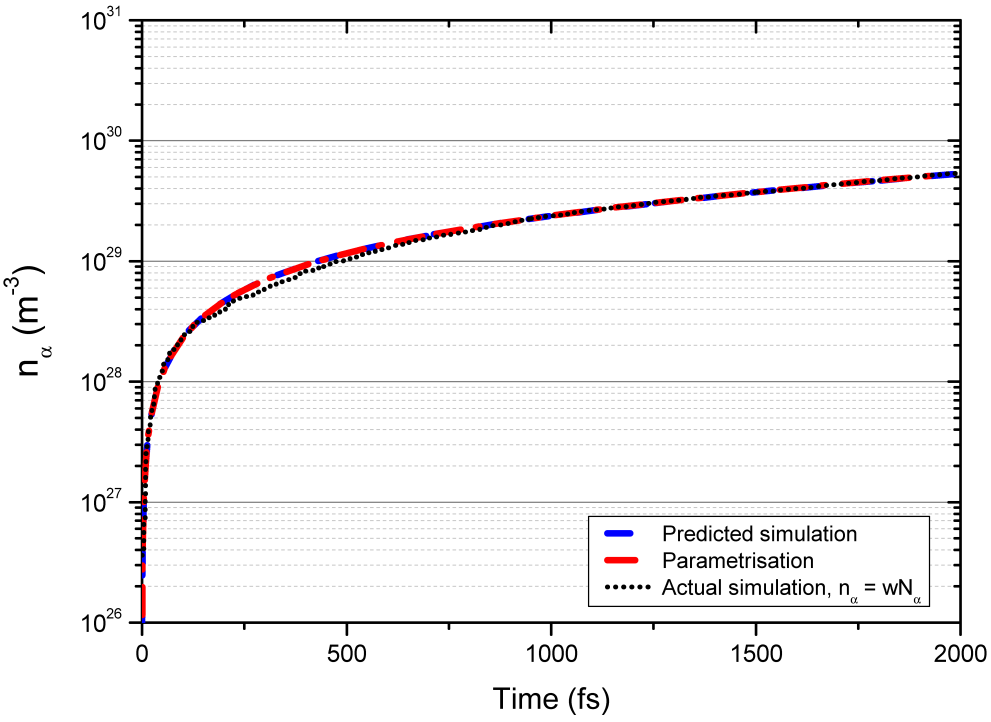

Figure 3.7: The second mode of operation in a 10 keV burning deuterium-tritium plasma, showing the creation of α particles.

density for those simulation collisions is recorded;

$$n_\alpha(t+\Delta t) = n_\alpha(t) + \frac{1}{N_{\text{Colls}}} \sum_{\text{Colls}} \sigma_{\text{F}}(v_{ij}) v_{ij} n_i(t) n_j(t) \Delta t \tag{3.5}$$

Fusion occurs for the two particles if, for a random $U \sim \mathcal{U}(0,1)$,

$$U \leq P_{\text{Fuse}} \equiv \sigma_{\text{F}}(v_{ij}) v_{ij} \min\{n_i, n_j\} \Delta t$$

In the case of fusion, the particles are removed from interactions in the code and

$$\mathbf{V} = \frac{\mathbf{v}_i m_i + \mathbf{v}_j m_j}{m_i + m_j}$$

which is the velocity of the centre of mass frame, is stored for each pair. α particles are then created for every successful fusion collision. They are created as being isotropic in the frame of the fusion collision, with $E_\alpha = \frac{1}{2} m_\alpha v_0^2 = 3.54$ MeV, but are thermally broadened by using the laboratory frame velocity

$$\mathbf{v}_{\alpha,\text{lab.}} = \mathbf{v}_0 + \mathbf{V}$$

If N fusion reactions occur, the new densities and number of simulation particles used by the simulation are

$$\begin{aligned} N_\alpha(t+\Delta t) &= N_\alpha(t) + N \\ n_\alpha(t+\Delta t) &= w\,(N_\alpha(t) + N) \\ N_{i,j}(t+\Delta t) &= N_{i,j}(t) - N \\ n_{i,j}(t+\Delta t) &= w\,(N_{i,j}(t) - N) \end{aligned}$$

but equation (3.5) is also recorded. Note that the densities predicted by these two methods should broadly agree, but that (3.5) is continuously recorded and $n_\alpha(t+\Delta t)$ is based upon the discrete number of collisions using a Monte Carlo process, and so is subject to greater noise. The latter is used for the simulation in order to be consistent with the number of α particles created. To ease computation, simulations using this mode of operation are always started with at least one α particle but, for a large enough total number of simulation particles, the initial n_α corresponding to this one particle is many orders of magnitude less than that of other species of interest. Comparison against theory is similar to in the first mode of operation, being given by the Bosch and Hale parametrisation of the reactivity, $\langle \sigma_{\text{F}}(v_{ij}) v_{ij} \rangle_{\text{MB}}$. The updated values of the Maxwell-Boltzmann theoretical

comparison after a timestep has passed are

$$n_\alpha(t+\Delta t) = \langle \sigma_{\rm F}(v_{ij}) v_{ij} \rangle_{\rm MB} n_i(t) n_j(t) \Delta t + n_\alpha(t)$$
$$N_\alpha(t+\Delta t) = \langle \sigma_{\rm F}(v_{ij}) v_{ij} \rangle_{\rm MB} n_i(t) n_j(t) \Delta t / w + N_\alpha(t)/w$$

An example of the code running with creation of α particles is shown in Fig. 3.7, with initial conditions of Maxwellian deuterium and tritium distributions with $n_d = n_t = 2 \times 10^{30}$ m^{-3}, $T_t = T_d = 10$ keV and $n_\alpha = 10^{25}$ m^{-3} corresponding to just one numerical α particle. The predicted simulation n_α is given by equation (3.5), but the actual value is $n_\alpha = wN_\alpha$ so is subject to statistical noise. However, the agreement between them is good and improves as N_α increases. The agreement with the reference, the Bosch Hale parametrisation of $n_\alpha(t)$, is also good.

3.3 Tests

The code must be robust in producing known analytical results, and also in dealing with arbitrary distribution functions. Various tests of its robustness are applied using an averaged Coulomb logarithm. Another test may be found in Figs. 5.4 and 5.5 of Chapter 5, but is more relevant to the other work presented in that Chapter.

3.3.1 Landau-Spitzer theory

The Monte Carlo code is benchmarked against Landau-Spitzer theory [28, 29] (see Appendix B). The ratio of the rates of energy loss (ν_E), stopping power (ν_s), perpendicular diffusion ($\nu_\perp$) and parallel diffusion ($\nu_\parallel$) are shown in Fig. 3.8. The timestep is the minimum over all species of $1/50\nu_{ij}$, where ν_{ij} is the basic relaxation rate defined in Appendix B. Each data point is made up of over 40,000 test α particles in an electron-deuterium background with roughly 4.5 million simulation particles. The agreement with Landau-Spitzer theory is generally strong but does suffer from noise, and the rate of energy loss goes through a discontinuity, as it changes sign, at $\langle E \rangle = T$, with T the background temperature. $\ln\Lambda$ is held fixed in this simulation. The median values for all of the rates are within 3%, and this increases to ∼5% with a factor 5 decrease in particle number *and* timestep.

Temperature equilibration is shown in Fig. 3.9, with $n_d = n_e = 2 \times 10^{30}$ m^{-3} and $T_{e,0} =$

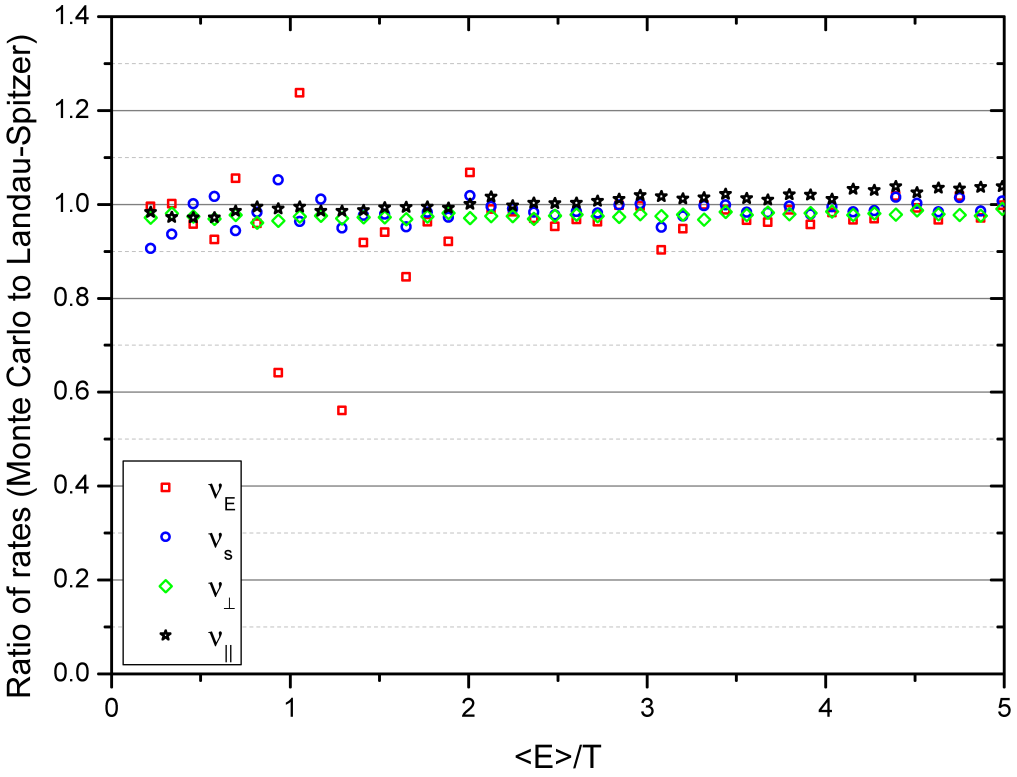

Figure 3.8: Ratios of Monte Carlo rates to Landau-Spitzer rates over a range of $\langle E \rangle / T$ values.

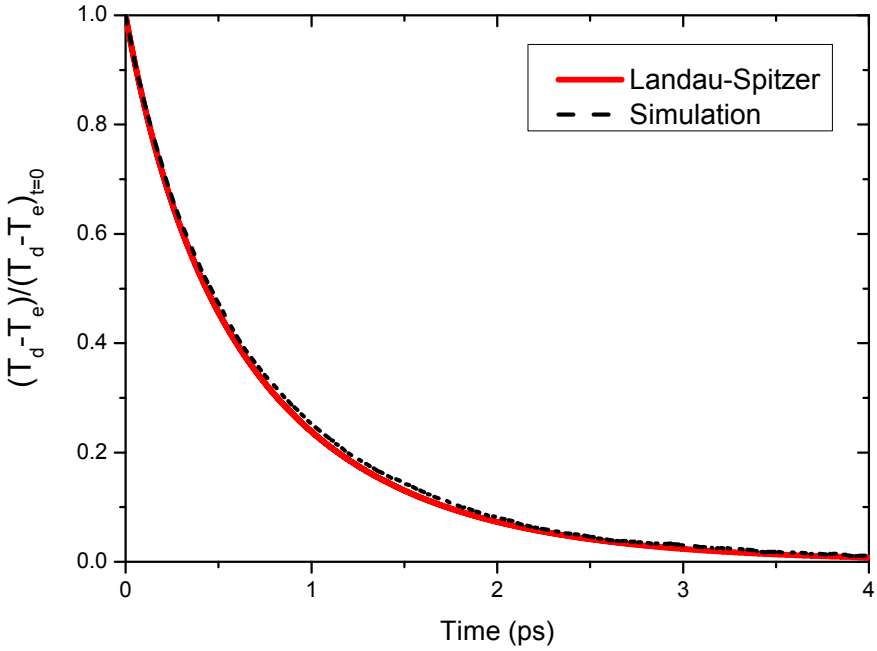

Figure 3.9: Temperature equilibration from a simulation shown against Landau-Spitzer theory.

$T_e(t=0) = 0.5$ keV, $T_{d,0} = 1$ keV. The rate of change of temperature is

$$\frac{\mathrm{d}T_i}{\mathrm{d}t} = \nu_{ij}^T \left(T_j - T_i\right)$$

with ν_{ij}^T from equation (B.1). The route through temperature taken by the simulation shows differences compared to Landau-Spitzer but the time taken to reach 90% of the final temperature is the same to within 2%. The noise is statistical, while the differences in route through temperature are probably due to slight departures from the perfect Maxwell-Boltzmann distributions which the Landau-Spitzer theory assumes.

The resistivity of a plasma, $\rho_{\mu\nu}$, is given by the generalised Ohm's Law [28]. Adopting the notation of Epperlein and Haines [61], and Braginskii [62], the transport coefficient for resistivity is given by

$$\left(en_e\right)^2 E_\mu = \alpha_{\mu\nu} J^\nu = \alpha_\parallel b_\mu b_\nu J^\nu + \alpha_\perp \epsilon_{\mu\nu\gamma} b^\nu \epsilon^{\gamma\delta\kappa} J_\delta b_\kappa - \alpha_\wedge \epsilon_{\mu\nu\gamma} b^\nu J^\gamma$$

where J_μ is current density, $b_\mu = B_\mu / \sqrt{B_\nu B^\nu}$ is the unit vector in the direction of the magnetic field and $\epsilon_{\mu\nu\gamma}$ is the Levi-Civita symbol. The Einstein summation convention applies, so that repeated indices are implicitly summed over. In the limit of $B_\mu \to 0$, $\alpha_\parallel = \alpha_\perp(0)$. Adopting this limit, restricting current density to the x-direction, and assuming isotropic global variables otherwise, only the x components of the resistivity tensor remain and $\rho \equiv \rho_{xx} = E_x / J_x$. Using simple first order transport theory without electron-electron collisions, a scenario also known as the Lorentz limit, the resistivity is

$$\rho = 3 m_e n_i \frac{\ln\Lambda}{e^2} \left(\frac{-q_i e^2}{4\pi\epsilon_0 m_e}\right)^2 \left[\int_0^\infty \frac{\partial f}{\partial v} v^6 dv\right]^{-1} \tag{3.6}$$

for $f(v)$ the distribution function of the electrons. For a Maxwell-Boltzmann distribution, there is an analytical expression:

$$\rho_{\mathrm{MB}} = \left(\frac{-q_i e^2}{4\pi\epsilon_0}\right)^2 \frac{\sqrt{m_e}}{16 e^2} \frac{n_i}{n_e} \ln\Lambda \left(\frac{2\pi}{T_e}\right)^{3/2} \tag{3.7}$$

The dimensionless transport coefficient for resistivity is $\alpha_\parallel^c$, and is constructed as

$$\alpha_\parallel^c = \alpha_\parallel \frac{\tau}{m_e n_e}$$

where

$$\tau^{-1} = \frac{4\sqrt{2\pi} n_i \ln\Lambda_{ie}}{3\sqrt{m_e} T_e^{3/2}} \left(\frac{q_i e^2}{4\pi\epsilon_0}\right)^2$$

is the inverse of the mean electron-ion collision time. Fig. 3.10 shows the simulation value of $\alpha_{\parallel}^{c}$ in the Lorentz limit for a Maxwellian against the prediction of equation (3.7) with the same conditions as the simulation, and also against the value listed in Epperlein and Haines' article [61].

3.3.2 Relaxation to equilibrium

Figs. 3.11, 3.12, 3.13 and 3.14 are snapshots of the relaxation of an initial delta function relaxing to a Maxwellian. The initial beam is mono-energetic with $f(E, t = 0) = \delta(E - E_0)$, $E_0 = 1.5$ keV and $\nu t = \nu(t)t \neq \nu(t = 0)t$. There is a significant change of scale between the first three figures due to the initial rapid relaxation from $f(E) = \delta(E - E_0)$. Another useful check on isotropy is kurtosis, which is examined for an arbitrary direction of velocity. Excess kurtosis is defined as $\kappa = \mu_4/\sigma^4 - 3$, where

$$\mu_n = \int (v_x - \mu)^n f(v_x) dv_x$$

is the nth centralised moment of the distribution function of v_x and σ is the standard deviation in the x-direction. It takes the value of zero for a (shifted) Gaussian, and its evolution to zero from an initially negative value is shown in Fig. 3.15, with red vertical lines marking the slices through time corresponding to Figs. 3.11, 3.12, 3.13 and 3.14. The first two slices, at $\nu(t)t = 0$ and $\nu(t)t = 1/5$, are too close to distinguish on the scale of the graph. $\langle E \rangle = 1.5$ keV throughout, with a final temperature of $T = 1$ keV.

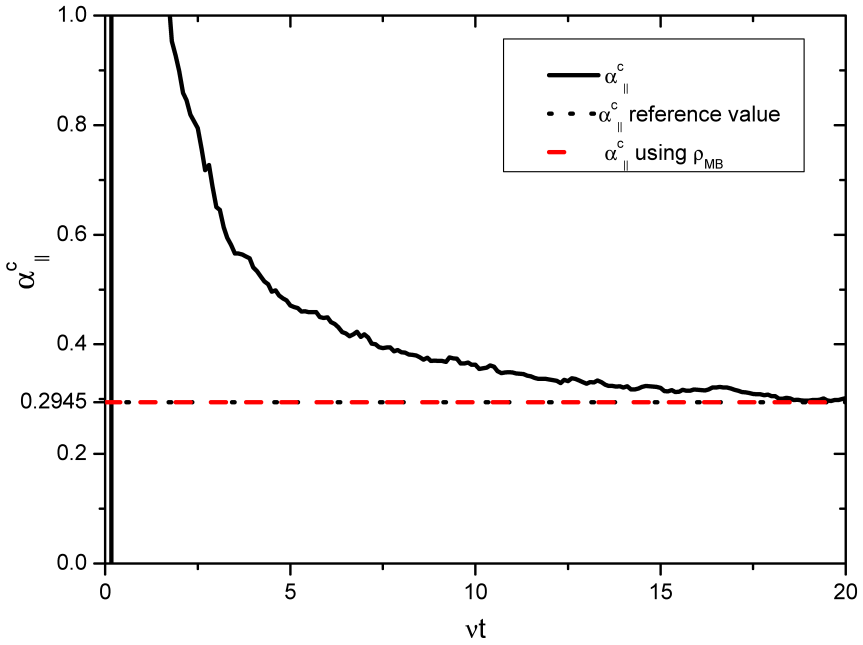

Figure 3.10: $\alpha^c_{\parallel}$ from simulation, theory, and a reference value [61], shown against $\nu(t)t$.

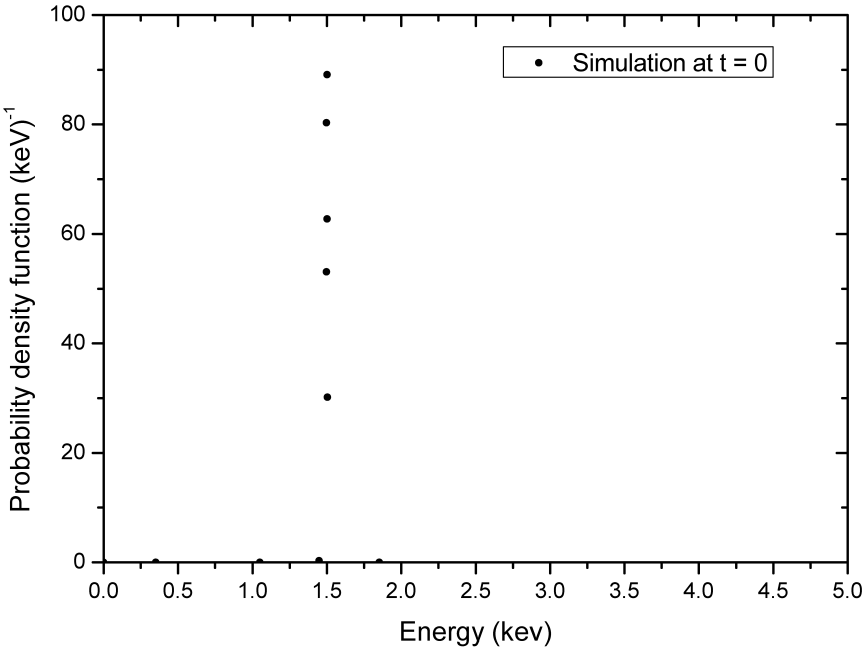

Figure 3.11: Delta function relaxation at $t = 0$.

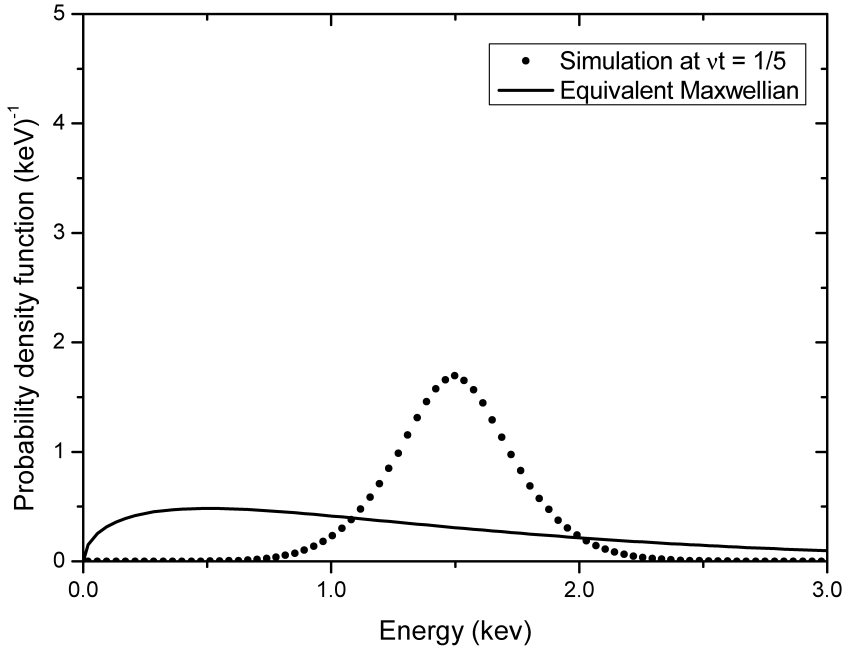

Figure 3.12: Delta function relaxation at $\nu t = 1/5$.

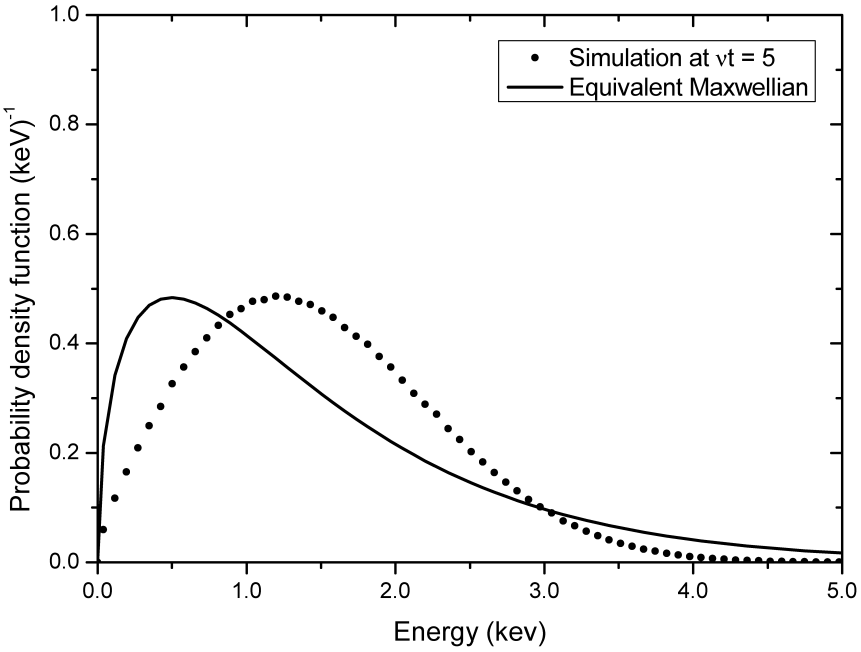

Figure 3.13: Delta function relaxation at $\nu t = 5$.

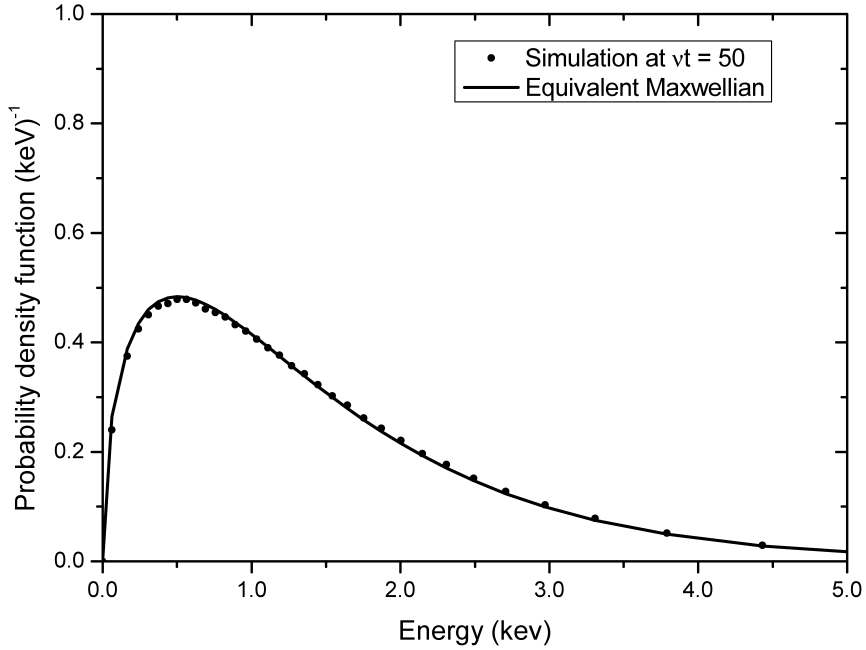

Figure 3.14: Delta function relaxation at $\nu t = 50$.

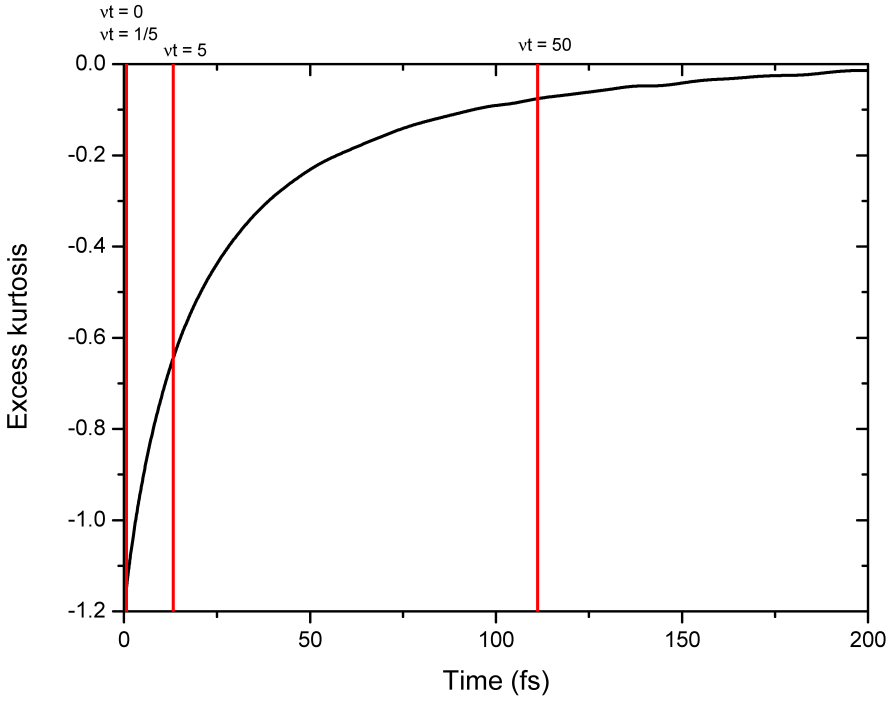

Figure 3.15: Excess kurtosis of v_x from an initial mono-energetic delta function as it relaxes to a Maxwellian distribution. Red vertical lines correspond to slices through time shown in Figs. 3.11, 3.12, 3.13 and 3.14.

Chapter 4

A Monte Carlo algorithm for degenerate plasmas

4.1 Introduction

In this Chapter, a procedure for performing Monte Carlo calculations of degenerate plasmas is presented, and much of it is drawn from published work [63]. At the heart of the degenerate Monte Carlo scheme is the code described in detail in Chapter 3, with modifications which allow Fermi-Dirac distribution functions and scattering via a Pauli blocked binary collision approximation.

Modelling degenerate plasmas is of interest in ICF, during compression of the cold fuel and capsule shell [21, 40, 64] and for putting fusion energy more directly into ion species [65], and in astrophysical situations such as white dwarf stars [41]. Relevant ICF problems are degenerate thermal equilibration and the stopping of high energy ions by degenerate electrons. Yield is particularly sensitive to electron-ion equilibration, with simulations of direct-drive implosions showing a $\sim$10% difference across several different models of temperature relaxation [35]. The stopping power of degenerate electrons at very high densities is also of interest in athermal fusion, a topic explored in §6.2.1. The algorithm is benchmarked against degenerate electron-ion equilibration and the degenerate resistivity transport coefficient from unmagnetised first order transport theory. The code is also applied to the cold fuel shell and α particle equilibration problem of ICF.

It is not appropriate in the limit of very strong coupling because of the eventual break down of the plasma theory underlying the Monte Carlo code in Chapter 3. It is noted that Monte Carlo techniques with degenerate capabilities have been developed for studying

transport in semi-conductors [66] but no such method exists for fully-ionised plasmas. Some of the techniques described are potentially applicable to other types of codes, for example, Particle-In-Cell (PIC) codes.

4.2 Degenerate plasmas

This discussion is with respect to degenerate electrons but the process is the same for any fermion. Applying the anti-commutation relation for identical fermions to free electrons gives rise to the Fermi-Dirac distribution [67];

$$f_{\mathrm{FD}}(E)\mathrm{d}E = \frac{(2m_e)^{3/2}}{2n_e\hbar^3\pi^2}\frac{\sqrt{E}\mathrm{d}E}{\exp\{\frac{E}{T_e}-\eta\}+1} \tag{4.1}$$

where η is the degeneracy parameter. $f(E)dE$ is normalised to 1, and the equation

$$\int \frac{(2m_e)^{3/2}}{2n_e\hbar^3\pi^2}\frac{\sqrt{E}\mathrm{d}E}{\exp\{\frac{E}{T_e}-\eta\}+1} = 1 \tag{4.2}$$

defines η as a function of n_e and T_e. The occupancy function is the measure of the proportion of states occupied at energy E, and is given by

$$f_o(E) = \frac{1}{\exp\{\frac{E}{T_e}-\eta\}+1} = f_{\mathrm{FD}}(E)/g(E) \tag{4.3}$$

where $g(E)\mathrm{d}E = \frac{(2m_e)^{3/2}}{2n_e\hbar^3\pi^2}\sqrt{E}\mathrm{d}E$ is the density of states between E and $E+\mathrm{d}E$. $\eta \longrightarrow -\infty$ corresponds to the classical limit in which the distribution function becomes a Maxwell-Boltzmann distribution. $\eta \longrightarrow \infty$ is the fully degenerate limit in which all of the particles are at energies below or equal to the Fermi energy, E_F, and the occupancy function becomes a step function

$$g(E) = 1,\ E \leq E_F; \quad g(E) = 0,\ E > E_F$$

where

$$E_F = \frac{\hbar^2}{2m_e}\left(3\pi^2 n_e\right)^{2/3}$$

is the Fermi energy. For a non-Maxwellian distribution, temperature and average energy no longer satisfy $T_e = \frac{2}{3}\langle E\rangle$. In the case of the Fermi-Dirac distribution, particles retain an energy even in the $T_e \longrightarrow 0$ limit as lower energy states have limited capacity and become fully occupied, so that remaining particles occupy energy states higher than the

ground state. In the zero temperature limit,

$$\eta \longrightarrow \frac{E_F}{T_e} \text{ and } \eta \longrightarrow \infty \tag{4.4}$$

There are many choices for the Coulomb logarithm, as specified in §2.3. Degenerate modifications to $\ln \Lambda$ are necessary because of the disparity between temperature and average energy, and because degenerate plasmas tend to occur at high density. The code does not explicitly require a particular Coulomb logarithm, and any could be used in the algorithm, as long as it includes degeneracy effects. There are logarithms available which include degeneracy corrections [68, 69]. In the simulations presented, Gericke, Murrillo and Schlanges' Coulomb logarithm number 6 [32] is employed as described in §2.3 but averaged over all simulation particles. However, due to the possibility of encountering the $T_e \longrightarrow 0$ limit, T_e is replaced by the 'effective' temperature defined by $T_e' = \sqrt{T_F^2 + T_e^2}$ where T_F is the Fermi temperature $T_F = E_F$. This is the same approximation as used by several authors including Brown and Haines [70], and Brysk, Campbell and Hammerling [71] who demonstrate that it matches Salpeter's [72] relation, where the $T_e \longrightarrow 0$ limit is avoided by multiplying by a factor $I_{1/2}(\eta)/I'_{1/2}(\eta)$, to within 5% for any η. $I_j(\eta)$ is the jth complete Fermi-Dirac integral (see Appendix A),

$$I_j(\eta) = \frac{1}{\Gamma(j+1)} \int_0^\infty \frac{t^j}{e^{t-\eta}+1} \mathrm{d}t$$

4.3 Algorithm

The Monte Carlo code is adapted to include Pauli blocking and the ability to initialise species with Fermi-Dirac distributions if required. As outlined in §3.2.1, distributions $f(x)$ which are everywhere integrable, can be integrated to the cumulative density function $\mathcal{C}(x)$, and the cumulative density function inverted so that randomly generated values of $U \sim \mathcal{U}(0,1)$ which are in the domain of $\mathcal{C}^{-1}(U)$ generate values of x that occur with frequencies determined by the original probability density function $f(x)$.

The Fermi-Dirac distribution is not integrable so this process cannot be done analytically, and numerical methods of calculating the inverse cumulative distribution function must be used. Numerical computations of energy values for initialising particles employ Hörmann and Leydold's algorithm [73]. It requires evaluations of $f(E)$, $\mathcal{C}(E)$ and initial boundary conditions. The domain of $\mathcal{C}^{-1}(U)$ is split into equally spaced sub-intervals and a cubic Hermite polynomial $H_n(U)$ is used to interpolate values of E given U, with $\mathcal{C}(E)_n \leq U \leq \mathcal{C}(E)_{n+1}$. Cubic Hermite polynomials have advantages over other methods

of interpolation of the same order because they are a local approximation, rather than a global one: if any interval does not reach the required level of approximation to the inverse cumulative distribution function, new points can be inserted locally without recomputing all interpolation points. Another advantage is that there is a relatively simple algorithm, which terminates if $f(E)$ is continuous, that can guarantee the monotonicity of $H_n(U) \,\forall\, n$ by creating new interpolation points [74]. Linear interpolation is also guaranteed to be monotonically increasing, but the number of points required for the same level of approximation to $\mathcal{C}^{-1}(U)$ is generally reduced by an order of magnitude or more by using cubic interpolation [73]. For the entire interpolation process, the maximal acceptable error

$$\epsilon_U = \max_{U \in [U_n, U_{n+1}]} |\mathcal{C}(H_n(U)) - U|$$

can be specified, and intervals are split until this is satisfied for every n. The result is a table of values of $[U_n = \mathcal{C}(x_n), x_n, f(x_n)]$.

With the creation of the table, values of U can be generated and the appropriately distributed values of E found. An indexed search is used to speed up the process of selecting an appropriate E for the given value of U [75]. Components of velocity are selected, and for isotropic distributions the method is the same as described in §3.2.1.

Initialised Fermi-Dirac distributions relax to Maxwell-Boltzmann distributions without Pauli blocking. To prevent this, all processes which lead to a change in a fermionic simulation particle's energy, such as scattering or acceleration by an electric field, must be subject to Pauli blocking. The blocking process must prevent electrons being scattering into an energy state E if that state is already occupied. The occupancy function, equation (4.3), is the measure of the proportion of states occupied at energy E. $f_o(E)$ takes values between 0 and 1 and, from the point of view of simulation, indicates whether a particular energy changing process should be blocked or not. The probability of accepting a change in electron energy to final energy E' should be $P = 1 - f_o(E')$ so that fully occupied states admit no more particles. This is consistent with the $(1 - f_0(E'))$ factor in the effective cross-section in equation (15) of Brysk's derivation of degenerate stopping and equilibration rates [76], and also in equation (7.1) of Brown and Singleton's Boltzmann collision operator with Fermi-Dirac statistics [69], which relaxes distributions to Fermi-Dirac distribution functions. The probability of accepting a new energy state is dependent on the degeneracy, so that the classical limit of $\eta \longrightarrow -\infty,\ f_o(E') \longrightarrow 0 \,\forall\, E'$ is reproduced. Fig. 4.1 shows a Fermi-Dirac distribution generated by the code at the start of a simulation, and its associated occupancy function.

To perform the Pauli blocking on changes in particle energy such that the final energy is E', the Monte Carlo simulation generates a random $U \sim \mathcal{U}(0, 1)$ and uses the following

procedure

$$\text{For } U \sim \mathcal{U}(0,1) \text{ and } E' \begin{cases} \text{block the change} & \text{if } U < f_o(E'); \\ \text{accept the change} & \text{if } U > f_o(E'). \end{cases} \tag{4.5}$$

For two-body processes, such as fermion-fermion scattering, this has a natural extension; with final energies E_1' and E_2', if,

$$U < f_o(E_1') + f_o(E_2') - f_o(E_1')f_o(E_2')$$

is true then the process is Pauli blocked. $f_o(E') = 0 \; \forall \; E'$ for non-degenerate particles. Fig. 4.2 shows that including the Pauli blocking algorithm maintains the Fermi-Dirac distribution function.

The average electron energy is recorded from the Monte Carlo simulation. However, diagnosing the electron temperature and degeneracy parameter from the average energy is non-trivial. The method employed is to is calculate the probability density function from simulation, $f_{\mathrm{MC}}(E_n)\mathrm{d}E$, in a number of bins. Then T_e, and therefore η by equation (4.2), can be varied until the root sum of square differences between the simulation distribution and the Fermi-Dirac distribution is minimised. The root sum of squares is

$$\sqrt{\sum_n \left(f_{\mathrm{MC}}(E_n)\mathrm{d}E - f(E_n, T_e, \eta)\mathrm{d}E\right)^2}$$

A golden section search [57] is used for the minimisation of the root sum square, and calculation of T_e. Initial guesses of $T^* \approx T_e$ and bounding values $T_{\max}$ and $T_{\min}$ are required for the golden section search, where $T_{\min} < T^* < T_{\max}$. As

$$\langle E \rangle = \frac{3\sqrt{\pi}}{8} \frac{T_e}{n_e} \frac{(2m_e T_e)^{3/2}}{\hbar^3 \pi^2} I_{3/2}(\eta) \tag{4.6}$$

where $\lim_{\eta \longrightarrow -\infty} \langle E \rangle = \frac{3}{2} T_e$, and $\lim_{\eta \longrightarrow \infty} \langle E \rangle = \frac{3}{5} E_F$,

$$T^* = \sqrt{\left(2\langle E \rangle / 3\right)^2 - \left(2E_F/5\right)^2}$$

is used as the initial guess, with $T_{\max}$ and $T_{\min}$ given, for example, by $T^* \pm 10\%$ respectively.

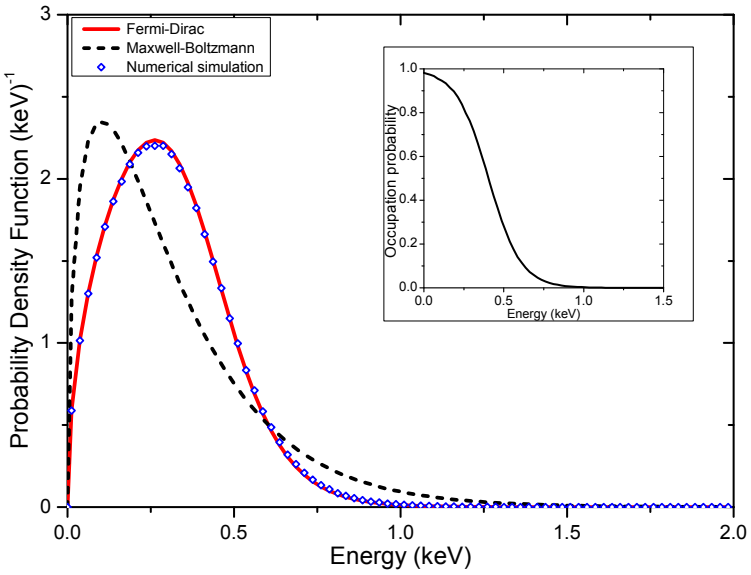

Figure 4.1: The degenerate Monte Carlo algorithm producing a 0D3V Fermi-Dirac distribution of electrons, for $T_e = 100$ eV, $n_e = 8 \times 10^{31}$ m^{-3} and $\eta = 4.2$. It is shown against Maxwell-Boltzmann and Fermi-Dirac distributions with the same parameters. There is good agreement between the analytic, and numerically generated, Fermi-Dirac distributions. INSET: The occupation function sampled from the simulation distribution function.

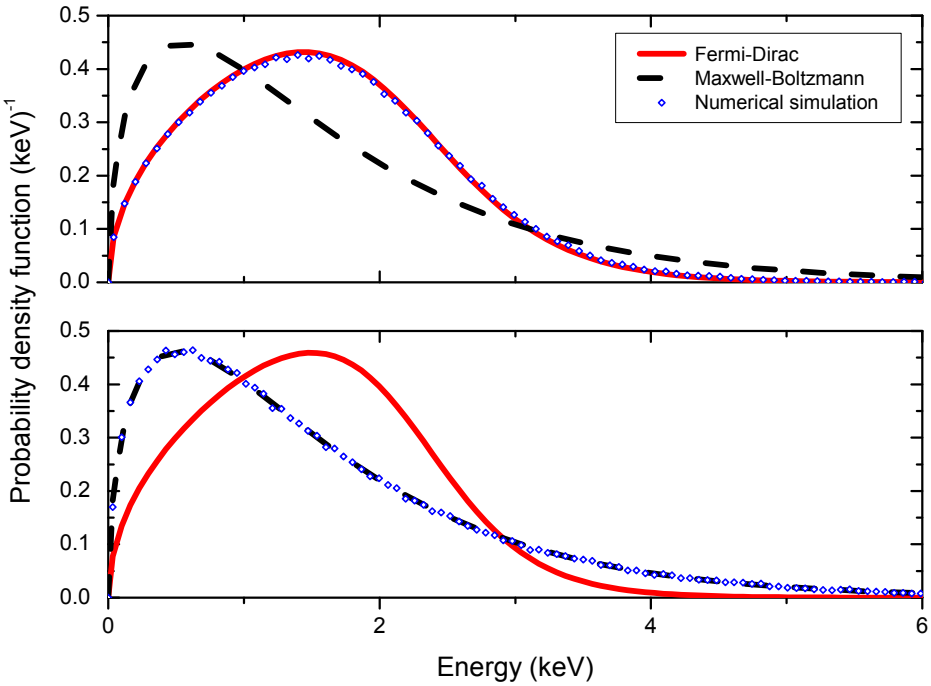

Figure 4.2: Simulations of initialised Fermi-Dirac distributions after a few timesteps both with (top) and without (bottom) Pauli blocking. The distribution with Pauli blocking matches the analytical Fermi-Dirac distribution with the same parameters, but the distribution with Pauli blocking disabled relaxes to a Maxwellian.

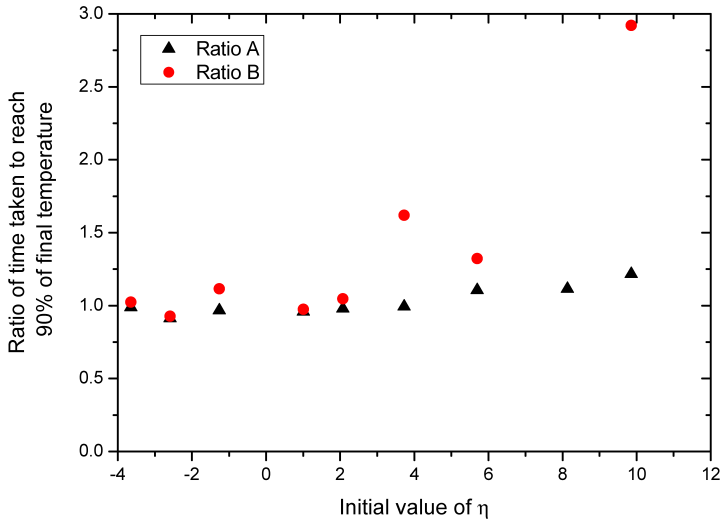

Figure 4.3: Equilibration with a range of starting electron and deuterium temperatures and densities, classified by initial electron degeneracy, η. The ratios shown are of the time taken to reach 90% of the final temperature as given by numerical simulation. Ratio A is of the degenerate Monte Carlo equilibration rate to the degenerate equilibration rate. Ratio B is of the degenerate numerical equilibration rate to the non-degenerate equilibration rate. The numerical equilibration rate to non-degenerate equilibration rate ratio for $\eta = 8.1$ is omitted as the non-degenerate electron temperature never reached 90% of the final temperature.

4.4 Tests

The rate of energy loss of an ion in a background of Fermi-Dirac electrons is given by Brysk [76] as

$$\frac{\mathrm{d}E_i}{\mathrm{d}t} = 4\left(\frac{q_i e}{4\pi\epsilon_0}\right)^2 \frac{(3T_e - 2E_i)\, m_e^2 \ln\Lambda_{ie}}{3\pi m_i \hbar^3 \left(1 + e^{-\eta}\right)} \tag{4.7}$$

for degenerate conditions in which $T_i/m_i \ll T_e/m_e$ with i representing ion species only. It is the degenerate analogue of the Landau-Spitzer energy loss equation in Appendix B. The Landau-Spitzer theory fails for weakly to strongly degenerate plasmas. Degenerate electron-ion temperature equilibration is given by

$$\frac{\mathrm{d}T_i}{\mathrm{d}t} = \sum_i \nu_{ie}(T_e - T_i) \tag{4.8}$$

with

$$\nu_{ie} = \frac{8}{3}\left(\frac{q_i e}{4\pi\epsilon_0}\right)^2 \frac{m_e^2 \ln\Lambda_{ie}}{\pi m_i \hbar^3 \left(1 + e^{-\eta}\right)} \tag{4.9}$$

from equation (4.7).

Fig. 4.3 compares the non-degenerate rate, the degenerate rate, and the degenerate Monte

Carlo algorithm for a range of degeneracies, with varying initial temperatures and densities. The numerical equilibration rate to non-degenerate equilibration rate ratio for $\eta = 8.1$ is omitted as the non-degenerate electron temperature never reaches 90% of the final temperature. This is because it is implicitly assumed that $T_e = \frac{2}{3}\langle E\rangle_e$ in the non-degenerate rate. The total energy in the degenerate case is higher though, as degenerate particles retain an energy even in the $T_e \longrightarrow 0$ limit. In scenarios where η drops over time, equation (4.6) forces T_e to rise for fixed $\langle E\rangle_e$. In a situation with $T_{i,0} > T_{e,0}$, this means that the classical $T_{e,f}$ may never reach the same, or a fraction of the same, value as in the degenerate case. An extreme case illustrates this more clearly; initial temperatures of two species, ions and electrons, with $T_{i,0} \gg T_{e,0}$ give a classical end temperature of $T_f = (T_{i,0} + T_{e,0})/2 \approx T_{i,0}/2$ for both electrons and ions. But if $T_{e,0} \ll T_F \ll T_{i,0}$ and the ions provide enough energy to force the electron distribution to become Maxwellian, the end temperature will be $T_f \approx (T_{i,0} + T_F)/2 > T_{i,0}/2$. The $\eta = 8.1$ data point has a lower $T_{i,0}/T_{e,0}$ ratio than that at the highest η plotted, but $T_F/T_{i,0}$ is higher so the disparity in final temperatures between the classical and degenerate cases is expected.

The agreement between the degenerate equilibration rate and the degenerate Monte Carlo equilibration rate is good for a range of initial values of the degeneracy, but does show variation. The origin of this variability is the inherent noisiness of Monte Carlo simulations, but in general the models agree to within 3% of the theoretical value averaged across all equilibration tests. There is a slight upward trend in Ratio A, that is the ratio of the time taken to reach 90% of the final temperature of the Monte Carlo algorithm relative to theory as governed by equation (4.8). This slight trend is probably partly due to small errors in diagnosing T_e from the Monte Carlo simulation, and partly due to evaluation of (4.8). In the degenerate theory, computation of new values of T_e and η using $\frac{d\langle E\rangle_e}{dt}$ from (4.8) self-consistently is non-trivial, and there are leading order corrections to (4.9) which are of relative size $\sim T_i m_e/T_e m_i$. All of these are sources of error which are worse at high degeneracy, but which affect the time taken to reach equilibration only slightly for regimes of physical interest.

To further verify the algorithm, it is applied to a problem with a known theoretical result; the resistivity of a degenerate plasma. The problem is restricted in the same way as described in §3.3.1; it is first order, unmagnetised transport theory with isotropic temperature and pressure conditions in which resistivity is simply given by $\rho = E_x/J_x$ for a current density in the x direction. The relevant integral is given by equation (3.6) but with the Fermi-Dirac distribution function so that $f(v) = f(E)\mathrm{d}E/4\pi\mathrm{d}^3v$, and $f(E)$ is taken from equation (4.1). Unlike the Maxwell-Boltzmann resistivity for this scenario, there is no analytical form of ρ_{FD} so it is calculated by numerical integration for comparison against simulation in Fig. 4.4. In keeping with other literature and Fig. 3.10, the

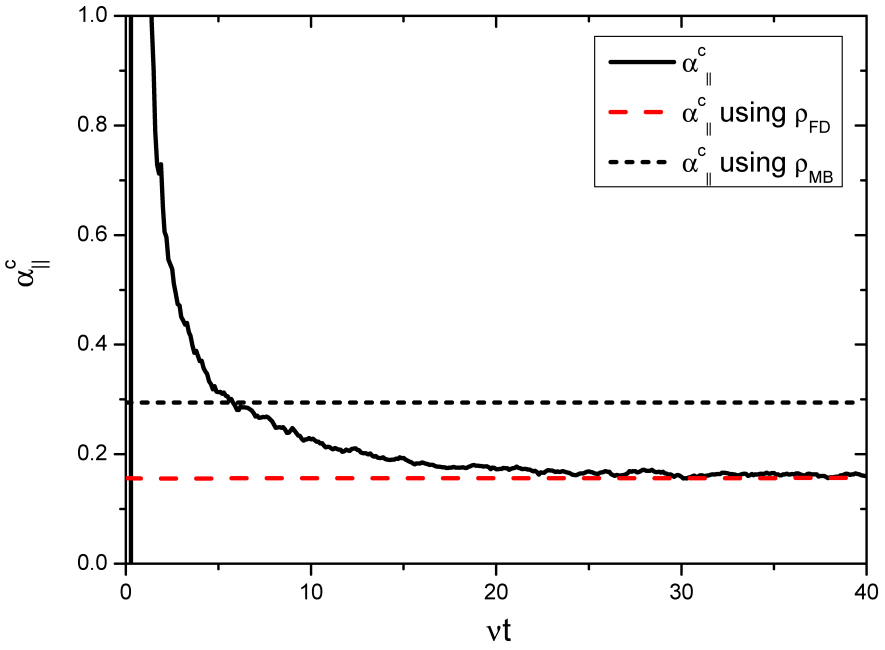

Figure 4.4: $\alpha^c_{\|}$ given by the Monte Carlo algorithm against $\alpha^c_{\|}$ for Maxwell-Boltzmann and Fermi-Dirac distributions according to equation (3.6), with the same T_e. Electron-electron collisions are omitted and there is no blocking of the acceleration by the applied electric field. The initial degeneracy is $\eta = 2.5$.

dimensionless transport coefficient for resistivity, $\alpha^c_{\|}$, is plotted in Fig. 4.4. For reference, the equivalent $\alpha^c_{\|}$ for a Maxwellian is also shown. All three approaches are in the Lorentz limit, and have no Pauli blocking of the acceleration by the electric field.

4.5 Results

A use of the code in a regime in which the theoretical rates presented are not applicable is explored. There are situations in ICF in which the validity condition of equations (4.7) and (4.9) are violated, for instance in the interaction between a population of fusion produced alpha particles and a background of cold, dense electrons. The algorithm as described is capable of modelling both of these features. Fig. 4.5 shows a situation with parameters approximately similar to inertial confinement fusion; an isotropic distribution of monoenergetic fusion produced alpha particles interacting with a cold fuel shell of deuterium, tritium and electrons. In both simulation and theory, the α particles start as a delta function with (4.7) being the appropriate theoretical comparison and $\langle E_\alpha \rangle = 3.54$ MeV. Equation (4.9) produces the same result as (4.7) even as the distribution function relaxes if the $\ln \Lambda$ dependence on E_i is ignored, as is common practice. This is because the single occurrence of E_i on the right hand side of equation (4.7) always yields $\langle E \rangle_i =$

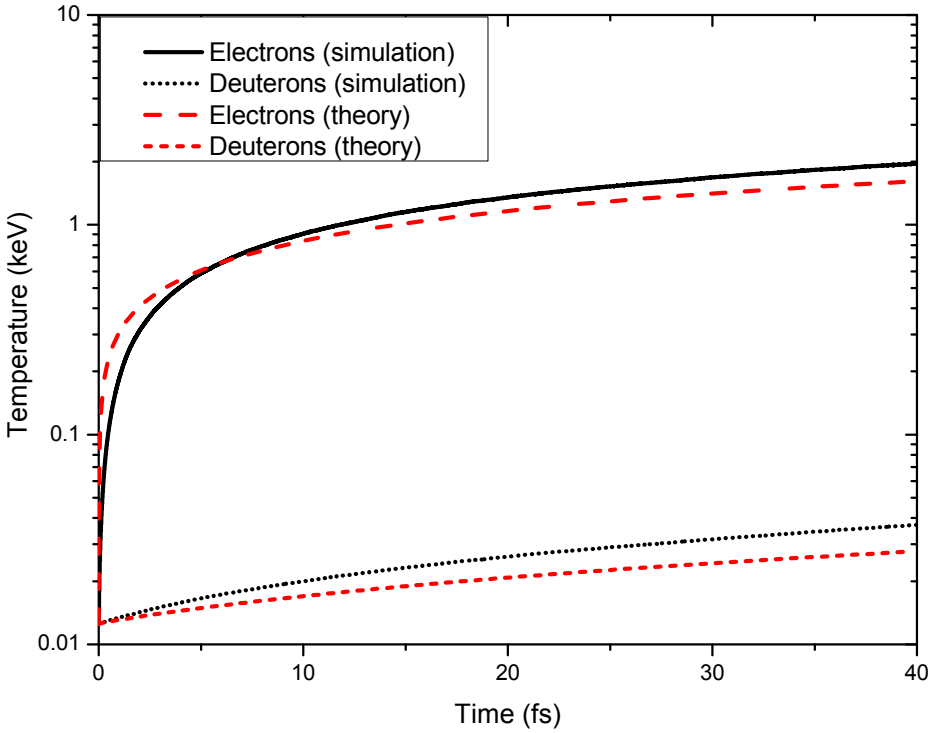

Figure 4.5: An equilibration scenario with parameters approximately similar to inertial confinement fusion. Only electrons and deuterons are shown. The analytical model is that of the degenerate rate given by equation (4.7). The evolution of the simulation η over time is shown in Fig. 4.6.

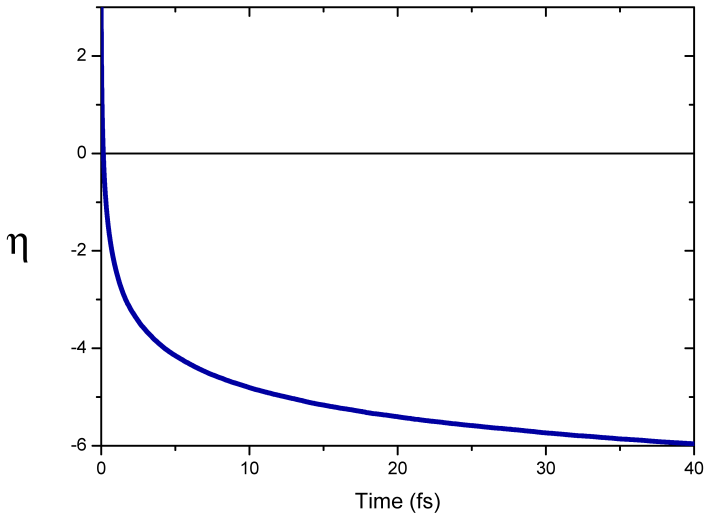

Figure 4.6: The degeneracy parameter of the numerical simulation in Fig. 4.5 over time from an initial value of $\eta = 3.2$.

$\int f_i(E)E\mathrm{d}E$ when integrated over the ion distribution function. The energy spread of α particles is less than 2% by 40 fs into the simulation. At the start of the simulation, $T_\alpha/m_\alpha > T_e/m_e$, and $\eta = 3.2$. The evolution of η is shown in Fig. 4.6. The main result of the simulation is that more energy is deposited into ions, and less energy into electrons at early times. At later times, the electrons become hotter than equation (4.7) predicts. The electrons do not remain degenerate for very long, having $\eta < -4$ after just 10 fs, but the initial difference means that the overall evolution is different, even when the electron temperature is reaching keV from an initial background temperature of just $T = 12.5$ eV. The deuterium is 33% hotter according to simulation, though the absolute difference is small. More importantly, as electrons and ions will subsequently equilibrate, the electrons are 21% hotter according to simulation and the absolute temperature difference of 0.34 keV is larger. Densities are $n_d = n_t = 1.2 \times 10^{30}$ m^{-3} and $n_\alpha = n_d/10$.

This degenerate modification to a Monte Carlo code successfully reproduces theoretical results for degenerate plasmas and can be used to study the microphysics of degenerate plasmas in ICF.

Chapter 5

Ion-ion inverse bremsstrahlung

5.1 Introduction

Bremsstrahlung, or 'braking radiation', of electrons is the process whereby an electron emits energy in the form of radiation when being accelerated. In plasmas, this often occurs in the field of the nucleus of an ion [27]. The reverse process, inverse bremsstrahlung (IB) [77], also happens; an electron under the influence of an external electric field collides with the nucleus of an ion, and its trajectory and momentum are changed. The electron is undergoing diffusion in velocity space, and field energy is converted into electron thermal energy. It is just one of many absorption mechanisms in the interaction of short pulse lasers with dense matter, which in general depend upon many factors such as laser intensity, electron density gradient, pulse shape, pulse polarisation, pulse incidence, electron mean free path, and so on [78]. Electron-ion inverse bremsstrahlung (IB) is a common, and often dominant, absorption mechanism in laser-plasma interactions with $n_e \approx n_c$ and 10^{12} W cm^{-2} μm^2 $< I\lambda_\mu^2 < 10^{17}$ W cm^{-2} μm^2, with λ_μ the laser wavelength measured in microns. This Chapter examines whether inverse bremsstrahlung could allow ion species with different charge-to-mass ratios to absorb energy directly from radiation.

The radiation considered is a linearly polarised electromagnetic (EM) wave. For a laser pulse, the electric field has the form

$$\mathbf{E}(\mathbf{x}, t) = \mathbf{E}_0(\mathbf{x}) \sin(\omega t + \phi)$$

where

$$E_0^2 = \frac{2I}{c\epsilon_0}$$

is the square of the amplitude of the electric field, I is the intensity of the laser pulse and ϕ is the initial phase. In the non-relativistic case, particles i in a linearly polarised laser

field have the equation of motion

$$m_i \frac{\mathrm{d}\mathbf{v}_i}{\mathrm{d}t} = q_i e \mathbf{E}_0 \sin(\omega t + \phi)$$

Taking $\mathbf{E}_0$ to be uniform in space, charged particles oscillate with

$$v_i(t) = -\frac{q_i e E_0}{m_i \omega} \cos(\omega t + \phi) + C \equiv v_{\mathrm{osc}} \cos(\omega t + \phi) + C \tag{5.1}$$

where C is an integration constant. So

$$v_{\mathrm{osc}} = -\frac{q_i e E_0}{m_i \omega}$$

As plasmas are opaque to electromagnetic waves with frequencies $\omega < \omega_{pe}$, and ω_{pe} is dependent on electron density, there is a critical density n_c' above which material mostly reflects incoming radiation. From the definitions, the critical density is

$$n_c' = \frac{\omega^2 \epsilon_0 m_e}{e^2}$$

Relativistic mass increase of electrons occurs with high intensity lasers so that $m_e \longrightarrow \langle\gamma\rangle m_e$, where the Lorentz factor $\gamma = \left(1 - \frac{v_e}{c}\right)^{-1/2}$ is averaged over all electron velocities. A useful definition is that of the dimensionless electric wave strength parameter

$$a_0 = \frac{e E_0}{m_e \omega c}$$

with m_e the electron rest mass [79]. It measures the transverse momentum imparted by an oscillating laser field upon an electron in units of $m_e c$, and $a_0 \geq 1$ corresponds to the relativistic regime. For linearly polarised laser beams $\langle\gamma\rangle = \sqrt{1 + a_0^2/2}$ and the relativistically corrected critical density is

$$n_c = n_c' \langle\gamma\rangle = n_c' \sqrt{1 + a_0^2/2} \tag{5.2}$$

This increases the effective critical density if $a_0 > 0$, and subsequent references to critical density are synonymous with the relativistically corrected version.

Isotropic distributions of electrons in a plasma as a function of speed, v, satisfy

$$\int_0^\infty 4\pi v^2 f(v) dv = n_e$$

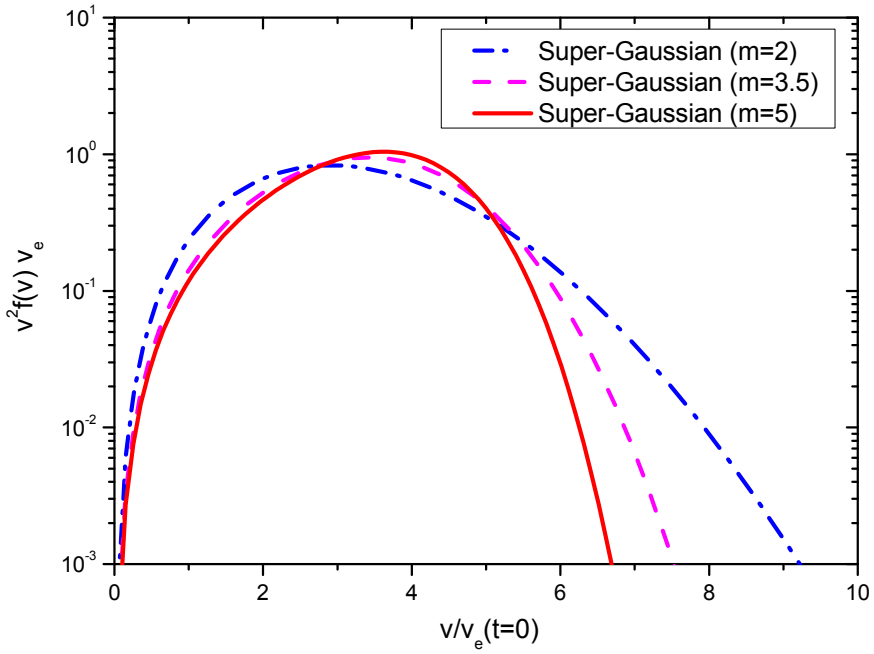

Figure 5.1: Three theoretical super-Gaussians with different values of m; $m = 2$ is a Maxwellian while $m = 5$ is the Langdon distribution.

The equilibrium distribution is given by the Maxwellian,

$$f_{\mathrm{MB}}(v) = n_e \left(\frac{m_e}{2\pi T_e}\right)^{3/2} \exp\left[-\frac{m_e v^2}{2T_e}\right]$$

Langdon first explored the eponymous non-Maxwellian distributions driven by electron-ion inverse bremsstrahlung (IB) heating [53] in the absence of electron-electron collisions. Subsequent work on IB [54, 80, 81, 82] showed that both laser absorption and thermal conductivity [83] are reduced by Langdon distributions. The advanced treatments also find that the inclusion of more physics in the kinetic equations, such as electron-electron collisions, leads to a more general class of driven distributions which are self-similar. Following Matte *et al.* [82], the isotropic distributions being driven by electron-ion IB take the form

$$f_m(v) = C_m \exp\left\{-\left(v/v_m\right)^m\right\}$$

where

$$v_m^2 = \frac{3T_e}{m_e}\frac{\Gamma(3/m)}{\Gamma(5/m)} \quad \text{and;} \quad C_m = \frac{n_e}{4\pi}\frac{m}{\Gamma(3/m)v_m^3}$$

$\Gamma(z)$ is the gamma function defined in Appendix A and $m \in [2, 5]$. $m = 2$ gives the Maxwell-Boltzmann distribution, $m = 5$ gives the Langdon distribution and any distribution with $m > 2$ is known as a super-Gaussian, some examples of which are shown in

Fig. 5.1. For electron-ion IB,

$$\alpha = Z_i \frac{v_{\rm osc}^2}{v_e^2} \quad \text{and;} \quad m(\alpha) = 2 + 3/\left(1 + 1.66/\alpha^{0.724}\right)$$

with $v_e^2 = T_e/m_e$. Other authors modified Langdon's absorption rates for higher intensity regimes [84, 85]. The persistence of super-Gaussians in laser heated systems has prompted much work on super-Gaussian transport theory, particularly in relation to ICF [86, 87].

5.2 Ion-ion inverse bremsstrahlung (IIB)

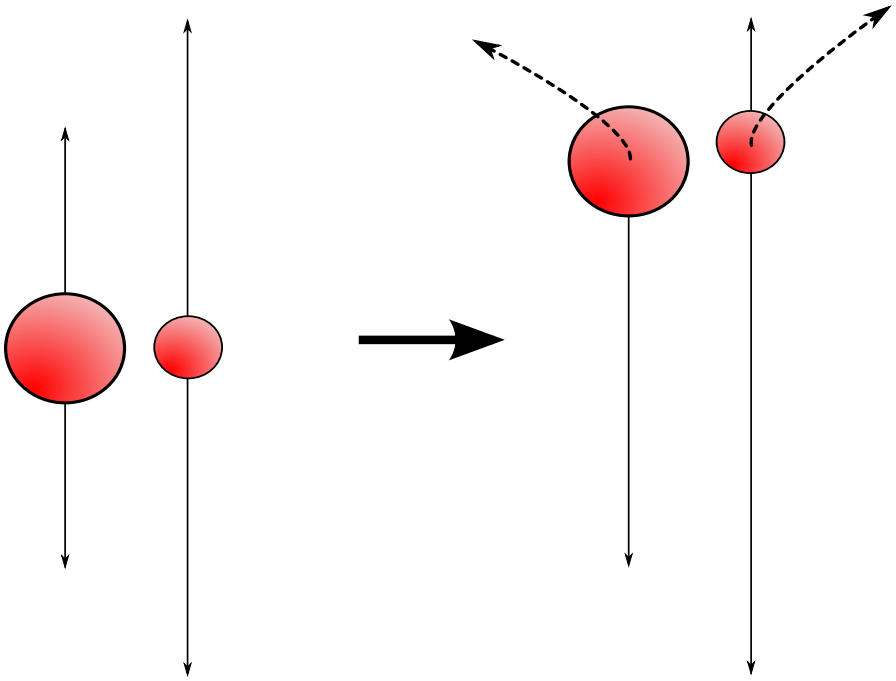

Figure 5.2: Schematic diagram of ion-ion inverse bremsstrahlung in the zero average momentum frame. Two ion species (spheres) undergo an oscillation in velocity space (solid lines) due to an applied field, followed by a collision in which they acquire a component of velocity transverse to the original direction of the field (dashed lines). Charge-to-mass ratios are inverse to the size of particle shown.

The difference in charge-to-mass ratios between species is key to the effect of IB absorption of laser radiation; it would hardly occur at all in a fully kinetic plasma consisting of particles of identical charge-to-mass ratio in a perfectly spatially uniform but time varying laser pulse. The absorption is not completely zero, for instance, with electrons, the non-vanishing time derivative of the electron-electron quadrupole moment and relativistic electron mass increase are sources of (inverse) bremsstrahlung, but these effects

are second-order [88, 89]. That the difference in charge-to-mass ratio gives rise to the largest contribution to electron-ion IB implies the effect could also happen with ions of different charge-to-mass ratios.

This process, ion-ion inverse bremsstrahlung (IIIB) absorption, is analogous to electron-ion IB. Fig. 5.2 is a schematic of the process for a linearly polarised laser field in the frame of zero average momentum (the zero momentum frame, or ZMF), showing that ions individually gain extra kinetic energy from their collisions during oscillation by the field. IIIB was first recognised by Mjolsness and Ruppel (M&R) [90] under the guise of driven collisional ion heating; the term IIIB is adopted in this work. Many of the tools developed to study electron-ion IB are based on $m_e/m_i \ll 1$, with ion masses taken to be infinite in some treatments. These approaches will not be useful for IIIB, and a full kinetic treatment of all ion species is required. The smaller differences in charge-to-mass ratios between ion species, relative to electrons and ions, mean that much higher intensities are likely to be needed if significant heating due to IIIB absorption is to occur. IIIB begins to happen with $I \sim 10^{19} - 10^{23}$ W cm^{-2} for which intensities electrons are very much in the relativistic, and possibly in the QED, regime.

The huge advances in high power lasers have opened up this regime of high intensity laser-plasma physics. Phenomena such as relativistic transparency, ion acceleration to ∼MeV energies [91, 92, 93], and enhanced absorption of laser energy [94], have been observed. Focused intensities of up to 10^{22} W cm^{-2} have been demonstrated [95], and the next generation of lasers will increase this by an order of magnitude [39]. Electron-positron pair-production, either by counter-propagating laser beams [96, 97, 98], or by striking an overdense solid [99], are expected to occur with focused intensities of 10^{23} W cm^{-2} and above, bringing laser-plasma interactions into a regime in which quantum electrodynamics (QED) theory must be included, and $a_0 > 100$. Access to this high-intensity regime is only currently available with short pulse lasers having durations of femtoseconds or picoseconds. Pulse shape becomes an important consideration for such short timescales, and the physics of the interaction becomes very complex.

IIIB is different to many of the other processes considered in this regime as it deposits energy *directly* into ion species; most absorption mechanisms primarily heat or accelerate electrons with ions subsequently gaining energy via either space-charge fields or by electron-ion equilibration. Anything which changes ion energies, or distribution functions, could have an effect on processes associated with laser-plasmas including fusion (particularly in direct-drive ICF [100] and beam fusion [101]), transport theory, and applications which require very monoenergetic ion sources e.g. hadron therapy [102].

M&R consider two ion species in a spatially uniform, time varying but unenveloped (no overall temporal shape) linearly polarised laser pulse. Electron motion and equilibration

are ignored and the distribution function of the ion species is assumed to satisfy

$$f_i(\mathbf{v}) = \left(\frac{m_i}{2\pi T_i}\right)^{3/2} \exp\left\{ -\frac{m_i}{2T_i}\left[\mathbf{v} - \mathbf{v}_{\rm osc}\cos(\omega t + \phi)\right]^2 \right\} \tag{5.3}$$

with T_i the temperature in the ZMF. Unless otherwise stated, temperatures are always given in the ZMF. A VFP equation is solved for the evolution of the two ion temperatures as a function of time and laser intensity and approximate equations for the time taken to heat ion species to a particular temperature given. The initiation of thermonuclear fusion is considered: a CO_2 laser with $I = 4\times10^{19}$ W cm^{-2} delivering 50 kJ in $\sim10^{-11}$ s is predicted to heat deuterium and tritium ions to $T \geq 4$ keV. There are currently no laser systems which could satisfy these conditions. IIIB is worth revisiting with knowledge of modern laser systems which can typically deliver higher intensities over shorter times than M&R foresaw.

The exploration of IIIB extends the work of M&R in several ways: there is no constraint on the distribution function of the ions, temporally non-uniform pulse shapes are used, and the effects of using more than two ion species are numerically simulated. M&R do suggest that mixing of three ion species could lower the constraints on laser power, but the VFP model they use does not allow quantitative evaluation of the effect.

As the interactions and absorption mechanisms of this regime of plasmas are so complex in the high intensity regime, the effect of IIIB is studied in isolation from other processes and ignoring depletion of the energy in the field, though physical situations where IIIB might occur are briefly discussed in §5.3.

5.3 Occurrence of IIIB

There are several situations where IIIB might occur, essentially they rely on space-charge fields due to electrons being absent for long enough for IIIB heating to take place. Magnetic fields are not considered for ions as $\mathbf{v}_i \times \mathbf{B} < \mathbf{E}$.

One obvious way to remove the complexity of electrons is to remove the electrons themselves, as with a laser pulse striking a non-neutral plasma comprised entirely of ions. The collisionless skin depth is larger due to the absence of electrons, becoming $\lambda_{\rm sk} = \frac{c}{\omega_{pi}}$ and $\omega_{pi} \sim \omega_{pe}\sqrt{Z_i m_e/m_i}$ with $n_i Z_i \approx n_e$. However the densities of such plasmas are extremely limited [103], being of the order of 10^{13} ions per cubic metre. The cylindrical volume heated is restricted in radius by the beam waist and in length by either the Rayleigh range, z_R, or the ion collisionless skin depth, depending on the ion density.

Assuming $\lambda = 1\mu$m, $z_R < \lambda_{\rm sk}$ for realistically achievable densities. Non-neutral plasmas have very long confinement times, and there are few loss mechanisms at work in a pure ion plasma, the most obvious being ion-ion bremsstrahlung emission. The ion temperature could be diagnosed from this emission, or by using a long-pulse probe beam.

Laser pulses propagating into dense gas jets could provide a scenario where IIIB occurs, but this is not considered.

A third scenario is a linearly polarised electromagnetic (EM) wave orthogonally incident on a foil assumed to be ionised (even for high Z ions). There are several recognised mechanisms for ion acceleration in such a scenario; target normal sheath acceleration [104], radiation pressure acceleration [93], 'breakout afterburner' [105], and Coulomb explosion [106]. The range of intensities specified covers all of these acceleration mechanisms but the predominant interest is in $I > 10^{21}$ W cm^{-2}.

For a foil with thickness l on the order of the collisionless skin depth $\lambda_{\rm sk} = c/\omega_{pe}$ and density n_c, the dominant regime is then Coulomb explosion, or directed Coulomb explosion [107] in which some 'light-sail' radiation pressure acceleration occurs [92]. A laser incident on a thin foil evacuates electrons from the focal spot via the $e\mathbf{v}_e \times \mathbf{B}$ force, leaving ions behind and setting up a charge-separation field parallel to the direction of laser propagation of $E_{||} = en_e l/(2\epsilon_0)$. Ions are subsequently accelerated by this field and gain an energy of the order of the Coulomb energy [108], $E_i \approx m_e c^2 a_0^2$. This acceleration takes time, during which the EM field of the laser is still interacting with the ions, and the ions mostly obtain directed, rather than thermal, energy as they are accelerated in the direction of the charge-separation field.

For thin foils with $l \approx \lambda_{\rm sk}$ it can be assumed that the field is constant over a cylinder which is as long as the foil itself, and which has a radius of approximately a few λ. Heating by IIIB absorption would have to act before the Coulomb explosion of the ions causes them to be ejected from the focal spot of the laser, and before the ion density drops significantly below its initial value of $n_i(t = 0)$. This assumes a high-contrast laser pulse. It is important to know just how long the ions remain before being ejected from the focal spot. Fourkal *et al.* [106] note that the acceleration time for protons is relatively long, $t \sim 100/\omega_{pe}$, and they develop a model for both the position and density of ions over time. Even for $I \sim 10^{24}$ W cm^{-2} at the relativistic critical density, $1/\omega_{pe}$ is roughly 60 fs. An ion density drop by an order of magnitude would change the interaction significantly; Fourkal's expression implies that this does not happen for a 30 fs pulse on a thin foil until the pulse is finished. Bulanov *et al.* [102] estimate that $1/\omega_{pi}$ is the explosion time, which means protons explode by time $\sqrt{\frac{m_p}{m_e}}/\omega_{pe}$. The times are more restrictive for high Z. Taking these limitations into consideration, the analysis of IIIB for a laser

striking a thin foil should be restricted to pulse lengths of 30 fs or below, ensuring the interaction between ions and the EM wave is still taking place at a density sufficiently close to $n_i(t=0)$, and that the electric field transverse to the beam motion is dominated by the laser field, $\mathbf{E}$, rather than the space-charge field $\mathbf{E}_{\rm sc}$. The space-charge field and acceleration are not prohibitive to the heating mechanism as long as $\mathbf{E}\cdot\mathbf{E}_{\rm sc}\approx 0$ and the bulk velocity gained by the ions is predominantly longitudinal. Ions must not be ejected from the focal spot by the laser oscillations: the field parallel displacement is given by

$$x_{\parallel}=\frac{eE_0Z_i}{\omega^2 m_i}=7.45\times10^{-20}\lambda_\mu^2\frac{Z_i}{A_i}\sqrt{\left(I\ /\ \mathrm{W\ cm^{-2}}\right)}\ \mathrm{m}$$

where any thermal velocity is ignored and A_i is the mass number of ion i. For deuterium with $I=10^{23}$ W cm^{-2} and $\lambda=1\mu$m this is 12nm, much less than the focal spot size which is on the order of λ. For such high intensities, any fusion produced α particles emitted anti-parallel to the field would be temporarily trapped. Transport effects, such as hotter ions losing energy to neighbouring, colder plasma regions are ignored in this simple model of a transiently non-neutral ion plasma. It is possible that two counter-propagating beams incident on a thin foil such that the $e\mathbf{v}_e\times\mathbf{B}$ force is eliminated could also give enough time for IIIB to occur. In practice, beams are not perfectly spatially uniform and typically have a Gaussian spatial profile across the focal spot. This creates a gradient in the electric field, i.e. $\mathbf{E}=\mathbf{E}(\mathbf{x})$. The ponderomotive force,

$$F_\nu=\frac{-e^2}{4m_e\omega^2}\nabla_\nu E^\alpha E_\alpha$$

then forces electrons down the field density gradient and out of the focal spot [109]. This sets up a transverse space-charge field $\mathbf{E}_{\rm sc}$, but some laser cycles could pass before $\mathbf{E}_{\rm sc}>\mathbf{E}$. A specially designed spatial profile of the beams could limit the escape of electrons from the focal spot, and the creation of $\mathbf{E}_{\rm sc}$. For instance, a profile with two equally sized peaks either side of a region of lower intensity would stop particles escaping from the centre of the heating region.

The calculations performed in §5.4 and §5.5 nominally have the thin foil scenario in mind but it is not clear based on this analysis that any significant heating could occur before the Coulomb explosion takes place. However, any volume with the ion density and spatially uniform, time varying fields described would produce the same heating, so the exact description of a suitable laser-target configuration is left to future work and the rate of heating is presented in abstraction from any specific configuration.

5.4 Modelling of IIIB

In the ZMF, the oscillation by the field causes the ions to have a velocity given by equation (5.1) which is transverse to the direction of beam propagation. Two ion species, i and j, gain a time-dependent relative velocity induced in the direction of the field of

$$v_{ij}(t) = \frac{eE_0}{\omega}\cos(\omega t + \phi)\left(\frac{Z_i}{m_i} - \frac{Z_j}{m_j}\right)$$

It is assumed that ions undergoing this motion interact with other ions via small-angle collisions, and this drives the heating.

There is evidence that the assumption of small-angle collisions breaks down for electron-ion IB absorption in a strong laser field [110, 111] due to either Coulomb focusing, also known as the parachute effect, or quasi-capture. Both effects rely on the electron oscillation amplitude being smaller than the average distance between ions. In Coulomb focusing, electrons are launched into the ion potential parallel to the oscillating field, while in quasi-capture electrons are launched orthogonally. The origin of the large-angle collisions, and associated increase in absorption, is the combination of oscillatory motion and mutual attraction between electron and ion causing electrons to become temporarily captured by one ion, repeatedly colliding until a large-angle collision imparts sufficient momentum for the electron to escape. The effect is stronger in the $v_{ei} \gg v_{\mathrm{th},ei}$ limit, where

$$v_{\mathrm{th},ei}^2 = 2\left(\frac{T_e}{m_e} + \frac{T_i}{m_i}\right)$$

Due to the mutual repulsion between ions, it seems unlikely that this complicated behaviour exists for IIIB absorption and the regime of interest for IIIB is $v_{ij} \approx v_{\mathrm{th},ij}$.

Jones *et al.* [112] give a dynamical friction heating rate, into which the expression for the time-dependent relative velocity can be inserted to give a rate for the change in temperature due to IIIB

$$\left(\frac{\mathrm{d}T_{ij}}{\mathrm{d}t}\right)_{\mathrm{IIIB}} = \left(\frac{Z_i Z_j e^2}{4\pi\epsilon_0}\right)^2 \frac{16\sqrt{\pi} n_j \ln\Lambda_{ij}}{3 m_i v_{ij}} \xi\left(\frac{v_{ij}}{v_{\mathrm{th}}}\right) \tag{5.4}$$

where

$$\xi(x) = \frac{\sqrt{\pi}}{2}\mathrm{erf}\,(x) - x\exp\left(-x^2\right) \tag{5.5}$$

and is shown in Fig. 5.3. $\mathrm{erf}\,(x)$ is the error function, and is defined in Appendix A. Note that the equation for the rate of change of temperature is similar, but slightly simpler,

than the expression given by M&R. The total energy absorbed is $\dot{W} = \dot{W}_i + \dot{W}_j$ where

$$\dot{W}_i = \frac{3}{2} n_i \left(\frac{\mathrm{d}T_{ij}}{\mathrm{d}t} \right)_{\mathrm{IIIB}} \tag{5.6}$$

Electron motion and collisions are ignored as the primary interest is in IIIB, and because the timescales considered are typically much shorter than electron-ion equilibration times. Taking i and j to be arbitrary ion species, and e to represent electrons, the ratio of IIIB absorption, (5.4), to electron-ion equilibration between e and i assuming $v_{ij} \approx v_{\mathrm{th},ij}$ is

$$\frac{(\mathrm{d}T_{ij}/\mathrm{d}t)_{\mathrm{IIIB}}}{(\mathrm{d}T_{ie}/\mathrm{d}t)_{\mathrm{Equil.}}} \approx Z_j^2 \frac{m_e}{v_{\mathrm{th},ij}} \frac{\ln \Lambda_{ij}}{\ln \Lambda_{ie}} \frac{n_j}{n_e} \left(\frac{T_i}{m_i} + \frac{T_e}{m_e} \right)^{3/2} (T_e - T_i)^{-1}$$

The equilibration time is given in Appendix B. Taking $\ln \Lambda_{ij} \sim \ln \Lambda_{ie}$ and $v_e^2 = T_e/m_e \gg T_i/m_i$,

$$\frac{(\mathrm{d}T_{ij}/\mathrm{d}t)_{\mathrm{IIIB}}}{(\mathrm{d}T_{ie}/\mathrm{d}t)_{\mathrm{Equil.}}} \approx Z_j^2 \frac{n_j}{n_e} \frac{v_e}{v_{\mathrm{th},ij}}$$

which is satisfied for sufficiently high ion density and hot electrons. This ignores the relativistic mass increase of the electrons, which can be significant, but is unimportant for the coupling if $v_{\mathrm{th},ij} \ll c$.

It is also interesting to note that IIIB always dominates ion-ion equilibration;

$$\frac{(\mathrm{d}T_{ij}/\mathrm{d}t)_{\mathrm{IIIB}}}{(\mathrm{d}T_{ij}/\mathrm{d}t)_{\mathrm{Equil.}}} \approx \frac{v_{\mathrm{th},ij}^2}{5} \left(\frac{T_j}{m_j} - \frac{T_i}{m_j} \right)^{-1}$$

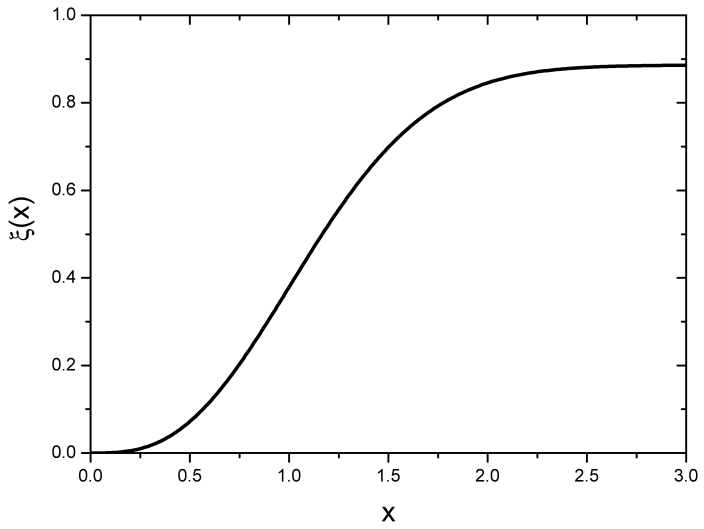

Figure 5.3: $\xi(x)$, equation (5.5).

using that, for $x = v_{\mathrm{th},ij}/v_{ij}$, $\overline{\xi(x)/x} \sim 0.2$ assuming $v_{ij} \approx v_{\mathrm{th},ij}$. Both of these relations require $v_{ij}(t) \neq 0$, so are only true during the pulse. Ion-ion equilibration is automatically included in numerical simulations.

An adaptation to the Monte Carlo code of Chapter 3 introduces the effects of a laser pulse into simulations. An acceleration of

$$\mathbf{a} = \frac{\mathbf{E}_0 e Z_i}{m_i} \sin(\omega t + \phi)$$

is applied to each ion, resulting in a change in velocity of $\mathbf{v}' = \mathbf{v} + \mathbf{a}\Delta t$ for each timestep Δt. The timestep must be set to some fraction of the shortest timescale of interest in the simulation; normally this would be the equilibration time. The motion through velocity space caused by the laser must also be fully resolved with $\mathbf{a}\Delta t \ll \mathbf{v}$. Successive oscillations of the laser pulse introduce numerical heating via the uncertainty in momentum. Simulations begin with $\langle m\mathbf{v}\rangle^2 \approx 0$ for each species (i.e. no net momentum within statistical limitations). At the end of each simulation it is checked that $(\langle m\mathbf{v}\rangle)^2 \ll \langle (m\mathbf{v})^2 \rangle$ which implies a good level of momentum conservation. Output temperatures are in the ZMF and are calculated from $T = 2\langle E\rangle/3$ where $\langle E\rangle$ is obtained from equation (5.3). This means that any systematic inaccuracies due to residual momentum should be eliminated. The average $\ln\Lambda$ is used.

High intensity lasers typically have short pulse lengths so that the pulse shape becomes a parameter. Uniform pulse shapes may be used but the default is a Gaussian shaped pulse, with

$$E(t) = E_0 \sin(\omega t + \phi) \cos^2[\omega_d (t - t_h)]$$

t_h is the time halfway through the pulse, $\omega_d = \pi/t_p$ is the decay period of the pulse, and t_p is the pulse duration.

The code is tested against electron-ion IB and compared to both a Maxwellian ($m = 2$) and a Langdon ($m = 5$) distribution in Figs. 5.4 and 5.5. $\alpha = 2$, electron-electron collisions are disabled and $Z = 1$ with just one ion species. The pulse is spatially and temporally uniform. Fig. 5.4 shows the distribution at the start of the simulation, and Fig. 5.5 at $\frac{t}{\tau_{ie}} = 8$ where τ_{ie} is the $t = 0$ value. The agreement with the $m = 5$ super-Gaussian is not exact, but this is expected as α changes over time. The results are in excellent agreement with those performed by Jones and Lee [54] (see their Fig. 5).

This test confirms that the additions to the code of Chapter 3 are appropriate for studying IIIB in isolation from other processes.

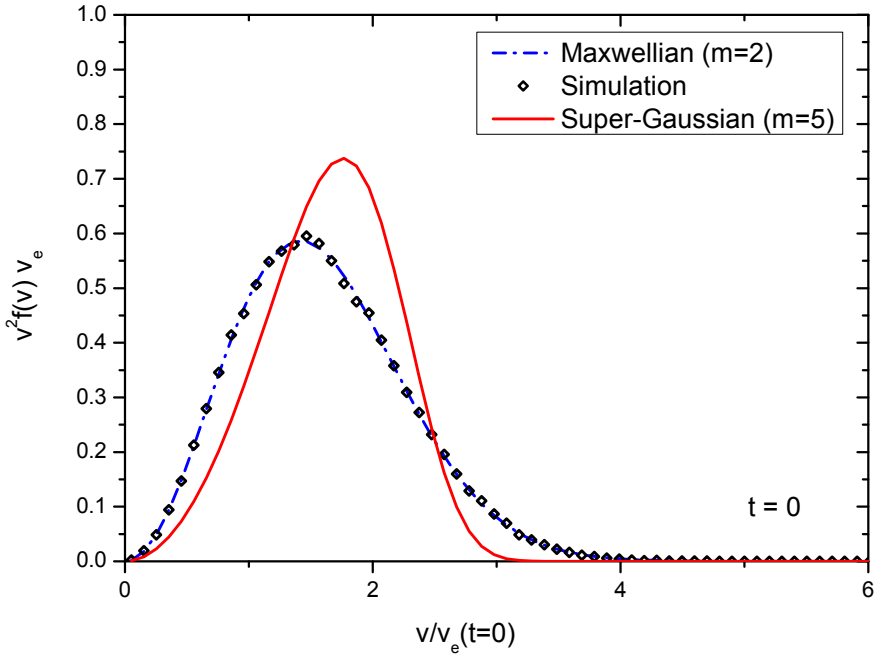

Figure 5.4: A simulation of electron-ion IB against the Maxwellian and Langdon distributions; all distributions are in the ZMF. $\alpha = 2$.

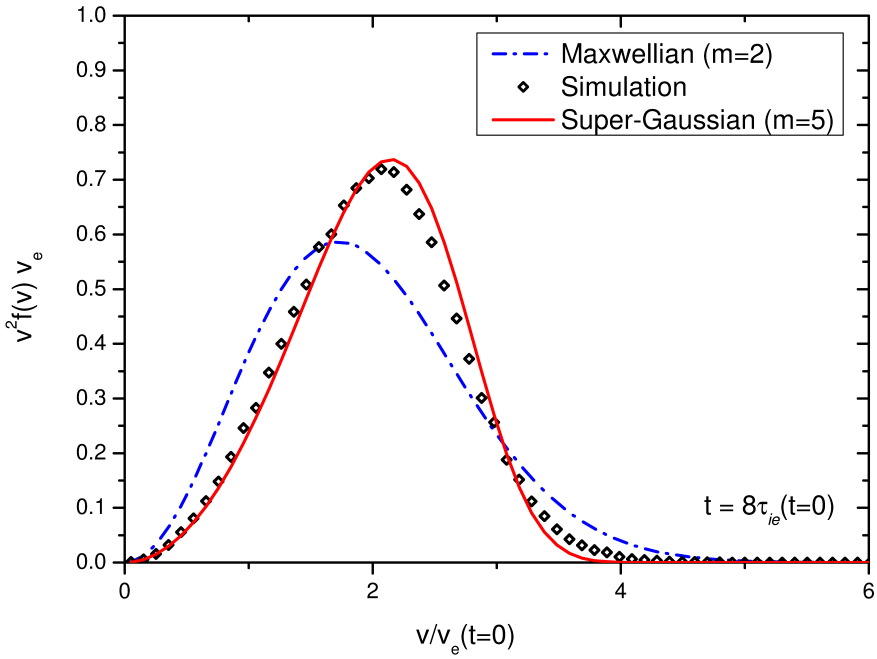

Figure 5.5: Fig. 5.4 at $t = 8\tau_{ie}(t = 0)$, showing the electron distribution becoming a super-Gaussian.

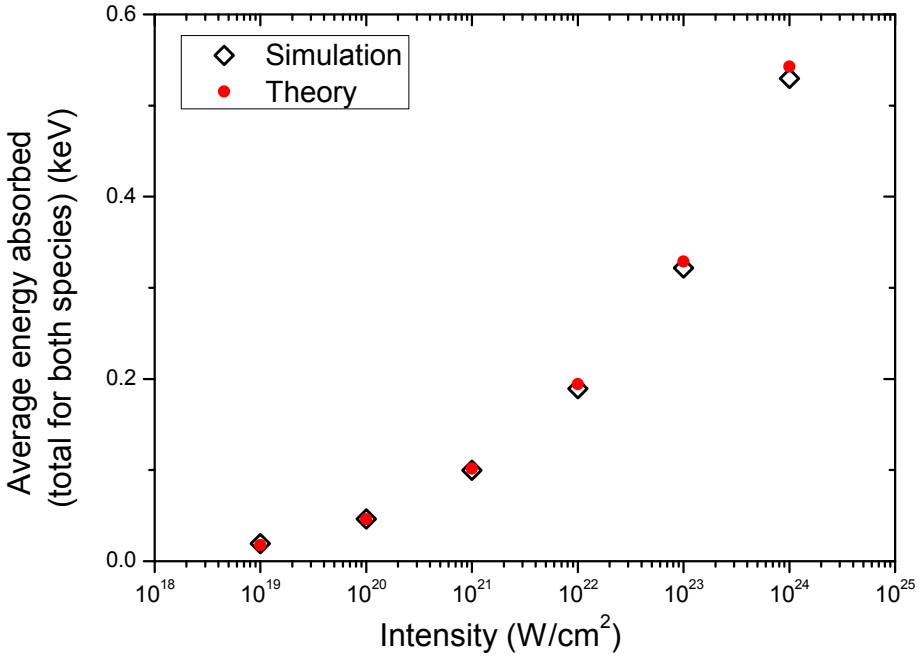

Figure 5.6: Ion-ion inverse bremsstrahlung absorption of laser radiation with 30 fs Gaussian pulses (peak intensities shown) at the relativistic critical density with protons and ^{12}C. The absorbed energy shown is $\langle E\rangle_{\mathrm{p}} + \langle E\rangle_{\mathrm{C}}$, with the theory referring to equation (5.6).

5.5 Results

Fig. 5.6 shows absorption according to equation (5.6) and Monte Carlo simulations over a range of intensities and using initial temperatures $T \leq 1$ eV. The ions are an equimolar mix of protons and ^{12}C. A Gaussian pulse shape of duration 30 fs is used; peak intensities are shown. The average energy absorbed including both species for the whole simulation is plotted, with each simulation performed at the relativistic density n_c (given by equation (5.2)) for that intensity, and each pulse having a wavelength of 1μm. Though the absorption is higher at higher intensities, keeping the density constant would not necessarily show the same relationship. The agreement with (5.6) is good for the lower densities and intensities, but is worse for higher densities and intensities. The most likely cause is departures from the simple model of two shifted Maxwellian distributions with perfect ion-ion relative speeds of $v_{ij}(t)$, indeed it will be shown that it is possible for non-Maxwellians to be driven, which tend to reduce absorption relative to a Maxwellian.

Intensities above 10^{23} W cm^{-2} are not currently feasible. However, the absorption is dependent on pulse shape in addition to intensity, density and Z. Using equation (5.6), an optimal E_0 for heating can be derived. If $x = v_{ij}/v_{\mathrm{th},ij}$, then taking $\frac{\mathrm{d}}{\mathrm{d}x}\left(\frac{\mathrm{d}T}{\mathrm{d}t}\right)_{\mathrm{IIIB}} = 0$

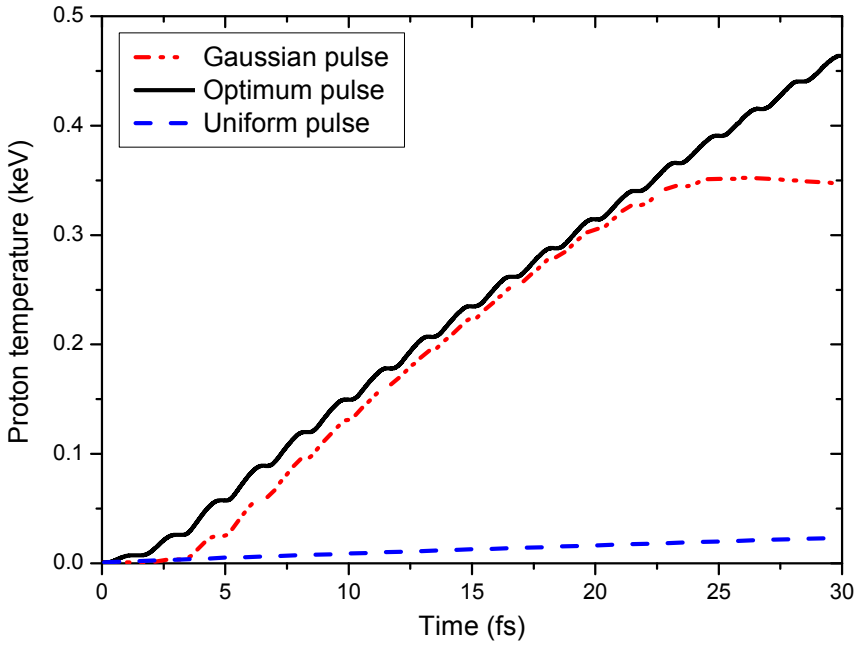

Figure 5.7: Three numerical simulations of different (temporal) pulse shapes. The ion species are fully ionised hydrogen and carbon, with an electron density of $n_e = 2.4 \times 10^{29}$ m^{-3} (kinetic electrons not included).

gives, to a good approximation, $x \approx 3/2$ as the largest positive root. Replacing cos and sin with their average values of $1/\sqrt{2}$, the optimum value of the electric field for heating is a peak value of

$$E_0 = \frac{3\omega}{e}\left(\frac{T_i}{m_i} + \frac{T_j}{m_j}\right)^{1/2}\left(\frac{Z_i}{m_i} - \frac{Z_j}{m_j}\right)^{-1} \tag{5.7}$$

for i given T_i, T_j, n_j, Z_i, Z_j etc. In Fig. 5.7 the performance of this 'optimum' electric field is compared with pulses with two other shapes; uniform and Gaussian. Each has the same average intensity of $I = 2.07 \times 10^{19}$ W cm^{-2} over 30 fs. The field for the optimum pulse is calculated every timestep. A pulse of wavelength 1μm is used, and the ion species are fully ionised equimolar hydrogen and ^{12}C. Only the hydrogen temperature is shown as it is much higher than the carbon temperature. Toward the end of the simulation, the proton temperature using the Gaussian pulse actually drops from its peak value; this is because energy is being lost to Carbon through ion-ion equilibration. The optimum pulse gives a 34% higher final temperature than the Gaussian pulse, and both strongly outperform the uniform pulse.

In electron-ion IB, non-Maxwellian distributions are driven if the rate of energy deposition into electrons by IB is faster than the electrons can self-thermalise. A similar situation can occur in IIIB; the condition for driving a non-Maxwellian in i for IIIB between i and

j is

$$\tau_i^{\mathrm{H}} < \tau_{ii}$$

where $\tau_i^{\mathrm{H}} = T_i n_i / \dot{W}_i$ is the e-folding time for heating and τ_{ii} is the ion-ion self-equilibration time (see Appendix B). The condition becomes

$$\frac{T_i}{m_i}\left(18\left[\frac{Z_j^2}{Z_i^2}\frac{\xi(x)}{x}\right]^2 - 1\right) > \frac{T_j}{m_j} \tag{5.8}$$

With the optimum pulse $\xi(x)/x \approx 0.35$, and the condition is satisfied if $\frac{T_i}{m_i}\left(\frac{441 Z_j^4}{200 Z_i^4} - 1\right) > \frac{T_j}{m_j}$. The derivation relies on both distributions being close to shifted Maxwellians; if j is far from equilibrium then the condition may not apply. Fig. 5.8 shows the distribution function of protons in an Au-proton mix with $n_{\mathrm{Au}} = n_p = 5.0 \times 10^{28}$ m^{-3} being heated by an optimum pulse with $\lambda = 1\mu$m. The snapshot is taken after 14 self-thermalisation times have passed (using the $t = 0$ value of v_p). The protons reach an $m = 5$ super-Gaussian, just as electrons do when being strongly heated. It is not really a surprise that this occurs, as the situation is somewhat similar to electron-ion IB with Au playing the role of the ion and protons the role of the electrons. The Au distribution (not shown) remains Maxwellian.

An optimum pulse heating a mix of ion species with $Z_i = Z_j$ and $v_i \sim v_j$ would not satisfy equation (5.8). To demonstrate this case, deuterium and tritium are used. The distributions of both show small signs of deviation from a Maxwellian, but only temporarily. The distribution of deuterium is shown, at its largest deviation from a Maxwellian, in Fig. 5.9. The tritium distribution is closer to a Maxwellian. Though these ion species are being driven with the optimum pulse, their similar masses mean that exchange of energy between them is relatively effective, giving a greater capacity to absorb distortions away from equilibrium. Deuterium comes closest to fulfilling equation (5.8), explaining why it has a larger deviation from a Maxwellian. For physical ion species only a small difference in Z and m (assuming the charge-to-mass ratios do not cancel) will result in the lighter ion species being driven with an $m > 2$ distribution.

One of the limitations of the analytical approach originally taken by M&R is that it is limited to two species of ion. The absorption equation, (5.6), does not apply to more than two species either. However, the Monte Carlo code is able to introduce a third species. If the optimum pulse defined in equation (5.7) is used to maximise the heating rate between any two of the three or more ion species present, a combination of ion-ion equilibration and IIIB will heat the remaining ion species.

A case of interest for producing fusion reactions is that of a large mass, high Z species

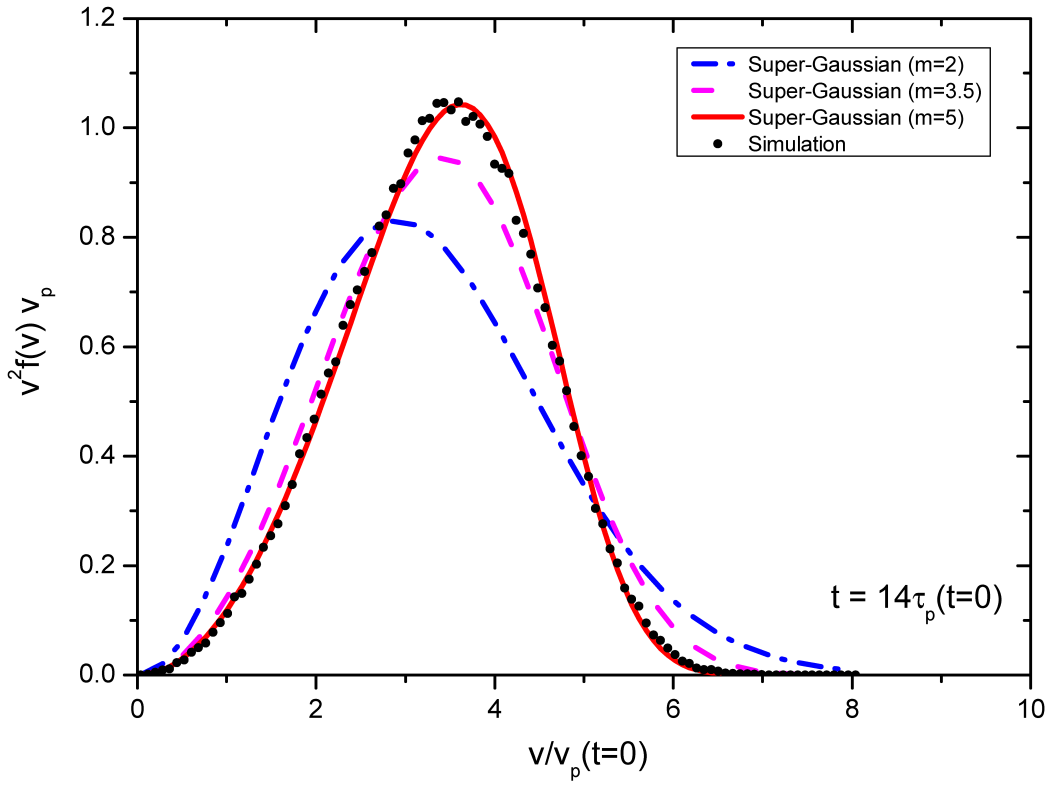

Figure 5.8: Distribution function of protons in an equimolar mix of protons and Au being heated by the optimum pulse. This situation satisfies the condition, given in equation (5.8), for driving a non-Maxwellian distribution in the protons. $v_p^2 = T_p(t)/m_p$ with T_p measured in the ZMF.

combined with deuterium and tritium. The similar masses of deuterium and tritium mean that the optimum field for heating them with the high Z species will not be very different quantitatively. Au is chosen as a 'driving' ion species due to its high Z. The effect of IIIB on a $n_{\mathrm{Au}} = n_d = n_t$ mix of cold Au, deuterium and tritium at the mass density of Au of 19.3 g cm^{-3} is shown in Fig. 5.10. The pulse shape is optimised for IIIB absorption between deuterium and Au, with a linearly polarised laser pulse of duration 30 fs. The Au is assumed to be fully ionised; further work would be required to establish whether this is the case for the thin foil scenario suggested in §5.3. The results shown are converged in the sense that halving the timestep and doubling the number of simulation particles leaves the result unchanged. In Fig. 5.10, non-Maxwellian distributions are driven in both light ion species. These distributions, taken at $t \approx 2\tau(t = 0)$ for both deuterium and tritium, are shown in Fig. 5.11. The distributions are clearly super-Gaussians with $2 < m < 3.5$. In Fig. 5.10, extremely high deuterium and tritium temperatures are achieved by using the optimum pulse and including Au as a dopant. Shorter interaction times, on the order of 15 fs, still produce temperatures of around 10 keV. More realistic mixtures of Au, deuterium and tritium could be expected to reach similar light ion temperatures, and fusion within the heated volume. Given the approximations made in calculating the final temperature, the possibility of transport or space-charge effects in reducing or disrupting the absorption, and the thinness of the foil, a more comprehensive model would be needed to determine the yield.

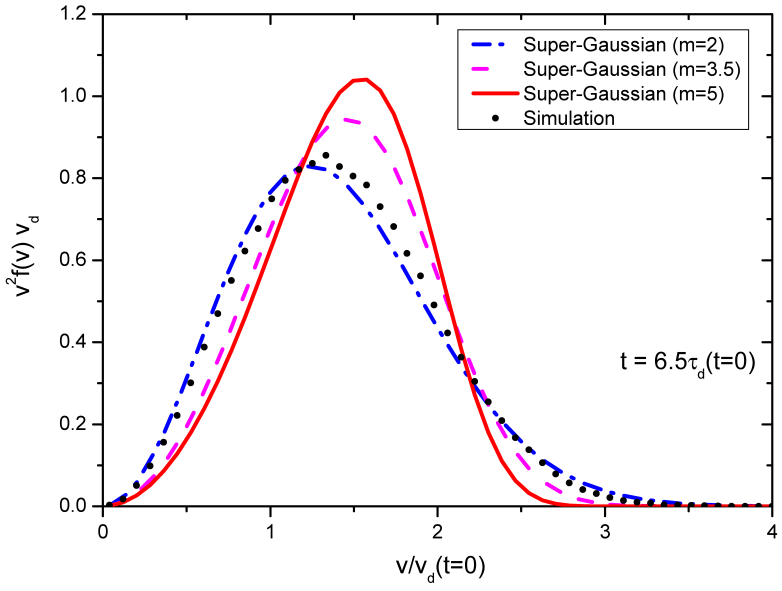

Figure 5.9: The maximum distortion away from a Maxwellian for deuterium being heated by an optimum pulse with $\lambda = 1\mu$m, in an equimolar deuterium-tritium mix. $v_d^2 = T_d(t)/m_d$ with T_d in the ZMF.

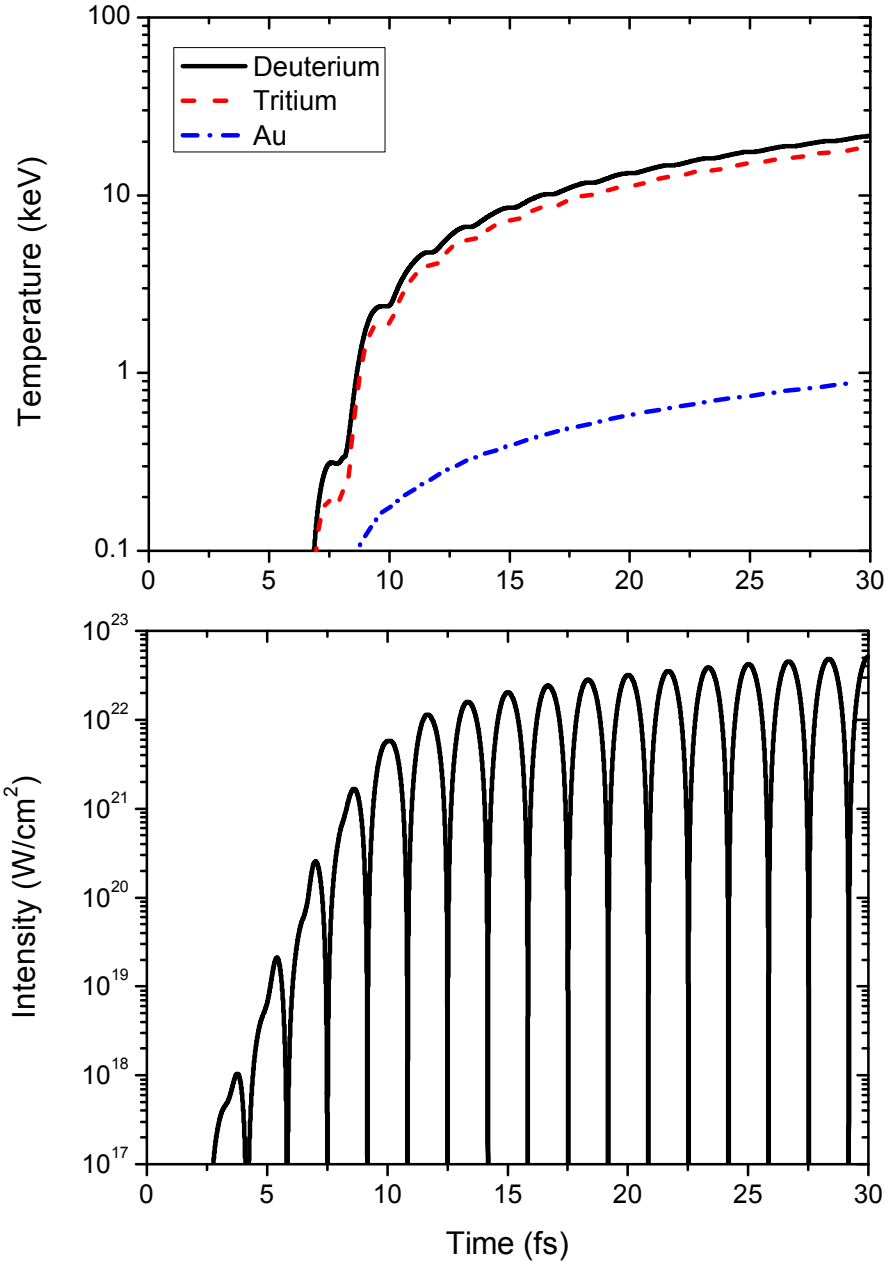

Figure 5.10: Top: Temperatures in the ZMF of a numerical simulation of a 30 fs laser pulse on equimolar Au, deuterium and tritium. Bottom: The intensity of the laser pulse over time. The pulse is optimised for IIIB between deuterium and Au and has $\lambda = 1\mu$m.

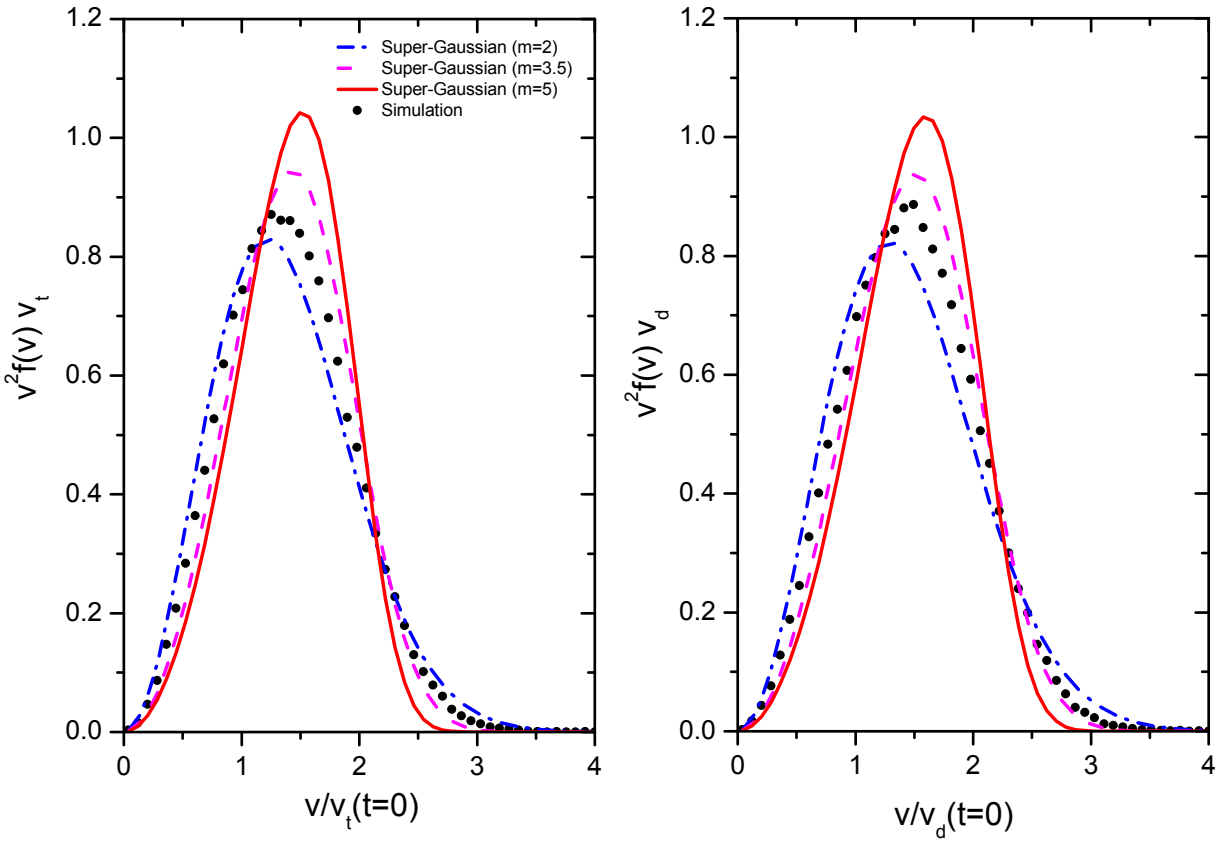

Figure 5.11: Light ion non-Maxwellian distribution functions being driven by $t \approx 2\tau(t = 0)$ in an Au-*d*-*t* mix, using a laser pulse optimised for absorption between deuterium and Au with $\lambda = 1\mu$m. $v_i^2 = T_i(t)/m_i$ with T_i measured in the ZMF. Left: Tritium. Right: Deuterium.

Chapter 6

Discrete collisions and large-angle scattering

6.1 Theory of discrete collisions

Many texts discuss the two different regimes of interaction in a plasma, the 'near' or 'close' collisions and the 'remote' ones [29, 113, 114, 115]. In Chapter 2, the relative importance of large- to small-angle scattering is established for basic cases of energy exchange, $\sim 1/\ln\Lambda$, and loss of momentum, $\sim 1/8\ln\Lambda$. With $\ln\Lambda \gg 1$ or $g \ll 1$, small-angle collisions dominate interactions.

These relations are approximate, and more precise definitions of what constitutes a large-angle, or 'close', collision allow an exploration of the phenomena that they are associated with. For the purposes of this work, the terms discrete collision and large-angle collision are more useful. Discrete interactions are those which have a short enough interaction time relative to the other timescales of the plasma to allow them to be taken to be instantaneous, and only involve two particles. They are true binary collisions. Large-angle collisions are those in which a significant transfer of energy or momentum occurs in one collision, so that the trajectory of a particle post-collision departs appreciably from its original trajectory. Discrete may be used interchangeably with near or close collisions, meaning those for which the impact parameter b is small. Though not all discrete collisions involve a large deflection, the term large-angle collision has also been used to mean near collision because discrete collisions often involve large deflections. All large-angle scattering is as a result of discrete collisions, but the reverse is not always true. Discrete collisions are in contrast to 'multiple' collisions, in which a test particle is simultaneously interacting with a large number of other particles in the plasma. In most

plasmas, the cumulative effect of the multiple collisions is far stronger than the discrete collisions which gives the relative importances for energy and momentum exchange of $\mathcal{O}(1/\ln\Lambda)$.

There are two different, but equivalent, pictures of the origin of the different regimes of interaction. The first is based on the distance over which the interaction acts, the second is based on the time the interaction takes to occur.

The first is motivated by the long range of the Coulomb force. A charged test particle going through a plasma is constantly being pushed and pulled in different directions due to the overall effective force of many other charged particles. This is multiple, small-angle scattering, in which the assumptions of the pure Rutherford cross-section are not applicable. Rutherford assumes two particles interacting solely with one another. In the multiple scattering case, the strongest influence on the test particle is not due to any single other particle but due to the ensemble of particles within a Debye length of the test particle. As the Coulomb force is proportional to r^{-2}, there must be some finite distance where the contribution to the electromagnetic potential from one single other charged particle becomes dominant over the rest of the ensemble. Let this distance be denoted b_c; the impact parameter where the cross-over between multiple scattering and discrete scattering occurs. At impact parameters below b_c, the interaction is discrete and the scattering angle is limited to being above $\theta_c = \theta_c(b_c)$ from equation (2.4). This can force discrete interactions to involve large deflection angles, in which case the average transfer of energy and momentum will be far higher per collision than with a remote interaction. The remote interactions are restricted to impact parameters $b > b_c$. Cohen, Spitzer and Routly [115], Trubikov [29], and Perkins and Cullen [113] all work within this picture. The former note that if there were no large deflections at all, then the change to plasma distribution functions would be fully described by a diffusion equation. It is also noted that the omission of the close, discrete encounters will introduce more errors as $\lambda_\mathrm{D}/b_\perp$ gets smaller - corresponding to small $\ln\Lambda$. Cohen, Spitzer and Routly also recommend that the interaction be split into a Boltzmann type collision operator and multiple scattering, diffusion terms dealt with by VFP, with the regimes of interaction being $b = 0$ to $b = b_c$ and $b = b_c$ to $b = \lambda_\mathrm{D}$ respectively. As the regime of most interest at the time of publication of the article was $\lambda_\mathrm{D} \gg b_\perp$, the authors suggested that the Boltzmann collision part of the change to the distribution function be ignored but that $b_c \longrightarrow 0$ could be used to approximately include the effect of close encounters in the diffusion terms. This remains the convention, even for small $\ln\Lambda$.

Sivukhin [114] discusses the second picture, starting from an acknowledgement that the apparent divergence in the Rutherford cross-section when considering increasingly small

deflections is because the cross-section is no longer applicable. The reason is that Rutherford implicitly assumes an infinite interaction time, but actually the time for a remote interaction is constrained. This approach yields non-divergent expressions for momentum transfer but the remote interactions are still effectively cut-off at λ_{D}. Discrete collisions are then those which have an interaction time which is so short that it is effectively instantaneous relative to the timescale for undergoing collisions with more than one particle, and a 'full' Rutherford collision takes place. The discrete and multiple interactions are effectively split by b_c such that the Coulomb logarithms in the momentum exchange expression are $\ln \frac{b_c}{b_\perp}$ and $\ln \frac{\lambda_{\mathrm{D}}}{b_c}$ respectively. The approach to the discrete collisions is discussed, and a strategy of either ignoring them or approximating them with remote collisions (using $b_c = 0$) recommended, with a statement that "Such an approach... cannot pretend to give a completely adequate description of the true situation."

These two approaches suggest that there is a cross-over impact parameter $b = b_c$ which separates the discrete and multiple collisions, without giving a physically motivated value for it.

Due to the dominance of multiple scattering, conventional approaches to plasma physics, such as those outlined in §2.5, do not attempt to account for large-angle collisions either because they are subject to a constraint equivalent to $g \ll 1$, because they do not permit large deviations from equilibrium distribution functions, or because they approximate discrete collisions as multiple collisions by including all b down to $b = 0$ in calculations. This is justified for $\ln \Lambda \gg 1$.

However, even for moderately coupled plasmas, with $2 \lesssim \ln \Lambda \lesssim 5$, the inclusion of the effects of large-angle collisions is necessary [48, 116] in order to get the fundamental rate of exchange of momentum and energy correct. Fig. 2.4 shows typical values of $\ln \Lambda$, while Fig. 2.5 shows $N_{\mathrm{D}} = \frac{4}{3}\pi n_e \lambda_{\mathrm{D}}^3$, the number of particles in a Debye sphere, which typically has to satisfy $N_{\mathrm{D}} \gg 1$ for conventional approaches to plasma physics to be valid. Plasmas with $\ln \Lambda \sim 1$ include a great many areas of research and practical interest including high intensity laser-plasma interactions [39], inertial confinement fusion [23], degenerate plasmas [40], and stellar cores [41, 42].

Possible changes to the fundamental rates of exchange and equilibration due to the relative strength of discrete and multiple scattering could have consequences for the shape and evolution of distribution functions, fusion reactivities, and associated neutron emission spectra, and transport. Despite large-angle collisions being secondary in number to small-angle collisions, there may be situations where the large transfers of energy and momentum *per collision* change the evolution of a plasma dramatically. Fusion is an interesting example; large-angle collisions could create high energy particles capable of

fusing right under the peak of the fusion cross-section and thus have a disproportionately large effect on reactivity. It is not only that the changes in energy are large that could lead to new effects, but also that they are discontinuous. This means areas in energy space may be occupied much earlier in time than might be expected from conventional models; an analogy is the loss of energy by an electron due to synchrotron emission - the discontinuous energy loss predicted by quantum electrodynamics broadens the electron energy spectrum relative to the classical continuous energy loss model [117].

A way of examining the inclusion of near interactions could be a useful tool in understanding plasmas where $\ln\Lambda$ is small. The introduction of a cross-over impact parameter of $b = b_c$ separating the discrete and multiple collisions, and a method of properly accounting for large-angle collisions, are required to facilitate this.

As an example, the first kinetic cross-section given by equation (2.10) is used with a cut-off; though the Coulomb logarithm will be the same with any kinetic cross-section.

$$\sigma_1 = \frac{\pi b_\perp^2}{2}\int \frac{(1-\cos\theta)\sin\theta}{\sin^4\left(\frac{\theta}{2}\right)}\mathrm{d}\theta = \frac{\pi b_\perp^2}{2}\left[8\ln\left(\sin\frac{\theta}{2}\right)\right] \tag{6.1}$$

From $\cot\frac{\theta}{2} = \frac{b}{b_\perp}$,

$$\sin^2\frac{\theta}{2} = \frac{b_\perp^2}{b_\perp^2 + b^2}$$

so

$$\frac{\pi b_\perp^2}{2}\left[8\ln\left(\sin\frac{\theta}{2}\right)\right] = 2\pi b_\perp^2\left[\ln\left(\frac{b_\perp^2}{b_\perp^2+b^2}\right)\right]$$

A cut-off at $b_c:\ 0 < b_c < \lambda_\mathrm{D}$ splits σ_1 into two distinct cross-sections; $\sigma_1 = \sigma_{1,\mathrm{M}} + \sigma_{1,\mathrm{D}}$

$$\sigma_{1,\mathrm{M}} = 2\pi b_\perp^2\ln\left(\frac{b_\perp^2+\lambda_\mathrm{D}^2}{b_\perp^2+b_c^2}\right) = 4\pi b_\perp^2\ln\Lambda_\mathrm{M}$$
$$\sigma_{1,\mathrm{D}} = 2\pi b_\perp^2\ln\left(\frac{b_\perp^2+b_c^2}{b_\perp^2}\right) = 4\pi b_\perp^2\ln\Lambda_\mathrm{D}$$

with logarithms $\ln\Lambda_\mathrm{M}$ and $\ln\Lambda_\mathrm{D}$ having absorbed a factor of $1/2$. 'M' and 'D' correspond to multiple and discrete scattering respectively. Note that the partial cross-sections have the following properties:

$$\lim_{b_c\longrightarrow 0}\sigma_{1,\mathrm{D}} = 0$$
$$\lim_{b_c\longrightarrow 0}\sigma_{1,\mathrm{M}} = \sigma_1$$
$$\lim_{b_c\longrightarrow b_\perp}\sigma_{1,\mathrm{D}} = 2\pi b_\perp^2\ln 2 \approx \pi b_\perp^2$$

6.1.1 A physically motivated cut-off in impact parameter

b_c is effectively a slider between discrete and multiple scattering, but there is no obvious physically motivated value for it. Trubnikov [29] suggested that the cut-off should be $b_c = 2b_\perp$ so that

$$\sigma_{1,\mathrm{M}} = 2\pi b_\perp^2 \ln\left(\frac{b_\perp^2 + \lambda_\mathrm{D}^2}{5b_\perp^2}\right) \approx 4\pi b_\perp^2 \ln\Lambda$$
$$\sigma_{1,\mathrm{D}} = 4\pi b_\perp^2 \ln\left(\sqrt{5}\right) \approx 4\pi b_\perp^2$$

The ratio is

$$\frac{\sigma_{1,\mathrm{D}}}{\sigma_{1,\mathrm{M}}} \approx \frac{1}{\ln\Lambda}$$

a relationship frequently occuring in the literature [48, 118] as being proportional to the large-angle corrections to multiple scattering. However, that choice of cut-off, $b_c = 2b_\perp$, is arbitrary and independent of density. Ballabio *et al.* [119] choose a cut-off of $b_c = 5.67b_\perp$. The other conventional approach is to approximate discrete collisions as multiple scattering collisions by allowing $b_c \longrightarrow 0$. Then the limits of the integration in equation (6.1) run over all values, $b \in (0, \lambda_\mathrm{D}) \Leftrightarrow \theta \in (\pi, \theta_{\min})$, so that the conventional first kinetic cross-section is recovered.

A more physically motivated value of b_c is desirable. One approach would be to try and extract a value of b_c from molecular dynamics (MD) simulations. Classical MD simulations have several potential problems which make this approach impractical, but the most important is that interactions in classical MD are often cut-off at short ranges using an arbitrary 'smoothing parameter'. This is introduced to stop electrons becoming infinitely bound to ions, but, because it is important on the same length scales as discrete scattering, the value of b_c determined this way would be sensitive to the value of the smoothing parameter, itself often set to be $\Delta t v_{ij}$, and therefore is not determined by fundamental physics.

A physically motivated value of b_c based on fundamental physics can be obtained by taking b_c to be proportional to the impact parameter at which the potential from one neighbouring particle is higher than the sum of the potentials of all other charged particles. Let the value of the cut-off based on this premise be b_ϕ. Finding b_ϕ requires an assumption about the form of the potential. David [120] found that a Yukawa potential, screened by λ_D, is a very good fit to the potential observed in molecular dynamics simulations even for strongly coupled plasmas with $g \sim 1$ (see David's Fig. 5.2(c)). Let i, j, and k, represent charged particles in a plasma, rather than species in the plasma. Between

particles i and j, the Yukawa potential of j on i is

$$\phi_{ji}(\mathbf{r}_j) = \frac{q_j e}{4\pi\epsilon_0}\frac{e^{-r_j/\lambda_\mathrm{D}}}{r_j}$$

where $r_j = |\mathbf{r}_j|$ is the distance of j from i. From the point of view of i, b_ϕ is the value of r_j which satisfies

$$\phi_{ji}(\mathbf{r}_j) = \sum_{k\neq i,j} \phi_{ki}(\mathbf{r}_k) \tag{6.2}$$

where j is the nearest neighbour (of its species) of i and k runs over *all* other particles. Substituting in $r_j = b_\phi(j,i)$ in (6.2),

$$\phi_{ji}(b_\phi) = \frac{q_j e}{4\pi\epsilon_0}\frac{e^{-\frac{b_\phi}{\lambda_\mathrm{D}}}}{b_\phi} = \sum_k \frac{q_k e}{4\pi\epsilon_0}\frac{e^{-\frac{r_k}{\lambda_\mathrm{D}}}}{r_k} \tag{6.3}$$

Calculating r_k time-dependently is as difficult as solving Liouville's equation, so an average model is used. Let s represent a species in the plasma. In the average model, it is assumed that the distance to the nearest particle of species s will be approximately found from letting $\frac{4}{3}\pi r_s^3 n_s = 1$. This is the single species equivalent of the particle sphere radius r_0 defined in §2.3 as $r_0 = (4\pi\sum_i n_i/3)^{-1/3}$. Let

$$r_s \equiv r_{s:1} = \left(\frac{3}{4\pi n_s}\right)^{1/3} \tag{6.4}$$

then, the next nearest particle of species s will be given by $\frac{4}{3}\pi r_{s:2}^3 n_s = 2$, and the mth, where $m \in \mathbb{N}$, by

$$r_{s:m} = m^{1/3} r_s \tag{6.5}$$

That the average distances between particles obey this relation is a strong assumption. Holtsmark theory, [46, 121] and references therein, gives the electric field distribution from a test point due to an ensemble of particles. Its application to a plasma with Debye shielding assumes that the potential is completely cut-off at $r > \lambda_\mathrm{D}$, and gives the highest probability density for electric fields at distances roughly between $0.8r_0$ and $1.3r_0$ for $N_\mathrm{D} = \infty$ and $N_\mathrm{D} = 3$ respectively. This supports the choice of r_0 as the average distance to the next nearest neighbour, but it is still an approximate theory.

With equation (6.5), equation (6.3) becomes

$$\phi_{ji}(b_\phi) = \sum_s \sum_m \frac{q_s e}{4\pi\epsilon_0}\frac{e^{-m^{1/3}r_s/\lambda_\mathrm{D}}}{m^{1/3}r_s} \tag{6.6}$$

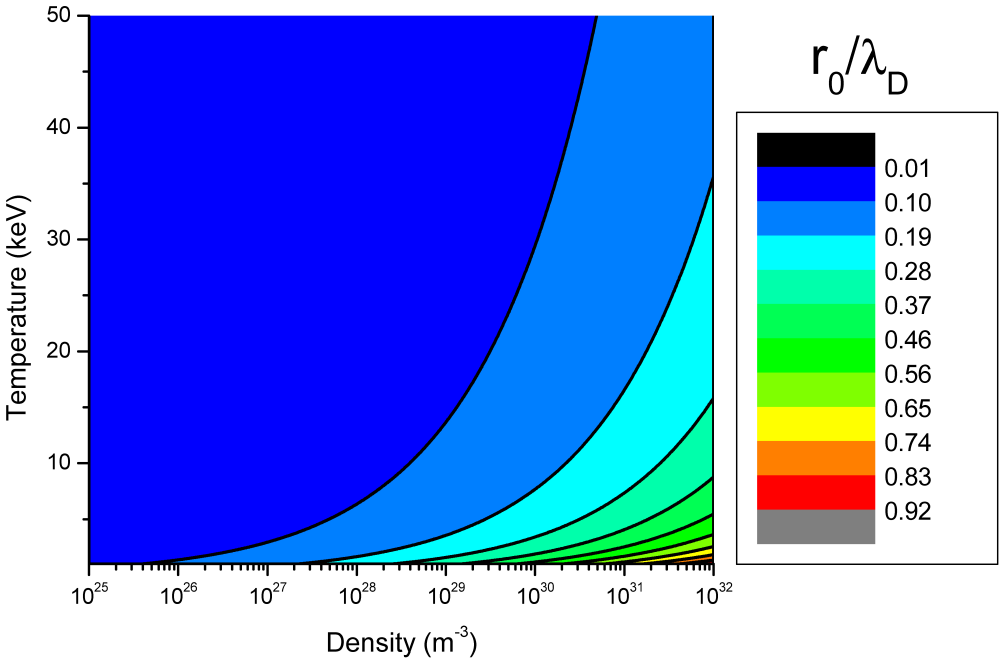

Figure 6.1: Values of $x = r_0/\lambda_\mathrm{D}$ in an equimolar deuterium-tritium plasma.

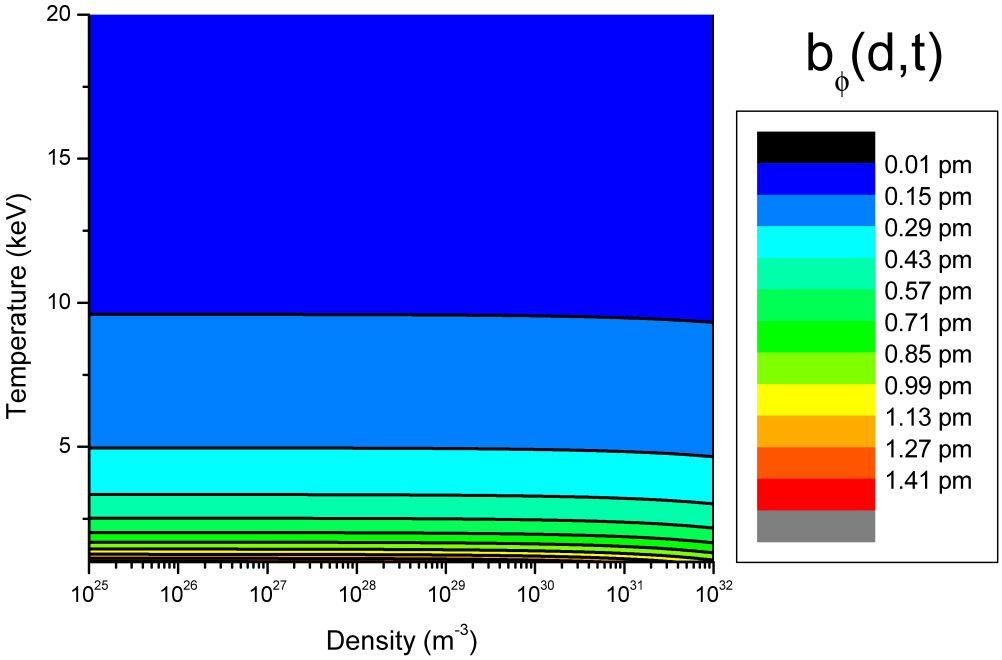

Figure 6.2: b_ϕ for an equimolar deuterium-tritium plasma in units of 10^{-12} m.

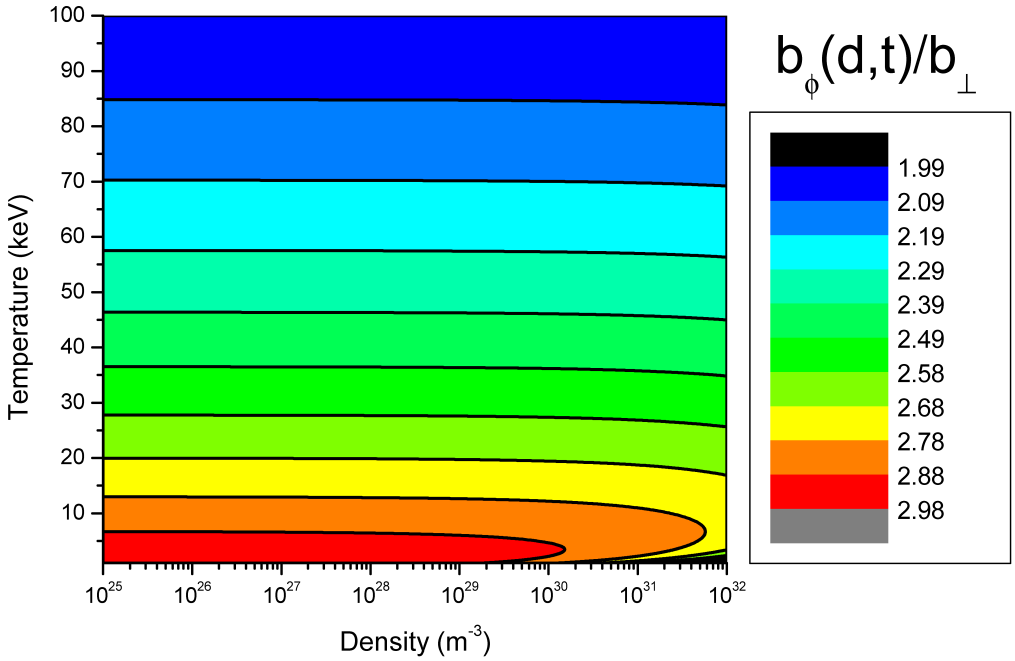

Figure 6.3: $b_\phi/b_\perp$ for an equimolar deuterium-tritium plasma.

where s is species, m runs over all particles which are members of species s, and it is assumed that the plasma has enough particles such that the $m \longrightarrow \infty$ limit can be taken, not an unreasonable assumption for most plasmas given that successively higher terms contribute less. The sum is not trivial. Firstly it must converge. Taking $a_m = \frac{e^{-m^{1/3}x}}{m^{1/3}}$ with $x = r_s/\lambda_\mathrm{D}$ as the mth term of the sequence, convergence can be determined using the integral test, which sets a function $f(m) = a_m$ and demands $f(m)$ be a positive, decreasing function $\forall\ m \in [1, \infty)$. Then,

$$F(k) = \int_1^k f(m)\mathrm{d}m = \int_1^{k^{1/3}} 3ye^{-yx}\mathrm{d}y = \left[-\frac{3}{x}e^{-yx}\left(y + \frac{1}{x}\right)\right]_{y=1}^{y=k^{1/3}}$$

using the substitution $y = m^{1/3}$. Then, for some finite number C,

$$\lim_{k\longrightarrow\infty} F(k) = C$$

guarantees that the series converges [122]. The behaviour of the ratio of terms

$$\lim_{m\longrightarrow\infty} \frac{a_{m+1}}{a_m} = \lim_{m\longrightarrow\infty} \left(\frac{m+1}{m}\right)^{1/3} \exp\left\{x\left[m^{1/3} - (m+1)^{1/3}\right]\right\} = 1$$

implies that the convergence may be logarithmic, meaning that $S_k = \sum_{m=1}^{k} a_m$ converges

very slowly using term by term evaluation. This presents difficulties for brute force calculation.

However, if the terms up to $m = k > 1$ are summed, the remainder may be approximated by an integral because the convergence is so slow;

$$\sum_{m=k}^{\infty} \frac{e^{-m^{1/3}x}}{m^{1/3}} \approx \int_k^{\infty} \frac{e^{-m^{1/3}x}}{m^{1/3}} \mathrm{d}m = \frac{3}{x} e^{-k^{1/3}x} \left(k^{1/3} + \frac{1}{x} \right)$$

giving the complete expression

$$S \approx S_k + \frac{3}{x} e^{-k^{1/3}x} \left(k^{1/3} + \frac{1}{x} \right) \equiv S_A(k) \tag{6.7}$$

This must be able to deal with a range of $x = r_0/\lambda_\mathrm{D} \propto n^{1/6}/T^{1/2}$ values as shown in Fig. 6.1 for a deuterium-tritium plasma. The most stringent limit is for small values of x with many, many particles in a Debye sphere, with the minimum being $x \sim 0.01$. In the limit of $x \longrightarrow 0$, the series becomes the over-harmonic series and no longer converges; physically this is because the limit corresponds to having no Debye shielding. Large values of x cause the *series* to converge more rapidly, but not necessarily the approximation $S_A(k)$. A parameter scan of x to find the smallest k giving a converged value of the ratio of $S_A(k)$ to $S_{5\times10^9}$ (taken to be the 'converged' value) found that larger values of x required higher values of k, but using $k = 50$ never produced an error of more than 0.15% for $x \in [0.01, 10]$. The equation to solve for $b_\phi(j, i)$ is then

$$\phi_{ji}(b_\phi) = \sum_s \frac{q_s e}{4\pi\epsilon_0 r_s} S_A(k) \tag{6.8}$$

where $k = 50$ is used, and the dependence of $S_A(k)$ on species s is suppressed. This equation is solved computationally using the Van Wijngaarden-Dekker-Brent method [123, 57].

$b_\perp(i, j)$ is symmetric in i and j, and λ_D is the same for all particles. Physically it is expected that b_ϕ be symmetric also; $b_\phi = b_\phi(i, j) = b_\phi(j, i)$, where $b_\phi(i, j)$ is the solution if the potential on the left hand side is ϕ_{ij}. Physically, it seems reasonable that b_c be symmetric. However, b_ϕ is not symmetric if there are two species with different charges, because $\phi_{ij} \neq \phi_{ji}$ but the right-hand side of equation (6.8) remains the same. For $q_i < q_j$, $b_\phi(j, i) < b_\phi(i, j)$ because j is more strongly coupled into all other particles than i. This method of finding a cut-off is based on discrete scattering dominating multiple scattering, and thus requires *both* particles to see their collision as being a true binary collision. The correct value of b_ϕ resulting from numerically solving equation (6.6) will therefore be the

lower of the two values of b_ϕ, meaning the equation need only be solved once for each pair i, j - the one with the smallest charge q.

Taking, for example, $b_c \approx b_\phi$, gives a physically motivated cut-off but it is still approximate. At b_ϕ, the interactions of all other particles are equally as strong as those from the nearest neighbour, so some $b_c < b_\phi$ is more likely to be a realistic answer. Values of b_ϕ for an equimolar deuterium-tritium(-electron) plasma over a wide range of temperatures and densities are shown in Fig. 6.2. Also informative is how the value of b_ϕ changes relative to $b_\perp$ as this determines θ_c, and $b_\perp$ is the preferred value of the cut-off for several authors. The ratio, shown in Fig. 6.3, is very stable over a wide range of temperatures and densities. Taking $b_c = b_\phi/e$ to give a b_c safely in the pure Rutherford regime, $b_c = \langle b_\perp \rangle$ appears to be a good approximation for equimolar deuterium and tritium in ICF conditions. However, this turns out to be a special case and b_ϕ can depart from $\langle b_\perp \rangle$ substantially, so that the approximation cannot be used in general.

This theory strongly relies on the approximations about the average locations of other particles and the form of the potential, and an improved theory would take account of these in a more satisfactory way. It represents a first step toward a theory of the relative strength of large-angle collisions based on physical reasoning.

6.1.2 Advanced discrete collisions

Although this chapter is primarily concerned with the effects on a plasma of large-angle Coulomb collisions, much of the previous work in this area concerns both Coulomb collisions, sometimes beyond pure Rutherford scattering, and 'large-angle' collisions due to the nuclear force. In order to understand the context of the work of this chapter, and possible directions of future work, a brief overview of the extra physics of elastic scattering which might be important for a plasma in a more advanced model is presented. However, it should be stressed that this physics is not currently included in the computational model described in Chapter 7.

The Rutherford cross-section, $\frac{\mathrm{d}\sigma}{\mathrm{d}\Omega}_{\mathrm{R}}$, is a classical approximation and assumes that species are non-relativistic, have no spin, and are point particles. Corrections to it are rarely considered in plasmas, but are common in particle physics where much higher collision energies are typical. Even the first order quantum mechanical calculation of the Rutherford cross-section, using the first Born-Approximation with a Yukawa potential $\phi(r) = \frac{qe}{4\pi\epsilon_0}\frac{e^{-r/\lambda_\mathrm{D}}}{r}$, recovers exactly the same cross-section in the small angle limit though with λ_{dB} as the minimum impact parameter rather than $b_\perp$. The corrections and deviations from pure Rutherford scattering are mostly at large angles. The most relevant

additional physics at large-angle for Coulomb collisions in plasmas are particle indistinguishability, spin statistics and the nuclear force via NES (nuclear elastic scattering). The consequences for the cross-section of including each of these is briefly examined.

Indistinguishability modifies the cross-section for scattering like particles. The consequence of indistinguishability is that particles cannot be tracked through collisions, and scattering through θ appears as likely as scattering through $\pi-\theta$. The explanation of this phenomena is that the cross-section for like-particle scattering is the sum of the Feynman diagrams at first order, which contains contributions from both the t and the u channels. While the t-channel is Rutherford scattering, the u-channel is the 'switch' between the two indistinguishable particles. The extra channel introduces a second divergence associated with Debye shielding, at $\theta = \pi$, for scattering in a plasma. It should be stressed that the extra channel can only contribute if the interaction happens on quantum lengthscales, i.e. a Compton wavelength for electron-electron scattering. This means it is unlikely to happen at small-angles, as they correspond to greater distances. The wavefunctions of the particles must be close enough to overlap; otherwise the interaction is classical. So the inclusion of indistinguishability is only relevant at large-angles.

Introducing spin further complicates cross-sections. Considering first order fermion point-particle scattering, the switch in the u-channel between two anti-commuting particles leads to a relative sign change between the contributions from each channel in the total scattering amplitude $\mathfrak{M}$, where

$$\frac{\mathrm{d}\sigma}{\mathrm{d}\Omega} = \frac{1}{64\pi^2(E_A+E_B)^2}\frac{p_f}{p_i}\left|\mathfrak{M}\right|^2$$

is the differential cross-section. This is for initial particles A and B with initial and final magnitudes of momentum p_i and p_f respectively. Furthermore, the scattering amplitude must be averaged over all incoming and outgoing spin states. At relativistic velocities, spin states can be flipped by the magnetic contribution to the scattering; this regime is not considered. The averaging over spins leads to the u- and t-channel scattering contributions, but also interference between them [124] yielding the differential cross-section

$$\frac{\mathrm{d}\sigma}{\mathrm{d}\Omega} = \frac{b_\perp^2}{4}\left(\frac{1}{\sin^4\frac{\theta}{2}} + \frac{1}{\cos^4\frac{\theta}{2}} - \frac{1}{\sin^2\frac{\theta}{2}\cos^2\frac{\theta}{2}}\right) \tag{6.9}$$

known as the non-relativistic Møller cross-section. Though the field theory viewpoint of channels and successive contributions is useful in examining the origin of the terms in the scattering amplitude, it still only provides a cross-section which is tractable in the non-relativistic limit and is restricted to point-particle interactions without a nuclear force contribution.

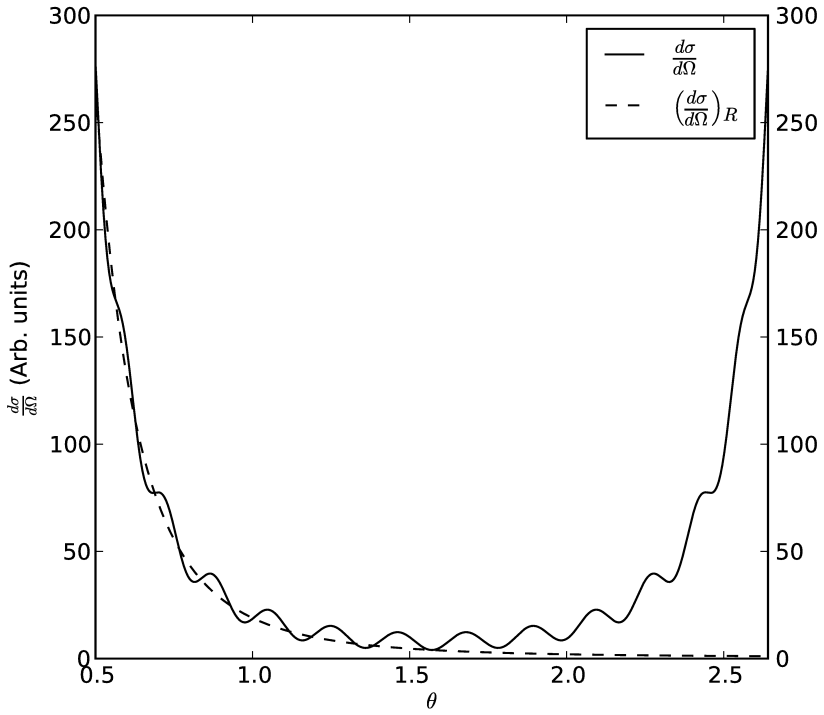

Figure 6.4: The cross-section of equation (6.13) against the Rutherford cross-section for proton-proton scattering at a relative collision velocity of 1.5×10^5 m s^{-1}. Interference from the third term in (6.13) causes the oscillatory behaviour.

NES, from the nuclear force, introduces nuclear structure. It not only changes the ion-ion scattering cross-section but also introduces a neutron-ion cross-section. NES has its origin in strong force interactions between all quarks with the strong force equivalent of charge, 'colour'. Though ions and neutrons are colour neutral, they are not uniformly so and just as van der Waals' forces exist between molecules but are much weaker than the bonding between individual atoms, so baryons in close contact may exert nuclear forces on each other which are much weaker than the strong force interactions holding quarks together. NES can be thought of as a discrete scattering process because it is dwarfed by the Coulomb scattering cross-section for small-angles (and, correspondingly, large physical separations). It is also a relatively high energy process; it is much smaller than Coulomb scattering cross-section for collision energies below 1 MeV. However, for neutron-ion scattering, it is always the dominant scattering mechanism in a plasma.

In order to unify spin, NES, and indistinguishability, it is necessary to adopt the quantum mechanics viewpoint of particles as wavefunctions which can scatter off of each other. This theory relies on finding forms for the scattering amplitudes of individual forces, such as

the Coulomb and nuclear forces [125, 126].

The evolution of a wave packet $\psi(\mathbf{r}, t)$ representing a particle after scattering is given by a plane wave part, changed only by a phase factor, and a scattered spherical wave which is a radially expanding image of the initial wave packet,

$$\psi(\mathbf{r}, t) = \psi(\mathbf{r} - \mathbf{v}_0 t, t) e^{i\omega_0 t} + \frac{f_{\mathbf{k}_0}(\hat{\mathbf{r}})}{r} \psi(r\hat{\mathbf{k}}_0 - \mathbf{v}_0 t, 0) e^{i\omega_0 t}$$

This assumes that the initial wave is scattered fairly continuously as a function of $\mathbf{k}$. $f_{\mathbf{k}_0}(\hat{\mathbf{r}})$ is the scattering amplitude, and the differential cross-section is given by

$$\frac{\mathrm{d}\sigma}{\mathrm{d}\Omega} = |f_{\mathbf{k}_0}(\hat{\mathbf{r}})|^2 \tag{6.10}$$

The Coulomb scattering amplitude, which gives the classical Rutherford cross-section, is [126, 125]

$$f_{\mathrm{C}}(\theta) = \frac{b_\perp}{2\sin^2\frac{\theta}{2}} \exp\left[-in \ln\left(\sin^2\theta/2\right) + i\pi + 2i\eta_0\right]$$

where $n = -\frac{q_i q_j}{4\pi\epsilon_0 \hbar v_{ij}}$ and $\eta_0 = \arg\Gamma(1 + in)$. To include spin for identical particles, a symmetrisation or anti-symmetrisation, for bosons and fermions respectively, must be performed on the scattering amplitude $f(\theta)$ to give the differential cross-section [126];

$$\frac{\mathrm{d}\sigma}{\mathrm{d}\Omega} = |f(\theta) \pm f(\pi - \theta)|^2 \tag{6.11}$$

$$= |f(\theta)|^2 + |f(\pi - \theta)|^2 + \frac{(-1)^{2s}}{2s+1} 2\Re\left[f(\theta) f(\pi - \theta)\right] \tag{6.12}$$

For Coulomb collisions alone, $f(\theta) = f_{\mathrm{C}}(\theta)$, the resulting cross-section is equivalent to the non-relativistic quantum field theory result of equation (6.9) but with an extra factor retained in the third term [127],

$$\frac{\mathrm{d}\sigma}{\mathrm{d}\Omega} = \frac{b_\perp^2}{4}\left[\frac{1}{\sin^4(\frac{\theta}{2})} + \frac{1}{\cos^4(\frac{\theta}{2})} + \frac{(-1)^{2s}}{2s+1} \frac{\cos\left(\frac{\alpha_f c}{v} \ln\tan^2\frac{\theta}{2}\right)}{\sin^2(\frac{\theta}{2})\cos^2(\frac{\theta}{2})}\right] \tag{6.13}$$

This is shown in Fig. 6.4 for proton-proton scattering vs. the Rutherford cross-section, $(\mathrm{d}\sigma/\mathrm{d}\Omega)_R$. The effects of identical particles having spin are considered in other work [128, 113]. The relevant cases for ICF are composite spin-0 (α-particles), spin-1/2 (electrons, protons, tritons), and composite spin-1 (deuterons).

Including NES means adding the scattering amplitude $f_N(\theta)$ so that the total cross-

section, for non-identical particles, is

$$\frac{\mathrm{d}\sigma}{\mathrm{d}\Omega} = |f_C(\theta) + f_N(\theta)|^2$$

In general, the form of $f_N(\theta)$ is not trivial. NES can substantially change the cross-section, an example is α-deuteron scattering which has a large resonance at $E_\alpha = 2.1$ MeV, $E_d \ll 2.1$ MeV, which *doubles* the total cross-section. NES also dominates Coulomb scattering for all angles $\theta > \pi/4$, for α-d and α-t scattering with $E_\alpha = 3.54$ MeV [119]. For identical particles, the symmetrisation must be carried out on the total scattering amplitude $f(\theta) = f_C(\theta) + f_N(\theta)$ as in equation (6.11). Over a wide range of different cross-sections, centre-of-mass frame collision energies of around 1 MeV are the turning point where NES effects begin to contribute. Cross-sections including NES are available for many scattering pairs including proton-proton [127], α-t and α-d [119], and neutron-d and neutron-t [129]. The methods used to obtain these cross-sections vary and the full details are beyond the scope of this work.

A full treatment of large energy transfers in a plasma requires the inclusion of some or all of these effects, depending on the application. Some work is required to determine the exact conditions in which they start to become important, but they are all short-distance, large-angle effects which do not occur in a classical plasma. The different cross-sections discussed produce further complications by giving rise to slightly different Coulomb logarithms, e.g. in the relativistic Møller cross-section [130]. Not discussed here, there are also important inelastic scattering processes and break-up reactions at work in a fusion plasma [131]. Another point to note is that large-angle Coulomb collisions may be modified so that the minimum impact parameter is not set to zero (see the derivation of the Coulomb logarithm in §2.3), and the finite nature of the charge distribution of individual particles thereby taken into account [31]. Again, the inclusion of all of these effects is left for future work.

Large-angle Coulomb collisions are a topic arguably less well explored in previous work than the other effects discussed. It is the aim of this work to develop a robust predictive capability for large-angle Coulomb collisions, but the methods employed are compatible with the future inclusion of the other effects.

6.2 Applications and models

6.2.1 Athermal chain-reaction fusion

A series of articles examining the effects of large-angle collisions, either Coulomb, NES or both, has led to several authors concluding that a critical chain of athermal fusion reactions might be possible. This is not thermonuclear fusion, in which reactions occur due to a high enough bulk temperature, but fusion in which an athermal population of ions exists, undergoes most of the fusion reactions in the plasma, and replenishes itself via the slowing of those fusion products. The process is that initial fusion produced particles, charged and neutral, which have very high energies may, via large-angle collisions of both kinds, knock bulk ions up to energies far higher than the bulk average. These athermal ions will then be much more likely to fuse, either with other athermal particles or with particles in the bulk population, due to the fusion cross-section peaking at much higher energies than the bulk average. Fig. 6.5 shows a figure of a typical deuterium distribution in equilibrium at 2 keV, 5 keV and 10 keV, and also the fusion cross-section found in Appendix C. For the right conditions, the reaction will become self-sustaining, but determining the relevant physics and the regime in which this could possibly happen is a difficult problem, partly because of the need to include large-angle collisions. These chains cannot happen with only small-angle, multiple scattering alone; that only permits small transfers of energy. Large-angle collisions, in contrast, allow a few high energy particles to transfer a significant fraction of their energy in a single collision in addition to suffering smaller continuous losses. An extra interesting facet to this is that the onset of electron degeneracy at very high densities could mean more of the energy of fusion products goes into up-scattering bulk ions to become athermal ions, as the largest contribution to continuous stopping of fast particles comes from electrons. Electrons radiate via bremsstrahlung, have a short self-equilibration time (so that athermal populations do not persist), and have a long equilibration time with ions due to the electron to ion mass ratio. Energy which goes into electrons is therefore less useful for fusion reactions than energy going into ion species. Exploring electron degeneracy as a process to slow the absorption of energy by electrons [65] is, in part, the motivation of Chapter 4.

Evans [128] considers the energy loss of a fast deuteron ($E_d > 2.5$ MeV) in a hot deuterium plasma ($T_e > 10$ keV) in order to determine whether the addition of NES makes a significant difference to the energy deposition of deuterons up-scattered by large-angle collisions. Evans also introduces an explicit large-angle component of the Rutherford cross-section by splitting the Coulomb stopping into continuous and discrete parts, the former covering electron-ion interactions and ion-ion interactions with $\theta \leq \theta_c$ with θ_c

an arbitrary cut-off in angle. In a discretised spherical geometry fast particles are in an assumed Maxwellian background of electrons and ions. For collisions, ions are picked from the Maxwellian background to scatter with and, if both are athermal after the collision, they are both followed. There is continuous loss as a function of time or distance, and a probability for undergoing large-angle collisions with $\theta > \theta_{\mathrm{c}}$ which is handled using a Monte Carlo approach. NES is included, and deuterons are assumed to be composite bosons with a spin of 1 for the purposes of deuteron-deuteron scattering. $\ln\Lambda$ is modified so as not to overcount stopping powers: rather than values $\theta \in (\theta_{\min}, \pi)$, $\theta \in (\theta_{\min}, \theta_{\mathrm{c}})$ is taken. The Monte Carlo decision on whether to allow a large-angle collision is determined in a similar way to a subsequent work by Brueckner, Brysk and Janda (BBJ) [132], whose notation is adopted. Let $\sigma_{\mathrm{L}}(E)$ be the 'large-angle' cross-section for collisions only taking into account the range $\theta \in (\theta_{\mathrm{c}}, \pi)$, and $\mathrm{d}E/\mathrm{d}x$ be the continuous loss with the modified $\ln\Lambda$, i.e. taking into account $\theta \in (\theta_{\min}, \theta_c)$. The probability of i having a large-angle collision with a background ion j of density n_j while crossing a slab of plasma $\mathrm{d}x$ and slowing by $\mathrm{d}E$ is

$$\sigma_{\mathrm{L}} n_j \mathrm{d}x = \sigma_{\mathrm{L}} n_j \left(\frac{\mathrm{d}E}{\mathrm{d}x}\right)^{-1} \mathrm{d}E \equiv -L(E)\mathrm{d}E$$

The probability of having no large-angle interaction in this infinitesimal slab is $1 + L(E)\mathrm{d}E$. If $S(E, E')$ is the probability of j losing energy from E to E' by continuous loss only, and subsequent crossings are independent, then the probability for $E \longrightarrow E' + \mathrm{d}E'$ can be found iteratively; $S(E, E' + \mathrm{d}E') = (1 + L(E')\mathrm{d}E')S(E, E')$. Re-arranging gives,

$$\lim_{\mathrm{d}E' \longrightarrow 0} \frac{S(E, E' + \mathrm{d}E') - S(E, E')}{\mathrm{d}E'} = L(E')S(E, E')$$

integrating this gives $S(E, E') = \displaystyle\int_E^{E'} L(E'')S(E, E'')\mathrm{d}E''$, which has solution

$$S(E, E') = \exp\left[-\int_{E'}^{E} L(E'')\mathrm{d}E''\right] \tag{6.14}$$

Note that this satisfies the property that $S(E_0, E_n) = \displaystyle\prod_{0 \le m < n} S(E_m, E_{m+1}) \; \forall \; m, n \in \mathbb{Z}$. Evans uses equation (6.14) to determine whether a collision occurs or not over an energy interval, and, in a similar manner to BBJ, defines the probability for a large-angle collision to scatter i from E to E' as

$$P(E, E'|\text{collision at } E)\mathrm{d}E' = \frac{\mathrm{d}\sigma_L(E, E')}{\mathrm{d}E'} \frac{\mathrm{d}E'}{\sigma_L(E)}$$

Analogous probabilities exist for NES. Using this formulation, Evans finds large differ-

ences in the stopping of fast (E_d∼4.5 MeV) deuterium ions between using continuous stopping versus large energy change Coulomb collisions and NES but only for $T_e > 10$ keV at liquid density. The general effect is to increase the overall stopping power.

Before adopting the above system of equations, Brueckner and Brysk [133] derived probabilities for stopping via large-angle collisions based on averaging the nuclear interaction and incorporating it into a continuous stopping power of the form $\mathrm{d}E/\mathrm{d}x$. Although the BBJ article uses a more advanced model, the original Brueckner and Brysk formulation raises an interesting possibility when considering the slowing of fast particles; that a fast particle could, in the course of its slowing, knock-on a sufficient number of ions to produce an ever-growing chain of fusion reactions, products and knock-ons. The specific example of an α particle slowing in a deuterium-tritium plasma is used, assuming a cold background of deuterium and tritium ions from which recoils could be produced. The results show that, dependent upon electron temperature, the original α gives rise to as many as 0.2 additional athermal fusion reactions with $n_e = 10^{33}$ m^{-3}. This ignored the discrete nature of NES, neutrons, and the background deuterium and tritium temperatures. It also ignored secondary knock-ons, particles two collisions removed from the original fusion created α particles. This increase in fusion reactivity cannot be predicted using small-angle methods, as no high energy recoils are created and the bulk remains cold.

BBJ [132] extended the analysis of Brueckner and Brysk considerably by considering discrete NES, neutrons, and defining a system of probabilities for energy loss (via any mechanism), for recoil generation and for reaction. Iteration over many discrete collisions, with continuous loss in-between, gives rise to Volterra equations (defined in Appendix A) of the form

$$P(E, E') = P^{(1)}(E, E') + \int_{E''}^{E} P^{(1)}(E, E'')P(E'', E')\mathrm{d}E''$$

where the superscript denotes the probability for one discrete collision along with continuous loss as described by equation (6.14). The limitations of this system of equations are that it assumes the athermal population to be a perturbation to an equilibrium distribution, and that there is again a cut-off, in energy rather than angle, which modifies the integration limits and $\ln \Lambda$. The cut-off is determined in this case by computational limitations, with the switch over to continuous loss taking place for changes in energy, ϵ, less than the size of one unit of the computational energy grid. There is an implicit assumption that multiple scattering may be approximated by binary collisions to arbitrary small values of $\epsilon = E - E'$ within computational limits. The most interesting result is on athermal chains with neutrons, which finds that an initial fusion created neutron (ignoring thermal broadening) produces an average of 1.05 α particles as a product of all of the

reactions of its recoils before they thermalise. This is for $T_e = 30$ keV and $n_e = 10^{33}$ m^{-3}. This is not a self-consistent calculation as it depends upon the athermal population of ions being small relative to the bulk population. However, these perturbations "could push an otherwise submarginal plasma past the ignition point".

Other authors [134, 135, 136] created a similar model but in the form of a full balance equation for the athermal particles resulting from injecting a flux of particles of species k at energy E_0. The balance is found by equating terms accounting for absorption and scattering out of the energy range $(E, E + \mathrm{d}E)$, down-scattering and up-scattering into the energy interval, creation of particles by reactions, and creation of particles by external sources for species i as a result of the injection of k. The assumptions are that there is a bulk cold plasma, that the athermal population has reached a steady state, and that only external sources contribute to the creation of particles in the energy interval $(E, E+\mathrm{d}E)$. This gives, for flux $\phi_i(E) = n_i(E)v_i$,

$$\begin{aligned}\phi_i(E)\sum_j n_j \int \sigma_{ij}(E, E'')\mathrm{d}E'' - \sum_j n_j \int \phi_i(E')\sigma_{ij}(E', E)\mathrm{d}E' \\ = \frac{\partial}{\partial E}\left\{\phi_i(E)\left[\left(-\frac{\mathrm{d}E}{\mathrm{d}x}\right)_{ie} + \sum_j \frac{n_j}{n}\left(-\frac{\mathrm{d}E}{\mathrm{d}x}\right)_{ij}\right]\right\} \\ + n_i \sum_j \int \phi_j(E')\sigma_{ji}(E', E' - E)\mathrm{d}E' + \delta_{ik}\delta(E - E_0) \quad (6.15)\end{aligned}$$

The first term is scattering out of the energy interval, the second is those down-scattered into the interval, and $n = \sum n_i$. Integration limits are set by kinematics. The first term on the right hand side represents continuous loss, which has been removed from the first term on the left hand side and only covers energy exchanges such that $\epsilon/E \ll 1$ with ϵ smaller than a computational energy grid unit, and again the assumption that multiple scattering and binary collisions are completely interchangeable. Though not explicitly clear, $\ln\Lambda$ would need to be modified in the continuous loss terms to avoid overestimating stopping. The last term represents the external source, and the remaining term is ions created by recoil from other particles. In the final paper in the series, the plasma is considered to be cold for the purposes of scattering but thermal for the continuous loss terms, and heating of the bulk by athermal ions is not considered. The flux is calculated for energies from 15.7 keV upwards, and a chain-reaction in a cold deuterium-tritium plasma is expected at ion densities greater than 8.4×10^{33} m^{-3}, with neutrons the main contributor to the chains.

Equation (6.15), even though it is simplified from the full problem, is difficult to solve self-consistently as all of the particle fluxes are coupled both to themselves, and to each other.

In [135], a simpler 'multi-group' model is detailed which, though requiring an initial guess for the form of the flux, is more amenable to numerical solution. The assumption that a steady state is reached is used, even if the equation is only applied for the 'first generation' of particles. Since different particles take different times to slow down, it is not clear that the first generation is a useful concept. To calculate the degree of criticality, $\phi_i(E)$ is solved in the first generation, and the source of particles h in the second generation is given by

$$S_{hk} = \sum_i \sum_j n_j \int \phi_i(E)\sigma_{ijh}(E)\mathrm{d}E$$

where σ_{ijh} represents the cross-section for production of h by i and j, and the k signifies that it was the injection of particles of type k which originally drove the athermal distribution function. The highest eigenvalue of the matrix with components S_{hk} is taken as being the multiplicative factor for generation-to-generation production of particles and summed geometrically, after Brueckner and Brysk [133], to find the result of an infinitely long chain of generations. This assumes both that the chain can be infinitely long, and that no change to the bulk plasma properties occurs during the generation of the chain of fast particles. With these assumptions, an athermal chain-reaction can proceed at densities close to $\sim 5 \times 10^{33}$ m^{-3}, compared to expected ICF peak hot spot densities of $\sim 10^{31}$ m^{-3} [23].

The various attempts to understand critical athermal fusion reactions imply that large-angle collisions, NES, neutrons, and even spin are all factors to include in models. Of these, the inclusion of neutrons appears to be the most important. Averaging out the effect of NES into a continuous stopping term can increase the number of fusion reactions compared to discrete NES. This is because continuous slowing via NES takes an energetic particle through the entire energy range, while discrete collisions lead to large jumps in energy space, potentially missing out sensitive regions where recoils are likely to be created with energies corresponding to the peak of the fusion cross-section (see Fig. 6.5). For this reason, discrete NES is more realistic. The issue of a cut-off between continuous loss terms and large energy transfer terms is ever present too, with the consensus being to allow $\epsilon \longrightarrow 0$ to within the capabilities of computation. This effectively assumes that as many as possible of the collisions are pure Rutherford scattering, which is a strong assumption. The models also generally use a cold background. As stopping powers are dependent on temperature, including a thermal bulk is necessary.

These models are all perturbative or assume a steady state, and this combined with them being relatively complicated from a computational point of view makes them unattractive for solving the full problem self-consistently. However, the ideas behind athermal fusion are worth pursuing because, even though the densities required by previous work currently

seem unrealistic, possible changes to ignition conditions are of great interest to ICF.

6.2.2 Driving non-Maxwellian distributions

The athermal populations in §6.2.1 are considered separately from the bulk population of ions, or employ assumptions about the bulk. The effects of large-angle collisions on models including the entire distribution function are considered. Much of the work done in this area has focused on magnetic confinement fusion (MCF), particularly with respect to collisions between beam-injected ions and bulk distribution ions.

Stroud and Gilligan [137] examined large-angle Coulomb collisions between an injected beam and a background in the context of MCF, finding that non-Maxwellians are driven. The enhancement in reactivity found is greater with a thermal, rather than cold, background population. High-energy tails on Maxwellian distribution functions solely from NES in the absence of any beam-injection, have also been identified, both using an averaged model for NES [138, 139, 140, 141, 142] and using the discrete model of equation (6.15) [143]. The lowering of the ignition conditions NES causes is for advanced fuels and high electron temperatures, $T_e \geq 30$ keV. Kamelander devised a hybrid VFP-NES equation to consider the effects of NES on ICF, finding that the cross-section for $d-d$ scattering was greatly modified for $E_d > 1$ MeV [144]. The method does not include large-angle Coulomb collisions due to the stopping power being handled by the VFP equation, equation (2.16), and a similar technique employed by Andrade and Hale [145] notes that the inclusion of NES in a Fokker-Planck formulation makes VFP sensitive to θ_c. Andrade and Hale show, in their Figs. 1–4, that scattering cross-sections taking into account NES for several combinations of d, t and α ions are as much two orders of magnitude greater with ∼MeV particle energies than Rutherford scattering alone would predict.

Ryutov [146], and Helander [147], note that tails on distribution functions are an inherent property of plasmas. By taking the background to be cold, ignoring the thermal broadening of fusion created α particles, and ignoring any $Z \neq 1$ drag on α particles, a distribution function for the high energy tail of ions of charge Z is given as

$$f_i(v_i) = \frac{16}{3\ln 2}\frac{n_\alpha n_i}{\nu_i v_i^6}\left(\frac{q_i e^2}{4\pi\epsilon_0}\right)^2 \frac{m_\alpha}{m_i^2(m_\alpha + m_i)} \begin{cases} 2 - \frac{3v_i}{v_i^*} + \left(\frac{v_i}{v_i^*}\right)^3, & v_i < v_i^*; \\ 0, & v_i > v_i^*; \end{cases} \tag{6.16}$$

where ν_i is the collision frequency due to electrons and ions and v_i^* is the maximum possible initial recoil speed of i after collision with α. The high energy tail is introduced as a possible diagnostic for the loss of particles to the walls of a tokomak.

The idea of using the high energy tail as an α diagnostic in MCF is extended in a paper by Gorini, Ballabio and Källne [148]. Assuming an average total cross-section of 1.1 barn in $\alpha + t$ and $\alpha + d$ NES, and using Monte Carlo techniques for the fusion reaction kinematics, a neutron spectrum due to the suprathermal population fusing is found. The work is refined in a subsequent paper [119] which considers thermally broadened fast ion sources and much more advanced NES cross-sections. Their treatment of the scattering cross-section includes spin, the Coulomb force, and the nuclear force with phase shifts up to $L = 3$. The inclusion of the higher order phase shifts means that the resonances in the $\alpha + t$ and $\alpha + d$ cross-sections are included. These resonances, in their Figs. 2–6, greatly modify the cross-section. Of particular note is the $\alpha + d$ resonance at $E_\alpha = 2.1$ MeV which doubles the total cross-section. In both cases, the NES total cross-section for α with d or t becomes approximately equal to, or greater than, the Coulomb total cross-section for collisions with α particles at $E_\alpha = 3.54$ MeV. The authors find it necessary to specify a cut-off in angle in order to carry out the cross-section calculations, and choose an arbitrary lower limit in the centre of mass frame of $\theta_{\min} = 20°$, equivalent to $b_c = 5.67 b_\perp$. The analysis of Ballabio *et al.* looks at the first generation of fast recoils from a thermally broadened source of fusion created α particles. The slowing of the α, d, and t particles is handled by a Vlasov-Fokker-Planck equation of the form

$$\frac{1}{v^2}\frac{\partial}{\partial v}\left(v^3 \nu_i f_i\right) = -Q_i \tag{6.17}$$

where Q_i is the source term of ions of type i. A distribution function based on the particles from this source slowing down is plotted, but the slowing neglects both NES and large-angle Coulomb collisions. This may not be a good approximation as the NES cross-section between a 1 MeV deuteron and a thermal deuteron is several times larger than for a 3.54 MeV α and a thermal deuteron [141]. Fisher [149] predicts the distribution functions of fast ions and neutron spectra using a similar source term approach, where the only slowing of created fast ions is due to small-angle collisions with electrons.

The first experimental observation of a non-Maxwellian distribution due to α particle knock-ons was seen in the JET (Joint European Torus) MCF reactor [150]. The flux of charged particles with energies $0.8 \leq E \leq 1.2$ MeV found by a neutral particle analyser was much larger than expected from the slowing of fusion created α particles. The flux appears before α particles created by fusion could reasonably be expected to have slowed to the energy range, whereas deuterons which have been knocked-up to high energies by large-angle collisions could appear in the flux immediately after fusion reactions begin. Subsequently, a neutron emission spectrum consistent with the athermal ion population predicted by Ballabio *et al.* was found on JET [151]. Though the model due to Ballabio,

Ryutov, and others, appears strong, some experimental evidence from JET suggests that it could substantially underestimate the size of the athermal ion population [152, 153] even when including all possible NES rates in a VFP equation. This may be an indication that the simplified slowing model in equation (6.17) is not sufficient, either because of the lack of large-angle Coulomb collisions, the averaging out of the NES interaction, or both.

Non-Maxwellian distributions in ICF have been considered in other work. Sherlock and Rose [154] found that a Monte Carlo approach [50] with only small-angles showed that no deviation to Maxwellian ion distributions is caused by the slowing of fusion produced α particles. A VFP model [155] including bremsstrahlung, inverse bremsstrahlung, Compton scattering, and light-ion fusion but no large-angle scattering or neutrons, showed little difference between Maxwellian averaged fusion rates and those taking into account the non-equilibrium distributions of fusion products. Some non-Maxwellian behaviour in tritium is driven by the $d + d \longrightarrow p\ (3\ \text{MeV}) + t\ (1\ \text{MeV})$ reaction, which has a 50% probability. Almost all of the non-equilibrium particles are products of fusion, and $\rho \sim 1000\ \text{g/cm}^{-3}$ corresponding to the relatively cold fuel surrounding the hotspot of an ICF capusle. The lack of large-angle collisions is acknowledged in both of these works.

6.2.3 ICF

Diagnosing conditions in the centre of an imploding NIF capsule presents real technical challenges. One of the most important parameters is the areal density, ρR, which must reach $\sim$1 g cm^{-2} in the fuel and $\sim$0.3 g cm^{-2} in the central hotspot of $T \sim 5$ keV for ignition to occur. Neutron time-of-flight (nTOF) spectrometers and a magnetic recoil spectrometer (MRS) are used to sample neutrons escaping from implosions and diagnose ρR and its asymmetries, ion temperature and yield. The calculation of $\rho R > 0.3$ g cm^{-2} depends upon the down-scattered neutron ratio (dsr), a measurement of

$$\text{dsr} = \frac{\text{no. neutrons with (10–12) MeV}}{\text{no. neutrons with (13–15) MeV}}$$

which is, to first order, proportional to ρR ignoring 3D geometrical effects [156]. Taking into account the geometry of NIF, the quantitative relationship is found to be [157, 158]

$$\rho R_{\text{total}}\left(\text{g cm}^{-2}\right) = (20.4 \pm 0.6) \times \text{dsr}$$
$$\rho R_{\text{fuel}}\left(\text{g cm}^{-2}\right) = (18.5 \pm 0.5) \times \text{dsr}$$

The dsr is primarily caused by fusion created neutrons being down-scattered by NES

collisions with thermal fuel ions. However, this process does not capture the entire possible spectrum of neutron energies as other processes can also contribute including the t(n,2n) and d(n,2n) break-up reactions, n+p and n+^{12}C elastic scattering, n+^{12}C inelastic scattering, and less probable fusion reactions [131]. The plastic ablator is the source of C and p ions. Large-angle scattering, including via Coulomb collisions [131], are a source of another, less probable, change to neutron spectra: tertiary neutrons [159]. Up-scattered fuel ions have a greater cross-section for fusion when colliding with bulk fuel ions due to the shape of the fusion cross-section, shown in Fig. 6.5. These produce so-called tertiary neutrons which can reach energies of up to 30 MeV, but kinematically can also be a source of neutrons in both of the energy ranges feeding into the dsr. This is in addition to their chance of knocking-on other fuel ions as they leave the dense fuel.

These knock-ons, and their effects on the dsr, are unimportant for low yields but could become a useful diagnostic as yields increase beyond 10^{15} neutrons, especially as they dominate spectra for energies > 16 MeV, and have consequences for measuring dsr. If many knock-ons are produced, then this area has much overlap with §6.2.2 and §6.2.1, and a fully consistent approach to understanding their propagation will be required. Recent results from NIF [160] with an unexpectedly large low energy neutron tail may be an indication that current models do not account for all of the athermal processes which occur, but the difficulty of taking account of various experimental response functions may also provide an explanation.

6.2.4 Summary

§6.2.2, §6.2.3, and §6.2.1 outline several reasons why large-angle collisions are of great interest; the possibility of athermal fusion chains, the driving of non-Maxwellian distributions, and diagnostically. Understanding exactly what conditions of temperature and density could produce critical fusion (with large-angle collisions) is a particular goal, as it could inform future fusion schemes. Less extreme distortions away from Maxwellian distributions, which are not critical, will still have consequences for fusion reactivity, down-scattered neutron ratios and equilibration time. Attempts to extend VFP models into the moderately coupled regime have produced results which are slightly different [48, 118] and it would be useful to determine which is more likely using a completely different approach.

However, the models currently used to study large-angle collisions are rarely self-consistent. They can be roughly grouped into two camps; flux models and VFP models. Flux models, such as in equation (6.15), model just the athermal part of the distribution function

under the assumption that the feedback on the bulk is negligible, even when the chain is critical. The introduction of an arbitrary cut-off in energy or scattering angle is also necessary to avoid the small-angle divergence. The cut-off is not chosen based on physical insight, but chosen based on computational limitations. Sivukhin's argument that particle interaction times may not be arbitrarily long imply that this is not true, because, in most cases, only partial scattering can occur between two particles before the scattering between other nearby particles takes over. The interactions of many fluxes of particles in these models are very difficult to solve, and the simplifications which yield results are not realistic - for instance the assumption that a steady state ($\partial n_i(E)/\partial t{=}0$) is established in equation (6.15). Even in a simplified form, the equations only yield the 'first-generation' of athermal particles, but given that stopping power has a strong energy dependency the results are not easily interpreted as a function of time.

VFP models inherently do not include Coulomb large-angle collisions. A cut-off in scattering angle is again an issue, implicitly for Coulomb collisions because of the VFP model or explicitly when including NES or integrating over cross-sections. The mixed model, used by Ballabio *et al.* [119] and others, uses a Maxwellian averaged α particle production spectrum and a numerically integrated source term for fast ions. This gives a good indication of the first-generation of fast ions given a θ_c, but the slowing of fast ions is handled with the VFP equation without any large-angle collisions, so the athermal distribution is likely to be incorrect, especially when considering time evolution. Experimental evidence that the Ballabio model underestimates the athermal ion population is consistent with this [152, 153].

The implication is that a more self-consistent model including large-angle collisions of both types is required. The most desirous features are thermal background populations, large-angle collisions applied to both slowing and creation of particles, no restriction on the size of perturbations to bulk distributions, time evolution, and a physically motivated approach to large-angle collisions.

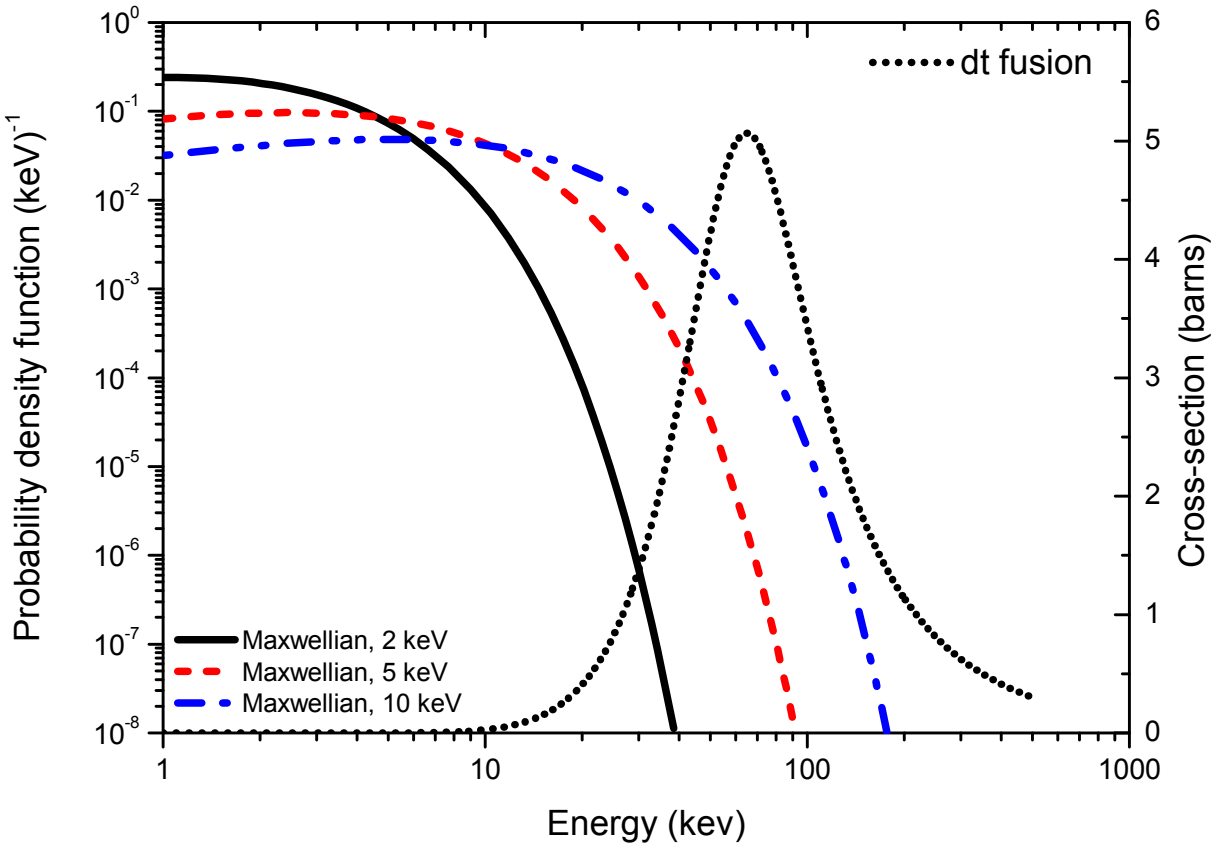

Figure 6.5: Deuterium Maxwellian distributions for three different temperatures alongside the deuterium-tritium cross-section for fusion.

Chapter 7

Discrete collisions with Monte Carlo

7.1 Motivation

The only Monte Carlo approach in Chapter 6 is that of Sherlock and Rose [154], which did not include discrete or large-angle collisions, nor did it explicitly conserve momentum. The Monte Carlo technique outlined in Chapter 3 has strengths relevant for large-angle scattering problems; it includes thermal broadening because energy and momentum are conserved, it allows self-consistent time evolution of distribution functions, and it is computationally simple. There are some issues. One is that the accuracy of the distribution functions scales as $1/\sqrt{N}$, another is that the code is 0D. The former problem depends upon using enough particles in simulations, while the latter is an acceptable compromise given the technique allows the problems associated with other models to be sidestepped. Useful comparisons highlighting the effects of discrete collisions can then be made against other 0D theories; particularly those of temperature equilibration and yield, as these have the greatest consequences for ICF. This Chapter presents an extension of Monte Carlo codes to include discrete and large-angle collisions.

7.2 Operation

To introduce discrete collisions, two different methods to generate angles given a cut-off in impact parameter of b_c are required; one for multiple scattering, and one for discrete scattering.

In multiple scattering, the Monte Carlo algorithm is much the same as described in Chapter 3 except that the derivation of $\langle\Theta^2\rangle$ has an impact parameter which is limited

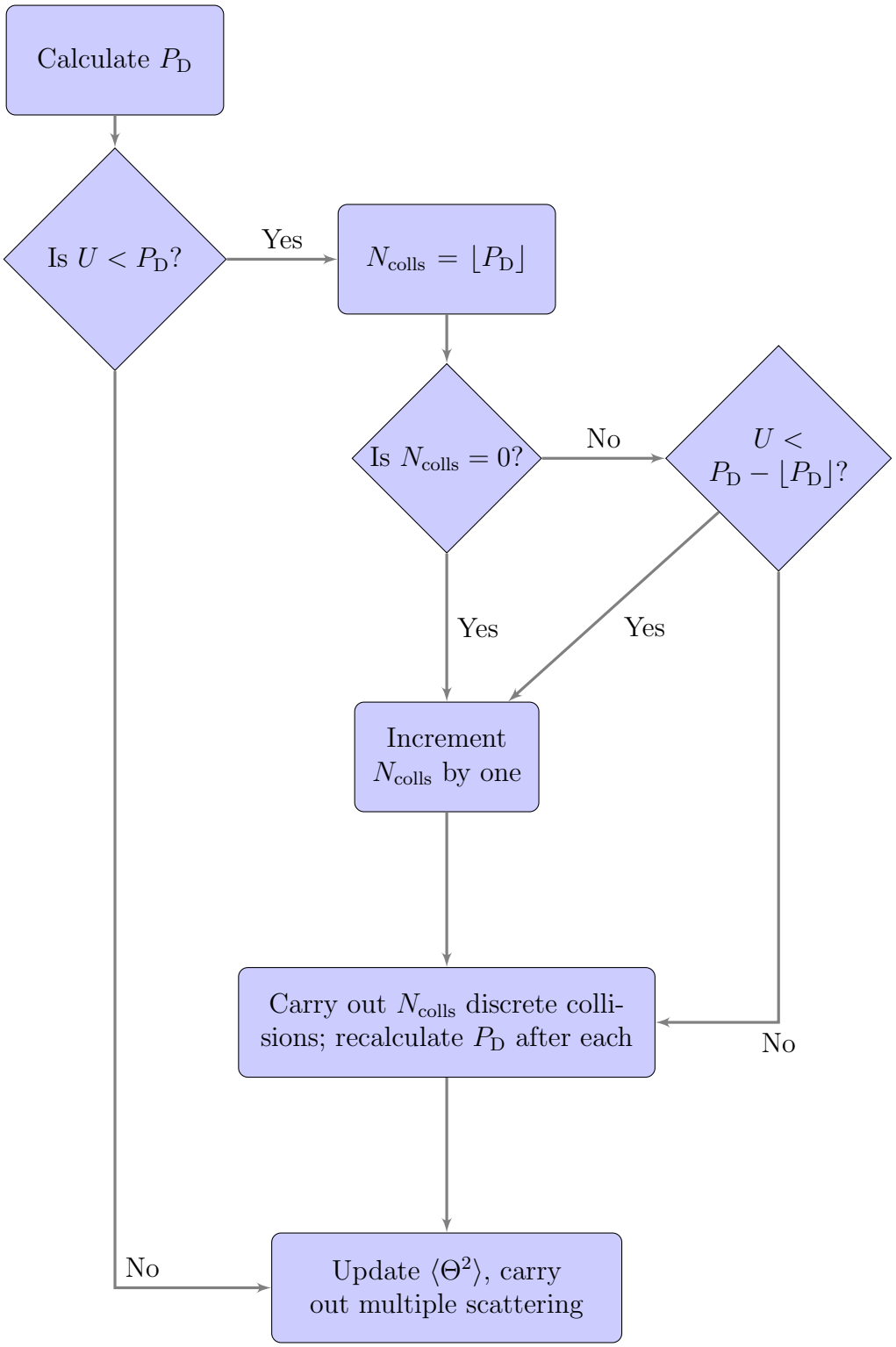

Figure 7.1: The scattering algorithm for two particles with multiple and discrete scattering. $U \sim \mathcal{U}(0, 1)$.

to $b \in (b_c, \lambda_{\mathrm{D}})$. As noted in Chapter 3, $\langle\Theta^2\rangle = 2P_{\sigma_1}$ with $\langle\Theta^2\rangle$ the variance of the distribution used to select the angles for small-angle scattering. So the variance modified to *only* include multiple, small-angle scattering with a cut-off at b_c is

$$\langle\Theta^2\rangle = nv_{ij}\Delta t 8\pi b_\perp^2 \ln\Lambda_{\mathrm{M}} = 2P_{\sigma_{1,\mathrm{M}}}$$

For discrete scattering, the differential cross-section is given by the Rutherford scattering formula

$$\frac{\mathrm{d}\sigma}{\mathrm{d}\theta} = \frac{\mathrm{d}\sigma}{\mathrm{d}\Omega}2\pi\sin\theta = \frac{\pi b_\perp^2}{2}\frac{\sin\theta}{\sin^4\left(\frac{\theta}{2}\right)}$$

and the full cross-section is

$$\sigma_{\mathrm{D}} = \frac{\pi b_\perp^2}{2}\int_{\theta_c}^{\pi}\frac{\sin\theta}{\sin^4\left(\frac{\theta}{2}\right)}d\theta = \pi b_\perp^2\left(\frac{1}{\sin^2(\frac{\theta_c}{2})} - 1\right) = \pi b_c^2$$

The species labels are implicit on θ_c, b_c and $b_\perp$. The probability of a discrete collision in a timestep Δt is $P_D = nv_{ij}\Delta t\pi b_c^2$. The discrete scattering probability density function *given that a discrete collision occurs* is defined as

$$\mathcal{P}_{\mathrm{D}}(\theta)\mathrm{d}\theta = \frac{1}{\sigma_{\mathrm{D}}}\frac{\mathrm{d}\sigma}{\mathrm{d}\theta}\mathrm{d}\theta$$

$\mathcal{C}_{\mathrm{D}}(x)$ is the cumulative density function for discrete collisions;

$$\mathcal{C}_{\mathrm{D}}(x) = \int_{\theta_c}^{x}\mathcal{P}_{\mathrm{D}}(\theta)\mathrm{d}\theta = -\frac{b_\perp^2}{b_c^2}\left[\frac{1}{\sin^2\left(\frac{\theta}{2}\right)}\right]_{\theta_c}^{x}$$

To find values of scattering angle, random numbers $U \sim \mathcal{U}(0,1)$ are generated and used with the inverse cumulative distribution function;

$$\theta = \mathcal{C}_{\mathrm{D}}^{-1}(U) = 2\sin^{-1}\left[\left(\frac{b_\perp^2}{b_\perp^2 + b_c^2(1-U)}\right)^{1/2}\right]$$

with the sign taken to be positive or negative with equal probability. Note that $\mathcal{C}_{\mathrm{D}}^{-1}(1) = \pi$ and $\mathcal{C}_{\mathrm{D}}^{-1}(0) = \theta_c$.

A schematic of the operation of the full scattering algorithm for two particles is shown in Fig. 7.1. If the probability of a discrete collision identically vanishes, i.e. $P_{\mathrm{D}} \equiv 0$, then the algorithm automatically reverts to multiple scattering only. It is possible that $P_{\mathrm{D}} > 1$, in which case $\lfloor P_{\mathrm{D}} \rfloor$ collisions are carried out with an extra collision if $U < P_{\mathrm{D}} - \lfloor P_{\mathrm{D}} \rfloor$. U is not being re-used as at least one collision is assured if $P_{\mathrm{D}} > 1$, and the random

number comparison is only applied to the non-integer portion of P_D in any situation. These measures ensure that the number of discrete collisions is insensitive to Δt, for Δt sufficiently small.

Further evidence of the independence of timestep can be seen in Figs. 7.2 and 7.4 which show an isotropic beam of fusion created α particles slowing down in an equimolar deuterium-tritium background for $b_c = b_\perp$ and $b_c = b_\phi$ respectively. The multiple scattering algorithm is turned off in these simulations, so any change is due to the large-angle algorithm alone. The two values of timestep, Δt, and $\Delta t/5$, show little difference in either the slowing of the beam or the distribution function of the background deuterium, shown in Figs. 7.3 and 7.5. This scenario would show up any discrepancy due to Δt. The temperatures are the same for each species for different Δt to better than 1%. The distribution functions for deuterium are numerically slightly different. This is due to the random nature of Monte Carlo, and is only noticeable in regions where the statistics are poor. It causes the stratification effect particularly evident in Fig. 7.5 despite using a total of 3 million simulation particles. The cumulative distribution functions are not noticeably different as the tail contributes a relatively small amount of the total probability density. Changing Δt with both types of collision enabled, multiple and discrete, also has no effect on the results obtained.

What constitutes 'sufficiently small' can be quite restrictive for discrete collisions, depending on the value of b_c. The discrete collision frequency between i and j is

$$\nu_{ij}^\mathrm{D} = \min\left\{n_i, n_j\right\} v_{ij} \pi b_c^2$$

where the species labels on b_c are suppressed. This gives $\Delta t = 1/10\nu_\mathrm{D}$ as the computational timestep appropriate for discrete collisions. Its value relative to the timescales for small-angle collisions depends upon the model used. The minimum timestep across all relevant collision frequencies (from discrete or multiple scattering) is always used.

Using $b_c = b_\perp$, $P_\mathrm{D} \propto v_{ij}^{-3}$, and there is a possibility that $P_\mathrm{D} \gg 1$ even with a physically sensible value of Δt. For fixed b_c, $P_\mathrm{D} \propto v_{ij}$ and $P_\mathrm{D} \gg 1$ may still happen. If, for any b_c, $P_\mathrm{D} \gg 1$ the discrete scattering is undertaken multiple times up to a maximum limit. These situations are analogous to the multiple scattering case of generating $|\theta| > \pi$, and, to avoid unnecessary looping of the algorithm when $P_\mathrm{D} \gg 1$, the Takizuka and Abe approach of using a $\theta \sim \mathcal{U}(0, \pi)$ is adopted.

For three particles combined in three pairs, $\langle\Theta^2\rangle/2$ is used for collisions instead of $\langle\Theta^2\rangle$ for multiple collisions (as in Chapter 3). For discrete collisions, the analogous probability is P_D so three particles combined in three pairs have a probability for a discrete collision of $P_\mathrm{D}/2$ between the pairs.

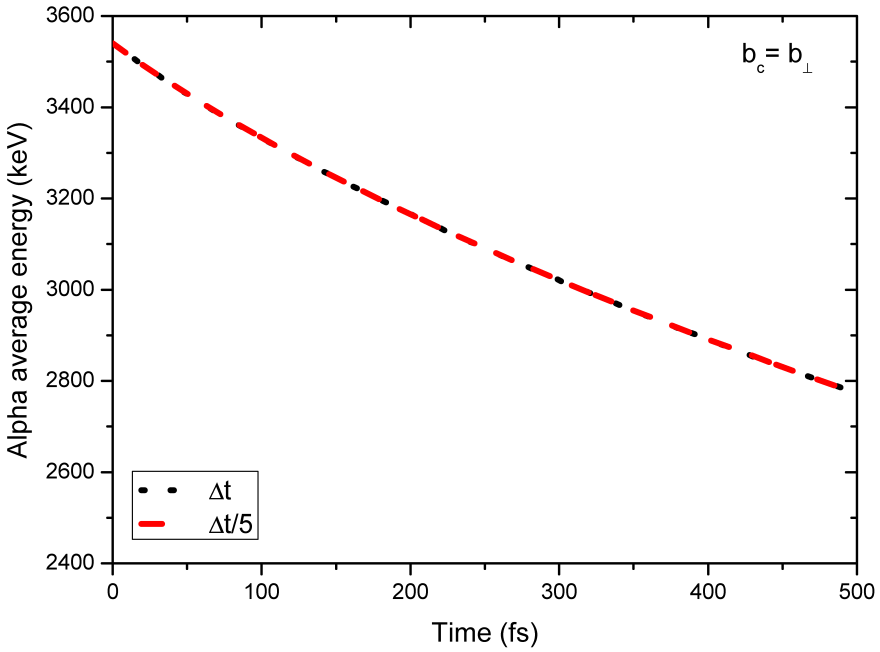

Figure 7.2: α slowing using $b_c = b_\perp$ with different timesteps.

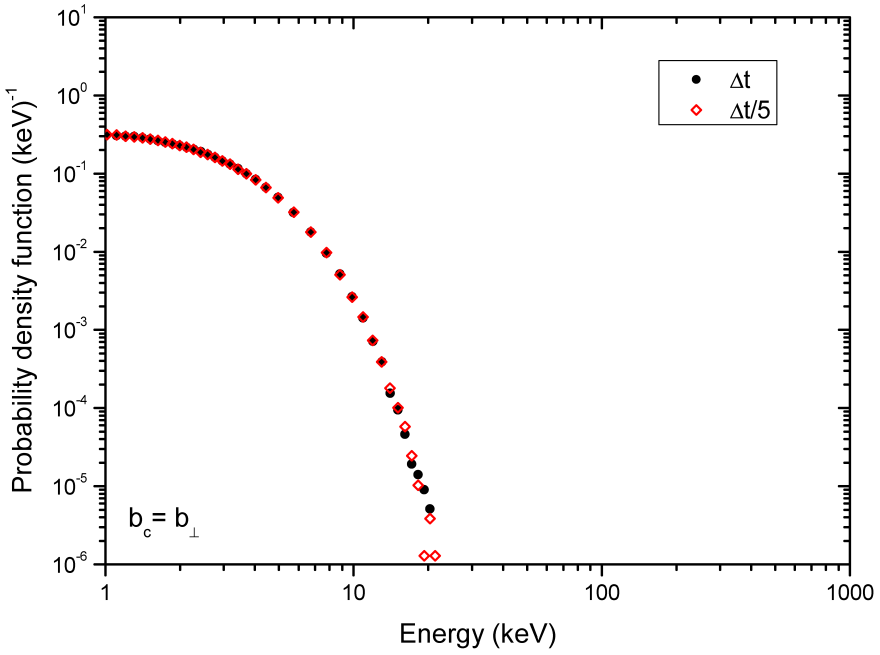

Figure 7.3: Distribution function of deuterium with $b_c = b_\perp$ at 500 fs.

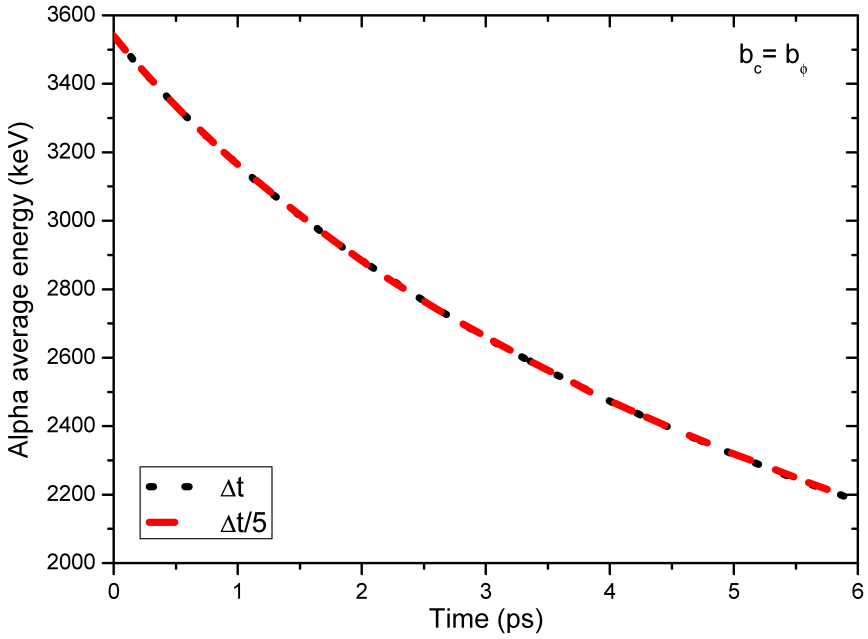

Figure 7.4: α slowing using $b_c = b_\phi$ with different timesteps.

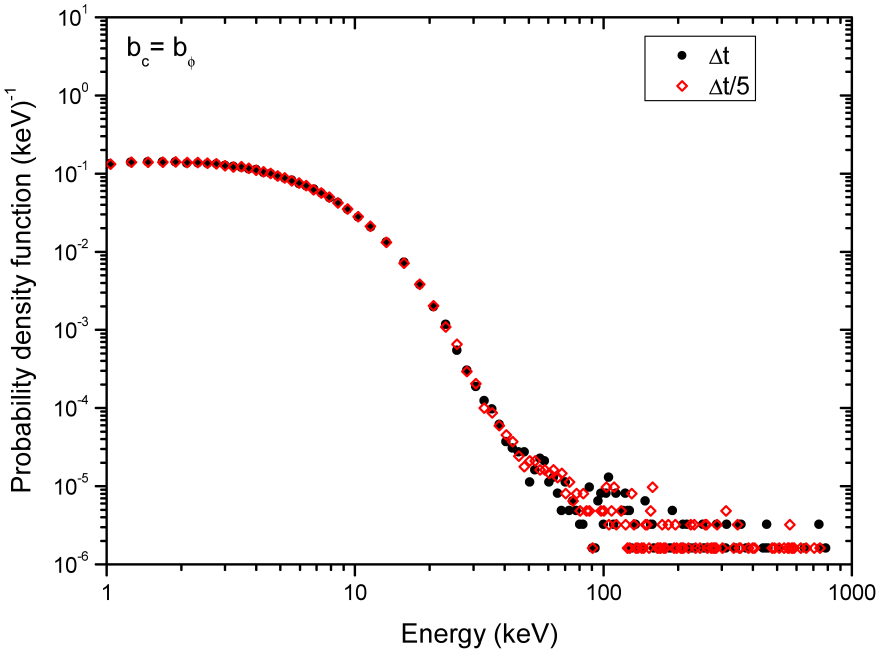

Figure 7.5: Distribution function of deuterium with $b_c = b_\phi$ at 6.65 ps.

The original Monte Carlo scattering algorithm [50] has $\mathcal{O}(N)$ operations for N computational particles. This is based on the statistical argument briefly outlined in Chapter 3. That statistical argument is not true for discrete collisions using the Rutherford cross-section. If *all* collisions, on any length scale, were dealt with as a pair particle interaction (such as in pure molecular dynamics simulations), it would be necessary to carry out N^2 collisions for N computational particles. This is not the case for the discrete algorithm, because the number of distinct collisions of both types is $(1+P_{\mathrm{D}})N$ for N computational particles (with the extra factor relative to multiple scattering only due to the inclusion of the discrete collisions). $P_{\mathrm{D}} = nv_{ij}\Delta t\pi b_c^2$ does not depend on the number of computational particles and so is not $\mathcal{O}(N)$, which means that the algorithm still requires $(1+P_{\mathrm{D}})N = \mathcal{O}(N)$ operations rather than $\mathcal{O}(N^2)$. The assumption that discrete collisions may only happen with impact parameters of $b \leq b_c$ severely restricts the number of pairs of particles which can have discrete collisions, and it is this assumption which restricts the order of P_{D}.

7.3 Results

7.3.1 Comparing multiple and discrete scattering

Fig. 7.6 shows the effects of different values of b_c for millions of samples (per individual plot) of the same deuterium-tritium collision, with parameters in Table 7.1. A longer than normal timestep is used to better show the features of the probability distribution function. Each count is a scattering event, so even if no discrete collision occurs it is counted as a $\theta = 0$ scattering event, which is why there is an anomalous point at $\theta = 0$ for all plots. If successive discrete collisions occur, they are counted separately. $b_c = 0$ corresponds to the multiple scattering only case, and the distribution is a Gaussian with an anomalous data point from all of the $\theta = 0$ 'large-angle' collisions. With $b_c \neq 0$, the discrete scattering begins to occur but, for $b_c < b_\perp$, only at $\theta > \pi/2$ and in rare events. Increasing b_c increases the probability of a discrete collision, as expected, but the probability density is added progressively toward the centre rather than at the extreme wings of the distribution. This means that the change to the particle energies and momenta will be less extreme. In the extreme $b_c = \lambda_{\mathrm{D}}/10$ case, the discrete and multiple scattering distributions overlap.

That some values of scattering angle are not obtainable with some values of b_c may appear unphysical but both of the distributions are dependent on timestep. Longer timesteps broaden the multiple scattering distribution, but in practice Δt must be kept

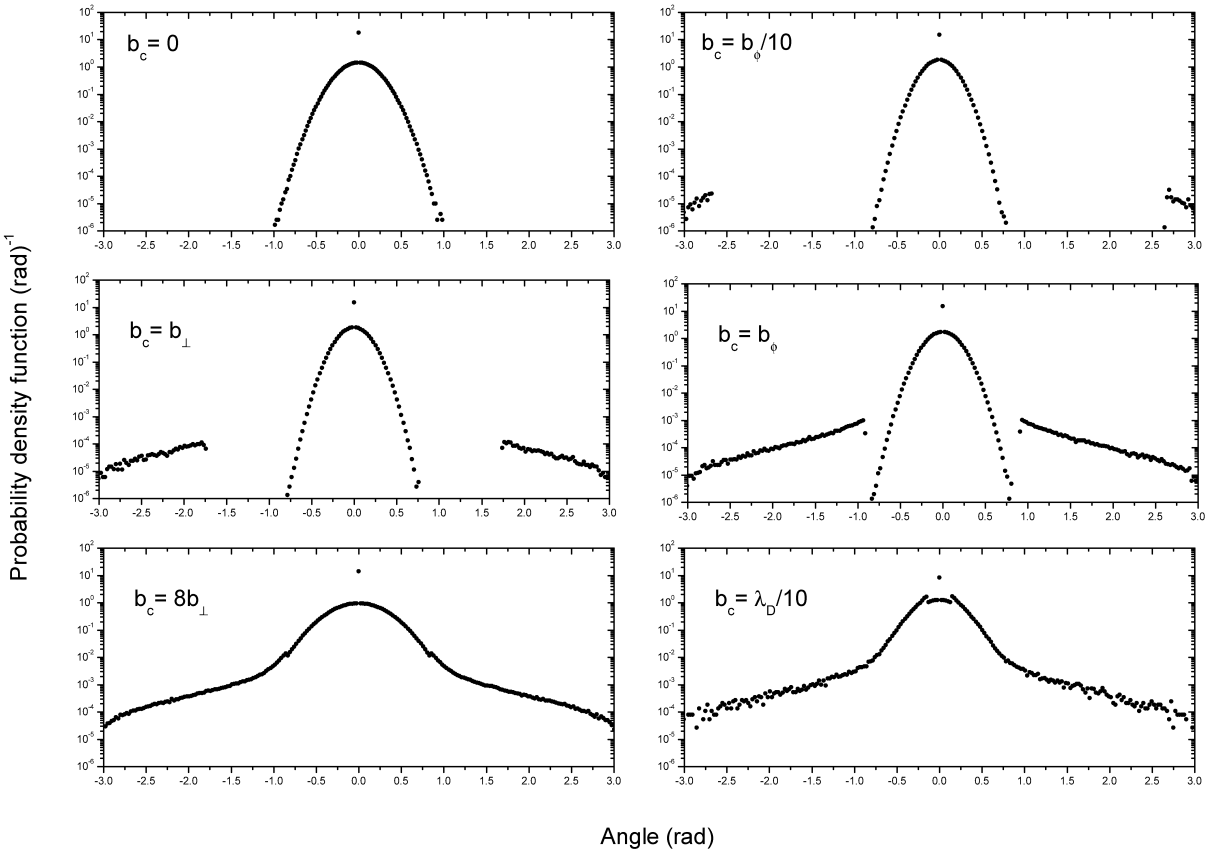

Figure 7.6: The probability distribution function of scattering angles from millions of samples of the same deuterium-tritium collision with particle energies of 2 keV each and plots in order of increasing b_c. The exact parameters are shown in Table 7.1.

Quantity	Value
n_d, n_t	2×10^{30} m^{-3}
E_d, E_t	2 keV
λ_D	1.2×10^{-10} m
$b_\perp$	2.8×10^{-13} m
b_ϕ	6.9×10^{-13} m
Δt	1.4×10^{-15} s

Table 7.1: Values of parameters from Fig. 7.6.

small to keep simulations physical and this restricts the horizontal extent of the multiple scattering portion of the distribution. So the apparent inability to reach some values in angle is actually due to the timestep, and the cumulative effect of subsequent multiple scattering will effectively broaden the distribution. Changing timestep has no effect on the breadth of the distribution due to discrete collisions, as this is determined solely by θ_c, but it does alter the height of the distribution - lowering it for shorter timesteps. This example is for the same particles repeatedly collided; averaging over many particles drawn from Maxwellian distributions will naturally smooth out the clean cut-off due to different values of $b_\perp$ for each collision.

Fig. 7.6 implies that discrete collisions will decrease timescales of exchange of energy and momentum as b_c increases, but also suggest that *smaller* (but non-zero) b_c will force distributions further away from equilibrium. This is because small b_c corresponds to a large θ_c and also a relatively small chance of a discrete collision. So bulk distribution particles may be up-scattered by a rare discrete collision with another, more energetic particle such that the final energy is much greater than the average of the bulk distribution. It will have a similarly small chance of a second discrete collision, so that it cannot easily return to the bulk though it will eventually via multiple scattering. This means that there is an optimal value of b_c for producing non-Maxwellian distributions. In general, a small (large) rate out of scattering out of the bulk means a small (large) rate of scattering back to the bulk: the size of any distortion away from a Maxwellian is self-limiting.

The consequences for scattering of using the physically motivated $b_c = b_\phi$ model are explored. Realistic values of b_ϕ for a range of temperatures and densities are shown in Fig. 6.2. Given that equilibration times and departure from Maxwellians are dependent on $\theta_c(b_\phi)$, it is interesting to examine its values over a wide range of physical conditions, as shown in Fig. 7.7 for an equimolar deuterium-tritium plasma. Also of interest is the modification to the Coulomb logarithm. Using the general change in logarithm for a cut-off of b_c of

$$\ln \Lambda_\mathrm{M} = \frac{1}{2} \ln \left(\frac{b_\perp^2 + \lambda_\mathrm{D}^2}{b_\perp^2 + b_c^2} \right) \tag{7.1}$$

$$\ln \Lambda_\mathrm{D} = \frac{1}{2} \ln \left(\frac{b_\perp^2 + b_c^2}{b_\perp^2} \right) \tag{7.2}$$

values of $\ln \Lambda_\mathrm{D} / \left(\ln \Lambda_\mathrm{D} + \ln \Lambda_\mathrm{M} \right)$ using $b_c = b_\phi$ are plotted in Fig. 7.8.

Fig. 7.7 and Fig. 7.8 have an interesting conclusion; that large-angle collisions, and the relative importance of discrete collisions, occur in two opposite areas of temperature space using the $b_c = b_\phi$ model. Large-angle collisions are relatively independent of density, with a slight preference for higher densities. This behaviour is because large-angle

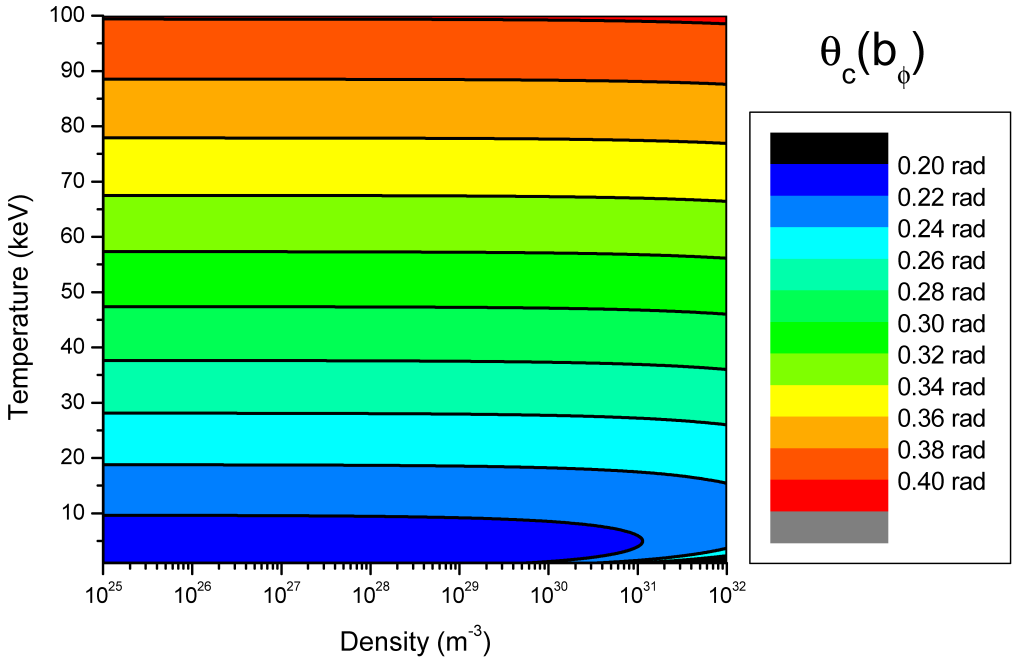

Figure 7.7: $\theta_c\,(b_c = b_\phi)$ for an equimolar deuterium-tritium plasma.

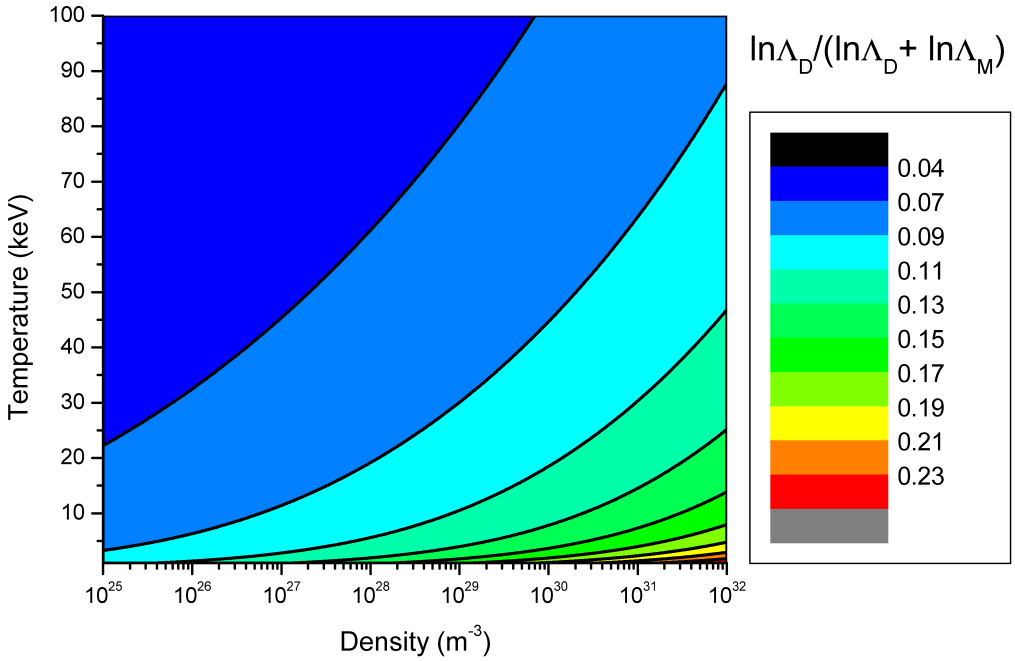

Figure 7.8: Ratio of Coulomb logarithms using $b_c = b_\phi$ for an equimolar deuterium-tritium plasma.

collisions require $b_c \approx b_\perp$ but the likelihood of discrete collisions relative to multiple collisions requires $b_c \gg b_\perp$. Very few discrete collisions occur for higher temperatures and low densities due to smaller values of b_ϕ, and many more occur at high density and at temperatures relevant to fusion though with smaller average θ_c. However, θ_c in Fig. 7.7 is the average over a Maxwellian so hides that some collisions, with sufficiently large $b_\perp$, will be large-angle.

The consequences of changing b_c for temperature equilibration are shown in Fig. 7.9 for deuterium and electrons. The Landau-Spitzer and $b_c = 0$ rates are, as expected, very similar to those shown in Fig. 3.9 of §3.3. Note that despite $b_\phi(d,t) > b_\perp(d,t)$ in Fig. 6.3, in general $b_\perp(e,i) > b_\phi(e,i)$ with i an arbitrary ion. b_ϕ has a very similar solution for all possible pairs of species while $b_\perp$ varies depending on temperature. If $(T_e/2T_i)\,/(m_e/m_i + 1) < 1$, which is true for ions and electrons in equilibrium, then $b_\perp(e,i) > b_\perp(i,i)$ and often $b_\perp(e,i) > b_\phi(e,i)$ even though $b_\phi(i,i) > b_\perp(i,i)$. The faster equilibration times in Fig. 7.9 are correlated with larger values of b_c. The excess kurtosis (not shown) has no consistent positive or negative trend, and it appears that the distribution functions of both species remain Maxwellian. Table 7.2 lists the parameters used, and Figs. 7.7 and 7.8 imply that this is a regime in which there is a good chance of discrete collisions but where the collisions are themselves not very large in angle, which is consistent with no excess kurtosis but faster equilibration times. Seen as though $T_{d,0} > T_{e,0}$ and electrons have a short self-equilibration time, it is not a situation in which it is likely for non-Maxwellians to develop. This leads to an important and interesting result; the large decrease in equilibration time with increasing b_c cannot be attributed to distortions of the distribution functions and must be solely due to the increased rates of energy transfer from discrete collisions.

The equilibration time relative to $b_c = 0$ is shorter by roughly a third for $b_c = b_\perp$, and half for $b_c = b_\phi$. That such large differences in equilibration time are found is surprising, especially as they exist even with the conservative (relative to other authors - see §6.1) value of $b_c = b_\phi$. It should be re-iterated that $\ln\Lambda$ becomes $\ln\Lambda_\mathrm{M}$ (see equation (7.1)) for the $b_c \neq 0$ cases, so the multiple scattering contribution to equilibration is reduced.

Quantity	Value
n_d, n_e	2×10^{30} m^{-3}
T_d	1 keV
T_e	0.5 keV

Table 7.2: Values of parameters used in Fig. 7.9.

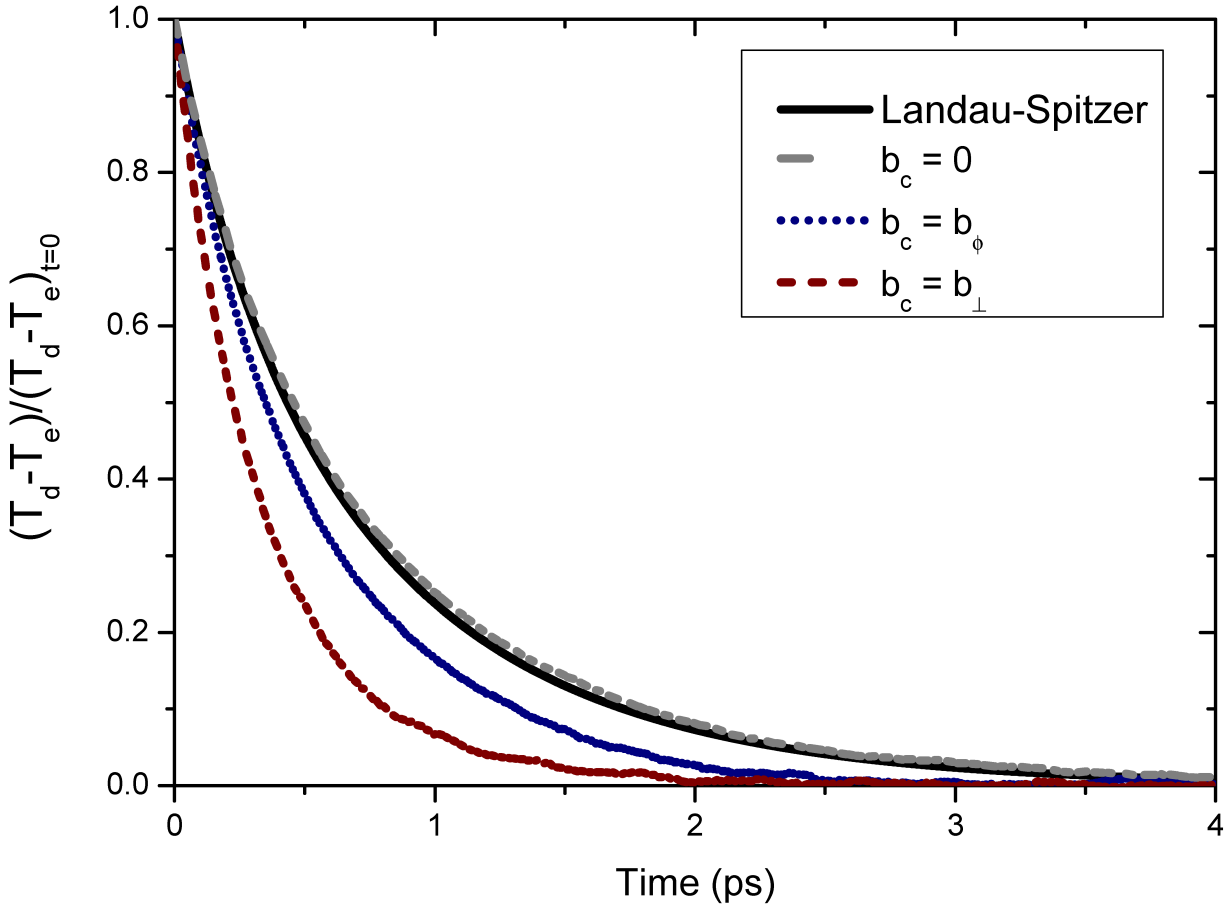

Figure 7.9: Temperature equilibration between electrons and deuterium with different values of b_c.

Given this, that overall equilibration times should be reduced is not immediately obvious or predictable. This temperature equilibration simulation lends support to other work [48] that energy losses are faster in moderately coupled plasmas than small-angle collisions alone would allow.

7.3.2 Driving non-Maxwellian distributions in ICF

Sherlock and Rose looked for non-Maxwellian distributions being driven by fusion created α particles using a small-angle Monte Carlo approach with a background electron fluid [154]. The parameters are shown in Table 7.3, and are those specified for the hotspot in a perfect deuterium-tritium implosion [23] (see Appendix D for a Table of ICF implosion parameters). The temperature used by Sherlock and Rose is relatively cold; it is expected that the hotspot will reach $T \sim 4 - 5$ keV for self-sustaining burn. The conditions are reproduced in simulations using the code described in §7.2 with the exception that there is creation of α particles and the electrons are fully kinetic. The yield is shown in Fig. 7.10, and there is little difference between different values of b_c. There is not enough energy from fusion to create a burn wave, so the number of fusion reactions increases only linearly with time.

A similar simulation, with a higher starting temperature of $T_d = T_t = T_e = 5$ keV, is shown in Figs. 7.11, 7.12, and 7.18, which are the temperature, yield, and excess kurtosis respectively over time of the three values of b_c. The expected 'burn' time for an ICF capsule filled with deuterium and tritium is ∼18 ps (see Appendix D), but the macroscopic parameters of a fully burning plasma may change over this timescale, and so the simulation is only run for ∼10 ps. Loss mechanisms, such as bremsstrahlung emission, and α particle escape, are ignored. Also omitted are the less likely fusion reactions involving $d + d$ and $t + t$.

The temperature, here taken to be $2\langle E\rangle/3$, shows great variation over the three models and is shown in Fig. 7.11. There is no loss mechanism included, so the increased yield of

Quantity	Value
$\rho_d = m_d n_d$	0.5×300 g cm^{-3}
$n_d, n_t, n_{dt}/2$	4.52×10^{31} m^{-3}
T_d, T_t	2 keV
n_α	$n_{dt}/10^3$, or $n_{dt}/10$

Table 7.3: Values of parameters used by Sherlock and Rose [154].

the $b_c = b_\perp$ model feeds straight back onto the temperature of the electrons, deuterium, and tritium. Fig. 7.12 shows the yield, which is very similar at early times, when all species except the αs are in equilibrium. As α particles are created, energy is transferred firstly to electrons, which can be seen in Fig. 7.11 for $b_c = 0$ and $b_c = b_\phi$. In the $b_\perp$ simulation, the ions are heated at a very similar rate to the electrons up until $t = 6$ ps, and an increased yield relative to $b_c = b_\phi$ and $b_c = 0$ becomes apparent as early as $t = 1.5$ ps.

Given Fig. 6.3, which shows that $b_\phi/b_\perp > 1$ for deuterium and tritium for a wide range of temperatures and densities, it is surprising that the largest difference relative to $b_c = 0$ is for $b_c = b_\perp$ and not for $b_c = b_\phi$. The reason is that $b_\perp(e, \alpha) > b_\phi(e, \alpha)$, and the electrons are heated first. The electrons have a short self-equilibration time and show no deviation from a Maxwellian for any b_c. Energy transferred to the electrons then heats up the ions, with a rate that is again faster for $b_c = b_\perp$. This pathway heats the bulk of the ions, and so is responsible for the increase in yield (rather than an athermal tail).

Evidence for this comes from the low excess kurtosis for $b_\perp$ at early times which is shown in Fig. 7.18, and that the α particles with $E_\alpha > 3.54$ MeV only ever make up a very small part of the α particle population. This can be seen in the distribution functions in Figs. 7.14, 7.15, and 7.16 which are taken at $t = 6$ ps. Figs. 7.19, 7.20, and 7.21 show the distributions for all three values of b_c of deuterium and α particles at the respective maximum excess kurtosis for deuterium. They corroborate that most of the α particles are created by bulk deuterium and tritium; the biggest α population above $E_\alpha = 3.54$ MeV (marked on the figures) is for $b_c = b_\phi$ and is around 2% of the total α population.

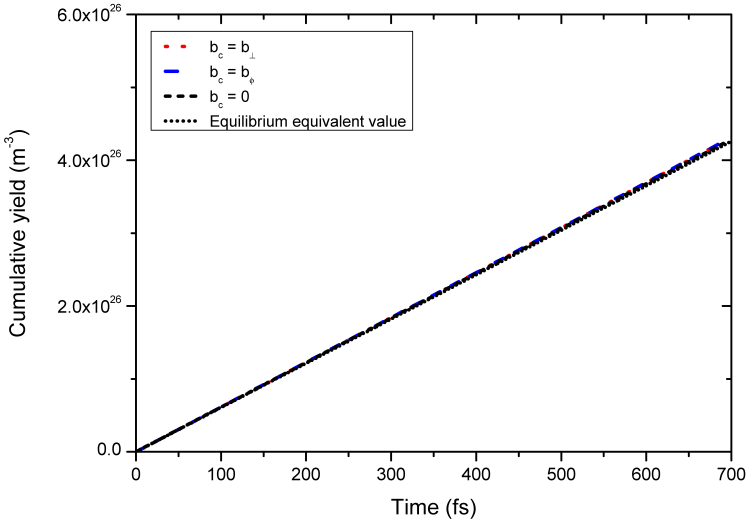

Figure 7.10: The yield using different values of b_c with parameters from Table 7.3 except that n_α is determined by fusion reactions.

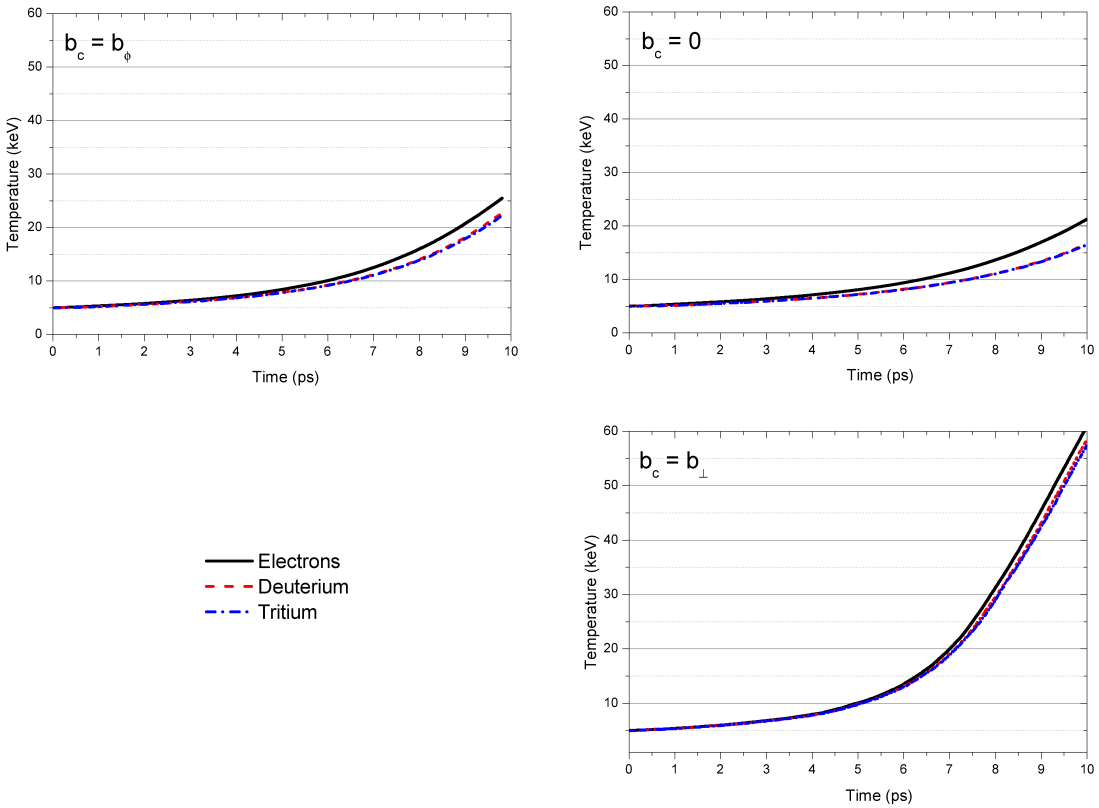

Figure 7.11: Temperature over time using different values of b_c, α particles not shown. $T = 2\langle E \rangle/3$. Note that the runaway temperatures are because of the feedback between higher fusion rates at higher temperatures, and the release of energy which fusion reactions cause. The high temperatures are not a direct result of the discrete collisions, but do cause the runaway to happen more quickly relative to $b_c = 0$.

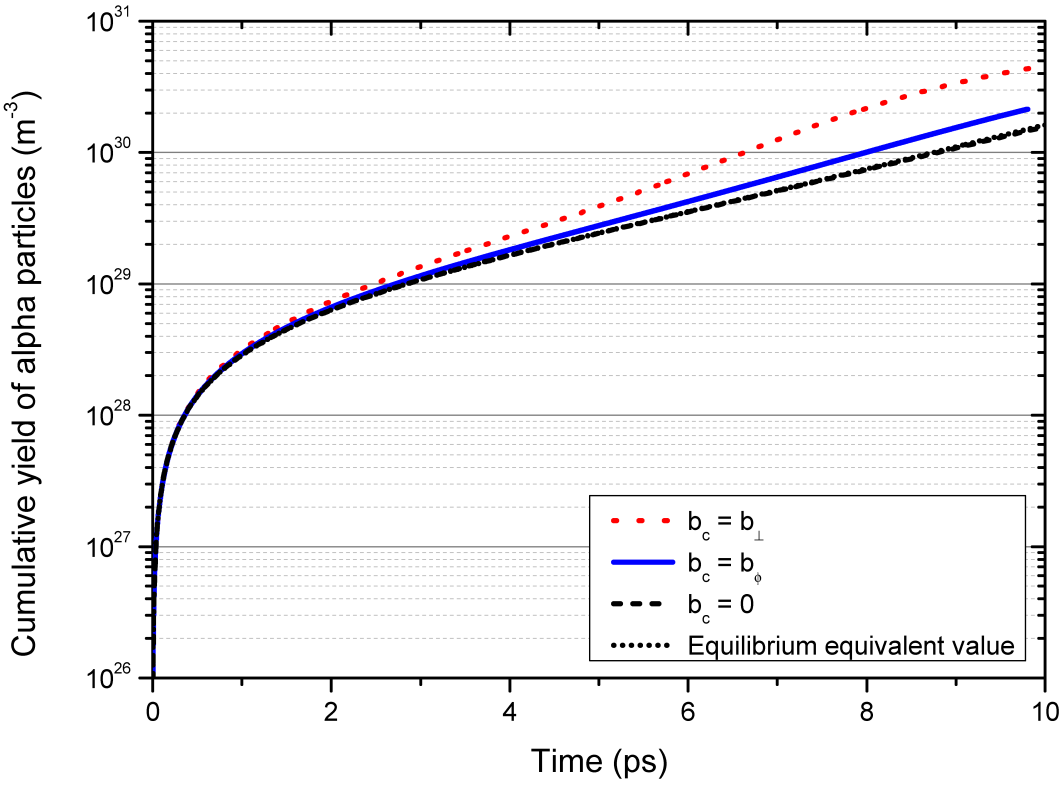

Figure 7.12: The yield over time using different values of b_c compared against the theoretical yield of an implosion with the $b_c = 0$ temperature-density history.

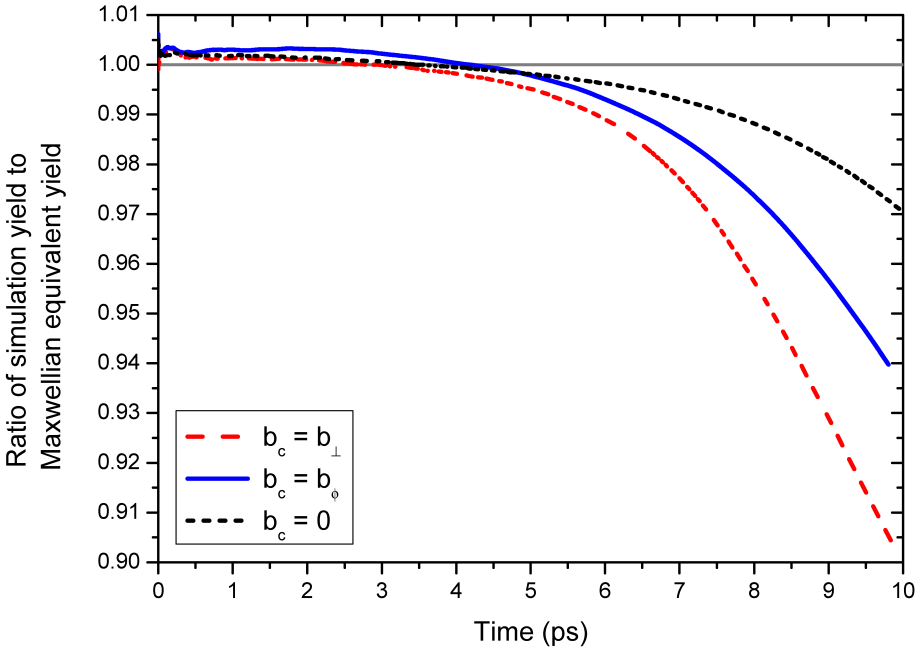

Figure 7.13: Ratio of simulation yield to prediction by theory of yield from a Maxwellian with the same average energy.

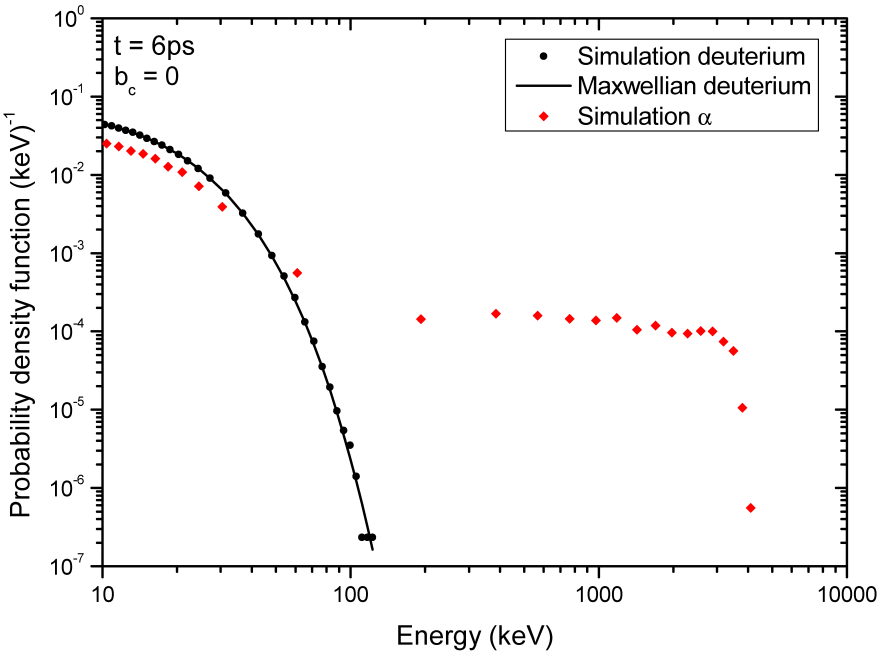

Figure 7.14: The deuterium distribution with $b_c = 0$ at $t = 6$ ps.

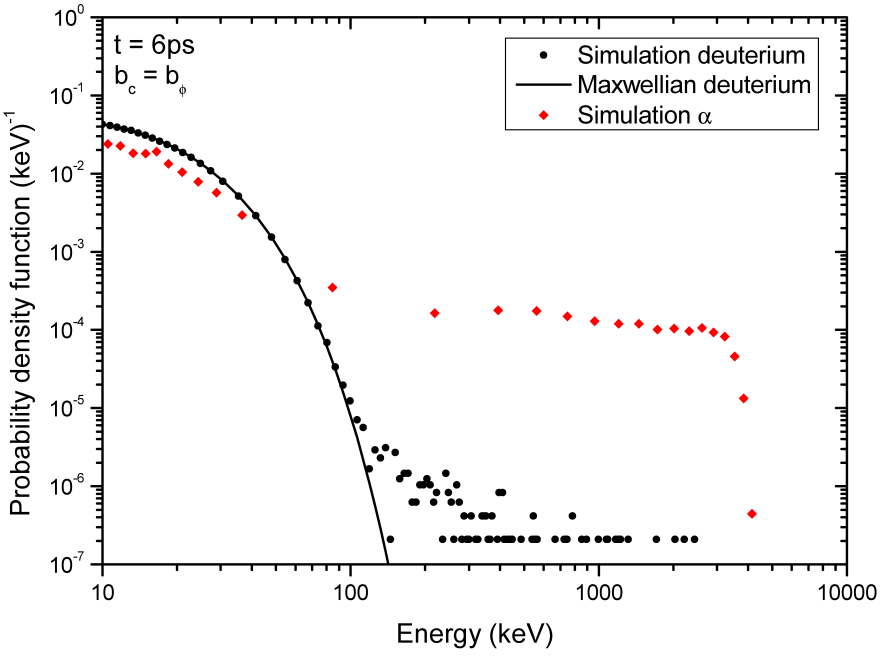

Figure 7.15: The deuterium distribution with $b_c = b_\phi$ at $t = 6$ ps.

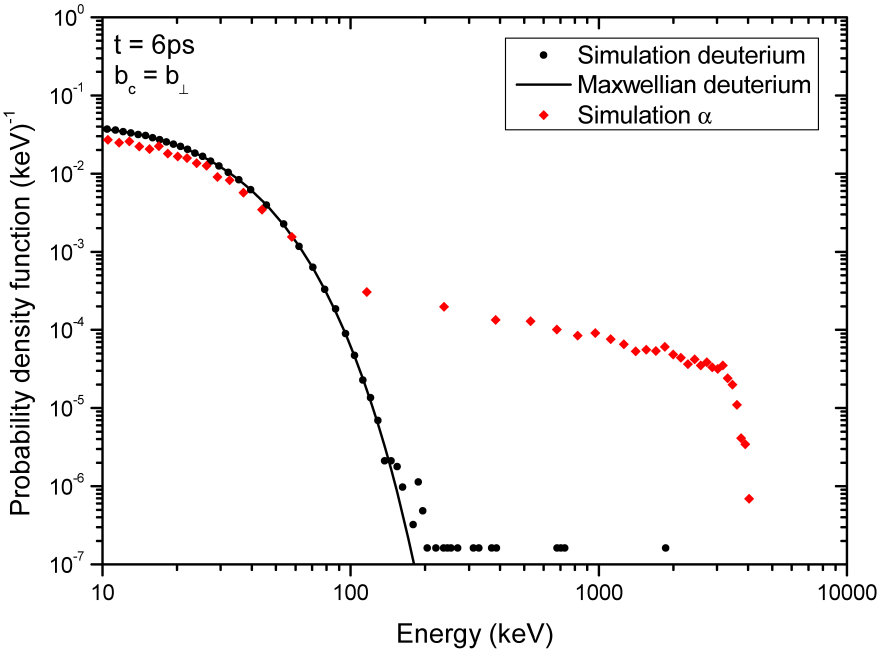

Figure 7.16: The deuterium distribution with $b_c = b_\perp$ at $t = 6$ ps.

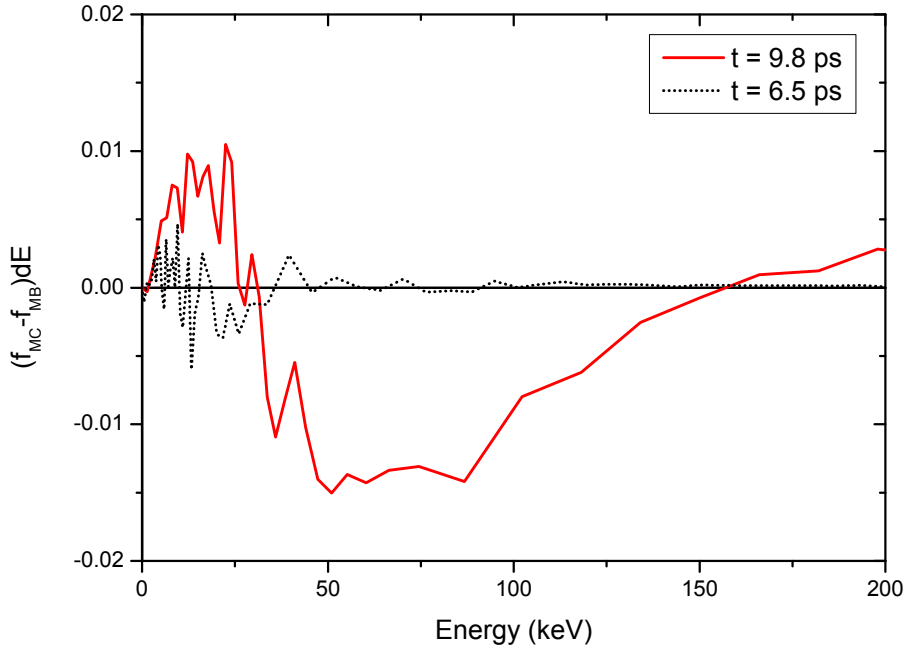

Figure 7.17: The deviation from a Maxwellian with the same average energy for $b_c = b_\phi$ at two different times during an ICF implosion.

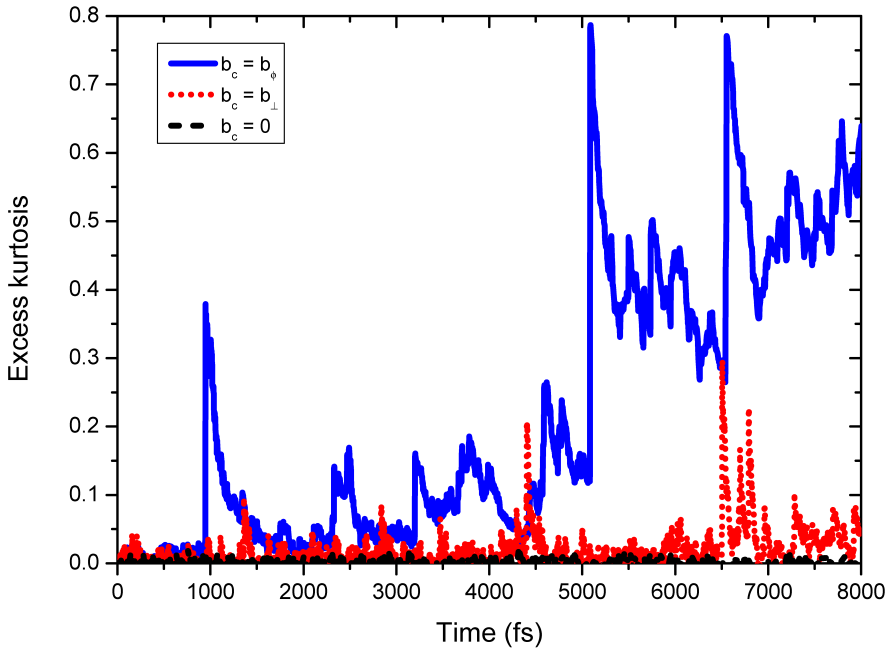

Figure 7.18: The excess kurtosis over time for the three different models.

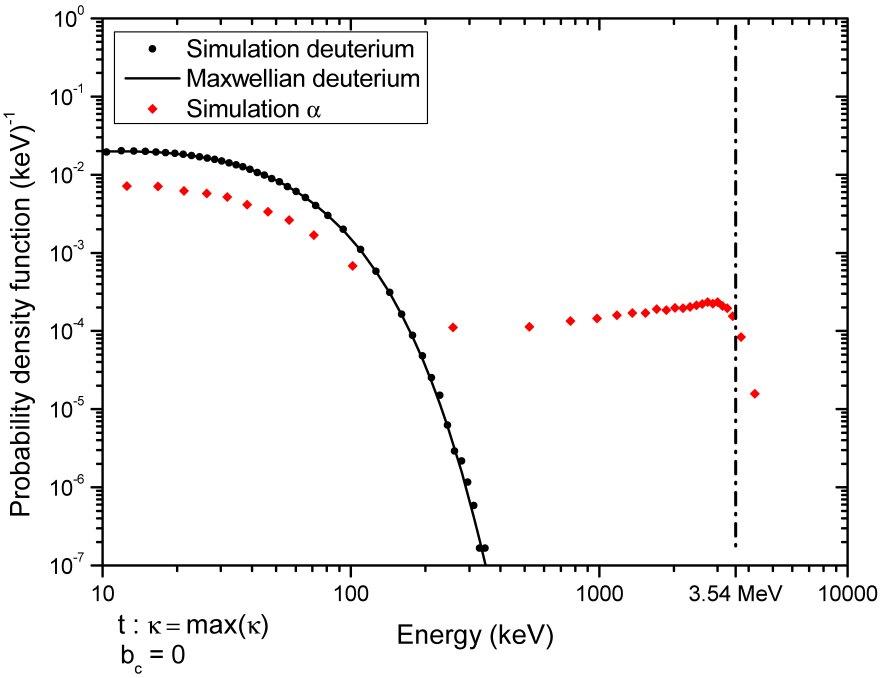

Figure 7.19: The maximum excess kurtosis distribution for deuterium using $b_c = 0$.

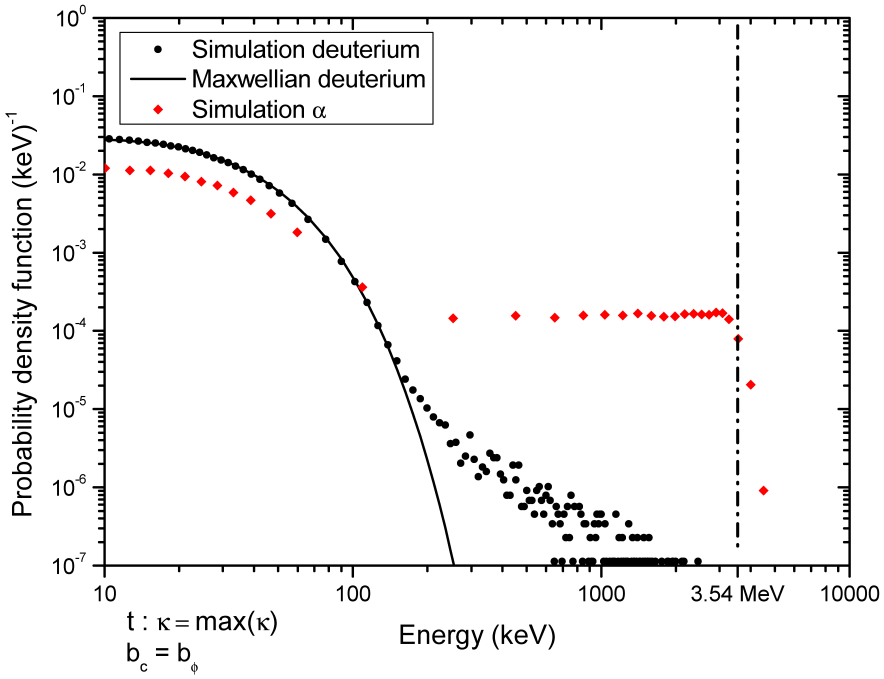

Figure 7.20: The maximum excess kurtosis distribution for deuterium using $b_c = b_\phi$.

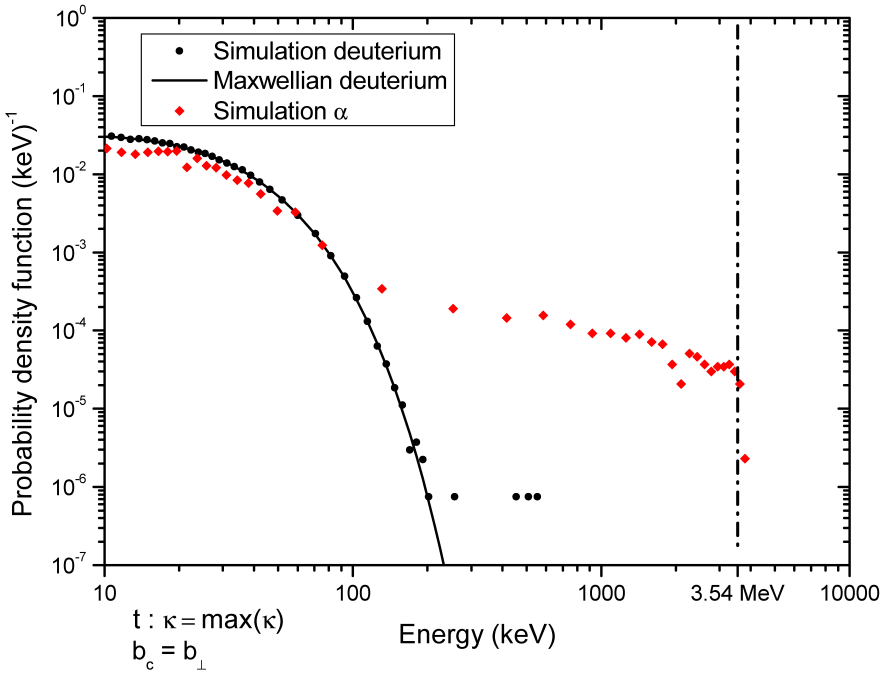

Figure 7.21: The maximum excess kurtosis distribution for deuterium using $b_c = b_\perp$.

Of course, there is some lag between maximum excess kurtosis and maximum athermal α production: a time-integrated neutron spectrum would be needed to provide stronger evidence. Tritium distributions show similar behaviour to the deuterium distributions, but are generally closer to equilibrium. The distributions show qualitative similarities with Ballabio *et al.*'s [119] simulations, particularly in the thermal broadening of the α particles, but their model is quite different. It is briefly described in §6.2.2.

The average effect of increasing b_c (equivalent to increasing the probability of discrete collisions) is to decrease the equilibration time between all species, as is shown by the correlation between increasing b_c and decreasing $T_e - T_i$ in Fig. 7.11. This is consistent with the temperature equilibration simulation in §7.3.1.

By $t = 4$ ps, the b_ϕ distribution is showing an increase in yield relative to the theory and to the $b_c = 0$ simulation too. By $t = 6$ ps, the increases in yield are 20% and 69% for b_ϕ and $b_\perp$ respectively, and are growing over time. At the end of the simulations, the $b_c = b_\perp$ model has a yield which is approximately *three* times higher than the $b_c = 0$ simulation, while the $b_c = b_\phi$ model produces a yield which is ∼46% higher. It seems that any increase in the number of discrete collisions will produce an increase in yield relative to considering only small-angle collisions.

The reason that b_ϕ produces a larger deviation from a Maxwellian consistently is that, for the transfer of an amount of energy which would drive a particle out of the bulk, $b_\perp > b_\phi$. This means that discrete collisions are less likely with b_ϕ, but that when they do occur, they produce larger angles. As up-scattering and down-scattering rates are approximately the same, any particles taken out of the bulk distribution by a discrete collision then have a small probability for losing their energy and returning to it in another discrete collision. Gradual energy loss by multiple scattering is also happening, but takes longer to return particles to the bulk. Contrast this with $b_c = b_\perp$ where the probability of a discrete collision is much bigger, but in both 'directions', so that particles can return to the bulk more easily. Also, the minimum angle ($\theta_c = \pi/2$) in a discrete collision is smaller for $b_\perp$ than it is for b_ϕ. For $b_\perp$, the distortions are smaller, and less durable, but higher average bulk energies earlier in time mean that it produces a higher yield.

An interesting feature is the increase in excess kurtosis with time of the $b_c = b_\phi$ deuterium and tritium distributions, as shown in Fig. 7.18 for deuterium. The trend appears to be for the distribution to depart further and further from equilibrium, with more of the population in the athermal tail. However, the relative numbers are still small. By the end of the simulation, at $t \approx 10$ ps, the population in the tail (defined relative to a Maxwellian fitted with $T = 2\langle E \rangle/3$) is still less than 0.5% implying that the athermal contribution to yield is not significant. Eventually, depletion will naturally limit the excess kurtosis.

A more complete picture of the effect of small changes in the distribution functions can be found from the ratio of yield from the simulation relative to a Maxwellian with the same average energy as that simulation for each of the values of b_c. This is shown in Fig. 7.13. The comparison is made to the Bosch-Hale expression for fusion reactivity, as described in Chapter 3 and Appendix C. Fig. 7.13 displays some interesting behaviour; there appears to be some systemic error in the early time yield showing a ratio greater than one. This is before a non-Maxwellian can have been established. In addition to the systematic error, small initial increases relative to a Maxwellian are apparent, as the particles which are most likely to fuse do so at the start of the simulation. After this initial high point, all of the rates reduce relative to the theory.

The $b_c = b_\phi$ distribution function, taken at two different times and shown in Fig. 7.17, provides some explanation of this. $(f_{\mathrm{MC}} - f_{\mathrm{MB}})\,\mathrm{d}E$ is plotted against E and, towards the end of the simulation, it is evident that the bulk of the distribution function is depleted relative to a Maxwellian for $E{\sim}50 - 150$ keV. This approximately coincides with where the largest contribution to fusion reactions would be coming from for a Maxwellian, thus explaining the drop in yield relative to theory. The low energy end of the distribution is enhanced, as is the tail. These are explained by particles low in energy being unlikely to fuse (despite existing in greater numbers) and the tail being enhanced by the slowing of fusion products as seen on the log-log figures. This is true for all three simulations, but $b_c = b_\phi$ is chosen as the relationship is particularly clear. The $b_c = b_\perp$ simulation shows depletion and enhancement too, but is less easy to interpret due to noise. For all simulations, a comparison against a Maxwellian with the same average energy does not accurately predict the yield in Fig. 7.13. The difference grows faster for the two $b_c \neq 0$ cases but is also apparent for $b_c = 0$, implying that none of the distributions remain Maxwellian. This is particularly interesting in the $b_c = 0$ case, which might be expected to agree with a perfect Maxwellian.

An alternative explanation is that the disparity in average energy between deuterium and tritium might be causing the difference in yield relative to two Maxwellians with the same temperature. Throughout the simulations, the difference in average energy between deuterium and tritium attains a maximum of less than 3% for all models over all time, and is generally much less. This small difference in temperature seems unlikely to be the cause of the difference in yield seen in Fig. 7.13.

Michta *et al.* [155] also see deviations from equilibrium distributions of deuterium and tritium in small-angle only simulations using a VFP code. There are significant differences with the simulations presented, including a higher density of $\rho = 1000$ g cm^{-3} (the cold fuel shell density), and the inclusion of more fusion reactions and radiation. Another

important difference is the lack of reaction-in-flight ions in their simulations. Their definition of equilibrium is based on two points on the distribution function, $E_1, f(E_1)$ and $E_2, f(E_2)$ with energies of keV or less and a bulk temperature defined as

$$T_{\text{bulk}} = (E_2 - E_1) \ln \left(\frac{f(E_1)\sqrt{E_2}}{f(E_2)\sqrt{E_1}} \right)$$

The percentage of particles not in equilibrium is given by

$$1 - f_{\text{eq}} = 1 - \frac{\sqrt{\pi} T_{\text{bulk}}^{3/2}}{2\sqrt{E_1}} f(E_1) \exp\left(E_1/T_{\text{bulk}}\right)$$

for each species. A possible future direction is to introduce these definitions as diagnostics and compare them for different values of b_c, allowing a clearer distinction between distributions which have the same average energies but quite different fusion reactivity. This would allow a more in-depth discussion of the effects observed in Fig. 7.13, and comparison with Michta *et al.*'s results. It seems reasonable that the discrete simulations will give a higher proportion of non-equilibrium particles than Michta *et al.* found for small-angle collisions only, according to the above definition.

A consequence of this work which might soon be apparent on NIF is that any inference about average energy made from the number of neutrons produced assuming Maxwellian distributions only will be incorrect when the yield curves separate in Fig. 7.12. This corresponds to fractional burn-ups greater than ∼0.2% for discrete collisions (both models) and ∼1% for small-angle collisions only. The average energy inferred from the yield based on a Maxwellian will be lower than the average energy in reality, because the yield for the same average energy is always reduced relative to a Maxwellian as shown in Fig. 7.13. This is for the particular parameters used, but the results of §7.3.3 indicate that the behaviour is general.

If any extra yield is only from the bulk of the distributions in the discrete simulations, then the down-scattered neutron ratio (dsr) may not be adversely affected. However, more work is needed in this area to determine just how much of a change to the dsr the small changes relative to a Maxwellian make; the distribution functions provide only a snapshot and a time-integrated neutron spectrum would be a better diagnostic.

It is worth speculating about what change to dsr is affected by the departures away from perfect Maxwellian ion distribution functions. A value of dsr based on a Maxwellian might expect fewer high energy neutrons than would be produced by the distributions found in the simulations, which have depleted bulks and enhanced tails. Any excess of neutrons with energies above 14 MeV could slow down slightly and be brought into

the $13 - 15$ MeV range, thus increasing the value of the denominator in the dsr despite the neutrons having actually been down-scattered due to a large ρR. The relationship between fuel ρR and dsr taking into account the implosion geometry on NIF, but not the discussed effect, is [157, 158]

$$\rho R_{\text{fuel}} \left(\text{g cm}^{-2}\right) = (18.5 \pm 0.5) \times \text{dsr}$$

So the dsr would need to be more than 2.5% different to be noticeable in implosions on NIF.

Some consideration should be given to the effect of discrete collisions on the ρR requirement for α particle stopping on NIF. This is generally taken to be $\rho R \sim 0.2 - 0.5$ g/cm^2 in order to completely stop α particles in the hotspot. The discrete collisions have two relevant effects; the first is to very slightly broaden the distribution of αs such that more escape, but this is a weak effect given the extent of thermal broadening seen in the simulations. The second effect is that the rates of energy loss, to ions and electrons, are increased relative to what might be expected from Landau-Spitzer theory using the Coulomb logarithm in §2.3. The overall consequence is that *lower* ρR values may be sufficient in order to stop most α particles in the hotspot.

7.3.3 Athermal chain-reaction fusion

The work described in §6.2.1 implies that the high energy products of fusion could cause a cascade of recoil particles which are more likely to fuse, starting a runaway chain. This is in contrast to thermonuclear fusion, where high bulk temperatures produce fusion reactions. The conditions recommended in the literature for athermal fusion, $n{\sim}10^{33}$ m^{-3} and $T{\sim}30$ keV, are extreme, and constitute a burning plasma in themselves - the temperature and density are far higher than is expected on NIF. With a large amount of bulk fusion occurring, the most interesting effect of athermal fusion would be a yield which is substantially higher than might otherwise be expected from thermal models. If so, achieving those extreme conditions would be particularly desirable for future fusion schemes.

The Monte Carlo code with discrete collisions and variable b_c is used on a simulation with the initial conditions as specified in Table 7.4. The work cited in §6.2.1 found that NES (including between neutrons and ions) is important or essential for these chains to proceed. The code does not currently implement NES, so only large-angle Coulomb collisions are present. The hallmarks of athermal chains will be a large tail on the deuterium and tritium distribution functions, and an ever broadening high energy (above

$\sim$4 MeV) population of α particles which can only have been created from the fusion of recoils. Successively higher generations of recoils fusing will create successively higher energy α particles, and the high energy tail of the αs will be broadened.

The yield is shown in Fig. 7.22, and all three models show very quick fuel burn, reaching over 2% burn-up before 10 fs. The $b_c = b_\perp$ model clearly outperforms the others in terms of yield in the middle of the simulation. This again seems to be due to equilibration rather than an athermal population as there is only a small tail. A quicker equilibration time allows the part of the distribution most likely to fuse be replenished more easily, and the bulk temperature to increase more rapidly. This is why the difference relative to the Maxwellian theoretical values, shown in Fig. 7.23, are smaller for $b_c = b_\perp$ than for $b_c = b_\phi$ even though $b_\perp > b_\phi$ for the important burn wave energy exchanges. There may still exist a fleeting athermal tail and athermal α population. A fleeting non-runaway athermal population is much less interesting than a chain, and would only have consequences for the neutron spectrum. This is because neutron spectra are partially 'frozen' in time due to their small cross-section for interaction when leaving the fuel, at least for the purposes of diagnostics.

A difference in expected yield (relative to the equivalent Maxwellian) is also perceptible in the $b_c = 0$ case, implying again that the distribution functions of deuterium and tritium are being distorted by depletion even with small-angle scattering only. A linear plot of that distortion at $t = 44$ fs is shown in Fig. 7.25. This is not surprising in a burning plasma. The differences between the models initially grow over time, but are eventually limited by depletion, and the yield of all models shows signs of convergence of yield by $t = 44$ fs.

Surprisingly, the $b_c = 0$ simulation is the furthest behind in yield relative to the others. The combination of distortions produced in the $b_c \neq 0$ simulations give a yield which is quite similar to assuming a Maxwellian distribution throughout by $t = 44$ fs, especially for $b_c = b_\phi$ which is overtaken in yield by the Maxwellian equivalent of the $b_c = 0$ simulation. The effect of large-angle collisions on yield attains a maximum value for $b_c = b_\perp$ of more than 30% (relative to the $b_c = 0$ simulation) in the middle of the simulation before

Quantity	Value
n_d, n_t	5×10^{33} m^{-3}
T_d, T_t	20 keV
n_α	6×10^{27} m^{-3}

Table 7.4: Athermal fusion parameters.

reducing again at later times.

The smaller increases in yield seen in these simulations relative to the more NIF-like simulation in §7.3.2 are most likely due to the hotter burning temperature. A hotter burning temperature brings the upper end of the bulk of the ion distribution functions into contact with the peak of the fusion cross-section (see Fig. 6.5). So the largest yield will be associated with the largest probability density in that region. As $b_c = b_\perp$ has the shortest equilibration time, it is hotter sooner than the theoretical Maxwellian equivalent of the $b_c = 0$ simulation, and so the probability density around the peak of the fusion cross-section is larger earlier on - explaining why it does better than the other models.

However, for $b_c = b_\phi$, the depletion around the peak of the cross-section is noticeable in both Figs. 7.28 and 7.29, as is the enhancement of the tail. But the severe effects on the yield of the bulk depletion are not countered by the appearance of a tail, because the energies are too high to substantially increase the rate of fusion reactions. Hence the overall yield being overtaken by the theoretical Maxwellian equivalent of the $b_c = 0$ simulation, despite $b_c = b_\phi$ having a faster equilibration time. It is not clear whether including loss mechanisms would decrease the energy of the tail for $b_c = b_\phi$ enough to increase the yield, but it is possible.

The hallmarks of athermal chain reactions are not strong as the populations of α particles above 4 MeV are actually fairly consistent at a few percent for all three models (at the same time). The broadening of the α distribution is similar for each model, with $b_c = b_\phi$ having only a very marginally broader distribution of αs despite having a striking athermal deuterium tail as shown in Fig. 7.28 and Fig. 7.29. Smaller, noisier depletions of the distribution can be observed for $b_c = 0$ and $b_c = b_\perp$, corresponding to the smaller differences relative to the theoretical value in Fig. 7.23. The tail in the $b_c = b_\phi$ simulation does appear to be transient from the excess kurtosis in Fig. 7.30, which is not surprising as so much of the fuel is burnt towards $t = 44$ fs that the pressure away from equilibrium grows far less strong. Overall, the evidence for athermal chains is poor and the increases in yield due to discrete collisions appear due to the bulk, rather than the tail, are dependent on the model, and are also dependent on the time the fuel is assembled. Most surprisingly, the yields of all models are less than predicted by Maxwellian distributions with the same average energy and density history by between 10% and 15% due to depletions in the distribution function.

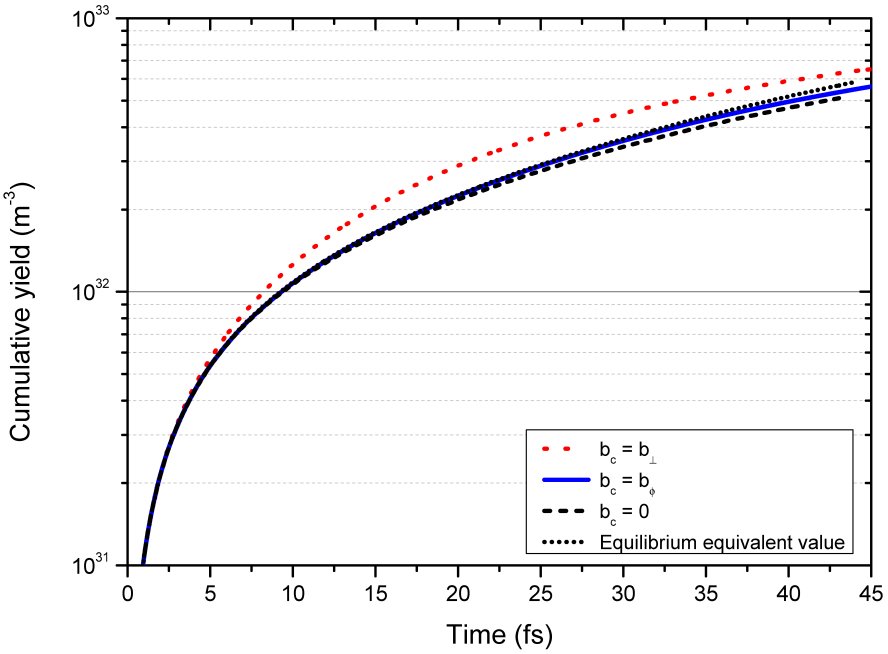

Figure 7.22: Yield over time using different values of b_c compared against the theoretical yield of an implosion with the $b_c = 0$ temperature-density history.

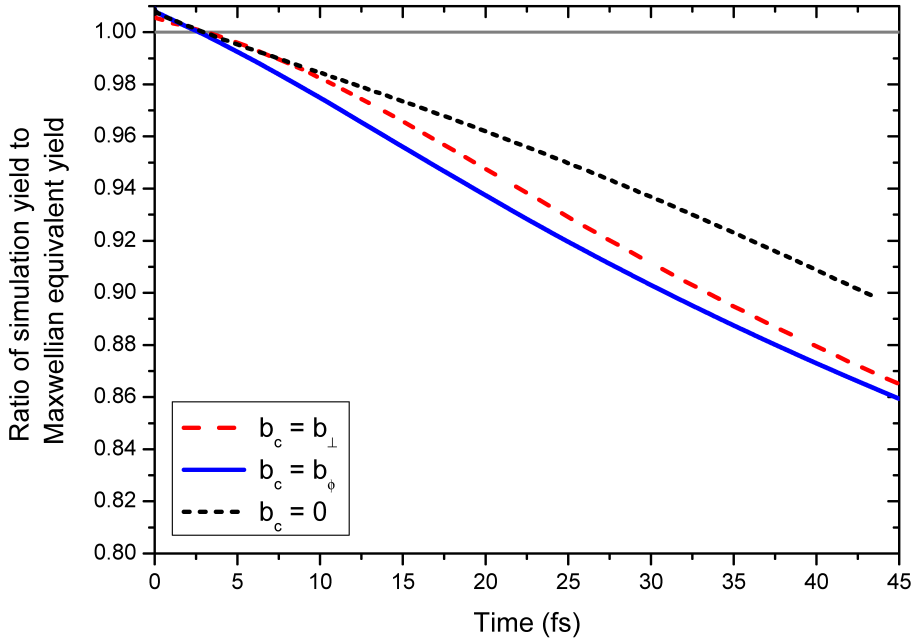

Figure 7.23: Ratio of simulation yield to prediction by theory of yield from a Maxwellian with the same average energy.

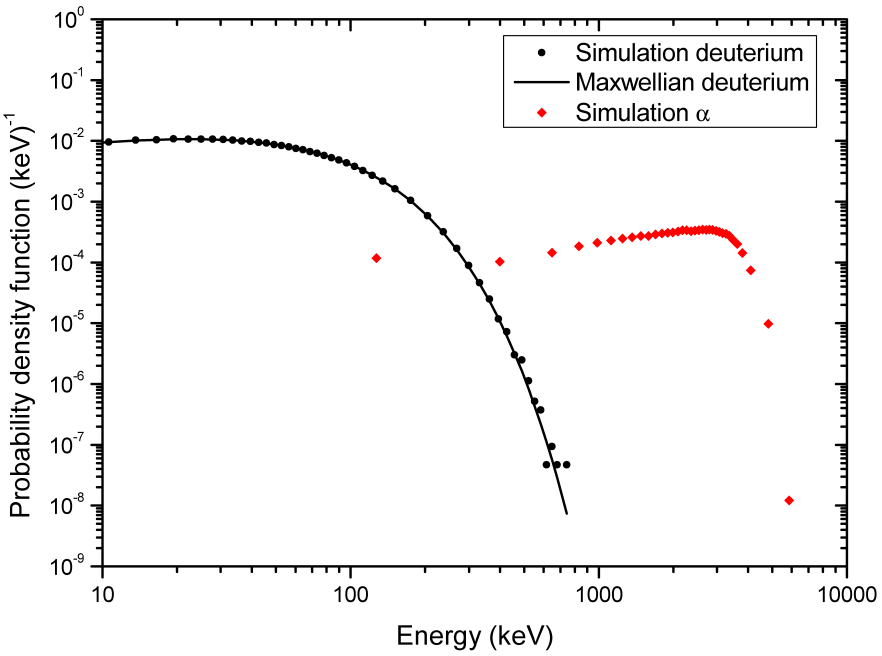

Figure 7.24: The distribution for deuterium using $b_c = 0$ at $t = 44$ fs.

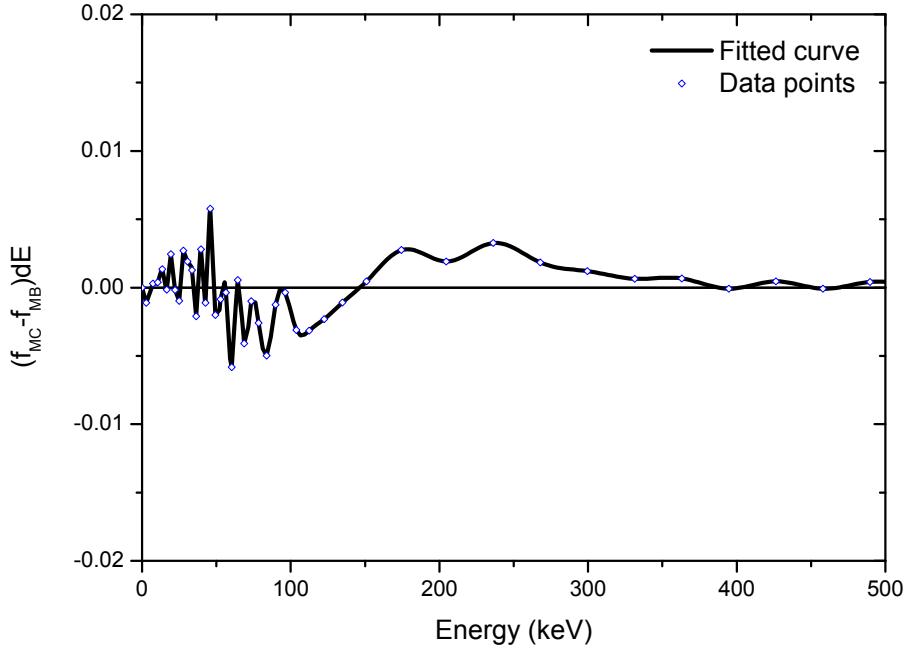

Figure 7.25: $(f_{\mathrm{MC}} - f_{\mathrm{MB}})\,\mathrm{d}E$ for $b_c = 0$ at $t = 44$ fs.

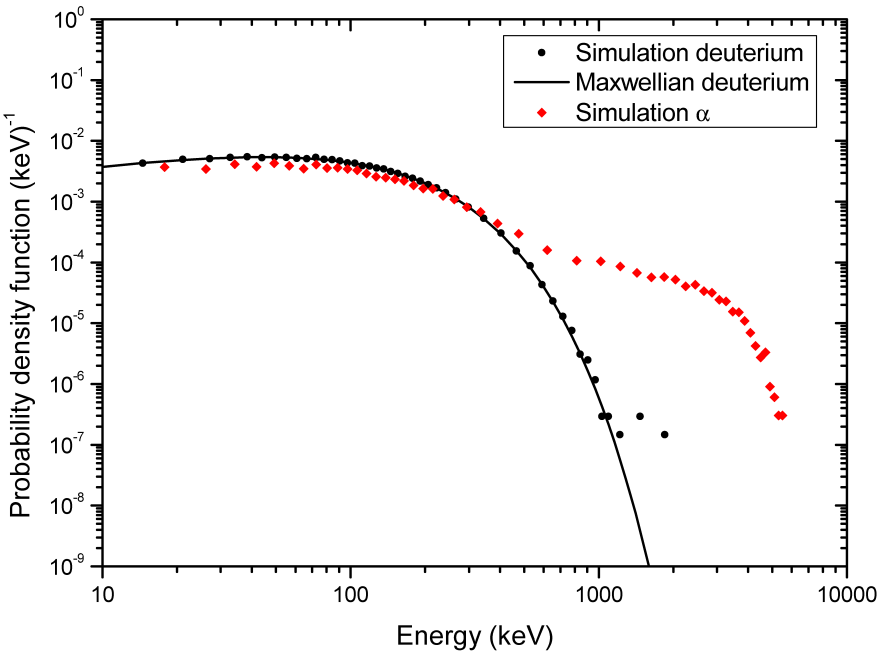

Figure 7.26: The distribution for deuterium using $b_c = b_\perp$ at $t = 44$ fs.

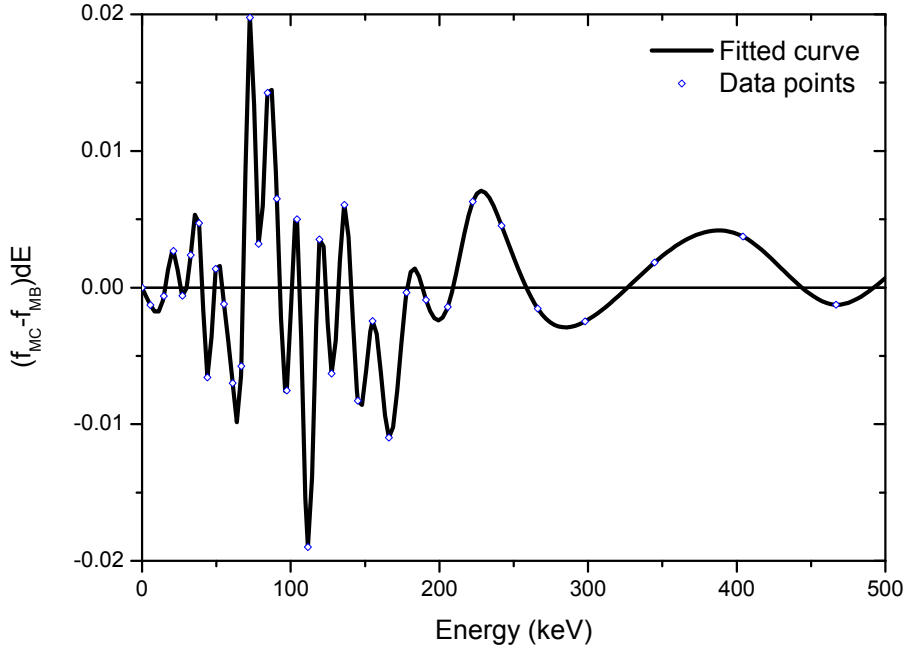

Figure 7.27: $(f_{\mathrm{MC}} - f_{\mathrm{MB}})\,\mathrm{d}E$ for $b_c = b_\perp$ at $t = 44$ fs.

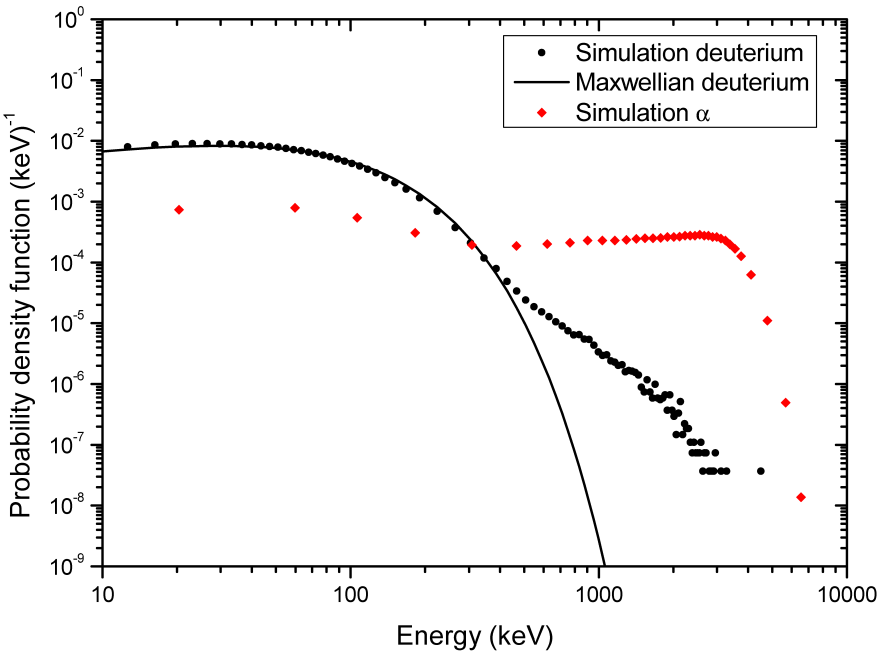

Figure 7.28: The distribution for deuterium using $b_c = b_\phi$ at $t = 44$ fs.

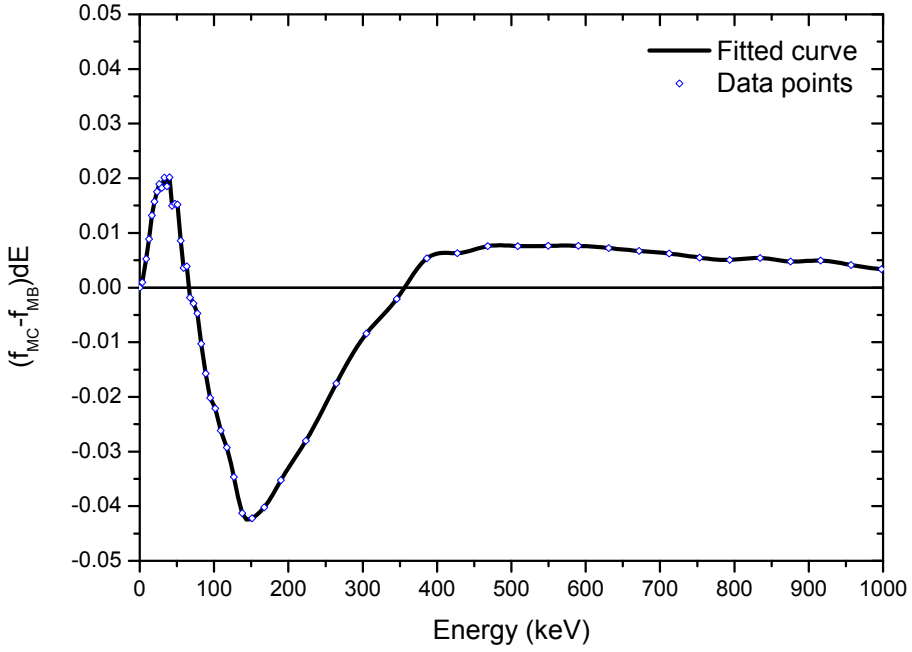

Figure 7.29: $(f_{\mathrm{MC}} - f_{\mathrm{MB}})\,\mathrm{d}E$ for $b_c = b_\phi$ at $t = 44$ fs.

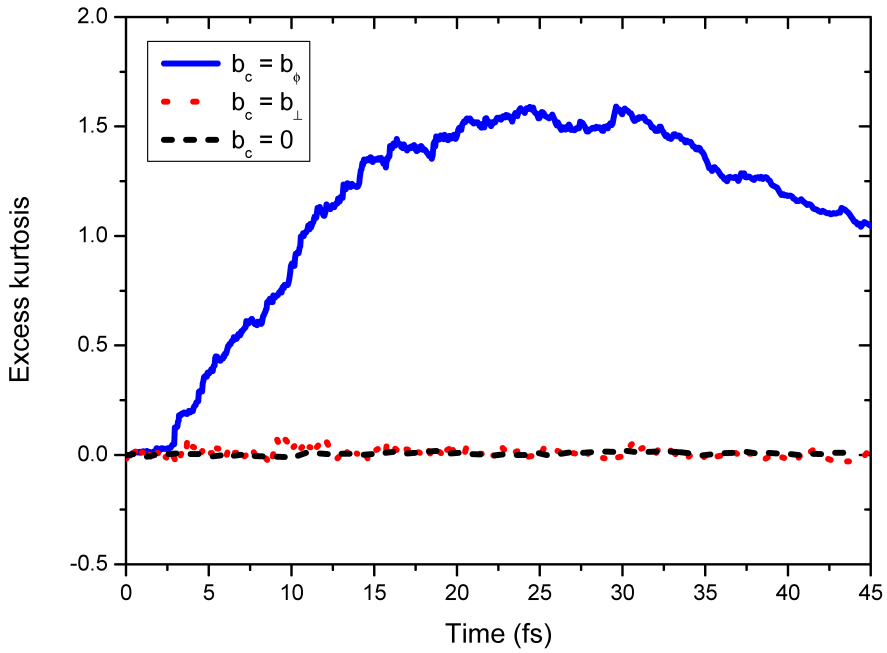

Figure 7.30: The excess kurtosis for deuterium for all three models.

Chapter 8

Conclusion

8.1 Summary of results

In Chapter 1, the motivation for this thesis is set out: to understand processes driving non-Maxwellian distributions in high energy density physics, with particular reference to ongoing efforts to produce fusion power. Much of the discussion is on the moderately to strongly coupled regime, with $\ln \Lambda \leq 5$, as distributions are slower to relax to equilibrium, collisions become important, and even the equilibrium distribution can be non-Maxwellian.

The basic computational tool used is Monte Carlo, with various modifications developed specifically for studying particular phenomena. The extensions of Monte Carlo methods to include fusion in Chapter 3, to degenerate plasmas in Chapter 4, for ion-ion inverse bremsstrahlung absorption of laser radiation in Chapter 5, and for large-angle collisions in Chapter 7, are hopefully a new and helpful resource in themselves.

Beyond the development of tools which other researchers may find of use, several interesting physical results have been obtained.

In Chapter 4, an algorithm is developed which successfully produces known results for the equilibration and resistivity of Fermi degenerate plasmas. It is found that conventional degenerate temperature equilibration does not give the correct evolution of temperature for ions or electrons in conditions relevant to the heating of the cold fuel shell by fusion produced α particles in ICF. This result is true even though the electrons are only transiently degenerate. After 40 fs, deuterium and electrons are found to be 33% and 21% hotter respectively than standard equilibration models predict, with an absolute difference of roughly 0.3 keV in the electron temperature long after the degeneracy parameter is below $\eta = -5$. Much of the material in Chapter 4 has been published [63].

The phenomenon described as ion-ion inverse bremsstrahlung (IIIB) absorption is studied in Chapter 5. Previous work is extended with a brief discussion of physical scenarios conducive to IIIB in §5.3, and, in §5.4, a simple expression for the rate of heating for $\mathrm{d}E_0/\mathrm{d}t = 0$ is found by adapting previous results. A method for finding the optimum laser pulse for heating by IIIB is described in §5.5, and conditions on driving non-Maxwellian distributions in ion species by IIIB are presented and confirmed by simulation. The distributions found are the ion-ion equivalent of Langdon distributions. For the first time, simulations of IIIB with a mixture of several ion species are presented. In favourable conditions, it is demonstrated that a mixture of light and high Z ions combined with the optimum pulse for heating could produce light ion temperatures above 10 keV on timescales of femtoseconds with lasers of $I > 10^{22}$ W cm^{-2}.

A review of the theory and research undertaken on discrete and large-angle collisions is presented in Chapter 6. For the first time, the effects and possible applications of discrete collisions are drawn together as a single reference resource in §6.2. For Coulomb collisions, definitions of small-angle, multiple scattering and discrete, possibly large-angle, scattering are developed based on the impact parameter of the two scattering particles. An entirely new theory of how to calculate the cut-off in impact parameter, b_c, between multiple and discrete scattering based on the potential between a single charged particle and all other plasma particles is described in §6.1. The cut-off based on the theory is $b_c = b_\phi$ and, as $b_\phi < b_\perp$ for most interactions, it is a conservative value of the cut-off compared with the values of $b_c \geq b_\perp$ typically used in other work. Also included is an overview of other effects which are important in the context of large-angle scattering in plasmas, some of which may become increasingly relevant in burning plasmas.

Chapter 7 uses the results and discussion of Chapter 6 in computational simulations. A Monte Carlo code capable of undertaking both discrete and multiple scattering is developed in §7.2. The differences between multiple and discrete collisions are explored in §7.3, and it is found that distortions to distribution functions due to a higher probability of discrete collision are self-limiting, so that there must exist an intermediate value of cut-off in impact parameter for which the largest and most persistent distortions away from Maxwellian distributions exist. Using the potential-based model developed in Chapter 6, it is found that discrete collisions are more likely in dense, cold conditions while the chance of those discrete collisions being large-angle is greater for high temperatures and only increases slightly with increasing density, and then only at the highest physically achievable densities. Given the reduction in the multiple scattering $\ln\Lambda$ when splitting collisions into multiple and discrete contributions, it is not intuitive that the transfer of energy between two distributions should be increased by the inclusion of discrete collisions. However, for both discrete collision models tested, the temperature equilibration

time is decreased by a factor of either 2 or 3 relative to small-angle collisions only. This effect genuinely seems to be the result of energy being exchanged more quickly rather than due to distortions to distribution functions. Previous work also suggests this reduction in moderately coupled plasmas [48] but without consensus as to the exact relationship, and this is the first time the effect has been shown with a model not based on the VFP equation.

Two ICF-like scenarios are simulated in §7.3. The results found for the NIF-like simulation in §7.3.2 with small-angle collisions only are in agreement with Michta *et al.*'s [155] work showing that non-Maxwellian distributions may be temporarily driven with small-angle collisions only. This is in contrast to similar work by Sherlock and Rose [154] though that is performed at a lower temperature.

A much greater difference relative to Maxwellian distributions is seen in simulations which include discrete collisions. These simulations show athermal tails developing on both deuterium and tritium distributions. The size of the tail is dependent on the model used, but both large-angle models seem to predict little direct effect of the athermal tail on the yield as the population of athermal αs produced is similar to the small-angle only case. The small population of athermally produced α particles suggests that there are few consequences of athermal tails for the down-scattered neutron ratio, but better diagnostics are needed to confirm this.

Interestingly, the *overall* yield is increased (relative to small-angle collisions only) with discrete collisions, and it is determined that faster equilibration times due to discrete collisions are the cause. This is corroborated by the temperature evolution of the NIF-like discrete collision simulations; the ions get hotter, faster - much hotter for the $b_c = b_\perp$ simulation. Increases in the absolute yield (relative to small-angle only simulations) of 20% and 69% are seen by $t = 6$ ps for the two discrete models using $b_c = b_\phi$ and $b_c = b_\perp$ respectively. This difference grows over time, and the $b_c = b_\perp$ simulation reaches *three times* the yield of the small-angle only simulation after $t = 10$ ps, at a fractional burn-up of 9.6%, while the $b_c = b_\phi$ ends with a 46% higher yield at a fractional burn-up of 4.7%. The quantitative value of yield at late times could change if loss mechanisms were taken into account, but a higher yield relative to small-angle collisions only is still likely.

As the fractional burn-up is increased, it is reasonable to expect the yields of all models to converge, but non-igniting ICF experiments have a very small fractional burn-up and even igniting spheres are unlikely to surpass 30%. For the NIF-like conditions simulated in §7.3.2, the size of the difference in yield between simulations becomes apparent at a fractional burn-up of ∼0.08%, and current ICF experiments are producing a fractional burn-up of less than 0.01%. As the experimental neutron yield increases on NIF, these effects could become apparent.

A simulation of the conditions suggested for athermal chain-reaction fusion are examined in §7.3.3, though they are at a much higher temperature and density than is envisaged on NIF. These simulations exhibit many of the same qualities as the NIF-like simulation in §7.3.2 but the increased yield for the two discrete simulations, relative to the small-angle only simulation, still appears to be due to faster equilibration and not an athermal chain of fusion reactions. That the α particle population above $\sim$4 MeV is again not enhanced for the simulations with discrete collisions implies that this is the case. At the high temperature considered ($T_{i,0} = 20$ keV), the tail of the distribution is well above the cross-section for deuterium-tritium fusion, which further suggests that the chain effect is not occurring, and cannot occur. Much of the literature describes the inclusion of nuclear elastic scattering (NES) as key to athermal chain-reaction fusion, and the omission of this class of scattering processes means that athermal chains cannot be completely ruled out.

In §7.3 it is found that, despite increases in absolute yield, all simulations display a *reduction* in yield relative to what would be expected for a Maxwellian with the same average energy. It is hypothesised that this is due to a depletion in the regions of the distribution function which contribute most strongly to the reactivity, and there is some evidence to support this. The kinetic models predict as much as 10%, and at least 3%, less yield than for a Maxwellian with the same average energy in NIF-like conditions, with the biggest differences for the largest cut-off in impact parameter. The difference increases to over 10% for the more extreme conditions simulated in §7.3.3. This has two very significant consequences.

Firstly, experimentally determined values of total yield cannot always be used to infer the average energy of the distribution function, or to determine a temperature for a Maxwellian distribution. The average energy deduced in such a manner will be lower than in reality, because the yield for the same average energy is always reduced relative to what would be expected for a Maxwellian. Secondly, the depletion and enhancement of the distribution function relative to a Maxwellian could cause an artificial increase in the denominator of the down-scattered neutron ratio (dsr), and mean that the value of ρR is underestimated. This effect becomes apparent at fractional burn-ups greater than $\sim$0.2% for discrete collisions and $\sim$1% for small-angle collisions only in NIF-like conditions of a hotspot temperature of $T = 5$ keV.

8.2 Future research

The work undertaken for this thesis has highlighted a number of interesting avenues to explore in future research.

Collisional simulations of ion-ion inverse bremsstrahlung in complex geometries are desirable as they would allow the likelihood of the effect being observable in experiments on high power laser facilities to be determined. PIC codes are an ideal way to do this, as they also include the important space-charge effects which limit the duration of the interaction of the electromagnetic field of the laser with the ions. The effects of a spatial profile of the laser, impossible to include in 0D Monte Carlo, are also easily determined in non-0D PIC codes. Another feature important for future research is the inclusion of the ionisation of the high Z ion, as the heating scales as Z^2 and the heating rate determines the temporal pulse shape for optimal heating. One further case where ion-ion inverse bremsstrahlung could occur is with a black-body radiation field, though this is significantly more complicated than with inverse bremsstrahlung absorption of laser radiation. One aspect not explored in this work is whether ion-ion bremsstrahlung *emission* could occur, how large an effect it could be, and in what conditions. For example, high Z impurities from the ablator mixing into an ICF hotspot could cause ion-ion bremsstrahlung emission with deuterium and tritium. This effect will be far smaller than electron-ion bremsstrahlung, but could be of interest, and would certainly be tractable for two ion species i and j in the $m_i/m_j \longrightarrow 0$ limit.

There is great scope for further research on discrete collisions. That the equilibration time is reduced by their inclusion even without significant distortions to distribution functions implies that they could have effects on other properties of plasmas. It is clear that stopping powers are affected for high energies from the simulations in §7.3.2. It is reasonable to expect a change to transverse diffusion with discrete, and particularly large-angle, collisions. Given that electrons were found to play an important role in the transfer of energy, the consequences of large-angle collisions on electron conduction might also be studied.

Developing an analytical framework which could properly account for the effects of large-angle collisions is desirable; though the methods outlined in this work can be used to study their effects, the computation required relative to evaluation of the Landau-Spitzer formulae in Appendix B make it prohibitive for many applications. Simple formulae that, for example, approximated the decrease in equilibration time with large-angle collisions (taking b_c as a parameter) would be of much more use to the wider plasma physics community. Additionally, simple analytical models of the modifications to processes due to the development of athermal tails on distributions, or more general enhancement and depletion relative to a Maxwellian distribution, would be useful.

In terms of the fundamental theory of discrete collisions, some of the assumptions which are used in the derivation of b_ϕ as the cut-off in impact parameter could be relaxed in

order to create a stronger argument for the value of b_c. This is important, as the effect of discrete collisions is sensitive to b_c and there is no consensus on what an appropriate value is.

Various processes not examined could also drive non-Maxwellian distributions in ICF, and though these are generally secondary effects relative to the processes already included, they may have a discernible effect on the evolution of distribution functions, particularly in simulations of ICF. Specifically, the deuterium-deuterium fusion reaction produces tritium at $E_t = 1$ MeV, and would be likely to occur in the tail of deuterium in the ICF-like simulations considered in §7.3. Previous work [155] shows that an athermal tritium tail occurs due to this reaction. There are other light-ion fusion reactions which could be included.

A key process not included is nuclear elastic scattering (NES). This could significantly change the evolution of distribution functions, particularly in the high energy parts and in burning plasmas. As is explained in §6.2.1, NES must be included as a discrete energy loss mechanism and the methods developed for discrete Coulomb collisions could be used for NES in a future code. NES, especially between neutrons and ions, is considered to be the key to athermal chains of fusion reactions, as reviewed in §6.2. There are other processes involving neutrons, such as break-up reactions, and the inelastic scattering processes, that would also be desirable but would have a smaller effect on the evolution of distribution functions due to their smaller cross-sections. Some consideration should be given to the other high energy scattering phenomena such as spin, indistinguishability, and finite-size particles.

Further work on athermal fusion which included the effects of degeneracy, large-angle Coulomb collisions *and* NES would give a very strong indication as to whether the chains of fusion reactions could ever produce runaway reactions. Another possibility to explore is whether the inclusion of energy loss mechanisms could actually make the chain stronger by limiting the energies in the tail of the ion distribution functions (whilst maintaining their probability density).

The computational diagnosis of the simulations presented is a focus for future research, particularly the equivalent bulk temperature and percentage of particles not in equilibrium (in the context of non-Maxwellian distributions). From Figs. 7.13 and 7.23 it is clear that even small deviations from a Maxwellian produce significant changes to fusion reactivity. A robust metric is needed, and would allow for better comparisons with other work.

A highly desirable diagnostic capability is that of a time-integrated neutron spectrum. This would shed further light on any athermal fusion reactions taking place in the tails of

distribution functions as (without NES) neutrons are 'frozen in' after they are produced. Thermal broadening of the neutron energy spectrum above 15 MeV would be an indication that tail reactions are happening, even in the simulations where ions are only transiently in the athermal tail (such as $b_c = b_\perp$). A combination of neutron spectra and NES would allow any microphysics effects of large-angle collisions on the important down-scattered neutron ratio (dsr) to be determined. Given that this is a measurable parameter of huge importance to the NIF campaign for ignition (dsr being directly proportional to ρR to first order), a change in dsr due to any distortion away from a Maxwellian would be significant.

The results presented are mostly concerned with nuclear fusion using deuterium and tritium through the central ignition scheme being pursued at NIF. However, there are many other prospective fusion schemes which could also be influenced by large-angle collisions. There is already some work on large-angle collisions in MCF, and modelling the experimentally observed data, with the inclusion of NES, is one attractive future option. It would also be of interest to consider the effect of discrete and large-angle collisions on fusion schemes which have yet to be explored with a full scale experimental facility, including magnetised liner inertial fusion [161, 162] and shock ignition [100].

Appendix A

Mathematical functions

The lower incomplete gamma function:

$$\Gamma(z,x) = \frac{2}{\sqrt{\pi}} \int_0^x t^{z-1} e^{-t} \mathrm{d}t$$

The gamma function:

$$\Gamma(z) = \frac{2}{\sqrt{\pi}} \int_0^\infty t^{z-1} e^{-t} \mathrm{d}t = \lim_{x \longrightarrow \infty} \Gamma(z,x)$$

The jth complete Fermi-Dirac integral:

$$I_j(\eta) = \frac{1}{\Gamma(j+1)} \int_0^\infty \frac{t^j}{e^{t-x}+1} \mathrm{d}t$$

The error function:

$$\mathrm{erf}\,(x) = \frac{2}{\sqrt{\pi}} \int_0^x e^{-t^2} \mathrm{d}t = \frac{1}{2} \Gamma\left(1/2, x^2\right)$$

The generalised Riemann zeta function:

$$\zeta(x,z) = \sum_{n=0}^{\infty} \frac{1}{(z+n)^x}$$

Volterra equations (of the second kind):

$$g(x) = f(x) + \int_{x_0}^x K\left(x, y, g(y)\right) \mathrm{d}y, \qquad x_0 \leq x$$

where $K\left(x, y, g(y)\right)$ and $f(x)$ are known, and g is unknown.

Appendix B

Landau-Spitzer theory

This appendix summarises the Landau-Spitzer equations of a plasma [28, 29, 18] in SI units for a test particle i in a background field of particles j with a Maxwellian distribution. The convention in this work is that the change is the energy or momentum *lost* by i to j. The relaxation times are given by $1/\nu_{ij} = \tau_{ij}$. Also,

$$x_{ij} = \frac{m_j v_i^2}{2T_j}$$

$\Gamma(3/2, x) \equiv \Gamma_{\frac{3}{2}}(x)$ is the lower incomplete gamma function defined in Appendix A, and is calculated numerically [57] in the Monte Carlo code.

$$\nu_{ij} = \frac{4\pi \ln \Lambda_{ij} n_j}{m_i^2 v_i^3} \left(\frac{e^2 q_i q_j}{4\pi\epsilon_0} \right)^2$$

Energy loss:

$$\frac{\mathrm{d}E_i}{\mathrm{d}t} = \nu_{ij}^E E_i = 2\nu_{ij} \left[\frac{m_i}{m_j} \Gamma_{\frac{3}{2}}(x_{ij}) - \Gamma'_{\frac{3}{2}}(x_{ij}) \right] E_i$$

Slowing down:

$$\frac{\mathrm{d}\mathbf{v}_i}{\mathrm{d}t} = \nu_{ij}^s \mathbf{v}_i = \nu_{ij} \left(1 + \frac{m_i}{m_j} \right) \Gamma_{\frac{3}{2}}(x_{ij}) \mathbf{v}_i$$

Transverse diffusion:

$$\frac{\mathrm{d}}{\mathrm{d}t} \left(\mathbf{v}_i - \bar{\mathbf{v}}_i \right)_\perp^2 = \nu_{ij}^\perp v_i^2 = 2\nu_{ij} \left[\left(1 - \frac{1}{2x_{ij}} \right) \Gamma_{\frac{3}{2}}(x_{ij}) + \Gamma'_{\frac{3}{2}}(x_{ij}) \right] v_i^2$$

Parallel diffusion:

$$\frac{\mathrm{d}}{\mathrm{d}t} \left(\mathbf{v}_i - \bar{\mathbf{v}}_i \right)_\parallel^2 = \nu_{ij}^\parallel v_i^2 = \nu_{ij} \frac{\Gamma_{\frac{3}{2}}(x_{ij})}{x_{ij}} v_i^2$$

Equilibration between two Maxwellian distributions; the change in temperature of species i is:

$$\frac{\mathrm{d}T_{ij}}{\mathrm{d}t} = \nu_{ij}^{T}\left(T_j - T_i\right)$$

$$\nu_{ij}^{T} = \frac{8\sqrt{\pi}}{3}\frac{\sqrt{2m_i}}{m_j}\left(\frac{e^2 q_i q_j}{4\pi\epsilon_0}\right)^2 \ln\Lambda_{ij} n_j \left(T_i + \frac{m_i}{m_j}T_j\right)^{-3/2} \tag{B.1}$$

Appendix C

Fusion cross-section

Fusion reactivity is given by

$$\langle \sigma_{\mathrm{F}} v_{ij} \rangle = \int \int f_i(\mathbf{v}_i) f_j(\mathbf{v}_j) \sigma_{\mathrm{F}}(v_{ij}) v_{ij} \mathrm{d}\mathbf{v}_i \mathrm{d}\mathbf{v}_j \tag{C.1}$$

in units of volume per unit time; reactions per unit volume per unit time are given by

$$\frac{\mathrm{d}R}{\mathrm{d}V} = \frac{n_i n_j}{1+\delta_{ij}} \langle \sigma_{\mathrm{F}} v_{ij} \rangle$$

This work is only concerned with fusion between Deuterium and Tritium, the T(d,n)^{4}He reaction. The Bosch and Hale [60] fusion cross-section parametrisation is used, with energy in keV and cross-sections in milli-barns;

$$\sigma_F(E) = \frac{S(E)}{E \exp B_G/\sqrt{E}}$$

where

$$S(E) = \frac{A_1 + E(A_2 + E(A_3 + E(A_4 + E \cdot A_5)))}{1 + E(B_1 + E(B_2 + E(B_3 + E \cdot B_4)))}$$

It is applicable for $E = 0.5 - 559$ keV.

Due to the difficultly of evaluating equation (C.1), a parametrisation of $\langle \sigma_{\mathrm{F}} v_{ij} \rangle$ averaged over Maxwellian distributions at a temperature T is used, also due to Bosch and Hale

and so consistent with the fusion cross-section.

$$\langle \sigma_{\mathrm{F}} v_{ij} \rangle = C_1 \cdot \theta \sqrt{\xi/(m_r c^2 T^3)} e^{-3\xi}$$
$$\theta = T \left[1 - \frac{T(C_2 + T(C_4 + T \cdot C_6))}{1 + T(C_3 + T(C_5 + T \cdot C_7))} \right]^{-1}$$
$$\xi = \left(\frac{B_G^2}{4\theta} \right)^{1/3}$$

It is applicable for $T = 0.2 - 100$ keV. The values of the constants are shown in Table C.1

Coefficient	Value
$B_G \left(\sqrt{\mathrm{keV}}\right)$	34.3827
A_1	6.927×10^4
A_2	7.454×10^8
A_3	2.050×10^6
A_4	5.2002×10^4
A_5	0
B_1	6.38×10^1
B_2	-9.95×10^{-1}
B_3	6.981×10^{-5}
B_4	1.728×10^{-4}
$m_r c^2$ (keV)	1124656
C_1	1.17302×10^{-9}
C_2	1.51361×10^{-2}
C_3	7.51886×10^{-2}
C_4	4.60643×10^{-3}
C_5	1.35000×10^{-2}
C_6	-1.06750×10^{-4}
C_7	1.36600×10^{-5}

Table C.1: Fusion parametrisation values

Appendix D

ICF Parameters

Table D.1 shows typical parameters [21, 23, 163, 24] of an indirect-drive central ignition implosion using deuterium and tritium. 'HS' refers to hotspot, fuel to the dense fuel shell, and values given are indicative rather than exact. As a burning capsule has different behaviour to a one which does not ignite, the values for an igniting capsule with α energy deposition are used.

Quantity	Value
$(\rho R)_{\mathrm{HS}}$	0.4 g/cm^2
$(\rho R)_{\mathrm{fuel}}$	1 g/cm^2
R_{HS}	35 μm
ρ_{HS}	100 g/cm^3
ρ_{fuel}	1000 g/cm^3
Fuel layer thickness	10μm
T_{HS}	5 keV
dsr	0.07
t_{burn}	18 ps
t_{bang}	21 ns
Peak laser power	500TW
Fuel mass	0.2 mg
Total mass of capsule	3 mg
Capsule diameter	2 mm
Implosion velocity	370 km/s

Table D.1: Typical values of ICF parameters

References

[1] H. G. Wells. *The World Set Free*. Macmillan & Co., 1914. 22

[2] G. McCracken and P. Stott. *Fusion: The Energy of the Universe*. Elsevier, 2005. 22, 23, 24

[3] C. M. Braams and P. E. Stott. *Nuclear fusion: Half a century of magnetic confinement fusion research*. Institute of Physics Publishing, 2002. 22

[4] J. L. Bromberg. *Fusion: Science, Politics, and the Invention of a New Energy Source*. The MIT Press, 1982. 22

[5] R. Carruthers. The beginning of fusion at Harwell. *Plasma Physics and Controlled Fusion*, 30(14):1993, 1988. 22

[6] F. M. Szas. *The Day the Sun Rose Twice: The Story of the Trinity Site Nuclear Explosion*. University of New Mexico Press, 1955. 22

[7] E. Teller. *Energy from Heaven and Earth*. W. H. Freeman and Co. Limited, 1979. 22

[8] R. Herman. *Fusion: The Search for Endless Energy*. Cambridge University Press, 1990. 22, 24

[9] J. Nuckolls. Grand challenges of inertial fusion energy. In *Inertial Fusion Sciences and Applications (IFSA)*, 2009. 23

[10] T. H. Maiman. Optical and microwave-optical experiments in ruby. *Phys. Rev. Lett.*, 4:564–566, Jun 1960. 23

[11] R. G. Evans. UK fusion breakthrough revealed at last. *Physics World*, page 23, March 2010. 24

[12] BP Statistical Review of World Energy 2013. Technical report, BP, 2013. 25, 27

[13] United Nations Department of Economic and Social Affairs/Population Division. World population to 2300. Technical report, United Nations, 2004. 25

[14] J. Anderson, J. Thundiyil, and A. Stolbach. Clearing the air: A review of the effects of particulate matter air pollution on human health. *Journal of Medical Toxicology*, 8(2):166–175, 2012. 25

[15] Department for Environment, Food, and Rural Affairs (DEFRA). Avoiding dangerous climate change. In *Scientific Symposium on Stabilisation of Greenhouse Gases*, 2005. 26

[16] D. J. C. MacKay. *Sustainable Energy - without the hot air*. UIT Cambridge, 2009. 27

[17] S. Atezni and J. Meyer-ter-Vehn. *The Physics of Inertial Fusion*. Number 125 in The International Series of Monographs on Physics. Oxford Science Publications, 2004. 28, 29

[18] Naval Research Laboratory. *NRL Plasma Formulary*. United States Navy, 2009. 19, 29, 62, 173

[19] J. D. Lawson. Some criteria for a power producing thermonuclear reactor. *Proceedings of the Physical Society. Section B*, 70(1):6, 1957. 29

[20] G. S. Fraley, E. J. Linnebur, R. J. Mason, and R. L. Morse. Thermonuclear burn characteristics of compressed deuterium-tritium microspheres. *Physics of Fluids*, 17(2):474–489, 1974. 30

[21] J. D. Lindl. Development of the indirect-drive approach to inertial confinement fusion and the target physics basis for ignition and gain. *Physics of Plasmas*, 2(11):3933–4024, 1995. 30, 31, 73, 177

[22] S. H. Glenzer, D. A. Callahan, A. J. MacKinnon, J. L. Kline, G. Grim, E. T. Alger, R. L. Berger, L. A. Bernstein, R. Betti, D. L. Bleuel, T. R. Boehly, D. K. Bradley, S. C. Burkhart, R. Burr, J. A. Caggiano, C. Castro, D. T. Casey, C. Choate, D. S. Clark, P. Celliers, C. J. Cerjan, G. W. Collins, E. L. Dewald, P. DiNicola, J. M. DiNicola, L. Divol, S. Dixit, T. Döppner, R. Dylla-Spears, E. Dzenitis, M. Eckart, G. Erbert, D. Farley, J. Fair, D. Fittinghoff, M. Frank, L. J. A. Frenje, S. Friedrich, D. T. Casey, M. Gatu Johnson, C. Gibson, E. Giraldez, V. Glebov, S. Glenn, N. Guler, S. W. Haan, B. J. Haid, B. A. Hammel, A. V. Hamza, C. A. Haynam, G. M. Heestand, M. Hermann, H. W. Hermann, D. G. Hicks, D. E. Hinkel, J. P.

Holder, D. M. Holunda, J. B. Horner, W. W. Hsing, H. Huang, N. Izumi, M. Jackson, O. S. Jones, D. H. Kalantar, R. Kauffman, J. D. Kilkenny, R. K. Kirkwood, J. Klingmann, T. Kohut, J. P. Knauer, J. A. Koch, B. Kozioziemki, G. A. Kyrala, A. L. Kritcher, J. Kroll, K. La Fortune, L. Lagin, O. L. Landen, D. W. Larson, D. LaTray, R. J. Leeper, S. Le Pape, J. D. Lindl, R. Lowe-Webb, T. Ma, J. McNaney, A. G. MacPhee, T. N. Malsbury, E. Mapoles, C. D. Marshall, N. B. Meezan, F. Merrill, P. Michel, J. D. Moody, A. S. Moore, M. Moran, K. A. Moreno, D. H. Munro, B. R. Nathan, A. Nikroo, R. E. Olson, C. D. Orth, A. E. Pak, P. K. Patel, T. Parham, R. Petrasso, J. E. Ralph, H. Rinderknecht, S. P. Regan, H. F. Robey, J. S. Ross, M. D. Rosen, R. Sacks, J. D. Salmonson, R. Saunders, J. Sater, C. Sangster, M. B. Schneider, F. H. Séguin, M. J. Shaw, B. K. Spears, P. T. Springer, W. Stoefflı, L. J. Suter, C. A. Thomas, R. Tommasini, R. P. J. Town, C. Walters, S. Weaver, S. V. Weber, P. J. Wegner, P. K. Whitman, K. Widmann, C. C. Widmayer, C. H. Wilde, D. C. Wilson, B. Van Wonterghem, B. J. MacGowan, L. J. Atherton, M. J. Edwards, and E. I. Moses. Cryogenic thermonuclear fuel implosions on the national ignition facility. *Physics of Plasmas*, 19(5):056318, 2012. 30

[23] M. J. Edwards, J. D. Lindl, B. K. Spears, S. V. Weber, L. J. Atherton, D. L. Bleuel, D. K. Bradley, D. A. Callahan, C. J. Cerjan, D Clark, G. W. Collins, J. E. Fair, R. J. Fortner, S. H. Glenzer, S. W. Haan, B. A. Hammel, A. V. Hamza, S. P. Hatchett, N. Izumi, B. Jacoby, O. S. Jones, J. A. Koch, B. J. Kozioziemski, O. L. Landen, R. Lerche, B. J. MacGowan, A. J. MacKinnon, E. R. Mapoles, M. M. Marinak, M. Moran, E. I. Moses, D. H. Munro, D. H. Schneider, S. M. Sepke, D. A. Shaughnessy, P. T. Springer, R. Tommasini, L. Bernstein, W. Stoeffl, R. Betti, T. R. Boehly, T. C. Sangster, V. Yu. Glebov, P. W. McKenty, S. P. Regan, D. H. Edgell, J. P. Knauer, C. Stoeckl, D. R. Harding, S. Batha, G. Grim, H. W. Herrmann, G. Kyrala, M. Wilke, D. C. Wilson, J. Frenje, R. Petrasso, K. Moreno, H. Huang, K. C. Chen, E. Giraldez, J. D. Kilkenny, M. Mauldin, N. Hein, M. Hoppe, A. Nikroo, and R. J. Leeper. The experimental plan for cryogenic layered target implosions on the national ignition facility—the inertial confinement approach to fusion. *Physics of Plasmas*, 18(5):051003, 2011. 34, 46, 107, 123, 143, 177

[24] A. J. Mackinnon, J. L. Kline, S. N. Dixit, S. H. Glenzer, M. J. Edwards, D. A. Callahan, N. B. Meezan, S. W. Haan, J. D. Kilkenny, T. Döppner, D. R. Farley, J. D. Moody, J. E. Ralph, B. J. MacGowan, O. L. Landen, H. F. Robey, T. R. Boehly, P. M. Celliers, J. H. Eggert, K. Krauter, G. Frieders, G. F. Ross, D. G. Hicks, R. E. Olson, S. V. Weber, B. K. Spears, J. D. Salmonsen, P. Michel, L. Divol,

B. Hammel, C. A. Thomas, D. S. Clark, O. S. Jones, P. T. Springer, C. J. Cerjan, G. W. Collins, V. Y. Glebov, J. P. Knauer, C. Sangster, C. Stoeckl, P. McKenty, J. M. McNaney, R. J. Leeper, C. L. Ruiz, G. W. Cooper, A. G. Nelson, G. G. A. Chandler, K. D. Hahn, M. J. Moran, M. B. Schneider, N. E. Palmer, R. M. Bionta, E. P. Hartouni, S. LePape, P. K. Patel, N. Izumi, R. Tommasini, E. J. Bond, J. A. Caggiano, R. Hatarik, G. P. Grim, F. E. Merrill, D. N. Fittinghoff, N. Guler, O. Drury, D. C. Wilson, H. W. Herrmann, W. Stoeffl, D. T. Casey, M. G. Johnson, J. A. Frenje, R. D. Petrasso, A. Zylestra, H. Rinderknecht, D. H. Kalantar, J. M. Dzenitis, P. Di Nicola, D. C. Eder, W. H. Courdin, G. Gururangan, S. C. Burkhart, S. Friedrich, D. L. Blueuel, l. A. Bernstein, M. J. Eckart, D. H. Munro, S. P. Hatchett, A. G. Macphee, D. H. Edgell, D. K. Bradley, P. M. Bell, S. M. Glenn, N. Simanovskaia, M. A. Barrios, R. Benedetti, G. A. Kyrala, R. P. J. Town, E. L. Dewald, J. L. Milovich, K. Widmann, A. S. Moore, G. LaCaille, S. P. Regan, L. J. Suter, B. Felker, R. C. Ashabranner, M. C. Jackson, R. Prasad, M. J. Richardson, T. R. Kohut, P. S. Datte, G. W. Krauter, J. J. Klingman, R. F. Burr, T. A. Land, M. R. Hermann, D. A. Latray, R. L. Saunders, S. Weaver, S. J. Cohen, L. Berzins, S. G. Brass, E. S. Palma, R. R. Lowe-Webb, G. N. McHalle, P. A. Arnold, L. J. Lagin, C. D. Marshall, G. K. Brunton, D. G. Mathisen, R. D. Wood, J. R. Cox, R. B. Ehrlich, K. M. Knittel, M. W. Bowers, R. A. Zacharias, B. K. Young, J. P. Holder, J. R. Kimbrough, T. Ma, K. N. La Fortune, C. C. Widmayer, M. J. Shaw, G. V. Erbert, K. S. Jancaitis, J. M. DiNicola, C. Orth, G. Heestand, R. Kirkwood, C. Haynam, P. J. Wegner, P. K. Whitman, A. Hamza, E. G. Dzenitis, R. J. Wallace, S. D. Bhandarkar, T. G. Parham, R. Dylla-Spears, E. R. Mapoles, B. J. Kozioziemski, J. D. Sater, C. F. Walters, B. J. Haid, J. Fair, A. Nikroo, E. Giraldez, K. Moreno, B. Vanwonterghem, R. L. Kauffman, S. Batha, D. W. Larson, R. J. Fortner, D. H. Schneider, J. D. Lindl, R. W. Patterson, L. J. Atherton, and E. I. Moses. Assembly of high-areal-density deuterium-tritium fuel from indirectly driven cryogenic implosions. *Phys. Rev. Lett.*, 108:215005, May 2012. 34, 177

[25] O. S. Jones, C. J. Cerjan, M. M. Marinak, J. L. Milovich, H. F. Robey, P. T. Springer, L. R. Benedetti, D. L. Bleuel, E. J. Bond, D. K. Bradley, D. A. Callahan, J. A. Caggiano, P. M. Celliers, D. S. Clark, S. M. Dixit, T. Doppner, R. J. Dylla-Spears, E. G. Dzentitis, D. R. Farley, S. M. Glenn, S. H. Glenzer, S. W. Haan, B. J. Haid, C. A. Haynam, D. G. Hicks, B. J. Kozioziemski, K. N. LaFortune, O. L. Landen, E. R. Mapoles, A. J. MacKinnon, J. M. McNaney, N. B. Meezan, P. A. Michel, J. D. Moody, M. J. Moran, D. H. Munro, M. V. Patel, T. G. Parham, J. D. Sater, S. M. Sepke, B. K. Spears, R. P. J. Town, S. V. Weber, K. Widmann, C. C. Widmayer, E. A. Williams, L. J. Atherton, M. J. Edwards, J. D. Lindl,

B. J. MacGowan, L. J. Suter, R. E. Olson, H. W. Herrmann, J. L. Kline, G. A. Kyrala, D. C. Wilson, J. Frenje, T. R. Boehly, V. Glebov, J. P. Knauer, A. Nikroo, H. Wilkens, and J. D. Kilkenny. A high-resolution integrated model of the national ignition campaign cryogenic layered experiments. *Physics of Plasmas*, 19(5):056315, 2012. 34

[26] B. K. Spears, S. Glenzer, M. J. Edwards, S. Brandon, D. Clark, R. Town, C. Cerjan, R. Dylla-Spears, E. Mapoles, D. Munro, J. Salmonson, S. Sepke, S. Weber, S. Hatchett, S. Haan, P. Springer, E. Moses, J. Kline, G. Kyrala, and D. Wilson. Performance metrics for inertial confinement fusion implosions: Aspects of the technical framework for measuring progress in the national ignition campaign. *Physics of Plasmas*, 19(5):056316, 2012. 34

[27] T. J. M. Boyd and J. J. Sanderson. *The Physics of Plasmas*. Cambridge University Press, 2003. 37, 51, 85

[28] L. Spitzer, Jr. *Physics of Fully Ionised Gases*. Interscience, New York, 1967. 38, 53, 65, 67, 173

[29] B. A. Trubnikov. *Reviews of Plasma Physics*, volume 1. Consultants Bureau, 1965. 38, 43, 50, 53, 65, 105, 106, 109, 173

[30] L. D. Landau and E. M. Lifshitz. *Mechanics*, volume 1 of *Course of Theoretical Physics*. Elsevier, 1976. 39

[31] J. D. Jackson. *Classical Electrodynamics*. John Wiley and Sons, 2nd edition, 1962. 42, 45, 61, 118

[32] D. O. Gericke, M. S. Murillo, and M. Schlanges. Dense plasma temperature equilibration in the binary collision approximation. *Phys. Rev. E*, 65:036418, Mar 2002. 44, 45, 48, 75

[33] C. A. Ordonez and M. I. Molina. Evaluation of the Coulomb logarithm using cutoff and screened Coulomb interaction potentials. *Physics of Plasmas*, 1(8):2515–2518, 1994. 45

[34] L. S. Brown, D. L. Preston, and R. L. Singleton, Jr. Charged particle motion in a highly ionized plasma. *Physics Reports*, 410(4):237 – 333, 2005. 45

[35] B. Xu and S. X. Hu. Effects of electron-ion temperature equilibration on inertial confinement fusion implosions. *Phys. Rev. E*, 84:016408, Jul 2011. 45, 73

[36] S. D. Baalrud. Transport coefficients in strongly coupled plasmas. *Physics of Plasmas*, 19(3):030701, 2012. 45

[37] L. X. Benedict, J. N. Glosli, D. F. R., F. H. Streitz, S. P. Hau-Riege, R. A. London, F. R. Graziani, M. S. Murillo, and J. F. Benage. Molecular dynamics simulations of electron-ion temperature equilibration in an $\mathbf{Sf}_6$ plasma. *Phys. Rev. Lett.*, 102:205004, May 2009. 45

[38] N. David and S. M. Hooker. Molecular-dynamic calculation of the relaxation of the electron energy distribution function in a plasma. *Phys. Rev. E*, 68:056401, Nov 2003. 45, 53

[39] G. A. Mourou, N. Naumova C. L. Labaune, M. Dunne, and V. T. Tikhonchuk. Relativistic laser-matter interaction: from attosecond pulse generation to fast ignition. *Plasma Phys. Control. Fusion*, 49:B667, 2007. 46, 89, 107

[40] Y. Setsuhara, H. Azechi, N. Miyanaga, H. Furukawa, R. Ishizaki, K. Nishihara, M. Katayama, A. Nishiguchi, K. Mima, and S. Nakai. Secondary nuclear fusion reactions as evidence of electron degeneracy in highly compressed fusion fuel. *Laser and Particle Beams*, 8(04):609–620, 1990. 46, 73, 107

[41] J. P. Cox and R. T. Giuli. *Principles of stellar structure volume II: applications to stars*. Gordon and Breach Science Publishers, 1968. 46, 73, 107

[42] S. J. Rose. The effect of degeneracy on the scattering contribution to the radiative opacity. *The Astrophysical Journal Letters*, 453(1):L45, 1995. 46, 107

[43] L. D. Landau and E. M. Lifshitz. *Statistical Physics Part I*, volume 5 of *Course of Theoretical Physics*. Elsevier, 3rd edition, 1980. 49

[44] L. D. Landau and E. M. Lifshitz. *Physical Kinetics*, volume 10 of *Course of Theoretical Physics*. Elsevier, 1981. 49

[45] N. N. Bogoliubov. Kinetic Equations. *Journal of Physics (USSR)*, 10:265–274, 1946. 49

[46] S. Chandrasekhar. Stochastic problems in physics and astronomy. *Rev. Mod. Phys.*, 15:1–89, Jan 1943. 50, 110

[47] M. N. Rosenbluth, W. M. MacDonald, and D. L. Judd. Fokker-Planck equation for an inverse-square force. *Phys. Rev.*, 107:1–6, Jul 1957. 51

[48] C.-K. Li and R. D. Petrasso. Fokker-Planck equation for moderately coupled plasmas. *Phys. Rev. Lett.*, 70:3063–3066, May 1993. 51, 107, 109, 127, 143, 165

[49] R. Dendy. *Plasma Physics: An introductory course*. Cambridge University Press, 1993. 51, 52

[50] T. Takizuka and H. Abe. A binary collision model for plasma simulation with a particle code. *Journal of Computational Physics*, 25:205–219, 1977. 53, 60, 126, 137

[51] N. Metropolis. The beginning of the Monte Carlo method. *Los Alamos Science*, 15:125–130, 1987. 53

[52] N. Metropolis, A. W. Rosenbluth, M. N. Rosenbluth, A. H. Teller, and E. Teller. Equation of state calculations by fast computing machines. *The Journal of Chemical Physics*, 21(6):1087–1092, 1953. 53

[53] A. B. Langdon. Nonlinear inverse bremsstrahlung and heated-electron distributions. *Phys. Rev. Lett.*, 44:575–579, Mar 1980. 53, 87

[54] R. D. Jones and K. Lee. Kinetic theory, transport, and hydrodynamics of a high-z plasma in the presence of an intense laser field. *Physics of Fluids*, 25(12):2307–2323, 1982. 53, 87, 95

[55] R. H. Miller and M. R. Combi. A coulomb collision algorithm for weighted particle simulations. *Geophysical Research Letters*, 21(16):1735–1738, 1994. 54

[56] K. Nanbu. Theory of cumulative small-angle collisions in plasmas. *Phys. Rev. E*, 55:4642–4652, Apr 1997. 54

[57] W. H. Press, W. T. Vetterling, S. A. Teukolsky, and B. P. Flannery. *Numerical Recipes in C++*. Cambridge University Press, 2nd edition, 2002. 54, 77, 113, 173

[58] G. E. P. Box and M. E. Muller. A note on the generation of random normal deviates. *The Annals of Mathematical Statistics*, 29(2):pp. 610–611, 1958. 57, 61

[59] R. Durstenfeld. Algorithm 235: Random permutation. *Commun. ACM*, 7(7):420, July 1964. 60

[60] H.-S. Bosch and G. M. Hale. Improved formulas for fusion cross-sections and thermal reactivities. *Nuclear Fusion*, 32(4):611, 1992. 62, 175

[61] E. M. Epperlein and M. G. Haines. Plasma transport coefficients in a magnetic field by direct numerical solution of the Fokker–Planck equation. *Physics of Fluids*, 29(4):1029–1041, 1986. 14, 67, 68, 69

[62] S. I. Braginskii. *Reviews of Plasma Physics*, volume 1. Consultants Bureau, 1965. 67

[63] A. E. Turrell, M. Sherlock, and S. J. Rose. A Monte Carlo algorithm for degenerate plasmas. *Journal of Computational Physics*, 249(0):13 – 21, 2013. 73, 163

[64] A. L. Kritcher, T. Döppner, C. Fortmann, T. Ma, O. L. Landen, R. Wallace, and S. H. Glenzer. In-flight measurements of capsule shell adiabats in laser-driven implosions. *Phys. Rev. Lett.*, 107:015002, Jul 2011. 73

[65] S. Son and N. J. Fisch. Ignition regime for fusion in a degenerate plasma. *Physics Letters A*, 356(1):72 – 78, 2006. 73, 119

[66] P. Lugli and D. K. Ferry. Degeneracy in the ensemble Monte Carlo method for high-field transport in semiconductors. *Electron Devices, IEEE Transactions on*, 32(11):2431 – 2437, nov 1985. 74

[67] C. Kittel. *Introduction to Solid State Physics*. John Wiley and Sons, Inc, 2005. 74

[68] Y. T. Lee and R. M. More. An electron conductivity model for dense plasmas. *Physics of Fluids*, 27(5):1273–1286, 1984. 75

[69] L. S. Brown and R. L. Singleton. Temperature equilibration rate with Fermi-Dirac statistics. *Phys. Rev. E*, 76:066404, Dec 2007. 75, 76

[70] S. R. Brown and M. G. Haines. Transport in partially degenerate, magnetized plasmas. Part 2. Numerical calculation of transport coefficients. *Journal of Plasma Physics*, 62(02):129–144, 1999. 75

[71] H. Brysk, P. M. Campbell, and P. Hammerling. Thermal conduction in laser fusion. *Plasma Physics*, 17(6):473, 1975. 75

[72] E. E. Salpeter. Electrons Screening and Thermonuclear Reactions. *Australian Journal of Physics*, 7:373, September 1954. 75

[73] W. Hörmann and J. Leydold. Continuous random variate generation by fast numerical inversion. *ACM Transactions on Modelling and Computer Simulation (TOMACS)*, 13:4:347–362, 2003. 75, 76

[74] C. de Boor and B. Swartz. Piecewise monotone interpolation. *Journal of Approximation Theory*, 21(4):411 – 416, 1977. 76

[75] H.-C. Chen and Y. Asau. On generating random variates from an empirical distribution. *A I I E Transactions*, 6(2):163–166, 1974. 76

[76] H. Brysk. Electron-ion equilibration in a partially degenerate plasma. *Plasma Physics*, 16(10):927, 1974. 76, 79

[77] L. Schlessinger and J. Wright. Inverse-bremsstrahlung absorption rate in an intense laser field. *Phys. Rev. A*, 20:3:1934–1945, 1979. 85

[78] P. Gibbon. *Short Pulse Laser Interactions with Matter: An Introduction*. Imperial College Press, 2005. 85

[79] Y. Y. Lau, F. He, D. P. Umstadter, and R. Kowalczyk. Nonlinear Thomson scattering: A tutorial. *Physics of Plasmas*, 10(5):2155–2162, 2003. 86

[80] R. Balescu. Heating of electrons and ions by inverse bremsstrahlung absorption: a self-similar state of the plasma. *Journal of Plasma Physics*, 27:553–570, 5 1982. 87

[81] C. T. Dum. Anomalous heating by ion sound turbulence. *Physics of Fluids*, 21(6):945–955, 1978. 87

[82] J. P. Matte, M. Lamoureux, C. Moller, R. Y. Yin, J. Delettrez, J. Virmont, and T. W. Johnston. Non-Maxwellian electron distributions and continuum x-ray emission in inverse bremsstrahlung heated plasmas. *Plasma Physics and Controlled Fusion*, 30(12):1665, 1988. 87

[83] P. Mora and H. Yahi. Thermal heat-flux reduction in laser-produced plasmas. *Phys. Rev. A*, 26:2259–2261, Oct 1982. 87

[84] N. David, D. J. Spence, and S. M. Hooker. Molecular-dynamic calculation of the inverse-bremsstrahlung heating of non-weakly-coupled plasmas. *Phys. Rev. E*, 70:056411, Nov 2004. 88

[85] S.-M. Weng, Z.-M. Sheng, and J. Zhang. Inverse bremsstrahlung absorption with nonlinear effects of high laser intensity and non-Maxwellian distribution. *Phys. Rev. E*, 80:056406, Nov 2009. 88

[86] C. P. Ridgers, A. G. R. Thomas, R. J. Kingham, and A. P. L. Robinson. Transport in the presence of inverse bremsstrahlung heating and magnetic fields. *Physics of Plasmas*, 15(9):092311, 2008. 88

[87] J. J. Bissell, C. P. Ridgers, and R. J. Kingham. Super-gaussian transport theory and the field-generating thermal instability in laser-plasmas. *New Journal of Physics*, 15(2):025017, 2013. 88

[88] T. J. Birmingham, J. M. Dawson, and R. M. Kulsrud. Contribution of electron-electron collisions to the emission of bremsstrahlung by a plasma. *Physics of Fluids*, 9(10):2014–2025, 1966. 89

[89] K. Papadopoulos. Enhanced bremsstrahlung from plasmas with relativistic electron tails. *Physics of Fluids*, 12(10):2185–2193, 1969. 89

[90] R. C. Mjolsness and H. M. Ruppel. Deuterium-tritium heating to thermonuclear temperatures by means of ion-ion collisions in the presence of intense laser radiation. *Phys. Fluids*, 15:9:1620–1629, 1972. 89

[91] B. M. Hegelich, B. J. Albright, J. Cobble, K . Flippo, S. Letzring, M. Paffet, H. Ruhl, J. Schreiber, R. K. Schulze, and J. C. Fernandez. Laser acceleration of quasi-monoenergetic MeV ion beams. *Nature*, 439:441–444, 2006. 89

[92] T. Esirkepov, M. Borghesi, S. V. Bulanov, G. Mourou, and T. Tajima. Highly efficient relativistic-ion generation in the laser-piston regime. *Phys. Rev. Lett.*, 92:175003, Apr 2004. 89, 91

[93] A. P. L. Robinson, M. Zepf, S. Kar, R. G. Evans, and C. Bellei. Radiation pressure acceleration of thin foils with circularly polarized laser pulses. *New Journal of Physics*, 10:013021, 2008. 89, 91

[94] Y. Ping, R. Shepherd, B. F. Lasinski, M. Tabak, H. Chen, H. K. Chung, K. B. Fournier, S. B. Hansen, A. Kemp, D. A. Liedahl, K. Widmann, S. C. Wilks, W. Rozmus, and M. Sherlock. Absorption of short laser pulses on solid targets in the ultrarelativistic regime. *Phys. Rev. Lett.*, 100:085004, 2008. 89

[95] S.-W. Bahk, P. Rousseau, T. A. Planchon, V. Chvykov, G. Kalintchenko, A. Maksimchuk, G. A. Mourou, and V. Yanovsky. Generation and characterization of the highest laser intensities. *Optics Letters*, 29:24:2837, 2004. 89

[96] J. G. Kirk, A. R. Bell, and I. Arka. Pair production in counter-propagating laser beams. *Plasma Physics and Controlled Fusion*, 51:085008, 2009. 89

[97] S. S. Bulanov, T. Z. Esirkepov, A. G. R. Thomas, J. K. Koga, and S. V. Bulanov. Schwinger limit attainability with extreme power lasers. *Phys. Rev. Lett.*, 105:220407, Nov 2010. 89

[98] E. N. Nerush, I. Yu. Kostyukov, A. M. Fedotov, N. B. Narozhny, N. V. Elkina, and H. Ruhl. Laser field absorption in self-generated electron-positron pair plasma. *Phys. Rev. Lett.*, 106:035001, Jan 2011. 89

[99] C. P. Ridgers, C. S. Brady, R. Duclous, J. G. Kirk, K. Bennett, T. D. Arber, A. P. L. Robinson, and A. R. Bell. Dense electron-positron plasmas and ultra-intense bursts of gamma-rays from laser-irradiated solids. *Phys. Rev. Lett.*, 108:165006, 2012. 89

[100] R. Betti, C. D. Zhou, K. S. Anderson, L. J. Perkins, W. Theobald, and A. A. Solodov. Shock ignition of thermonuclear fuel with high areal density. *Phys. Rev. Lett.*, 98:155001, Apr 2007. 89, 169

[101] M. Roth, T. E. Cowan, M. H. Key, S. P. Hatchett, C. Brown, W. Fountain, J. Johnson, D. M. Pennington, R. A. Snavely, S. C. Wilks, et al. Fast ignition by intense laser-accelerated proton beams. *Phys. Rev. Lett.*, 86(3):436–439, 2001. 89

[102] S. V. Bulanov and V. S. Khoroshkov. Feasibility of using laser ion accelerators in proton therapy. *Plasma Physics Reports*, 28:5:453–456, 2002. 89, 91

[103] T. M. O'Neil. Trapped plasmas with a single sign of charge. *Physics Today*, 52(2):24–30, 1999. 90

[104] S. C. Wilks, A. B. Langdon, T. E. Cowan, M. Roth, M. Singh, S. Hatchett, M. H. Key, D. Pennington, A. MacKinnon, and R. A. Snavely. Energetic proton generation in ultra-intense laser–solid interactions. *Physics of Plasmas*, 8(2):542–549, 2001. 91

[105] B. J. Albright, L. Yin, Kevin J. Bowers, B. M. Hegelich, K. A. Flippo, T. J. T. Kwan, and J. C. Fernández. Relativistic buneman instability in the laser breakout afterburner. *Physics of Plasmas*, 14(9):094502, 2007. 91

[106] E. Fourkal, I. Velchev, and C.-M. Ma. Coulomb explosion effect and the maximum energy of protons accelerated by high-power lasers. *Phys. Rev. E*, 71:036412, Mar 2005. 91

[107] S. S. Bulanov, A. Brantov, V. Yu. Bychenkov, V. Chvykov, G. Kalinchenko, T. Matsuoka, P. Rousseau, S. Reed, V. Yanovsky, D. W. Litzenberg, K. Krushelnick, and A. Maksimchuk. Accelerating monoenergetic protons from ultrathin foils by flat-top laser pulses in the directed-Coulomb-explosion regime. *Phys. Rev. E*, 78:026412, Aug 2008. 91

[108] T. Esirkepov, Y. Sentoku, K. Mima, K. Nishihara, F. Califano, F. Pegoraro, N. Naumova, S. Bulanov, Y. Ueshima, T. Liseikina, V. Vshivkov, and Y. Kato. Ion acceleration by superintense laser pulses in plasmas. *JETP Letters*, 70:82–89, 1999. 10.1134/1.568134. 91

[109] W. L. Kruer. *The Physics of Laser Plasma Interactions*. Westview Press, 2003. 92

[110] G. M. Fraiman, A. A. Balakin, and V. A. Mironov. Coherent effects of ion–electron collisions in a strong laser field. *Physics of Plasmas*, 8(5):2502–2509, 2001. 93

[111] A. Brantov, W. Rozmus, R. Sydora, C. E. Capjack, V. Yu. Bychenkov, and V. T. Tikhonchuk. Enhanced inverse bremsstrahlung heating rates in a strong laser field. *Physics of Plasmas*, 10(8):3385–3396, 2003. 93

[112] M. E. Jones, D. S. Lemons, R. J. Mason, V. A. Thomas, and D. Winske. A grid-based Coulomb collision model for PIC codes. *Journal of Computational Physics*, 123:169–181, 1996. 93

[113] S. T. Perkins and D. E. Cullen. Elastic nuclear plus interference cross sections for light charged particles. *Nuclear Science and Engineering*, 77:1:20–39, 1981. 105, 106, 117

[114] D. V. Sivukhin. *Reviews of Plasma Physics*, volume 4. Consultants Bureau, 1966. 105, 106

[115] R. S. Cohen, L. Spitzer, Jr., and P. McR. Routly. The electrical conductivity of an ionized gas. *Phys. Rev.*, 80:230–238, Oct 1950. 105, 106

[116] R. E. Robson. The significance of high momentum-transfer collisions in ionized gases. *Journal of Physics B: Atomic and Molecular Physics*, 5(4):839, 1972. 107

[117] C. S. Shen and D. White. Energy straggling and radiation reaction for magnetic bremsstrahlung. *Phys. Rev. Lett.*, 28:455–459, Feb 1972. 108

[118] X. Zha, S. Han, Z. Xu, and Y. Wang. Collision operator including large-angle scattering for moderately coupled plasma. *High Energy Density Physics*, 2(34):70 – 76, 2006. 109, 127

[119] L. Ballabio, G. Gorini, and J. Källne. α-particle knock-on signature in the neutron emission of dt plasmas. *Phys. Rev. E*, 55:3358–3368, Mar 1997. 109, 118, 125, 128, 151

[120] N. David. *Molecular Dynamic Calculations of Collisional Effects in Plasmas*. PhD thesis, Christ Church College, University of Oxford, 2005. 109

[121] D. Mihalas. *Stellar Atmospheres*. W. H. Freeman and Company, 2nd edition, 1939. 110

[122] M. Spivak. *Calculus*. Cambridge University Press, third edition, 1967. 112

[123] R. P. Brent. *Algorithms for Minimization without Derivatives*. Dover Publications, Inc, 1973. 113

[124] F. Halzen and A. D. Martin. *Quarks and Leptons*. John Wiley and Sons, 1984. 115

[125] E. Merzbacher. *Quantum Mechanics*. John Wiley and Sons, 3rd edition, 1998. 117

[126] L. Schiff. *Quantum Mechanics*. McGraw-Hill, 3rd edition, 1968. 117

[127] S. Stepney. *Relativistic thermal plasmas*. PhD thesis, Institute of Astronomy and Newnham College, University of Cambridge, 1983. 117, 118

[128] Foster Evans. Energy deposition of a fast deuteron in a hot deuterium plasma. *Physics of Fluids*, 16(7):1011–1020, 1973. 117, 119

[129] J. A. Frenje, C. K. Li, F. H. Seguin, D. T. Casey, R. D. Petrasso, D. P. McNabb, P. Navratil, S. Quaglioni, T. C. Sangster, V. Yu Glebov, and D. D. Meyerhofer. Measurements of the differential cross sections for the elastic n-^{3}H and n-^{2}H scattering at 14.1 mev by using an inertial confinement fusion facility. *Phys. Rev. Lett.*, 107:122502, Sep 2011. 118

[130] T. Yokota, Y. Nakao, T. Johzaki, and K. Mima. Two-dimensional relativistic Fokker-Planck model for core plasma heating in fast ignition targets. *Physics of Plasmas*, 13(2):022702, 2006. 118

[131] J. A. Frenje, R. Bionta, E. J. Bond, J. A. Caggiano, D. T. Casey, C. Cerjan, J. Edwards, M. Eckart, D. N. Fittinghoff, S. Friedrich, V. Yu. Glebov, S. Glenzer, G. Grim, S. Haan, R. Hatarik, S. Hatchett, M. Gatu Johnson, O. S. Jones, J. D. Kilkenny, J. P. Knauer, O. Landen, R. Leeper, S. Le Pape, R. Lerche, C. K. Li, A. Mackinnon, J. McNaney, F. E. Merrill, M. Moran, D. H. Munro, T. J. Murphy, R. D. Petrasso, R. Rygg, T. C. Sangster, F. H. Séguin, S. Sepke, B. Spears, P. Springer, C. Stoeckl, and D. C. Wilson. Diagnosing implosion performance at the National Ignition Facility (NIF) by means of neutron spectrometry. *Nuclear Fusion*, 53(4):043014, 2013. 118, 127

[132] K. A. Brueckner, H. Brysk, and R. S. Janda. Athermal neutrons and ions in a fusion plasma. *Journal of Plasma Physics*, 11:403–409, 1974. 120, 121

[133] K. A. Brueckner and H. Brysk. Fast charged particle reactions in a plasma. *Journal of Plasma Physics*, 10:141–147, 1973. 121, 123

[134] A. Peres and D. Shvarts. Fusion chain reaction - a chain reaction with charged particles. *Nuclear Fusion*, 15(4):687, 1975. 122

[135] E. Greenspan and D. Shvarts. A multigroup model for the slowing-down of energetic ions in plasmas. *Nuclear Fusion*, 16(2):295, 1976. 122, 123

[136] Y. Afek, A. Dar, A. Peres, A. Ron, R. Shachar, and D. Shvarts. The fusion of suprathermal ions in a dense plasma. *Journal of Physics D: Applied Physics*, 11(16):2171, 1978. 122

[137] P. Stroud and J. Gilligan. Effects of Coulombic large-energy-transfer collisions in fusion-grade plasmas. *Nuclear Fusion*, 24(4):455, 1984. 124

[138] Y. Nakao, M. Ohta, and H. Nakashima. Effects of nuclear elastic scattering on ignition and thermal instability characteristics of d-d fusion reactor plasmas. *Nuclear Fusion*, 21(8):973, 1981. 124

[139] H. Matsuura, Y. Nakao, and K. Kudo. Up-scattering of beam ions by nuclear elastic scattering and its effect on energy loss rate in thermonuclear plasmas. *Nuclear Fusion*, 39(2):145, 1999. 124

[140] H. Matsuura and Y. Nakao. Effect of nuclear elastic scattering on ion heating characteristics in deuterium-tritium thermonuclear plasmas. *Physics of Plasmas*, 13(6):062507, 2006. 124

[141] H. Matsuura and Y. Nakao. Distortion of bulk-ion distribution function due to nuclear elastic scattering and its effect on t(d,n)^{4}He reaction rate coefficient in neutral-beam-injected deuterium-tritium plasmas. *Physics of Plasmas*, 14(5):054504, 2007. 124, 125

[142] H. Matsuura and Y. Nakao. Modification of alpha-particle emission spectrum in beam-injected deuterium-tritium plasmas. *Physics of Plasmas*, 16(4):042507, 2009. 124

[143] J. Galambos, J. Gilligan, E. Greenspan, P. Stroud, and G.H. Miley. Discrete nuclear elastic scattering effects in Cat-d and d-^{3}He fusion plasmas. *Nuclear Fusion*, 24(6):739, 1984. 124

[144] G. Kamelander. Investigations of nuclear elastic scattering effects by means of the Boltzmann Fokker-Planck equation. *Nuclear Science and Engineering*, 86:4:351–361, 1984. 124

[145] A. Andrade and G. M. Hale. Nuclear effects on ion heating within the small-angle charged-particle elastic-scattering regime. *Phys. Rev. A*, 30:1940–1947, Oct 1984. 124

[146] D. Ryutov. Energetic ion population formed in close collision with fusion alpha-particles. *Physica Scripta*, 45(2):153, 1992. 124

[147] P. Helander, M. Lisak, and D. D. Ryutov. Formation of hot ion populations in fusion plasmas by close collisions with fast particles. *Plasma Physics and Controlled Fusion*, 35(3):363, 1993. 124

[148] G. Gorini, L. Ballabio, and J. Källne. Alpha-particle kinetic effects in the neutron emission of burning dt plasmas. *Review of Scientific Instruments*, 66(1):936–938, 1995. 125

[149] R. K. Fisher, P. B. Parks, J. M. McChesney, and M. N. Rosenbluth. Fast alpha particle diagnostics using knock-on ion tails. *Nuclear Fusion*, 34(10):1291, 1994. 125

[150] A. A. Korotkov, A. Gondhalekar, and R. J. Akers. Observation of MeV energy deuterons produced by knock-on collisions between deuterium–tritium fusion alpha-particles and plasma fuel ions. *Physics of Plasmas*, 7(3):957–962, 2000. 125

[151] J. Källne, L. Ballabio, J. Frenje, S. Conroy, G. Ericsson, M. Tardocchi, E. Traneus, and G. Gorini. Observation of the alpha particle "knock-on" neutron emission from magnetically confined dt fusion plasmas. *Phys Rev Lett*, 85(6):1246–9, 2000. 125

[152] F. S. Zaitsev, A. Gondhalekar, T. J. Johnson, S. E. Sharapov, D. S. Testa, I. I. Kurbet, and JET EFDA contributors. Suprathermal deuterium ions produced by nuclear elastic scattering of ICRH driven He-3 ions in JET plasmas. *Plasma Physics and Controlled Fusion*, 49(11):1747, 2007. 126, 128

[153] F. S. Zaitsev, A. Gondhalekar, T. J. Johnson, V. G. Kiptily, S. E. Sharapov, and JET EFDA contributors. Simulations to elucidate suprathermal deuterium ion tail observed in He-3 minority icrf heated jet plasmas. In *35th EPS Conference on Plasma Physics*, volume 32D of *ECA*, 2008. 126, 128

[154] M. Sherlock and S. J. Rose. The persistence of Maxwellian d and t distributions during burn in inertial confinement fusion. *High Energy Density Physics*, 5(12):27 – 30, 2009. 19, 126, 131, 143, 165

[155] D. Michta, F. Graziani, T. Luu, and J. Pruet. Effects of nonequilibrium particle distributions in deuterium-tritium burning. *Physics of Plasmas*, 17(1):012707, 2010. 126, 152, 165, 168

[156] J. A. Frenje, D. T. Casey, C. K. Li, F. H. Séguin, R. D. Petrasso, V. Yu. Glebov, P. B. Radha, T. C. Sangster, D. D. Meyerhofer, S. P. Hatchett, S. W. Haan, C. J. Cerjan, O. L. Landen, K. A. Fletcher, and R. J. Leeper. Probing high areal-density cryogenic deuterium-tritium implosions using downscattered neutron spectra measured by the magnetic recoil spectrometer. *Physics of Plasmas*, 17(5):056311, 2010. 126

[157] J. A. Frenje, D. T. Casey, C. K. Li, J. R. Rygg, F. H. Séguin, R. D. Petrasso, V. Yu Glebov, D. D. Meyerhofer, T. C. Sangster, S. Hatchett, S. Haan, C. Cerjan, O. Landen, M. Moran, P. Song, D. C. Wilson, and R. J. Leeper. First measurements of the absolute neutron spectrum using the magnetic recoil spectrometer at OMEGA (invited). *Review of Scientific Instruments*, 79(10):10E502, 2008. 126, 154

[158] M. G. Johnson, J. A. Frenje, D. T. Casey, C. K. Li, F. H. Séguin, R. Petrasso, R. Ashabranner, R. M. Bionta, D. L. Bleuel, E. J. Bond, J. A. Caggiano, A. Carpenter, C. J. Cerjan, T. J. Clancy, T. Doeppner, M. J. Eckart, M. J. Edwards, S. Friedrich, S. H. Glenzer, S. W. Haan, E. P. Hartouni, R. Hatarik, S. P. Hatchett, O. S. Jones, G. Kyrala, S. Le Pape, R. A. Lerche, O. L. Landen, T. Ma, A. J. MacKinnon, M. A. McKernan, M. J. Moran, E. Moses, D. H. Munro, J. McNaney, H. S. Park, J. Ralph, B. Remington, J. R. Rygg, S. M. Sepke, V. Smalyuk, B. Spears, P. T. Springer, C. B. Yeamans, M. Farrell, D. Jasion, J. D. Kilkenny, A. Nikroo, R. Paguio, J. P. Knauer, V. Yu Glebov, T. C. Sangster, R. Betti, C. Stoeckl, J. Magoon, M. J. Shoup, III, G. P. Grim, J. Kline, G. L. Morgan, T. J. Murphy, R. J. Leeper, C. L. Ruiz, G. W. Cooper, and A. J. Nelson. Neutron spectrometry—an essential tool for diagnosing implosions at the National Ignition Facility (invited). *Review of Scientific Instruments*, 83(10):10D308, 2012. 126, 154

[159] Y. Tabaru, Y. Nakao, H. Nakashima, and K. Kudo. Areal density diagnostics using suprathermal fusion reaction for laser-imploded d-t pellets. *Laser and Particle Beams*, 16:153–176, 2 1998. 127

[160] M. J. Moran, E. J. Bond, T. J. Clancy, M. J. Eckart, H. Y. Khater, and V. Yu. Glebov. Deuterium–tritium neutron yield measurements with the 4.5 m neutron-time-of-flight detectors at NIF. *Review of Scientific Instruments*, 83(10):10D312, 2012. 127

[161] S. A. Slutz, M. C. Herrmann, R. A. Vesey, A. B. Sefkow, D. B. Sinars, D. C. Rovang, K. J. Peterson, and M. E. Cuneo. Pulsed-power-driven cylindrical liner implosions of laser preheated fuel magnetized with an axial field. *Physics of Plasmas*, 17(5):056303, 2010. 169

[162] S. A. Slutz and R. A. Vesey. High-gain magnetized inertial fusion. *Phys. Rev. Lett.*, 108:025003, Jan 2012. 169

[163] O. L. Landen, R. Benedetti, D. Bleuel, T. R. Boehly, D. K. Bradley, J. A. Caggiano, D. A. Callahan, P. M. Celliers, C. J. Cerjan, D. Clark, G. W. Collins, E. L. Dewald, S. N. Dixit, T. Doeppner, D. Edgell, J. Eggert, D. Farley, J. A. Frenje, V. Glebov, S. M. Glenn, S. H. Glenzer, S. W. Haan, A. Hamza, B. A. Hammel, C. A. Haynam, J. H. Hammer, R. F. Heeter, H. W. Herrmann, D. G. Hicks, D. E. Hinkel, N. Izumi, M. G. Johnson, O. S. Jones, D. H. Kalantar, R. L. Kauffman, J. D. Kilkenny, J. L. Kline, J. P. Knauer, J. A. Koch, G. A. Kyrala, K. LaFortune, T. Ma, A. J. Mackinnon, A. J. Macphee, E. Mapoles, J. L. Milovich, J. D. Moody, N. B. Meezan, P. Michel, A. S. Moore, D. H. Munro, A. Nikroo, R. E. Olson, K. Opachich, A. Pak, T. Parham, P. Patel, H.-S. Park, R. P. Petrasso, J. Ralph, S. P. Regan, B. A. Remington, H. G. Rinderknecht, H. F. Robey, M. D. Rosen, J. S. Ross, J. D. Salmonson, T. C. Sangster, M. B. Schneider, V. Smalyuk, B. K. Spears, P. T. Springer, L. J. Suter, C. A. Thomas, R. P. J. Town, S. V. Weber, P. J. Wegner, D. C. Wilson, K. Widmann, C. Yeamans, A. Zylstra, M. J. Edwards, J. D. Lindl, L. J. Atherton, W. W. Hsing, B. J. MacGowan, B. M. Van Wonterghem, and E. I. Moses. Progress in the indirect-drive national ignition campaign. *Plasma Physics and Controlled Fusion*, 54(12):124026, 2012. 177